Dissertation

submitted to the

Combined Faculty of Natural Sciences and Mathematics

of Heidelberg University, Germany

for the degree of

Doctor of Natural Sciences

Put forward by

Valentina Montoya

born in:	Medellin, Colombia
Oral examination:	30-01-2025

Phenomenology of very small local dark matter structures

Institute for theoretical physics

Department of physics and astronomy

Ruprecht-Karls-University Heidelberg

Referees: **Prof. Dr. Joerg Jaeckel**

Prof. Dr. Luca Amendola

Abstract

This thesis focuses on studying small-scale dark matter structures. On the one hand, we study very small dark matter structures within the solar system formed by two primary candidates, axions and WIMPs. Exploring how these particles may cluster and produce signals, we test their detectability in light of current and future ground-based experiments. On the other hand, we also study the density profiles of small dark matter halos to address the core-cusp problem, placing these dark matter structures in the broader context of dark matter's distribution on cosmic scales.

For axions, we study the detection of axion miniclusters via haloscope measurements to determine their gravitational potential and density. Our method allows us to measure the axion-photon coupling and the dark matter density separately from a single experiment. We also examine quantum states of axion dark matter, focusing on axion-nucleus interactions and the origin of relevant oscillation frequencies, in particular, on how the quantum state of axions influences observables in experiments. We focus on spin interactions using a Jaynes-Cummings approach and discuss suitable observables for experiments like CASPEr. Nonetheless, the insights gained in our approach can be extrapolated to other experimental setups, such as haloscope cavities.

For WIMPs, we analyze the time-structure signatures of small-scale dark matter clumps, comparing spectral densities of homogeneous versus clumpy distributions. This helps characterize potential time-dependent signals of clumps and estimate detectability in light of future experiments like XENONnT, DARWIN, and future extensions. Finally, looking into small-scale structures, yet larger than the local scale, we explore how exothermic processes in warm dark matter, specifically self-annihilations of SIMPs and ELDERs, impact density profiles of dark matter halos in dwarf galaxies, particularly focusing on how $2 \to 2$ and $3 \to 2$ reactions flatten these profiles, offering insights into dark matter's role on slightly larger scales.

This work provides new insights into the detection and characterization of axion and WIMP dark matter, contributing to understanding their role in the cosmic structure and local distribution.

Zusammenfassung

Diese Dissertation konzentriert sich auf die Untersuchung kleinräumiger Strukturen der Dunklen Materie. Einerseits analysieren wir sehr kleine Dunkle-Materie-Strukturen im Sonnensystem, die durch zwei primäre Kandidaten, Axionen und WIMPs, gebildet werden. Wir untersuchen, wie sich diese Teilchen klumpen und Signale erzeugen können, und testen ihre Nachweisbarkeit im Kontext aktueller und zukünftiger bodengebundener Experimente. Andererseits untersuchen wir die Dichteprofile kleiner Dunkle-Materie-Halos, um das Kern-Krater-Problem zu adressieren, und setzen diese Strukturen in den größeren Zusammenhang der Verteilung Dunkler Materie auf kosmischen Skalen.

Für Axionen untersuchen wir den Nachweis von Axionen-Minikluster mittels Haloskop Messungen, um ihr Gravitationspotential und ihre Dichte zu bestimmen. Unsere Methode ermöglicht es, die Axion-Photon-Kopplung und die Dichte der Dunklen Materie separat in einem einzigen Experiment zu messen. Wir analysieren auch die Quantenzustände von Axionen-Dunkler-Materie mit Fokus auf Axion-Kern-Wechselwirkungen und die Herkunft relevanter Oszillationsfrequenzen. Insbesondere konzentrieren wir uns darauf, wie der Quantenzustand von Axionen experimentelle Beobachtungen beeinflusst. Dabei analysieren wir Spin-Wechselwirkungen mittels eines Jaynes-Cummings-Ansatzes und diskutieren geeignete Observable für Experimente wie CASPEr. Die gewonnenen Erkenntnisse können jedoch auch auf andere experimentelle Aufbauten, wie Haloskop-Kavitäten, extrapoliert werden.

Für WIMPs analysieren wir die zeitabhängigen Signaturen kleinräumiger Dunkle Materien Klumpen, indem wir spektrale Dichten homogener und klumpiger Verteilungen vergleichen. Dies hilft, potenzielle zeitabhängige Signale von Klumpen zu charakterisieren und die Nachweisbarkeit im Hinblick auf zukünftige Experimente wie XENONnT, DARWIN und deren Weiterentwicklungen abzuschätzen. Schließlich betrachten wir größere Strukturen im kleinräumigen Maßstab und untersuchen, wie exotherme Prozesse in warmer Dunkler Materie, insbesondere Selbstvernichtungen von SIMPs und ELDERs, die Dichteprofile von Dunkle Materie Halos in Zwerggalaxien beeinflussen. Wir konzentrieren uns dabei auf $2 \to 2$- und $3 \to 2$ Reaktionen, die diese Profile abflachen und neue Einblicke in die Rolle Dunkler Materie auf etwas größeren Skalen liefern.

Diese Arbeit bietet neue Erkenntnisse über den Nachweis und die Charakterisierung von Axionen- und WIMP-Dunkler-Materie und trägt zum Verständnis ihrer Rolle in der kosmischen Struktur und ihrer lokalen Verteilung bei.

Preface

All the work presented below was performed during my PhD studies at Heidelberg University, ITP.

A version of Chapter 3.3 was published in *JCAP* 05 (2024) 035. Prof. Joerg Jaeckel was the supervisory author of this project and was involved throughout the project in concept formation, analysis, and discussion. I was involved in the discussion and the analytical description of mini-clusters together with Dr. Virgile Dandoy. I contributed to the discussion of the general method for reconstructing the axion-photon coupling and performed the estimation of the rate of encountering suitable axion miniclusters. Prof. Joerg Jaeckel, Virgile Dandoy, and I were involved in manuscript composition and edition. Figs.3.1, 3.2, 3.4, most equations in the main text, and some information and structure in Appendix B.2 and B.3 were kept from [1]. All the results presented in this thesis are used with permission from all researchers involved.

A version of Chapter 3.4.1 was published in *Annalen Phys.* 536 (2024) 1,2300151. Prof. Joerg Jaeckel was the supervisory author on this project and was involved throughout the project in concept formation, analysis and discussion. I was involved in performing the model description and inspecting the simple case of a single spin together with Cedric Quint. I also contributed to describing and discussing suitable measurement procedures for oscillations with the axion mass. Prof. Joerg Jaeckel, Cedric Quint and I were involved in manuscript composition and edition. Figs.3.7, 3.8, 3.9, 3.10 most equations in the main text, and some information and structure in Appendix C.1 were kept from [2]. All the results presented in this thesis are used with permission from all researchers involved.

For the projects located in Chapter 4 and Chapter 5, I was majorly responsible for areas of concept construction, resolution, and analysis, as well as the manuscript composition. In Chapter 4, Prof. Joerg Jaeckel was the supervisory author on this project and was involved throughout the project in concept formation, analysis discussion, and manuscript composition. In Chapter 5, Prof. Laura Covi was the supervisory author on this project and was involved throughout the project in the concept formation analysis discussion. Prof. Joerg Jaeckel contributed to the discussion of analysis and the clarity and composition of the manuscript.

This thesis provides an expanded, modified, and edited discussion of the collaborative work conducted with the co-authors mentioned above, particularly [1,2], while retaining a similar structure. Additionally, tools such as ChatGPT and Grammarly were used to ensure grammatical accuracy, and DeepL was utilized to translate the abstract into German.

Contents

Chapter 1

Introduction

One of the biggest challenges in modern cosmology is understanding the nature of dark matter (DM). The puzzle behind DM is characterized by questions about its composition, the type of interactions DM may have, and how it is distributed on both large and small scales [3]. The DM discussion emerged in 1933 when Fritz Zwicky conducted a study on the Coma cluster, in which he discovered a very high-velocity dispersion within the cluster. This observation led him to conclude that, in order to maintain the stability of the system, the average mass density in the cluster had to be higher than the observed matter [4]. Subsequent investigations of rotation curves highlighted discrepancies in expected versus observed mass distributions, hinting at an unseen gravitational influencer - dark matter [5]. Concisely, spiral galaxies exhibit consistent speeds of stars and gas beyond specific distances from the galactic core. While rotation curves typically follow an anticipated rise and plateau pattern, some deviate with unexpected steep rises, indicating an imperceptible gravitational influence. From this point onwards, extensive measurements of galactic masses have been made to confirm that most of the mass holding a galaxy is *invisible* [6–8].

In the late 20th century, a model including ordinary matter (baryons), a cosmological constant Λ accounting for accelerating expansion, and a cold dark matter (CDM) component was proposed [9–11]. This model is known as the ΛCDM standard cosmological model and has been widely accepted for its ability to explain fundamental observations of the Universe. Notable achievements of the model include the existence and structure of the cosmic microwave background (CMB) [12], the accelerating expansion of the universe [13–15], as well as the observed abundances of hydrogen, helium, lithium, and deuterium, which were formed during the Big Bang Nucleosynthesis (BBN) [16]. In particular, the model successfully explains the large-scale distribution of galaxies [17], attributing it to a cold dark matter (CDM) component that constitutes about 30% of the Universe [18]. CDM is characterized by its low temperature, resulting in negligible particle velocities before galaxy formation, a feature that designated it ”cold”, distinguishing it from faster-moving candidates such as neutrinos. This characteristic makes CDM the most robust candidate to date, especially because of its compatibility with the observed ages of galaxies and the hierarchical formation of small galactic structures [19–24].

While the model performs well in predicting various observational and theoretical aspects of the

Universe, as we previously mentioned, it still faces important limitations in capturing and explaining others [25]. Specifically, there are many challenges regarding the medium and small scales for cold dark matter, mainly because better alignment between predictions derived from numerical simulations and observational data remains a challenge [26, 27], due to limited observational data availability [25–30]. One of the main discrepancies is that simulations produce cusped internal density profiles for halos, whereas low-mass galaxies have shallow or flat density cores. An interesting way to reconcile these discrepancies involves exploring scenarios where the power spectrum asymptotically approaches specific slopes, affecting cluster collapses across mass ranges [31, 32]. The power spectrum slope is sensitive to the formation and evolution of cosmic structures like galaxies, clusters, and voids: a shallower slope favors larger structures, while a steeper slope favors smaller ones. One other way to solve this is Fuzzy Dark Matter (FDM). FDM consists of extremely light scalars that, in dwarf galaxy halos, for example, manifest a wavelike behavior that would avoid cusps due to the Heisenberg uncertainty principle and that at large scales recovers the CDM behavior [33–35]. A further avenue of exploration that is of particular interest for one part of this thesis, is to consider the possibility that DM is not entirely collisionless. This hypothesis suggests that interactions or deviations from purely collisionless behavior could explain the observed discrepancies between simulations and galactic observations. In this direction, the possibility of explaining the problem by self-heating-dark-matter (mainly by $2 \rightarrow 2$ processes) has been studied extensively [36–38]. Aligned to this idea, we explore candidates such as Elastically Decoupling Dark Matter (ELDERs) that are also self-heating candidates that may undergo $3 \rightarrow 2$ processes, the so-called *cannibalization* process [39, 40].This mechanism, which takes place in the inner, denser regions of dwarf galaxies, injects kinetic energy and heats the particle medium. This results in a redistribution of the energy density, which can explain the absence of the cusp.

Another issue concerning small scales arises from the discrepancy between simulations and observations, where models predict more dwarf galaxies than the observed. This phenomenon, known as the missing dwarf problem [41], raises the question of why substructures should be disrupted in galactic halos and how dark matter is distributed in such scales. In addition, there are unresolved issues at even smaller scales, such as the scale of the Solar System, where the properties and distribution of dark matter remain poorly understood.

Dark matter is generally believed to be sparsely distributed and diffuse across the Universe, which means that structures like dark matter subhalos or minihalos are difficult to detect due to their low density. Their faint gravitational effects and minimal interaction with ordinary matter make them challenging to observe. Furthermore, detecting and characterizing such structures requires extremely high precision and sensitivity. These, along with the background noise from various astrophysical sources, such as stars, galactic dust, and other celestial objects, make distinguishing faint signals from dark matter structures a significant challenge.

These challenges motivate us to explore the nature of such small DM structures, and we do so by studying viable dark matter candidates such as weakly interacting massive particles (WIMPs) [42] and Axions [43], that can also naturally account for very small structures. These two dark matter candidates we have mentioned, WIMPs and Axions, have remained very relevant in the field and are the focus of our study. For this reason, we have studied specific characteristics of detectable signals for these candidates in some experiments. In this way, our goal is to understand, based on the imprints that these candidates are likely to leave in ground-based experiments, the distribution of dark matter in our locality. This study is particularly important because some experimental efforts are underway to detect these dark matter candidates, and we aim to test whether they can provide additional insights. Moreover, we emphasize that these experiments have the potential to detect small clumps of dark matter in the neighborhood of our Solar System. While we explore this possibility in this thesis, it is worth clarifying that the detection of structures like axion miniclusters has already been studied by others [44–47].

This work gains significance as ongoing experimental efforts aim to detect these candidates. Specifically, WIMPs have long been considered one of the most promising ones. This is partly due to their weak interactions with the Standard Model (SM) and the potential for detection via elastic scatterings on Earth. Some popular versions of WIMPs include a fourth-generation neutrino [48,49], Super-symmetric WIMPs like the neutralino [50, 51], and simple extensions to the standard model such as odd scalar singlets under Z_2 symmetry [52], among others. Although these models have been the subject of extensive studies, their status in current research remains inconclusive; nonetheless, the research for WIMPS continues. The latest and most significant experimental effort planned to expand and cover the range of parameter space of WIMPs is known as DARWIN [53]. This experiment stands out as another search that has the potential to observe sub-structures by detecting DM through weak/feeble interactions with the Standard Model (SM). While it offers excellent sensitivity to the WIMP-nucleon cross-section, its ability to detect small-scale structures is ultimately limited by irreducible neutrino backgrounds. Despite these, DARWIN's high sensitivity makes it a potential tool for detecting substructures, though future extensions of this capability will likely be needed to probe the small-scale dark matter distribution. One of the goals of this thesis is to study very small dark matter structures in the solar system neighborhood, focusing on WIMPs. We examine particle-like DM interactions within ground-based detectors, we test the detectability of such structures. Comparing this analysis with recent direct detection projections, we aim to determine the minimum detection time required for identifying these very small dark matter structures.

As mentioned above, a second type of DM candidate in which we are interested are axions. These were initially proposed to solve the strong charge-parity (CP) problem but have emerged as a promising dark matter candidate. They are electrically neutral cold bosons, exhibiting slow-motion characteristics that make them suitable for this role. In addition, axions offer increased opportunities for detection in a wide range of experiments [43]. In the context of axion dark matter searches, experiments such as ADMX [54] offer a promising approach to take advantage of the high spectral sensitivity of axion-photon conversion power spectrum measurements. These measurements enable the exploration of parameters associated with the axion and facilitate the refinement of local astronomical measurements. For example, some studies have demonstrated that substructures observed in simulations of Milky Way-like halos exhibit distinct features in the resolved axion power spectrum [55]. In this thesis, we measure the coupling of dark matter axions using a single haloscope experiment, such as ADMX, focusing on detecting axion miniclusters to determine the coupling parameter $g_{a\gamma\gamma}$. Since measurements typically yield a combination of the coupling $g_{a\gamma\gamma}$, and the minicluster density ρ, disentangling these two quantities provides valuable insights into both the coupling strength and the contribution of axions to the overall dark matter density in the galaxy.

Continuing on axion detection, nuclear resonance experiments can offer further understanding of the dynamics of the axion field, exploring its interaction with nucleons [56,57]. Approaching fundamental aspects of the axion, in our case, by exploring the coupling with nucleons, could provide valuable insights into the quantum behavior of these particles. This exploration has the potential to gain insights into how axions distribute among different energy levels and gives some understanding of how these dynamics could impact measurements in DM detection experiments. Beyond this fundamental view, exploring concepts like coherent states, energy eigenstates, and occupation numbers in the study of axions serves as a first step toward understanding the formation of structures. These structures could potentially serve as constituents of DM, such as axion stars and axion miniclusters. Concretely, we explore how the quantum mechanical nature of axions, specifically in scenarios where Earth's gravitational field binds them, impacts experiments aimed at detecting these particles, such as the Cosmic Axion Spin Precession Experiment (CASPEr). [56]. This scenario is challenging since detecting axions bound to Earth's gravity is extremely difficult due to their subtle interactions. While most axions are not expected to be bound to Earth, exploring the scenario of bound axion states can still provide insights that may apply to more general cases. So, studying the time evolution of signals in axion dark matter experiments from a quantum perspective is an initial step into comprehending axion dynamics and anticipates potential signals arising from interactions.

This thesis is organized as follows. In Chapter 2, we review the DM candidates to be studied and some direct detection experiments that can be adapted for the direct search of small structures. In Chapter 3, we review the axion as a DM candidate. Specifically, we consider how the direct detection of an axion mini cluster can provide insights on the dark matter fractions inferred from its gravitational potential (and density). Similarly, we study the quantum nature of the oscillation frequencies present in some Nuclear Magnetic Resonance (NMR)-like experimental setups when considering axions occupying the ground state of the Earth's potential. Chapter 4 studies the detectability of small dark matter structures for WIMPs using sensitivity projection curves from experiments such as DARWIN. Chapter 5 briefly examines the density profile of dark matter halos, reviewing the cusp problem by proposing DM overlying 3 to 2 processes. Finally, in Chapter 6, we summarize and conclude the work done throughout this thesis.

Chapter 2

Dark Matter Preliminaries

In chapter 1, we have discussed that there is a non-baryonic matter component in the Universe [3–8, 58–61]. A further understanding of the density distribution of DM and its measurement is a challenging task, mainly because of the lack of observational data. Several relevant studies have investigated the energy density in small and large-scale DM structures, such as Refs [62–69]. These studies explore a wide range of factors contributing to the dark matter energy density. They range from valuable contributions to the study of techniques to detect smaller dark matter structures like subhalos and clumps in the Milky Way and galaxy clusters, to the cosmological implications of identifying dark matter clumps, strings, and domain walls. These, and multiple other works we will mention in this thesis, motivate us to continue in this line of study.

In the following, we review the dark matter candidates of interest to us, Axions and WIMPs, to study in the following chapters (Chapter 3 and Chapter. 4, 5, respectively) the contribution to the local dark matter density energy based on the potential of these candidates to explain small structures. We also review in the following some specific direct detection configurations to which our study can be applied. The brief review we give below is in the framework of standard cosmology.

2.1 Dark Matter Candidates

When describing a DM candidate, one has to consider characteristics coming from macroscopic features inferred from astrophysical evidence. In general, DM should have either suppressed or absent electromagnetic interaction since there is no evidence of photons scatterings [70–72]. Another characteristic is that we have not seen collision products from these particles, so in principle, DM is assumed to be collisionless. However, the possibility that dark matter has self-interactions or some fraction of the total dark matter has them, is not entirely ruled out and can still be explored [36,73–75]. Another characteristic is that DM is considered cold, i.e., non-relativistic. This assumption aligns with the structure formation hierarchy [76–78]. More specifically, a cold DM candidate enables density perturbations in the early Universe to grow linearly towards the matter domination period, providing early potential wells that launch the growth of baryonic matter density perturbations [79].

Another essential matter concerns the vast range of masses allowed for the candidates to have.

This can be taken as an advantage since it allows for exploring many options and amplifies the experimental research opportunities. From this perspective, one can explore two major approaches regarding treating dark matter: considering it either as a *particle* or as a *wave*, depending on its mass. When considering low mass particles with masses, for example, with masses around 30 eV [80] or lighter, their de Broglie wavelength becomes larger than the average distance between particles at a given location. As a result, in this specific location, these particles can be effectively treated as classical waves. This is, for example, the case of axions. Axions are quantum field bosons, which allows for large excitations in specific field modes, that is, large occupation numbers. Each mode corresponds to a distinct momentum or energy state of the axion. The collective behavior arising from the combination of these modes gives rise to the overall wave-like characteristics observed in axions.

In contrast, if we consider a description of individual particles that are more massive than the previous case, dark matter is described in the particle-like framework [81]. What makes it particle-like is that these particles are localized with well-defined positions and momenta, allowing them to behave as individual entities. In this case, DM can interact with other particles through various forces[1], such as the weak nuclear force in the case of the traditional WIMP; they are also nonrelativistic, and on cosmological scales, particle-like DM is often assumed to behave as a collisionless fluid[2]. This distinction leads to different interpretations and theoretical frameworks for understanding the nature of dark matter. We explore in this thesis both sides, acknowledging WIMPs for particle regime, Sec. 2.1.1, and axions for the wave description, Sec. 2.1.3.

In what follows, we discuss in detail how to produce WIMPs and how to detect WIMPs and Axions (we return to the axions and its detection also in Chapter 3). We focus especially on the experimental setups relevant to this thesis and make a special mention of the experiments that can be used to detect very small DM structures in our vicinity.

2.1.1 WIMPs and other particle-like candidates

WIMPs consist of a dominant fraction of cold, stable, massive, non-relativistic DM expected to interact only weakly with the SM. For our discussion, any DM particle-like candidate detectable by the elastic scatter of a DM particle off a nucleus, or simply by a single register of *clicks* on a detector, is considered a WIMPs, as we study in Chapter 4. These candidates encompass weakly and feebly interacting particles, self-interacting particles, and cold thermal relics, usually known as elastically decoupling relics (ELDERs)[3], [39, 42, 74, 83].

One of the most popular mechanisms to produce such particles is the so-called *freeze-out*, which operates as a thermal production mechanism and provides a predictive framework for understanding

[1] Axions, of course, also have interactions that we will discuss in detail in Sec. 2.1.3

[2] Notably, the collisionless fluid approach can also apply to wave-like dark matter if the mass is not too low, allowing such fields to retain coherence while acting similarly to collisionless particle ensembles on large scales

[3] ELDERs are cold thermal relics whose abundance is set by their elastic scattering cross-section with Standard Model particles. Their decoupling occurs when the scattering rate drops below the Hubble expansion rate, with their final density determined by the efficiency of this process rather than annihilation [82]

the relic abundance of particles in the universe. In this scenario, DM is initially assumed to be in thermal equilibrium with the visible sector during the early stages of the universe. However, as the universe expands and the interaction rate decreases, the chemical equilibrium can no longer be maintained, leading to the decoupling of DM from the plasma. In the following, we will explain in more detail the freeze-out mechanism, alongside a brief mention of an alternative mechanism called *freeze-in*.

Freeze-out

The freeze-out process applies to thermal relics, which are particles that share the same energy spectrum as the surrounding plasma in thermal equilibrium until they decouple. As the universe expands and cools, the interaction rates among particles gradually decrease and become comparable to the Hubble expansion rate, $\Gamma_{\text{ann}} \sim H$ [9,84]. This causes the particles to decouple from the thermal bath because the interactions become inefficient at this moment, and particles are no longer in chemical equilibrium with the surrounding medium. This allows the relic particles to freeze out and retain their abundance, preserving it as the universe continues to expand and cool.

To study the dynamics of the freeze-out process, we study the Boltzmann equations for radiation and DM particles. These equations provide a framework for understanding the interplay between the expansion of the universe, the annihilation rate of DM particles, and the thermal equilibrium between radiation and dark matter during the freeze-out phase [9],

$$\frac{d\rho_R}{dt} = -4H\rho_R + \langle \sigma_{ann} v\rangle \langle E\rangle (\eta_{\text{DM}}^2 - \eta_{\text{DM},eq}^2), \tag{2.1}$$

$$\frac{d\eta_{\text{DM}}}{dt} = -3H\eta_{\text{DM}} - \langle \sigma_{ann} v\rangle (\eta_{\text{DM}}^2 - \eta_{\text{DM},eq}^2), \tag{2.2}$$

where ρ_R is the radiation energy density, $\langle E\rangle$ is the averaged energy of DM particles annihilating and η is the number density of DM particles. From here we can obtain an approximate formula for today's DM abundance,

$$\Omega_{\text{DM}} h^2 \simeq \frac{\rho_{\text{DM}}}{\rho_c} h^2, \tag{2.3}$$

where $\rho_c \approx 8 \times 10^{-47} h^2 \text{G}^6$ is the critical density. Given the annihilation rate $\Gamma_{\text{anh}} = \eta_{\text{DM}} \langle \sigma_{\text{ann}} v\rangle$, one can express the abundance as, see [9],

$$\Omega_{\text{DM}} h^2 \simeq \frac{m_{\text{DM}} \eta_{\text{DM}}(T_0)}{\rho_c} h^2 = \frac{T_0^3}{\rho_c} \frac{x_f}{M_p} \frac{h^2}{\langle \sigma_{\text{ann}} v\rangle_f}, \tag{2.4}$$

where the entropy density goes as $s \sim T^3$, $T_0 \approx 2.3 \times 10^{-13}$GeV is the temperature of the Universe today, $x_f = m_{\text{DM}}/T$ at freeze out. The velocity considered in the thermal average represents the relative velocities between the two particles in the center of mass frame.

Now, the popularity of WIMPs comes from the following reasoning. Assume that in the moment of freeze-out the number density of particles corresponds to the non-relativistic number density [86] and that the range of masses to considered is between $100\text{GeV} - 10\text{TeV}$, which is a scale of masses

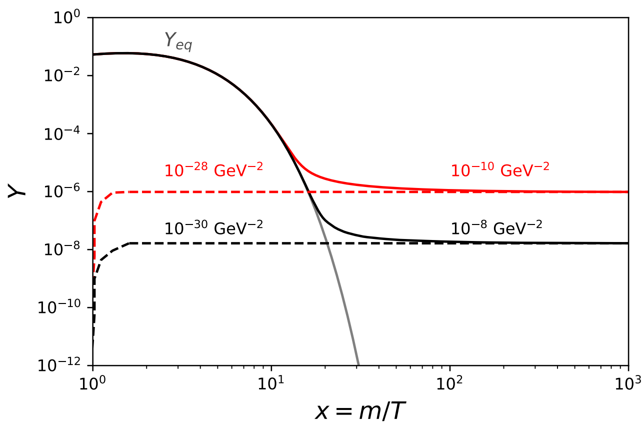

Figure 2.1. Evolution of DM abundance in the early universe inspired by [85]. Here are the freeze-out (solid lines) and freeze-in (dotted lines) are represented as a function of $x = m/T$, for several rates for $m_\chi = 100$ GeV and the solid gray line represents the equilibrium distribution. The corresponding rates for each case, WIMPs(solid lines) and FIMPs (dashed lines), are indicated above each line.

accessible experimentally [42]. One can roughly estimate $x_f \approx 30$, by considering that the number density of DM particles is equal to the non-relativistic equilibrium number density around freeze-out, $\eta_{\text{DM}} \sim \eta_{\text{DM},eq} \sim g(m_{\text{DM}}T/2\pi)^{3/2} \exp\left(-m_{\text{DM}}/T\right)$, where g is the degrees of freedom. Then taking (2.4) for $\Omega_{\text{DM}}h^2 \approx 0.12$ one gets,

$$x_f^{3/2} e^{-x_f} \approx \frac{10^{-8}}{m_{\text{DM}}}. \tag{2.5}$$

This value gives [42, 87, 88],

$$\langle \sigma_{\text{ann}} v \rangle_f \approx 3 \times 10^{-26} \text{cm}^3/s, \tag{2.6}$$

which remarkably coincides with the electroweak scale. In Figure 2.1 we present an illustrative example, showing the behavior of WIMPs (solid lines) before and after decoupling and the freeze-out of relic densities for different annihilation rates. As the annihilation rate is closely related to the interaction coupling with SM particles λ, the behavior of the solid lines in Fig 2.1 points to the fact that the relic density will increase for a smaller λ. Such behavior is not sustainable because the relic density should go to zero rather than infinity as the coupling goes to zero. This is because dark matter should interact with other particles to be thermally produced in the early Universe. Therefore, other well-motivated alternative frameworks for the WIMP paradigm can be proposed.

One alternative to explain the relic abundance of DM for the same mass range is through Feebly Interacting Massive Particles (FIMPs). Unlike WIMPs, FIMPs do not reach thermal equilibrium with the rest of the particles in the universe. Instead, they are produced through collisions or decays of other particles within the thermal plasma. The production process becomes inefficient as the interaction rate decreases, leading to a freeze-in mechanism [89]. The distinction between Feebly

Interacting Massive Particles (FIMPs) and Weakly Interacting Massive Particles (WIMPs) is significant. FIMPs are never in thermal equilibrium with the existing plasma, and they freeze in with a yield that increases as their interaction strength with the thermal bath becomes stronger, as depicted by the dashed lines in Figure 2.1. In contrast, WIMPs freeze out with a yield that decreases as their interaction strength increases. This difference is related to the coupling (λ) with the SM: WIMPs have a coupling of around $\lambda \sim 10^{-4}$ to annihilate, while FIMPs have a coupling of approximately $\lambda \sim 10^{-11}$ for decay or collision processes [83]. Although both scenarios are valid, thermal relics like WIMPs are typically more experimentally accessible since they have larger couplings with the SM.

Existing strategies for detecting DM encompass a wide range of approaches, from direct detection (DD) experiments conducted in laboratories to the search for indirect signals arising from dark matter annihilation or decay. These strategies rely on the assumption that DM consists of a gas composed of freely moving particles with a sufficiently high number density. This high density facilitates the detection of rare DM events by generating a significant flux of DM, thus also giving us insight into the DM distribution. In the following subsection, we will focus specifically on DD experiments for particle-like DM candidates.

2.1.2 WIMP Detection

To detect DM and measure its properties, such as mass, coupling, and interaction cross-section with the SM, several approaches can be taken. One method, known as indirect detection (ID), involves detecting the decay/annihilation products of DM in regions with high DM density, such as the galactic center [90–92]. Furthermore, an exciting option that is very relevant for this thesis is direct detection, where ultra-sensitive experiments aim to detect individual DM-WIMP nucleus scattering processes [93–95]. The concept of direct detection was first proposed by Goodman and Witten [96], who suggested that DM can elastically scatter off atomic nuclei, leading to detectable nuclear recoils. In the following, we will briefly discuss the principles of DD.

DD focuses on searching for scatterings between DM and nuclei in a detector. Since DM particles move at non-relativistic speeds in the halo, the recoil energy of the nucleons can be estimated as,

$$E_R = \frac{1}{2} m_{\mathrm{DM}} v^2 \frac{4 m_{\mathrm{DM}} m_N}{(m_{\mathrm{DM}} + m_N)^2} \frac{1+\cos\theta}{2}, \tag{2.7}$$

where m_N is the mass of the target. The maximal energy is then achieve when $m_{\mathrm{DM}} = m_N$ in a frontal collision, so $E_{\mathrm{R\,max}} = (m_{\mathrm{DM}} v^2)/2$. The number of events expected after and observation time t, can be understood as the product of the DM flux times the number os targets N_T times the scattering cross-section, $N = \phi N_t \sigma t$. The energy spectrum can be obtain by making explicit the energy dependence as,

$$\frac{dN}{dE_R} = \frac{\rho_0 M}{m_{\mathrm{DM}} m_N} \int_{v_{min}}^{v_{esc}} d\vec{v} f(\vec{v}) v \frac{d\sigma}{dE_R}, \tag{2.8}$$

where M is the target mass of the detector and $f(\vec{v})$ is the velocity distribution function for the particles . All the velocities are well defined, and there is an extended study of this velocity distribution in Refs [97–100].

We are particularly interested in studying the strength of the interaction because the amplitude of the recoil spectrum depends on it. More specifically, when a WIMP interacts with a nucleus in a detector, it imparts momentum to the nucleus, causing a recoil. If the WIMP's scattering cross-section is large enough, it can interact coherently with several nucleons simultaneously, provided the WIMP's de Broglie wavelength is comparable to or larger than the size of the nucleus. This coherent interaction leads to constructive interference of the scattered signals from the individual nucleons. The amplitude and shape of the recoil spectrum observed in detectors depend on the distribution of momentum transferred during the interaction. The study and analysis of such momentum transfer is important in discriminating between background events and potential dark matter signals [101,102]. It is important to point out that the interaction of interest is unknown, so to be general, the cross-section must include spin-dependent (e.g axial-vector) and independent (e.g. scalar) coupling [103],

$$\frac{d\sigma}{dE_R} \propto (\sigma_{SD} F_{SD}^2(E_R) + \sigma_{SI} F_{SI}^2(E_R)). \tag{2.9}$$

The factors F_{SD} and F_{SI} account for the loss of coherence that can occur in the interaction with heavy targets. The loss of coherence is caused when the de Broglie wavelength of the WIMP gets reduced by large momentum transfers, $\lambda = 1/q$, so only part of the nucleus participates in the interaction. In the spin-independent case, for example, one has,

$$\sigma_{SI} = \sigma_n \frac{\mu^2}{\mu_n^2} A^2, \tag{2.10}$$

where σ_n is the WIMP-nucleon cross section, μ is the reduced mass, μ_n is the reduced mass of the WIMP-nucleon system and A is the atomic number of the nucleus. This expression assumes that the coupling strength of neutrons and protons is equal. From Eq. (2.10), we see that the heavier the target nuclei, the higher the event rate [104]. The minimum detectable interaction cross-section between dark matter and nucleons in the target material typically characterizes the sensitivity of a direct detection experiment [93, 105, 106]. Different mass ranges can have distinct effects on the sensitivity of direct detection experiments. Heavier particles can transfer more energy to the detector upon interaction, resulting in more significant detectable signals. This is the case for DM particles with masses in the range of GeV to TeV.

The sensitivity of direct detection experiments can be challenging for DM with masses in the range of MeV to GeV; see Fig. 2.3. The sensitivity typically exhibits a characteristic shape reflecting the detector's response to different dark matter masses and interaction cross-sections. At lower dark matter masses, the sensitivity curve often appears relatively flat. This is because lighter particles result in lower energy depositions, making the detector less responsive to interactions. However, the number density of dark matter particles compensates for this, allowing for some sensitivity in this region. As the dark matter mass increases, the sensitivity curve rises sharply until the sensitivity peaks at a particular dark matter mass. The detector is most efficient at detecting DM interactions at this optimal mass range. Beyond the peak sensitivity point, the sensitivity starts to decline. This decrease is due to the reduced interaction rates and energy depositions of heavier dark matter particles into the detector.

Independent of this, to generate a signal, one must account for the energy loss during the interaction, as a significant portion of the recoil energy is transferred to the target material in different forms. A part of this recoil energy is lost to heat, specifically due to nuclear interactions, where the energy is transferred to the nucleus, causing atomic motion. This is referred to as nuclear loss. Additionally, some of the recoil energy is transferred to electrons, ionizing the target atoms, which is referred to as electronic loss. The total energy loss is then the sum of these two components, i.e., $dE_{tot} = dE_{elec} + dE_{nucl}$. Detectors based on the noble liquid Xenon, exploit different targets and model both heat losses, e.g., *cryogenic detectors* [107], and ionization, e.g., *Noble Liquid Detectors* [108]. In what follows, we will focus on experimental setups such as the one for XENON nT [109] and DARWIN [53], because these experiments represent state-of-the-art technologies in the search for direct dark matter interactions. These detectors are also capable of minimizing backgrounds through various shielding and signal identification techniques, enhancing their ability to detect rare interactions and providing a good chance to test very small DM structures as we study in Chap. 4.

Noble Liquid Detectors

Detectors detect mechanical movement or recoil of the material itself, which results from the momentum imparted to the target during the interaction. This recoil can be detected through various means, such as thermal signals in cryogenic detectors. The combination of light and ionization signals provides a way to identify the type and energy of the interaction, while the mechanical recoil helps to quantify the momentum transfer. The interaction products, such as excited states of atoms or ionized atoms, can also contribute to these signals, but the primary focus is on detecting the momentum transfer and subsequent material movement.

Noble gases are known for their stability and inertness because they possess a full valence shell of electrons. However, under certain conditions, noble gases can be easily ionized. Some cases in which ionization can occur are through electron impact, photon absorption, or thermal ionization [110, 111]. In particular, Argon and Xenon are good DM targets when liquefied. The idea of such a detector is to detect photons coming from the de-excitation of the products of the interaction. More specifically, when an interaction occurs within the target material, it can create excited states X^* and ionized atoms X^+. These excited states have the potential to combine with neutral atoms within the material, forming diatomic molecules in excited states, X_2^*. These excited diatomic molecules subsequently decay to lower energy states, emitting ultraviolet photons. The detection of these emitted photons serves as a signal for the original interaction within the detector [108, 112],

$$X^* \xrightarrow{+\mathrm{X}} X_2^* \to 2X + hv. \tag{2.11}$$

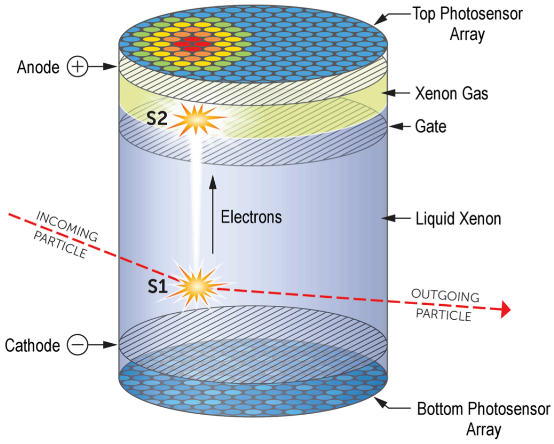

Figure 2.2. Dual-phase TPC Detector using the liquid noble gases argon or xenon as WIMP target. Illustration taken from [112].

Now, the ions X^+ can also combine with neutral atoms and form ionized molecules X_2^+. Using a strong electric field one can remove the ionized electrons to avoid the formation of excited states that will decay as indicated above,

$$X^+ + e^- \xrightarrow{+2X} X_2^+ + X \xrightarrow{+e^-} 2X + X^* + \text{heat} \to 4X + hv. \tag{2.12}$$

Dual-phase time projection chambers (TPC), see Fig. 2.2, by detecting both scintillation light and ionization produced by particles, can provide complementary information that enhances the precision and resolution of energy measurements, like distinguishing different types of particles and interactions, for the purpose of background rejection, improving the overall performance of the detector. Such detectors observe the scintillation signal S1, by placing arrays of photo-multiplier tubes (PMTs) above and below the target tank. An electric field is created on the liquid part of the target to remove the ionization electrons and deviate them to the top of the detector where the gas is. An additional field is required to drive electrons into the gas phase, where a secondary scintillation signal S2 can be detected. This signal is proportional to the number of electrons and measured with the PMTs. The study of the ratio S2/S1 and ionization density leads to the ability to distinguish electronic from nuclear recoils [113].

The XENON collaboration currently operates liquid Xenon at the Gran Sasso Underground Laboratory (LNGS). Starting from liquid dual-phase time projection chambers (TPC) such as the XENON10 [114] and XENON100 [115, 116], the collaboration is now operating with a ton-scale target that is until now, the most sensitive DM detector. Since 2020, the update phase of such experiment has been operating with 3x times larger target mass able to reach a lower background [117,118]. DARWIN, a future update, projects for an exposure of $200t \times y$ (ton-years), that a spin-independent WIMP sensitivity of $2.5 \times 10^{-49}\text{cm}^2$ can be reached at a WIMP mass $m_\chi = 40\text{GeV}/c^2$. The DARWIN experiment aims to achieve very high time resolution capabilities of the order of milliseconds to microseconds[4] [118]. The new sensitivity projected in this experiment could differentiate between individual particles and small clusters of particles. In the context of this thesis, this means that it would be possible to test the presence of tiny structures within the dark matter distribution.

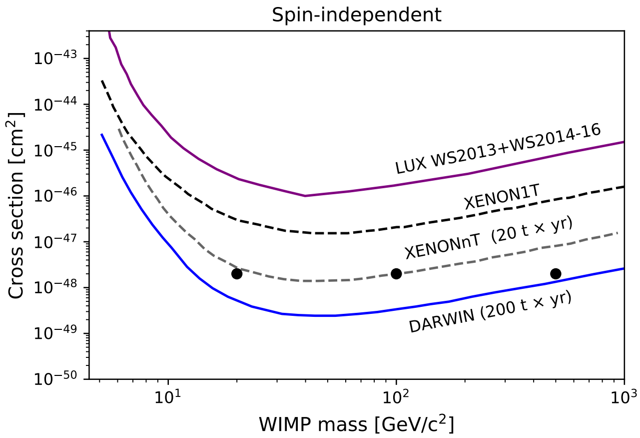

Figure 2.3. Projections for DARWIN experiment(solid line), together with upper limits on the spin-independent WIMP-nucleon cross section for XENON1T (black dashed line), XENONnT (gray dashed line) and LUX (purple solid line), adapted from [53, 112, 119], respectively. The black dots represent benchmark points with masses and couplings not yet excluded for which, in a very simplified way, we have estimated the number of usable events that would be obtained at an exposure of $200t \times y$ (ton-years) and fixed cross section $2 \times 10^{-48}\mathrm{cm}^2$. The corresponding number of events are 16, 21, and 6 for WIMP masses of $20\mathrm{GeV}/c^2$, $100\mathrm{GeV}/c^2$, $500\mathrm{GeV}/c^2$.

Building on the idea of potentially testing very small dark matter structure, we take a look into the corresponding number of detectable events expected for DARWIN. In the case WIMP masses of $20\mathrm{GeV}/c^2$, $100\mathrm{GeV}/c^2$, $500\mathrm{GeV}/c^2$ the number or events are 154, 224, and 60, respectively. They used a fixed cross-section of $2 \times 10^{-47}\mathrm{cm}^2$ and exposure of $200t \times y$ (ton-years) for estimating the number of usable events we mentioned above. Such a cross-section is close to the sensitivity limit of XENON1, as shown in Fig. 2.3. We return to this data later to estimate the detection time of small clumps; see Table 4.3. In order to project later (see, Chapter 5) on possible detections of small clumps, we can roughly estimate the number of events for a cross-section close to the XENONnT limit $2 \times 10^{-48}\mathrm{cm}^2$, assuming the same exposure as before is 16, 21, and 6 for WIMP masses of $20\mathrm{GeV}/c^2$, $100\mathrm{GeV}/c^2$, $500\mathrm{GeV}/c^2$, respectively. Increasing the exposure to $500t \times y$ improves this sensitivity to $\sim 1.5 \times 10^{-49}$ cm^2. DARWIN project [53] is a proposal to explore the entire parameter space available for WIMPs, thus providing a great opportunity to test this candidate, as well as providing a chance to detect small structures due to its sensitivity and projected detection time. Another important alternative, with a lot of power to detect low recoil energies, is the LZ project [120]. AS a concrete example, we study the DARWIN case in Chapter 5, where we estimate and show in Table 4.3 projection of observation times for small structure detection, using the above mentioned sensitivities.

[4]The exact achievable time resolution may vary based on specific detector configurations and experimental conditions

2.1.3 The QCD Axion and other wave-like candidates

The QCD axion and other Axion-like-particles (ALPs) are good DM candidates. One statement that can help us guide our discussion is the fact that for every particle, there is a wave and vice versa, and in the axion case, the wavelength of matter waves can be large $\lambda = 1/mv$. This allows multiple axions to occupy the same quantum state. As the occupation number of these axions grows to macroscopic levels, meaning the number of axions in the same state becomes large enough that quantum mechanical effects average out, they can be effectively described by a classical field rather than a quantum field theory. This classical description emerges because, at macroscopic occupation numbers, the quantum mechanical wavefunction becomes sharply peaked, i.e highly localized in phase-space. In this limit, the quantum fluctuations become negligible, and the axion field behaves as a classical field described by a continuous wave. Therefore, axions are an excellent example of a DM wave-like candidate on which we will focus a large part of this thesis.

Axion DM consists of energy stored in both the spatial and temporal gradients of the axion field, which, along with its mass energy, contributes to the total energy density of dark matter in the Universe. The spatial gradients of the field are typically much smaller in comparison to the mass energy, but they still play a role in defining the dynamics and distribution of axions. The cosmological evolution of the axion, a crucial aspect for our analysis of small structures, will be the focus of an entire section 3.1. This section will underscore the significance of understanding the axion's cosmological evolution in the broader context of dark matter research. In the following, we will give some details about the QCD axion, which is of particular interest to us.

The Axion was originally proposed as a dynamic solution to the strong CP problem [121]. Briefly, the problem arises when considering the Lagrangian of QCD. After imposing gauge symmetries, local symmetries, the particle content, and including all renormalizable hermitian operators, the θ-term is allowed [122],

$$\mathcal{L}_{\text{QCD}} = \theta_{\text{QCD}} \frac{g^2}{32\pi^2} \text{Tr}[F^{\mu\nu} \tilde{F}_{\mu\nu}], \tag{2.13}$$

where F is the strength tensor, $\tilde{F}^{\mu\nu} = \epsilon^{\alpha\beta\mu\nu} F_{\alpha\beta}$ its dual and the trace is running over the group generators. The θ-term is a topological term since it is a total derivative and does not affect the classical equations of motion. Quantum mechanically it has implications, for example, it allows CP-violating interactions such as the neutron electric dipole moment (EDM), d_n. From theory, $d_n \sim \times 10^{-16} \theta_{\text{QCD}}\ e$cm, where e is the electron charge [123], and the experimental constrained is $|d_n| < 2.9 \times 10^{-26}$, suggesting $\theta \leq 10^{-10}$ [124–127]. The smallness of the θ_{QCD} parameter in the QCD Lagrangian is considered fine-tuned because its natural value is expected to be of order unity, as there is no intrinsic mechanism in the theory to suppress it. The smallness of θ_{QCD} is then the cornerstone of the matter, see App A.1.1.

Recently there has been some discussion as to whether the CP problem really exists, and some alternative explanations have been given [128–131]. In this thesis we follow the standard assumptions, and to do so we consider the most popular solution that was proposed by Peccei-Quinn in 1977, and it is obtained by minimally extending the SM with a new global symmetry that is classically conserved, $U(1)_{PQ}$ under which some quarks are charged, inducing a chiral symmetry that is anomalous [121,132–134]. To break the symmetry a complex scalar field is included, $\phi_{\mathrm{PC}} = |\phi| e^{a/f_a}$ with a potential, Fig 2.5a,

$$V(\phi_{\mathrm{PQ}}) = \mu \left(|\phi|^2 - \frac{f_a^2}{2} \right)^2 , \tag{2.14}$$

where f_{a} represents the scale for the spontaneous symmetry breaking of $U(1)_{\mathrm{PC}}$, and a becomes the Nambu-Goldstone boson of the broken symmetry, known as the axion. As a consequence the axion has then a shift symmetry, Fig 2.5b, so that,

$$a \to a + \langle \alpha \rangle f_a , \tag{2.15}$$

where $\langle \alpha \rangle$ is dimensionless parameter with the range $0 \leq \langle \alpha \rangle \leq 2\pi$ [133, 134]. This means that its value can be shifted by a constant without affecting the physics of the system. It ensures that the axion potential is periodic and allows the axion to have a naturally light mass. Now the $U(1)$ chiral current is not conserved and therefore the axion field acquires anomalous coupling to gluons as shown in Fig 2.4. The Lagrangian becomes,

$$\mathcal{L} \propto \frac{1}{2} \partial_\mu a \partial^\mu a + \mathcal{L}_{\text{int}}[\partial^\mu a / f_a, \Psi] + (\theta + \xi \frac{a}{f_a}) \frac{g^2}{32\pi^2} F_a^{\mu\nu} \tilde{F}^a_{\mu\nu}, \tag{2.16}$$

with Ψ are quarks fields. From here, one can see that the potential of the axion has a minimum at $-\theta f_a / \xi$. Therefore,

$$\left\langle \frac{\partial V_{\text{eff}}}{\partial a} \right\rangle = -\frac{\xi}{f_a} \frac{g^2}{32\pi^2} \langle F_a^{\mu\nu} \tilde{F}^a_{\mu\nu} \rangle_{\langle a \rangle = -\frac{f_a}{\xi} \theta} = 0. \tag{2.17}$$

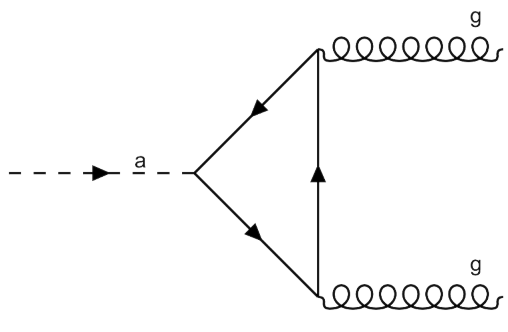

Figure 2.4. Axion-gluon- gluon coupling diagram.

At this point, where the effective potential derivative is zero, the CP-violating term in the QCD Lagrangian arising from $F\tilde{F}$ is zero, and therefore solves the strong CP problem, see App A.2.

In what follows, we will briefly summarize the interactions of the axion with the standard model relevant to the experimental searches and the approaches to describing dark matter as an axion pertinent to this thesis.

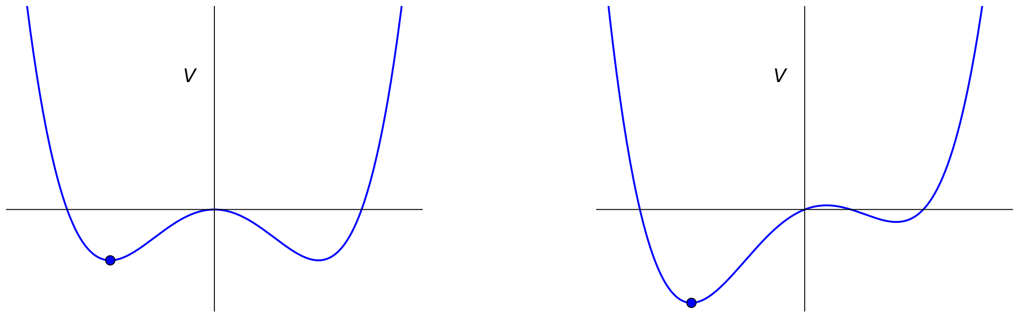

(a) Potential of the PQ field. **(b)** Broken Axion shift symmetry.

Figure 2.5. In the left panel an illustration of the potential of PQ field after symmetry breaking is shown. The right panel illustrates that after symmetry breaking, when the QCD effects take place, the potential shifts or deforms, leading to a non-zero minimum at $\langle a \rangle = -\theta f_a/\xi$. The right panel, exaggerates the shift for illustrative purposes.

Axion interactions with SM

A general interaction Lagrangian at low energies [135–137],

$$\mathcal{L}_{int} = -\frac{g_{\phi\gamma\gamma}}{4}\phi F^{\mu\nu}\tilde{F}_{\mu\nu} + i\sum_{f=n,p,e}\frac{g_{\phi f}}{2m_f}(\partial_\mu\phi)\overline{\Psi}_f\gamma^\mu\gamma_5\Psi_f - i\sum_{f=p,n}\frac{g_{\phi f\gamma}}{2m_f}\phi F^{\mu\nu}\overline{\Psi}_f\sigma_{\mu\nu}\gamma_5\Psi_f,$$

where $g_{\phi f}$ are dimensionless under this convention, $g_{\phi\gamma\gamma}$ has mass-dimension -1 and $g_{\phi f\gamma}$ has mass-dimension -2 [138]. All the couplings are proportional to $1/f_\phi$, one can introduce dimensions-less couplings to see explicitly,

$$g_{\phi\gamma\gamma} \equiv \frac{\alpha}{2\pi}\frac{C_{\phi\gamma\gamma}}{f_\phi}, \quad g_{\phi f} \equiv \frac{C_{\alpha f} m_f}{f_\phi}, \quad g_{\phi f\gamma} \equiv \frac{C_{\alpha f\gamma}}{f_\phi}. \tag{2.18}$$

Estimations of the values for the coupling constants mentioned above can be performed for KSVZ and DFSZ models throughout some QCD calculations (see Ref [139]).

Of particular interest are the observational implications of the interactions of the axion with the SM. In the following, we briefly outline the interactions and some experiments of interest.

Axion-Photon coupling

The axion to photon coupling, $g_{\phi\gamma\gamma}$, describes, in principle, a decay of one axion into two photons $\phi \to 2\gamma$, with frequency per photon of $\omega = m_a/2$. For the axion DM case, the breaking scale is sufficiently large so that the lifetime of the axion is longer than the age of the universe. Nonetheless, this coupling also describes the axion mixing to a photon in the presence of strong electromagnetic fields. This process is known as the Primakoff effect. One of the experimental techniques to access this channel, consists of a laser directed through a strong magnetic field toward a wall. The photons in the magnetic field can convert into axions, and very weakly interacting axions can penetrate the

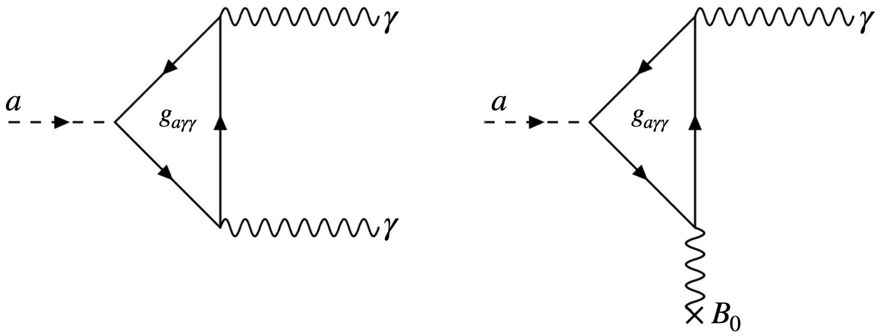

Figure 2.6. Axion decay into photons. Left) Decay in vacuum. Right) Inverse Primakoff effect in a static magnetic field (B_0).

wall. If a strong magnetic field behind the wall is applied, the axions can convert them back into detectable photons; such experiments are called light shining through a wall (LSW) [140–143].

For DM axions, one can use the inverse Primakoff effect Fig. 2.6, by using a microwave cavity with a strong magnetic field as a haloscope, assuming that axions permeate the Earth constantly [144]. The idea is to induce a resonant mixing with photons to produce a microwave signal; later in this chapter we go into more detail on this topic. **ADMX** [145, 146], has been the leading contributor to the search for axion cold dark matter. It consists of a large superconducting solenoid, with the field of $\sim$ 7.6 Tesla. As mentioned above, when the axion field interacts with this strong magnetic field inside the cavity, it can convert into a photon. This conversion process is governed by the Primakoff effect to convert dark matter axions into low-energy photons. A cylindrical microwave cavity is used to resonate the decay signal, coupled to an antenna, to maximize such signal. Some limits on the axion-photon coupling in a parameter range were reported [54, 147, 148]. In Section 2.1.4, we discuss in more detail the haloscope experimental setup, which is very relevant for studying objects like axion miniclusters. This setup not only provides a detection opportunity but also offers valuable insights into these structures. The experiment enables precise measurement of the energy spectrum, allowing us to potentially determine the depth of the gravitational well during encounters with gravitationally bound objects. In Section 3.3, we use this method to reconstruct the axion coupling and further explore its implications.

Axion-Nucleon coupling

The axion coupling to nucleons provides some interesting new concepts that could be tested. Mainly, it can be probed indirectly in astrophysics through the effects on the cooling of neutron stars and from the analysis of the observed neutrino signal in supernovae [149–155]. In this case, the crucial process is nucleon-Bremsstrahlung $n + n \to n + n + a$. Some limits on the coupling can be found in Ref. [156].

For the purposes of this thesis the crucial feature is that DM direct is also possible considering the interaction of the DM axion background field with the spin of the nucleon. An experiment of particular interest devoted to this direct search is CASPEr [157]. **CASPEr**, uses an NMR technique to search for axion dark matter, see Sec 2.1.4, based on dark-matter-driven spin precession. The interaction here is treated considering first a magnetic field B as a driving field. Then, a sample of polarized nuclear spins with an initial magnetization oriented by a leading field, B_0, is taken. If the Larmor frequency, $\omega_L = \gamma I B_0$, where γI is the gyromagnetic ratio of the nucleus, is equal to the frequency of the driving field B, the nuclear spins will perform precession into the transverse plane. The resulting precessing magnetization generates a magnetic field that a suitable detector can measure. We use this approach in Section 3.4.1 to explicitly check and discuss how the signals and the different relevant time scales expected from the standard classical calculation arise in a quantum mechanical picture for this type of axion experiment.

In what follows, we will detail some direct detection experiments that are of interest to this thesis.

2.1.4 Axion Direct Detection

The search for axions can be extended to their different interactions with the SM. As we have previously announced in Sec. 2.1.3, it is of interest to delve a little into the DD of axions by exploring axion-to-photon coupling [144] and axion-to-nucleon coupling [155, 157], since the studies developed throughout this thesis specifically employ these couplings and the specific setups we are about to describe. For this reason, and in a simple and simplified way, we will gather basic information about the setups for which the study described in Chapter 3 can be performed.

Axion-to-photon coupling: Strategies for axion searches mostly rely on the axion-to-photon coupling [144]. In this case, the principle consists of a strong magnetic field that generates virtual photons that can interact with axions and, as a result, be converted into real photons, see Fig. 2.6. Haloscopes have provided the most sensitive axion searches by constraining DM halo signals using microwave resonators. Specifically, we are referring to experimental configurations that resemble the ones employed by the ADMX collaboration [158,159]. Other relevant setups include ORGAN [160], QUAX [161], and CAPP [162].

One can aim to detect very weak conversions of an axion to microwave photons when a strong magnetic field is present using a resonant microwave cavity. In general, in the presence of the axion field, one has [163, 164] [5],

$$\nabla \times \boldsymbol{E} = -\frac{\partial \boldsymbol{B}}{\partial t}, \tag{2.19}$$

$$\nabla \times \boldsymbol{B} = \frac{\partial \boldsymbol{E}}{\partial t} - g_{a\gamma\gamma}\boldsymbol{B}\frac{\partial a}{\partial t}. \tag{2.20}$$

If an external magnetic field B_o permeates the cavity, the axion photon coupling $g_{a\gamma\gamma}$ will induce an external electric field that can be measured as,

$$(\partial_t^2 - \nabla^2)\boldsymbol{E}_{\text{ind}}(\boldsymbol{x}, t) = g_{a\gamma\gamma}\boldsymbol{B_0}(\boldsymbol{x})\partial_t^2 a(\boldsymbol{x}, t). \tag{2.21}$$

[5] We assume that no charge or electromagnetic current are present in the resonant cavity.

The axion field $a(\boldsymbol{x},t)$ entering in a cavity will interact with the static magnetic field $\boldsymbol{B}(\boldsymbol{x})$ set inside it. This interaction will produce an electric field $\boldsymbol{E}(\boldsymbol{x},t)$ that we could detect afterwards. To reconstruct the axion field in terms of the photon signal, one can expand the axion field in Fourier modes,

$$a(\boldsymbol{x},t) = \int \frac{d^3k}{(2\pi)^3} \left(a(\boldsymbol{k}) e^{-i\boldsymbol{k}.\boldsymbol{x}} e^{i\omega(\boldsymbol{k})t} + c.c. \right), \tag{2.22}$$

with $\omega(\boldsymbol{k}) \approx k^2/(2m) + m$.
Likewise, the photon field can be written as a superposition of the cavity modes $\boldsymbol{E}_i(\boldsymbol{x})$,

$$\boldsymbol{E}(\boldsymbol{x},t) = \sum_i \alpha_i(t) \boldsymbol{E}_i(\boldsymbol{x}), \tag{2.23}$$

where $\int_V d^3x \boldsymbol{E}_i(\boldsymbol{x}).\boldsymbol{E}_i^*(\boldsymbol{x}) = 1$ [1]. The projection of each cavity mode results from integrating Eq (2.21),

$$(\partial_t^2 + \omega_i^2)\alpha_i(t) = \int \frac{d^3k}{(2\pi)^3} \left(a(\boldsymbol{k}) \omega^2(\boldsymbol{k}) \mathcal{G}_i(\boldsymbol{k}) e^{i\omega(\boldsymbol{k})t} + c.c. \right), \tag{2.24}$$

with

$$\mathcal{G}_i(\boldsymbol{k}) = g \int_V d^3x\, \boldsymbol{E}_i^*(\boldsymbol{x}) \cdot \boldsymbol{B}(\boldsymbol{x}) e^{-i\boldsymbol{k}\boldsymbol{x}}, \tag{2.25}$$

as the geometric factor. The solution of this equation can be written as [165, 166],

$$\alpha_i(t) = \int \frac{d^3k}{(2\pi)^3} \left(a(\boldsymbol{k}) \omega^2(\boldsymbol{k}) \frac{\mathcal{G}_i(\boldsymbol{k})}{(\omega_i^2 - \omega(\boldsymbol{k})^2)} e^{i\omega(\boldsymbol{k})t} + c.c. \right), \tag{2.26}$$

where photons oscillate back and forth within the cavity with a specific frequency that corresponds to the axion mass, such resonant behavior can be seen through the denominator $(\omega_i^2 - \omega(\boldsymbol{k})^2)$ that manifests as delta-like peak in the signal and that, overall, will enhance the resolution as we are about to explain in the following (in Appendix B.1, we calculate the extraction of the axion field from some cavity shape.).

This formalism can be applied to setups such as ADMX, Fig. 2.7a, and others testing the axion-to-photon coupling. In particular, our interest is focused on their potential to test and study structures such as miniclusters (see Sec. 3.2.3) due to the good spectral resolution they usually have. This is because the Fourier analysis provides a spectrum representing the frequency distribution, allowing for precise identification and measurement of individual frequency components [167]. Frequency resolution also plays a crucial role. This appears as a narrow peak in the output spectrum of the detector. Axions within the galactic halo exhibit non-relativistic behavior, meaning that the energy of an individual axion with mass m_a and velocity v is,

$$E = m_a c^2 + \frac{1}{2} m_a v^2, \tag{2.27}$$

where c is the speed of light. The axion-to-photon conversion process upholds energy conservation, meaning that an axion with energy E_a transforms into a photon with a frequency $\nu = E_a/h$. If the frequency ν falls within the bandwidth of a cavity mode, the conversion process experiences resonant enhancement. Consequently, the signal manifests as a peak in the spectrum detected [168].

Having established the physics of the experiment, let us take a more detailed look at one particular the setup of the experiment to get a general idea of how it works[6]. It consists of a right circular cylinder with 30 cm of diameter and around a meter tall. The cylinder is copper-coated and acts as a microwave cavity inside an 8 Tesla superconducting magnet [169]. Two copper and dialectic rods are moved from the edge to the cavity center, allowing the photon conversion in the resonant modes of the cavity. When photons are captured by an antenna positioned at the top of the cavity (exhibiting wave-like behaviour), they are transported to microwave amplifiers for further processing.

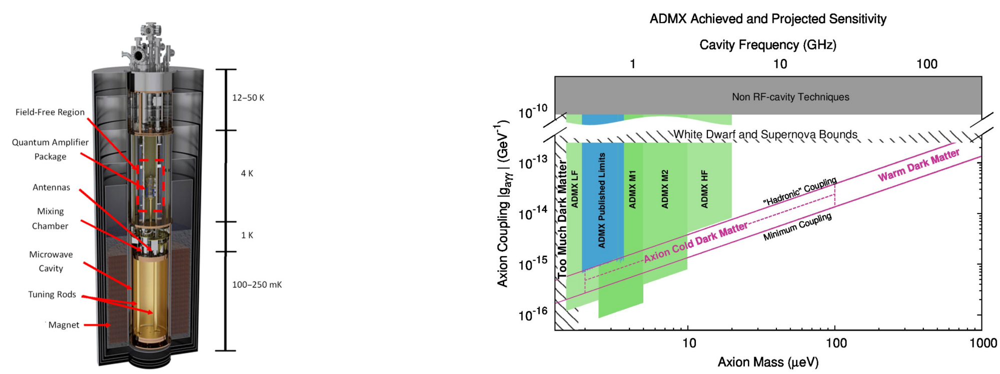

(a) Design of ADMX experiment

(b) Target of ADMX experiment

Figure 2.7. ADMX experiment. On the left side we present and illustrative Design of ADMX experiment. Taken from [169]. On the right hand side, the target of ADMX experiment. The green regions are target to be explored in the upcoming years meanwhile the blue region represents the already excluded parameter. Taken from [169].

ADMX can probe a range for the parameter space of mass and coupling, which includes DM axions regardless of the fraction of energy density that is represented by such candidate. The target range this experiment is aiming to probe can be seen in Fig. 2.7b.

Axion-to-nucleon coupling : the axion search can also be driven by exploring the axion-nucleon interaction. In principle, the axion is an oscillating field, $a(t) = a\cos(\omega_a t)$, seen by a detector on the Earth. To detect it, one can consider [56, 139, 170],

$$\mathcal{L}_{\text{EDM}} \approx -\frac{i}{2} g_d a(\vec{r},t)\overline{\Psi}_n \sigma_{\mu\nu}\gamma_5 \Psi_n F^{\mu\nu}, \tag{2.28}$$

where F is the electromagnetic field strength tensor, g_d parameterizes the axion-gluon coupling that generates nuclear EDMs and Ψ_n is nucleon wave function. The interaction $\mathcal{L}_{\text{EDM}}$ describes an oscillating nuclear electric dipole moment generated by the axion field along the direction of the nuclear spin,

$$\vec{d}_n(t) = g_d a_0 \cos\omega_a t \hat{\vec{\sigma}}_n, \tag{2.29}$$

[6]There are several setups to attain axion detection. We focus on one particular experiment that can be used to implement the studies proposed in this thesis.

that interacts with an external electric field. The non-relativistic Hamiltonian describing this interaction is,

$$H_{\mathrm{EDM}} = \vec{d}_n(t) \cdot \vec{E}, \tag{2.30}$$

with the corresponding spin torque $\vec{\tau}_{\mathrm{EDM}} = \vec{d}_n(t) \times \vec{E}$. Considering that the average influence on the nuclear spins is zero due to the oscillation of the dipole moment, one needs to include a magnetic field B orthogonal to the electric field to rotate the spins such that the effect of the torque always adds up and a measurable signal can be obtained.

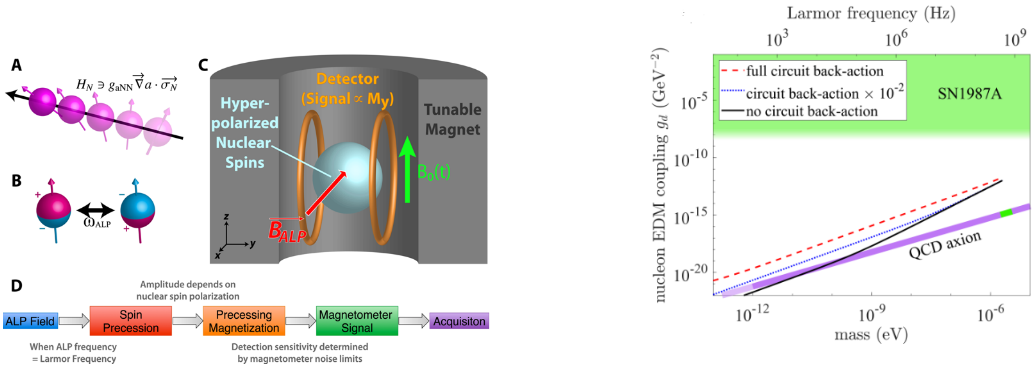

(a) Design of CASPEr-e. **(b)** Spin-projection-noise limits.

Figure 2.8. In the left hand side and illustrative design of CASPEr-e is shown, taken from [171]. In the left hand side the spin-projection-noise limits for magnetic resonance-based searches are shown. The green regions are already excluded by analysis of cooling in supernova SN1987A. Taken from [172].

The CASPEr setup consists of a large number of nuclear spins that are pre-polarized and placed in an external magnetic field $\vec{B}_{ext}$ with an electric field $\vec{E}$ applied perpendicular to $\vec{B}_{ext}$. When there is a nucleon EDM, the nuclear spins precess around the electric field in a reference frame rotating with the Larmor frequency of the spins, simplifying the analysis of their dynamics. As a result, the spins become magnetized at an angle to the magnetic field and start to rotate around this field at a specific rate (Larmor frequency) in the lab frame. This rotation yields a detectable oscillation of the transverse magnetization caused by the magnetic moment of the spins in resonance; that is, the Larmor frequency of the nuclear spins must be equal to the axion frequency, very similar to NMR set ups [56, 173], see Fig. 2.8. We make use of relation between the axions and NMR-like experiments like CASPEr-e to gain an understanding of oscillation frequencies in a quantum mechanical picture, as well as insights on suitable possible measurements to feature an oscillation with the axion mass, see Sec 3.4.1.

Chapter 3

Exploring Axions as Dark Matter: Detection, Miniclusters, and Quantum Dynamics

Among the many extensions of the SM predicting dark matter candidates, axions are very well-motivated. The axion is a spin-zero, parity odd field resulting from the spontaneous breaking of the PQ symmetry as a pseudo-Goldstone boson. As we reviewed in Sec 2.1.3, they were initially proposed as a solution to the strong CP problem for quantum chromodynamics (QCD), but they can also address the dark matter puzzle [43, 121, 133, 134, 174–176]. Throughout this chapter, we review the axion cosmology, establish the conceptual and theoretical basis for our study of axion as DM, and we present our study of its phenomenology (below, we establish the structure of the chapter in more detail). To this end, in the following, we set the stage in the early universe that we are interested in as a starting point for describing the axion cosmology.

Observations of the CMB suggest that the early Universe was flat and uniform [177, 178]. Additionally, the isotropy of the CMB yields crucial insights into the dense state of the early Universe, implying that specific events like inflation [179] could have established the necessary initial conditions for the hot Big Bang epoch, characterized by a maximum temperature T_{hot} and time t_{hot}. Now, the axion field emerges from the spontaneous breaking of the Peccei-Quinn (PQ) symmetry, as detailed in Section 2.1.3. Generally, axion fields resulting from PQ symmetry breaking perform later oscillations, making them a compelling candidate for dark matter. However, axions contributing to dark matter can be studied based on when the PQ phase transition occurs relative to a specific temperature scale. As we will discuss in Section 3.1, PQ symmetry breaking creates causally disconnected patches, each with a different value of θ_{PQ}. While not all patches produce topological defects, those that do can influence the formation and evolution of large, medium, and small structures in the early Universe through their gravitational effects. If the PQ phase transition occurs before a particular temperature scale $T_{PQ} > T_{hot}$, meaning it takes place during the inflationary period, the rapid expansion during inflation leads to the dilution of relics associated with the phase transition. As a result, the patches of different θ_{PQ} values get stretched, resulting in a uniform value of θ_{PQ} throughout the Hubble volume at the end of inflation [180–182]. Such initial value of θ_{PQ} has a random value selected from a uniform distribution, meaning the axion can be described as a random field. Such a field provides the required dark matter energy density since it comprises a large population of non-relativistic axions that are effectively collisionless [165, 176, 183].

On the other hand, if the PQ phase transition occurs after the temperature scale ($T_{PQ} < T_{hot}$), that is, after inflation, the axion field is not homogenized, such that the present-day Universe is made up of many patches that had different initial values of $\theta_{\rm PQ}$. This diversity in the initial values of θ_{PQ} has important implications for the cosmological and astrophysical phenomena associated with abundance, distribution, and potential observational signatures. Interesting dark matter objects called axion miniclusters can be described in this scenario, accounting for small dark matter structures [184, 185]. We explore the phenomenology of this case using haloscopes as a guiding example, which allows us to study the characteristics of typical axion miniclusters and get insights into the density distribution of dark matter. We additionally explore NMR-like experimental arrangements to study the quantum mechanical states for axions and how they might affect the observables. To this aim, we focused on axions occupying the ground state of the potential of the Earth as our contribution towards comprehending the detection characteristics and fingerprint of the axions in the case of an encounter.

In this chapter, we study the DM axion by exploring the axion-photon and axion-nucleon coupling, and we seek to learn details about DM from such couplings in DD experiments. To set the scene we first, in Sec 3.1, review non-thermal production mechanisms in the early Universe for DM axions. In Sec 3.2, we present basic concepts for studying axion miniclusters and extend the haloscope formalism (already introduced in Sec 2.1.4)for the particular case we are studying. Moreover, we explore in Sec 3.3 the size of the axion-photon coupling by studying the spectral information available in haloscopes. Such information provides the gravitational potential within the minicluster and, therefore, an opportunity to measure density and coupling separately, providing a good opportunity to measure the density of dark matter and the fraction it represents. Finally, in Sec 3.4.1, we study the time evolution of signals of a spin precession experiment such as CASPEr from a quantum perspective.

3.1 Axion Cosmology

DM axions can, in theory, constitute a substantial fraction of the energy density of the Universe. Small axion masses imply large occupation numbers, so the action can be described by solving the classical field equations, as we mention in Sec.2.1.3. After symmetry breaking, the action of an axion can be described as a minimally coupled scalar field [9, 165, 186],

$$\mathcal{S}_a = \int d^4x\sqrt{-g}\left[\frac{1}{2}(\partial a)^2 - V(a)\right]. \tag{3.1}$$

Taking the variation of the action w.r.t a one gets the equation of motion,

$$\Box a - \frac{\partial V}{\partial a} = 0. \tag{3.2}$$

where $\Box = 1/\sqrt{-g}\partial_\mu(\sqrt{-g}g^{\mu\nu}\partial_\nu)$. For a FRW metric and a potential of the form $m_a^2 a^2/2$, Eq. (3.2) provides the equation of motion for a spatially uniform axion field. To show this, let us first rewrite the d'Alembertian operator in terms of the Hubble rate, $H(t) = \dot{R}(t)/R(t)$,

$$\Box = -\frac{1}{R(t)^3}\frac{\partial}{\partial t}\left(R(t)^3\frac{\partial}{\partial t}\right) + \nabla^2,$$

here $R(t)$ represents the scale factor. Since we are considering a homogeneous and isotropic universe, the Laplacian term acts on the spatial part of the field, which should be zero for a homogeneous field. Then Eq. (3.2) becomes,

$$-\left(\frac{1}{R(t)^3}\frac{\partial}{\partial t}\left(R(t)^3\frac{\partial}{\partial t}\right)\right)a - m_a^2 a = 0, \tag{3.3}$$

$$\ddot{a} + 3H\dot{a} + m_a^2 a = 0. \tag{3.4}$$

When the Universe is dominated by matter or radiation, Eq. (3.4) has an exact solution depending on the set initial conditions, leading to different production regimes. In the following section, we briefly discuss a suitable production mechanism for axion DM.

3.1.1 Axion Production Mechanisms

In the early universe, it is possible to produce axions thermally and non-thermally. Typically, when axions are produced thermally, they have relativistic velocities, making them less likely to form the observed dark matter structures [43, 184, 185]. Additionally in this case when considering that axion and DM relic abundances are comparable [43], the axion must have a mass of $\sim$ eV; otherwise, the contribution to the energy density will be insufficient, and for smaller masses or couplings, the thermal fraction becomes too small. For this reason, we focus on describing the non-thermal production mechanism for the QCD axion in the following section.

3.1.2 Non-Thermal production of axions

Non-thermal production is the basis for a relevant cosmological contribution of axions and ALPs to the relic DM density. One mechanism to produce axions consists of considering that initially, at a particular scale, the axion field will be single-valued over a fraction or entire Universe, depending on the scenario we are studying, as we will mention in further detail in the next sections. Non-perturbative QCD effects, will cause a potential for the axion field, and when such effects become significant, the axion field begins to oscillate around the minimum of the potential and generate axion particles, see Sec. 2.1.3. These oscillations do not decay and contribute to the local energy density. This is the so-called vacuum realignment mechanism[1] [165, 176, 186, 190]. This production case allows two physical analyses depending on the moment the phase transition occurs, before or after inflation. In the following, we review these pre- and post-inflationary production cases as a preamble to our study.

[1] Additionally, PQ symmetry breaking can lead to the formation of topological defects, such as domain walls and strings, which emit axions during their evolution and further enhance the dark matter density [187–189].

Pre-Inflation Scenario

From Eq.(3.4), one can identify that the field starts to oscillate with a frequency, $\omega = m_a$ as soon as $H(T) \lesssim m_a(T)$, hence an ansatz for solving the equation [9, 165, 186],

$$\theta(t) = A(t)e^{i\Phi(t)},$$

where $A(t)$ and $\Phi(t)$ are real. The equation of motion becomes,

$$\frac{\ddot{A}}{A} - \dot{\Phi}^2 + 3H\frac{\dot{A}}{A} + m_a^2 = 0, \tag{3.5}$$

where we define H from now on as $H = \dot{R}/R$.

For the WKB approximation we have that $\ddot{A}/A, H\dot{A}/A \leq \dot{\Phi}^2, m_a^2$, meaning that $A(t)$ varies slow w.r.t t. From such assumption we find,

$$\dot{\Phi}^2 = m_a^2 \qquad \Rightarrow \Phi(t) = \int dt' m_a(t') + C, \tag{3.6}$$

and,

$$\dot{A} + A\left(\frac{3}{2}H + \frac{\dot{m}_a}{2m_a}\right) = 0 \qquad \Rightarrow A(t) = \frac{C}{R^{3/2}\sqrt{m_a(t)}}. \tag{3.7}$$

Substituting these solutions into Eq. (3.5) one gets,

$$\theta(t) = \frac{C}{R^{3/2}\sqrt{m_a(t)}} \cos\left(\int_{t_0} dt' m_a(t')\right), \tag{3.8}$$

where the constant C depends on the initial conditions, and can be determined analysing the behaviour of the energy density before and after the field starts to oscillate. This implies,

$$\begin{aligned} &\text{for} \quad H > m_a & \rho_a(t) &= \frac{1}{2} f_a^2 m_a^2(t)\theta_I^2, \\ &\text{for} \quad H < m_a & \langle\rho_a(t)\rangle &= \frac{C^2}{2m_a(t)}\frac{f_a^2 m_a^2(t)}{R^3}, \end{aligned}$$

where we have taken the mean value for the fast oscillation performed by Eq. (3.8). The above energy densities should be equal at $t = t_{osc}$ or, $T = T_{osc}$. Setting $3H(T_{osc}) = m_a(T_{osc})$ one gets,

$$C^2 = m_a(T_{osc})R^3(T_{osc})\theta_I^2, \tag{3.9}$$

$$\rho_a(T) \simeq \frac{1}{2} f_a^2 m_a(T_{osc}) m_a(T) \left(\frac{R(T_{osc})}{R(T)}\right)^3 \theta_I^2, \;\; T < T_{osc}. \tag{3.10}$$

The above results show that the energy stored in the axion field is sensitive to the specific time at which the field begins to oscillate; such a feature allows some fine-tuning to obtain the right density for DM.

Post-Inflation Scenario

In this scenario, the Peccei-Quinn symmetry breaks after inflation has ended. The axion field independently acquires random values between $(-\pi, \pi]$ for each causally disconnected region [165].

However, as the observable universe encompasses numerous causally disconnected regions, the energy density of axions in the present-day universe can be computed by taking an average across these regions, as in Eq. (3.10),

$$\overline{\rho_a} = \frac{1}{V} \int d^3x \rho_a(\vec{x}),$$

the total sum will obey,

$$\overline{\rho}_a \backsimeq \frac{1}{2} f_a^2 m_a(T_{osc}) m_a(T) \left(\frac{R(T_{osc})}{R(T)} \right)^3 \overline{\theta}_I^2, \tag{3.11}$$

where $\overline{\rho_a}$, and $\overline{\theta}_I$ represent the mean energy density and the sum over all the random draws θ_I, respectively. For a rough estimation, let us consider that when the oscillations begin, the axion field comprises numerous distinct patches with varying values of θ_I. In this scenario, the energy density of each patch is contingent on its starting misalignment angle θ_I, but should otherwise follow Eq. (3.10), so that the mean depends on the sum over all patches $\overline{\theta}_I$. An estimate of $\overline{\theta}_I$ can be made by assuming it follows a flat probability distribution $\mathcal{F}(\theta)$, so that,

$$\overline{\theta}_I^2 = \int d\theta \mathcal{F}(\theta) \theta^2 = \frac{\pi^2}{3}, \tag{3.12}$$

in the interval $(-\pi, \pi]$.

Here, the energy density is independent of any value of θ_I and unlike the pre-inflationary case, the density is fixed by f_a and m_a, which makes this scenario more predictable.There may be additional exciting phenomena linked to this scenario since there may also be significant local DM overdensities and, thus, a highly non-linear evolution. Topological defects, cosmic strings and axion miniclusters are examples of such interesting phenomena [191–193]. In the following, we will devote particular importance to the phenomenology of axion miniclusters since they are the cornerstone for our study of small DM structures in the locality of the Solar System.

3.2 Axion Miniclusters

As mentioned, the post-inflationary scenario gives inhomogeneous initial conditions to the axion field that cause large isocurvature fluctuations in the energy density. These fluctuations, while potentially significant, do not pose a problem for axion dark matter because, after inflation, the axion field undergoes a slow-roll phase where these inhomogeneities smooth out over time[2]. Additionally, large overdensities can decouple from the Hubble expansion at high redshifts and collapse into gravitationally bound objects, such as axion miniclusters [184,185,197]. If a significant fraction of DM is in miniclusters, this could impact DD experiments targeting the high mass regime[3] suggested by the

[2]Such fluctuations can have other interesting phenomenological consequences for axion DM. Cosmic strings are interesting phenomenological consequences worth mentioning, nonetheless they are not the main topic of our work. In the following references some more information about them can be found [194–196]

[3]Since experiment subsets are optimized to detect DM within specific mass ranges, as discussed in Chapter 2, the high mass regime in this context refers axions with masses up to a few MeV.

relic density from defect decay. Impacts between axion miniclusters and Earth have been estimated to be rare. However, such events open a new window for diverse searches that can be carried out by experiments such as axion DM direct detection in haloscopes, as we will discuss later.

A complete and consistent description of the axion minicluster enables us to test its footprint in detection and aids in extracting valuable information about the dark matter itself, which is one of the main goals of the work presented in this chapter. Once dark matter detection is successful, the subsequent challenge becomes even more significant: understanding the nature of the signal and extracting information about the specific fraction of dark matter to which the detection pertains. Multiple detections by one or several experiments are necessary to analyze this. To this aim, one has to consider that each experiment is influenced by different powers of the coupling strength times the dark matter density, $g^n \rho_{DM}$. This variation in sensitivity introduces challenges in accurately determining the coupling strength, as the extraction process is often affected by inherent degeneracies between the coupling and the dark matter density.. To address this problem, we propose an optimistic approach that takes advantage of the internal structure of axion miniclusters. The idea is to use a single DD experiment to reconstruct the axion-photon coupling. Haloscope searches achieve high spectral resolution, see Sec. 2.1.4, which facilitates the study of the internal structure of the minicluster, in the case of encountering one, and therefore it is possible to gain insights into the properties of the axion field and potentially obtain valuable information about the coupling strength [1].

We will now give a general description of an axion minicluster, where we explore the typical sizes and masses of these objects.

The following subsections are based on Ref. [1]. This work was done by Virgile Dandoy, Joerg Jaeckel, and Valentina Montoya. I was involved in the discussion and the analytical description of miniclusters, in Sec. 3.2.3, together with Virgile Dandoy. I contributed to the discussion of the general method for reconstructing the axion-photon coupling and performed the estimation of the rate of encountering suitable axion miniclusters, Sec. 3.2.3. The complete work was included with additional explanations since it is essential to understand the context properly. All the results presented in this thesis are used with permission from all researchers involved.

3.2.1 Axion Minicluster general overview

Based on cosmological principles of structure formation in the early Universe [9, 198, 199], one can estimate the typical size and mass of an axion minicluster, assuming that it has been created from a fluctuation that has collapsed in the matter radiation equality era [9, 184]. After that point in the evolution, matter began to dominate the energy density of the Universe, leading to the gravitational collapse of structures. The size of the minicluster is then related to the scale of the fluctuation that led to its formation, providing a way to infer its characteristic size [200],

$$R_{AMC} \sim \frac{R(T_{eq})}{R(T_{osc})H(T_{osc})}, \tag{3.13}$$

where,

$$H(T) = 1.66\sqrt{g_*(T)}\frac{T^2}{M_{PL}}, \tag{3.14}$$

where g_* is the number of degrees of freedom at a given temperature. Using the conservation of the entropy density, we can calculate the radii ratio as $s(T_{osc})R^3(T_{osc}) = s(T_{eq})R^3(T_{eq})$, with $s(T) = (4\pi^2/45)g_{s*}(T)T^3$ and $g_{s*}(T)$ as the weighted relativistic degrees of freedom,

$$R_{AMC} \sim \left(\frac{g_{s*}(T_{osc})}{g_{s*}(T_{eq})}\right)^{1/3} \frac{M_{PL}}{T_{osc}T_{eq}} \frac{0.06}{\sqrt{g_*(T_{osc})}}, \tag{3.15}$$

where $g_{s*}(T_{osc})$ is the number of relativistic degrees of freedom at a given temperature. Expressing the oscillation temperature for $\Lambda = 75.5\text{MeV}$ as [184, 201],

$$T_{osc} = 1.2\text{GeV}\frac{1}{g_*(T_{osc})^{1/8}}\left(\frac{10^{12}\text{GeV}}{f_a}\right)^{1/6}, \tag{3.16}$$

and for $g_*(T_{osc}) = 100$, $g_{s*}(T_{eq}) = 3$ and $T_{eq} = 2.3 \times 10^{-9}$ GeV,

$$R_{AMC} \sim 4.5 \times 10^8\text{km}\left(\frac{f_a}{10^{12}\text{GeV}}\right)^{1/6}. \tag{3.17}$$

Now, we can estimate the mass from the definition of the average density in Eq. (3.11) ,

$$M_{AMC} \sim \frac{4}{3}\pi\overline{\rho}_a(T_{osc})R_H^3(T_{osc}), \tag{3.18}$$

where $R_H(T_{osc}) = \pi/H(T_{osc})$ is the corresponding size of the Hubble patch [202]. Since we are considering the oscillations start in the radiation era, we can define $m_a(T_{osc}) = 3H(T_{osc})$, and $m_a(T) = \Lambda^2/f_a$. We therefore find that the typical mass is of about $M_{AMC} \sim 10^{-11}\text{M}_\odot$ for $f_a = 10^{12}$ GeV. Therefore, an axion minicluster would typically be of a mass similar to transneptunian objects like 120347 Salacia (minor planet) with a size comparable to that of the Sun. The mass and the radius of the minicluster in what follows will be taken as free parameters for simplicity.

One question that arises now is how to make a late time description of the miniclusters in a self-consistent way. To target this question, we can consider the clusters as not-too-dense self-gravitating objects in the nonrelativistic and low-density regime, which, as we will explain momentarily, is typically well described by the Schroedinger equation [203–205],

$$\frac{\partial}{\partial t}\Psi(x,t) = \left[-\frac{\hbar^2}{2m}\frac{\partial^2}{\partial x^2} + V(x,t)\right]\Psi(x,t). \tag{3.19}$$

In this context, we can consider a complex scalar field denoted as $\Psi(x,t)$ and establish a naive connection between the complex field ψ and the real field ϕ,which serves as our starting point for the axion. This connection is made possible by recognizing that while the real field undergoes oscillations with a frequency of $\omega = m_a$, it exhibits gradual variations in its density field within the nonrelativistic regime. To capture this behavior, we neglect the rapid oscillations of the field, resulting in the introduction of a complex field. Subsequently, we identify this complex field as the positive frequency component of the real scalar field, with the removal of a phase factor [205–207],

$$\phi(\vec{r},t) = \frac{1}{\sqrt{2m_a}}(e^{-im_a t}\psi(\vec{r},t) + e^{+im_a t}\psi^*(\vec{r},t)), \tag{3.20}$$

in other words, $\phi = \mathrm{Re}[e^{-im_a t}\psi]$ with the oscillating phase factor $e^{\pm im_a t}$ removed from the complex field. In the limit where the time derivatives of ψ are much smaller than its mass, $\dot{\psi} \ll m\psi$, we can write the action for the system as,

$$\begin{aligned}\mathcal{S} = \int dt \int d^3r \left(\frac{i}{2}(\psi\dot{\psi} - \dot{\psi}^*\psi)\right) - \frac{1}{2m_a}\nabla\psi^* \cdot \nabla\psi \\ - V_{eff}(\psi^*\psi) - m_a\psi^*\psi\Phi - \frac{1}{8\pi G}\nabla\Psi\nabla\psi.\end{aligned}$$

The variational equations are,

$$i\dot{\psi} = -\frac{1}{2m_a}\nabla^2\psi + m_a\Phi\psi + V'_{eff}(\psi^*\psi)\psi, \tag{3.21}$$

$$\nabla^2\Phi = 4\pi G m_a\psi^*\psi. \tag{3.22}$$

The above set of equation can be identified as the Gross-Pitaevskii-Poison system for a specific effective potential, and as expected, recovers the Schroedinger-Poisson system for $V_{eff} = 0$.

One can analytically attempt to solve this equation by decomposing the wave function into energy eigenmodes of the Schroedinger equation and averaging over the complex coefficients a_i described by the Poisson equation. Without this decomposition, solving the Poisson equation becomes challenging due to the time dependency of the interference between different modes. Therefore,

$$\begin{aligned}\left(-\frac{\nabla^2}{2m_a} + m_a\phi(\boldsymbol{x})\right)\psi_i(\boldsymbol{x}) = E_i\psi_i(\boldsymbol{x}), \\ \nabla^2\phi(\boldsymbol{x}) = 4\pi G m_a\langle|\psi(\boldsymbol{x},t)|^2\rangle = 4\pi G m_a\sum_i |a_i|^2|\psi_i(\boldsymbol{x})|^2.\end{aligned} \tag{3.23}$$

The average performed is an ensemble average. In this sense, an individual minicluster will still carry a density featuring (time-dependent) fluctuations due to the interference terms,

$$\rho = m_a|\psi(\boldsymbol{x},t)|^2 = m_a\sum_i |a_i|^2|\psi_i(\boldsymbol{x})|^2 + m_a\sum_{i\neq j} a_i a_j^*\psi_i(\boldsymbol{x})\psi_j^*(\boldsymbol{x})e^{-i(E_i-E_j)t}, \tag{3.24}$$

where the fluctuations in the AMC density profile appear in the second term on the right-hand side. These *granules* have a characteristic length scale of the order of the de Broglie wavelength,

$$\ell_{\text{gran}} \sim \lambda_{\text{dB}} \sim 1/(m_a v), \tag{3.25}$$

and a characteristic time scale

$$T_{\text{gran.}} \sim 1/(m_a v^2), \tag{3.26}$$

where v is the typical velocity dispersion of the cluster [208–210]. In the context of our study, the fluctuations due to this granule structure play an important roll, as they represent density variations that limit the precision in measuring the coupling, as discussed in Section 3.3.1.

In Appendix B.2, the general set up for the construction of the wave function of a self-gravitating system is discussed in more detail, based on a random phase assumption [211] for the coefficients of each mode.

3.2.2 Explicit Axion minicluster Wave Functions in the WKB Approximation

To describe axion miniclusters, we need to obtain the stationary solutions of the Schroedinger equation in the WKB approximation, Refs. [204,210] (see also [211–213]). Let us take the relevant wave equation for non-relativistic axions,

$$H_0\psi_E(\vec{r}) \equiv \left[-\frac{1}{2m_a}\nabla^2 + m_a\phi(\vec{r})\right]\psi_E(\vec{r}) = E\psi_E(\vec{r}). \tag{3.27}$$

One can assume a potential that is spherically symmetric, so it is possible to describe the potential in terms of the spherical harmonics,

$$\psi_{nlm}(\vec{r}) = R_{ln}(r)Y_{lm}(\theta,\phi), \tag{3.28}$$

where n, l and m are the radial , angular and magnetic quantum numbers. We can obtain the radial wave functions R_{nl} by solving Eq.(3.27) as,

$$-\frac{\hbar^2}{2m_a}\frac{d^2u}{dr^2} + \left[\frac{\hbar^2}{2m_a}\frac{l(l+1)}{r^2} + m_a\phi(r)\right]u = Eu, \tag{3.29}$$

where $u \equiv rR_{nl}(r)$. The expression inside brackets represents the effective potential for which we will assume slow variations w.r.t the de Broglie wavelength λ. Since we are dealing with a potential that slowly varies and the wavelength being much smaller than the characteristic length scale of the potential , the WKB approximation is handy [214],

$$\frac{\lambda}{2\pi} = \frac{1}{\sqrt{2m_a(E_n - V_{eff})}} \ll \frac{E_n - V_{eff}}{|dV_{eff}/dr|} \sim D, \tag{3.30}$$

where D represents the he characteristic size of the system. For the effective potential, as consequence of the WKB approximation [215]: $l(l+1)$ is approximated as $\to (l+1/2)^2$. Adding $1/2$ in the parentheses is a correction term that helps improve the accuracy of the approximation, which becomes l^2 in the limit $l \gg 1$. Therefore,

$$V_{eff} = \frac{\hbar^2}{2m_a}\frac{l^2}{r^2} + m_a\phi(r). \tag{3.31}$$

The solution for $R_{nl}(r)$ at next-to-leading order is given by,

$$R_{nl}(r) = \frac{1}{\sqrt{\mathcal{N}_{nl}}}\frac{1}{r}\frac{1}{[2m_a(E_n - V_{eff}(r))]^{1/4}}\sin\left(\int^r dr'\sqrt{2m_a(E_{nl} - V_{eff}(r'))} + c\right), \tag{3.32}$$

where the normalization constant $\mathcal{N}_{nl}$ and c will be determined by the the energy of the bound states after averaging over fast oscillations.

To construct a self-consistent wave function so that the gravitational potential is fixed, one has to solve Eq. (3.23) and derive a general expression for the coefficients $|a_i|$, for which the wave function becomes [204, 210],

$$\psi(r,\theta,\phi) = \sum_{nlm} a_{nlm} e^{i\phi_{nlm}} R_{nl}(r) Y_{lm}(\theta,\phi). \tag{3.33}$$

The energies E_{nl} of the modes are assumed to be independent of the quantum number m due to the spherical symmetry, and the l-dependence also becomes unimportant in the continuum limit of large miniclusters. The radial part is defined following the above assumptions as,

$$R_{nl}(r) = \frac{1}{\sqrt{\mathcal{N}_{nl}}} \frac{1}{r} \frac{1}{[2m_a\,(E_n - V_l(r))]^{1/4}} \sin\left(\int^r dr' \sqrt{2m_a\,(E_n - V_l(r'))} + \pi/4\right), \tag{3.34}$$

where $V_l(r)$ is the effective potential for a given angular momentum and $\mathcal{N}_{nl}$ is a constant for correct normalization. With that, the Poisson part of Eq. (3.23) yields [204, 210],

$$a_{nlm} = 4\pi \sqrt{m_a \mathcal{N}_{nl} \frac{f(E_n)}{g_l(E_n)}}, \tag{3.35}$$

where $g_l(E_n) = 2m_a\, , \mathcal{N}_{nl}/\pi$ is the density of states for a given angular momentum l[4] and $f(E_n)$ is the distribution function of the AMC. The latter is directly derived from $\phi(r)$ and $\rho(r)$ [216].

It is important to make two remarks for the axion miniclusters that can be described by this formalism. First of all, only clusters satisfying,

$$1 \ll 1.2 \times 10^4 \left(\frac{m_a}{50\mu\text{eV}}\right) \left(\frac{M}{10^{-5}\text{M}_\odot}\right)^{1/2} \left(\frac{R}{10^{-4}\text{pc}}\right)^{1/2}, \tag{3.36}$$

will be considered for now on. The reason for imposing such a condition is that we must avoid contributions from the exponential tail of the WKB wave functions for low energy modes (classical forbidden regions) that signify the decay of the wave function into the classically forbidden region, reflecting the probability of finding the particle in those regions due to quantum tunneling effects [217, 218]. These considerations become significant when approaching the wavelength limit specified in equation (3.30) since, as we have mentioned already, the WKB approximation is most reliable when the system's size significantly exceeds the de Broglie wavelength. In this regime, the classical behavior dominates, and the WKB approximation provides a good approximation of the quantum behavior.

To ensure high accuracy in measuring the gravitational potential using the axion energy spectrum, we need to impose stricter conditions. Specifically, we require that $\sqrt{2m_a|\phi(r) - \phi(r-\Delta)|}\Delta >> 1$, ensuring that no contributions from low-energy modes interfere up to a defined turning point $(r - \Delta)$ and establish a substantial potential energy barrier. By estimating $\phi \sim m_a GM/R$ as detailed in [204] (assuming $b \sim R$), with M representing the cluster mass and R its radius, we derive the condition $\lambda/R \ll (\Delta/R)^{3/2}$. Assuming a reasonable precision of $\Delta/R \sim 0.01$ (which also approximates the relative precision of the potential), we arrive at the inequality above. Consequently,

[4]Note that, we will actually never need to calculate the density of states since it will drop out when the continuous approximation for the energy levels is taken (see Ref. [204]).

we disregard the exponentially decaying segment of the WKB wave function. Furthermore, it is important to note that the wave functions formulated within this framework cannot capture non-equilibrium states resulting from stellar interactions. Therefore, our analysis is limited to considering only miniclusters in virial equilibrium.

The assumption of virial equilibrium in our system allows us to draw a comparison with spherically symmetric galactic systems. In both cases, we can assume that the phase-space density is uniformly sampled, meaning that the distribution function is isotropic in both systems. This similarity provides a foundation for extending the methods used in galactic dynamics to the case of axion miniclusters. To make this connection explicit, we will first review the formalism used for astrophysical systems that exhibit spherical symmetry and isotropy. Then, we will derive the distribution function that describes the minicluster case.

Isotropic systems

By definition, an isotropic system has a velocity dispersion tensor isotropic everywhere. Thus, every system with an ergodic distribution function (DF) is isotropic [219]. Let us take a closer look at that statement.

In a steady-state potential $\phi(\mathbf{x})$, the Hamiltonian is an integral of motion, and one can aim to describe an equilibrium system just by taking the f as a non negative function of H. This constitutes an ergodic DF, meaning the system uniformly explores its energy surface in phase space. We can take a look at the mean velocity of the system for a constant potential [219–221],

$$\overline{\mathbf{v}}(\mathbf{x}) = \frac{1}{\nu(\mathbf{x})} \int d^3\mathbf{v}\mathbf{v} f\left(\frac{1}{2}v^2 + \Phi\right), \tag{3.37}$$

where $\nu(\mathbf{v}) \equiv \int d^3\mathbf{v} f(\mathbf{x}, \mathbf{v})$. As we can see, the integrand is an odd function of v, and since the integration limits include the whole velocity space, $\overline{\mathbf{v}}(\mathbf{x}) = 0$ everywhere. A similar analysis can be done to the velocity dispersion tensor of the system,

$$\sigma^2(\mathbf{x}) = \frac{1}{\nu(\mathbf{x})} \int dv_z v_z^2 \int dv_x dv_y f\left(\frac{1}{2}(v_x^2 + v_y^2 + v_z^2) + \Phi(\mathbf{x})\right), \tag{3.38}$$

$$= \frac{4\pi}{3\nu(\mathbf{x})} \int_0^\infty dv v^4 f\left(\frac{1}{2}v^2 + \Phi\right), \tag{3.39}$$

such that $\sigma_{ij}^2 = \overline{v_i v_j} = \sigma^2 \delta_{ij}$. Then the velocity dispersion tensor is isotropic.

In the case of a spherical system confined by a known spherical potential $\Phi(r)$, we can derive a unique ergodic DF based on the Hamiltonian. To do so, let us look the probability density for this particular case,

$$\nu(r) = 4\pi \int dv v^2 f\left(\Psi - \frac{1}{2}v^2\right) \to \nu(\Psi) = 4\pi \int_0^\Psi d\mathcal{E} f(\mathcal{E})\sqrt{\Psi - \mathcal{E}}, \tag{3.40}$$

where $f = 0$ for $\mathcal{E} \leq 0$ and $\Psi = -\Phi + \Phi_0$. Differentiating w.r.t Φ,

$$\frac{1}{\sqrt{8}\pi} \frac{d\nu}{d\Psi} = \int_0^\Psi d\mathcal{E} \frac{f(\mathcal{E})}{\sqrt{\Psi - \mathcal{E}}}. \tag{3.41}$$

The above equation has a solution of the type,

$$f(\mathcal{E}) = \frac{1}{\sqrt{8}\pi}\frac{d}{d\mathcal{E}}\int_0^{\mathcal{E}} \frac{d\Psi}{\sqrt{\Psi - \mathcal{E}}}\frac{d\nu}{d\Psi}, \tag{3.42}$$

known as the Eddington's formula [219, 222]. Given a spherical density distribution, one can get an ergodic DF that generates the required model.

This procedure is commonly used in galactic dynamics. For the axion minicluster case, we have to make some conditions explicit so the AMC can be treated as described above. Let us consider the AMC described by Eq. (3.33). Moreover, let us look at an average minicluster by taking the ensemble average over the random phases ϕ_{lmn}, such that the average density can be expressed as,

$$\rho(r) = m_a\langle|\psi(r, \theta, \phi)|^2\rangle = m_a \sum_{nlm} |a_{nlm}|^2 R_{nl}(r)^2 |Y_{lm}(\theta, \phi)|^2. \tag{3.43}$$

Here, we need to also perform an average over the fast oscillations in R^2_{nl}. Is important to note that the whole ensemble average leads to an spherically symmetric distribution. We can rewrite the density as,

$$\rho(r) = \frac{4\pi m_a^2}{r^2}\int_{m_a\phi(r)}^0 dEf(E)\int_0^{l_{max}(E,r)} dl \frac{l}{\sqrt{2m_a(E - V_{eff}(r))}}. \tag{3.44}$$

For the angular momentum at a given r and E, the allowed $l_{max}(r, E)$, will be given by $E = V_{eff}(r)|_{l_{max}}$, as well as the integral dE will run from the effective potential $V_{eff}(r)|_{l_{max}}$ to 0. Therefore the density,

$$\rho(r) = 4\pi m_a^2 \int_{m_a\phi(r)}^0 dEf(E)\sqrt{2m_a(E - m_a\phi(r))} \tag{3.45}$$

which brings us to the case of Eq. (3.40), i.e., the astrophysical case.

3.2.3 Axion miniclusters in Haloscope Experiments

After addressing the question of how to describe the minicluster, we now face the question of how to detect them from Earth to extract some information about their potential and density from the spectral power of the detection. As a specific case of study, we expand the discussion in Sec. 2.1.4 on cavity haloscopes [163] for the case of axion miniclusters.

Let us recall that for cavity experiments, one can, through the interaction of the axion with the magnetic field in the cavity, have access to the induced electric field as in Eq. (2.21).

We can expand the electric field into cavity modes (cf., e.g., [163, 223, 224]),

$$\boldsymbol{E}_{\text{ind}}(\boldsymbol{x}, t) = \sum_j \alpha_j(t)\boldsymbol{E}_j(\boldsymbol{x}), \qquad \int_V d^3x|\boldsymbol{E}_j(\boldsymbol{x})|^2 = C_j, \tag{3.46}$$

where $\boldsymbol{E}_j(\boldsymbol{x})$ stands for the mode j and $\alpha_j(t)$ the time dependent coefficient, we can rewrite the equation of motion as,

$$(\partial_t^2 + \frac{\omega_j}{Q}\partial_t + \omega_j^2)\alpha_j(t) = -b_j\partial_t^2 a(\boldsymbol{x}, t), \tag{3.47}$$

where Q is the quality factor in the cavity and $b_j \propto g_{a\gamma\gamma} \int_V \mathrm{d}^3x \boldsymbol{E}_j^*.\boldsymbol{B_0}$. Now we can extract the power per mode of the cavity in terms of the time averaged electric field [223],

$$P_j = \frac{\omega_j}{Q}\frac{1}{2}\int_V \mathrm{d}^3x\, \langle|\alpha_j(t)|^2\rangle |\boldsymbol{E}_j(\boldsymbol{x})|^2. \tag{3.48}$$

In a more realistic case, what is measured is an average over a total measurement period T. Therefore the average power can be written as,

$$\begin{aligned} P_j &= \frac{\omega_j}{2Q}\int_V \mathrm{d}^3x\, \frac{1}{N_T}\sum_{n=0}^{N_T-1} |\alpha_j(t_n)E_j(\boldsymbol{x})|^2, \\ &= \frac{\omega_j}{2Q}\frac{1}{N_T^2}\sum_{d=0}^{N_T-1} |\alpha_j(w_d)|^2 \int_V \mathrm{d}^3x\, |E_j(\boldsymbol{x})|^2, \\ &= \frac{\omega_j}{Q}\frac{1}{4\pi}\sum_{d=0}^{N_T-1} \Delta\omega \frac{T}{N_T^2}|\alpha_j(w_d)|^2 \int_V \mathrm{d}^3x\, |E_j(\boldsymbol{x})|^2, \end{aligned} \tag{3.49}$$

where we have related the time average with a sum over Fourier modes of the electric field amplitude through the Parseval theorem. For a finite measurement time T, only discrete frequencies enter in the sum, $\Delta\omega = 2\pi/T$. Here, the argument of the sum is identified as the spectral power (cf., e.g, [55, 225, 226]).

Now, due to the random phases the axion field is a Gaussian random field meaning that the spectral power will be exponentially distributed (as already pointed out in Refs. [225, 226]) and follows the probability distribution,

$$P(S(\omega_d)) = \frac{1}{\bar{S}(\omega_d)} e^{-S(\omega_d)/\bar{S}(\omega_d)}. \tag{3.50}$$

For a fixed AMC mean density $\rho(r)$ and gravitational potential $\phi(r)$, we can calculate the mean value $\bar{S}(\omega_d)$ by solving the differential equation (3.47) for the electric field amplitude $\alpha_j(t)$ and then proceed to calculate its discrete Fourier transform for a measurement period T. Following Refs. [225, 226] we obtain the spectral power,

$$S(\omega_d) \approx \frac{1}{T}|\sum_{nlm} C_{nlm} \int_{-T/2}^{T/2} dt\, e^{i\omega_d t} \left(a_{nlm}\psi_{nlm}(\boldsymbol{x})e^{-i\omega_{nlm}t} + c.c.\right)|^2, \tag{3.51}$$

where $\Delta t = T/N_T$ and we have introduced the coefficients C_{nlm} as

$$C_{nlm} = \sqrt{(g_{a\gamma\gamma}B_0)^2\, \mathcal{G}_j\, V} \frac{\omega_{nlm}^2}{\sqrt{2m_a}\left(\omega_j^2 - \omega_{nlm}^2 - i\omega_j\omega_{nlm}/Q\right)}, \tag{3.52}$$

where B_0 is the magnetic field in the cavity and V is volume, $\mathcal{G}_j$ is the usual geometry factor of the employed cavity mode with frequency ω_j[5] [227]. We assume that the typical wavelength of the axion field is much larger than the size of the haloscope, meaning that the field can be approximated as constant over the cavity volume. However, it is important to note that the spectral peak of the

[5]Note that we are now in the laboratory frame so that the velocities will be shifted due to a boost by the cluster velocity. We will make this explicit later in the calculation

axion signal may be narrower than the cavity's resonance width. In this context, spectral resolution plays an important role in the sensitivity of the axion haloscope. Higher spectral resolution enhances the detector's ability to detect weak axion signals that may be buried within the noise. In Eq. (3.52), the denominator carries the resonance that enhances the signal's power, resulting in a peak in the spectrum, as discussed in Chap 2.1.4. The measurement is then assumed to be taken at a location $\boldsymbol{x}$ inside the cluster, in a frame with the origin at the center of the AMC. Finally, note that the bin width of the spectral power is inversely proportional to the measurement time T, $\Delta\omega = 2\pi/T$, such that ω_d are discrete frequencies.

The time integral can be solved easily, noting that

$$\frac{1}{T}\int^{T/2} -T/2dte^{i\omega_d t}e^{-i\omega nlmt} = \text{sinc}\left((\omega_{nlm}-\omega_d)\frac{T}{2}\right). \tag{3.53}$$

With this, the power spectral density becomes,

$$S(\omega_d) \approx T|\sum_{nlm} C_{nlm}a_{nlm}\psi_{nlm}(\boldsymbol{x}), \text{sinc}\left((\omega_{nlm}-\omega_d)\frac{T}{2}\right)|^2. \tag{3.54}$$

The power spectral density given in Eq. (3.54) shows that the sinc function enhances the resolution of the spectrum. This enhancement arises from the fact that the sinc function's Fourier transform is a rectangular function, which effectively limits the range of frequencies in the signal, resulting in a narrower frequency response. Thus, the sinc function characterizes the distribution of the signal in frequency space by providing a windowed frequency response that increases resolution.

While the sinc function can serve as an approximation for the Dirac delta function, especially in situations where the delta function is not well-defined, it becomes a limiting case of the sinc function as its width approaches zero,

$$\lim_{\epsilon\to 0}\text{sinc}(x\epsilon) = \lim_{\epsilon\to 0}\frac{\sin(x\epsilon)}{x\epsilon} = \delta(x). \tag{3.55}$$

Thus, a long detection time leads to a more precise frequency measurement, translating into better resolution in detecting axion signals. For further details, see Sec. 2.1.4.

The average value of the power spectral density is obtained by taking the average over the random phases,

$$\bar{S}(\omega_d) = T\sum_{nlm}|C_{nlm}a_{nlm}\psi_{nlm}(\boldsymbol{x})|^2\,\text{sinc}^2\left((\omega_{nlm}-\omega_d)\frac{T}{2}\right). \tag{3.56}$$

Given the coefficients a_{nlm} as defined in Eq. (3.35), and considering a velocity shift $\boldsymbol{v}\to\boldsymbol{v}+\boldsymbol{v_c}$, where $\boldsymbol{v_c}$ is the cluster velocity, we have,

$$\begin{aligned}\bar{S}(\omega_d) = 4\pi^2 m_a^2\tilde{v}_d\int d\theta\sin(\theta)\,f(\tilde{v}_d^2+v_c^2-2\tilde{v}_d v_c\cos(\theta))|C(\tilde{v}_d^2+v_c^2-2\tilde{v}_d v_c\cos(\theta))|^2 \\ \times\Theta\left(\sqrt{-2\phi(r)}-(\tilde{v}_d^2+v_c^2-2\tilde{v}_d v_c\cos(\theta))\right)\Theta\left(\tilde{v}_d^2+v_c^2-2\tilde{v}_d v_c\cos(\theta)\right),\end{aligned} \tag{3.57}$$

where as further simplification we have assumed that the distribution function $f(v)$ is constant over the width of the sinc. Here we recall that f is the energy distribution function associated to the

density profile. Moreover, v_c is the velocity of the cluster relative to Earth and we define $\tilde{v}_d = \sqrt{2/m_a\,(\omega_d - m_a\phi(r) - m_a)}$.
From Eq. (3.57) we can see that the signal will be limited to be in the following frequency range,

$$\frac{m_a}{2}v_c^2 + m_a - m_a\sqrt{-2\phi(r)}v_c \leq \omega_d \leq \frac{m_a}{2}v_c^2 + m_a + m_a\sqrt{-2\phi(r)}v_c. \tag{3.58}$$

Hence, measuring both the starting and end points of this signal leads to a direct measurement of the potential energy $m_a\phi(r)$ and the velocity v_c [6]. A step-by-step description of this calculation can be found in Appendix B.3.

From the power spectral density, the overall power induced in cavity would just be the sum over the spectral power,

$$\begin{aligned} P &= \frac{\omega_j}{Q}\frac{1}{4\pi}\sum_d \Delta\omega S(\omega_d), \\ &\approx \frac{\omega_j}{Q}\frac{1}{4\pi}\int d\omega S(\omega). \end{aligned} \tag{3.59}$$

Again, it is important to remember that due to the statistics of the axion field, the power is randomly distributed as well. From Eq. (3.57), the mean power is easily calculable and is given by,

$$\bar{P} \approx \frac{g_{a\gamma\gamma}^2\rho(r)}{4m_a}B_0^2\mathcal{G}\,V\min\left(Q, Q_a\right), \tag{3.60}$$

such that we recover the usual result that the power is proportional to $g_{a\gamma\gamma}^2\rho(r)$ [163,228].
The variance of this distribution, σ_P, is directly proportional to the mean power $\bar{P}$ and inversely proportional to the square root of the ratio of the granule integration time T_{gran} to the total measurement time T. Explicitly,

$$\begin{aligned} \frac{\sigma_P}{\bar{P}} &\sim \sqrt{\frac{2\pi}{T}\frac{1}{m_a\phi(r)}}, \\ &\sim \sqrt{\frac{T_{\text{gran}}}{T}}. \end{aligned} \tag{3.61}$$

We recall that the time scale of the granules defined in Eq. (3.24), as $T_{\text{gran}} \sim 1/(m_a v^2) \sim 1/(m_a\phi)$, where v is the velocity dispersion in the cluster at radius r, are key to to impose constraints on the accuracy of measuring the coupling, see Sec. 3.2.1

3.3 Using Axion Miniclusters to Disentangle the Axion-photon Coupling and the DM Density

As mentioned before, the spectral power, Eq. (3.57), offers a direct measurement of the axion minicluster gravitational potential. A measurement of the gravitational potential gives us access to the density of the cluster, which allows us to reconstruct the axion-photon coupling later. However,

[6] Of course this measurement suffers from an error resulting from the finite bin width as well as from the noise/background signal. This will be discussed in the next section.

specific additional considerations are necessary for this reconstruction. Specifically, we assume for simplicity that the axion mass is no longer an unknown parameter (as referenced in [55]), and importantly, we also assume that the typical signal generated by an AMC is significantly stronger than in the case of a background axion field signal.

In the following, we construct a formalism based on the Poisson equation that enables us to disentangle the coupling from the density as just described. We then apply this method to simulated signals in order to delineate the region in the AMC parameter space where a reconstruction can be successful.

3.3.1 Reconstruction of the Axion-Photon Coupling

The AMC is a self-gravitating object, its density $\rho(r)$ and gravitational potential $\phi(r)$ are therefore directly related via the Poisson equation,

$$\nabla^2\phi(r) = 4\pi G\rho(r). \tag{3.62}$$

We can access the gravitational power as a function of time, t from the spectral power. To use of Poisson equation, we have to parameterize the radial motion of the Earth throughout the AMC,

$$r(t) = \sqrt{b^2 + \left(vt - \sqrt{R^2 - b^2}\right)^2}, \tag{3.63}$$

where v is the velocity of the Earth (in a frame with the origin at the center of the AMC), b is the impact parameter and R the radius[7]. In a more realistic scenario, the Earth would not simply pass through the minicluster along a straight path, as we have assumed[8]. Various factors, including the trajectory angle within the minicluster concerning the $(\mathbf{b}, \mathbf{v})$ plane, could be significant. This underscores the limitations of our study's straight-line approximation. Nonetheless, the relevant velocities in our picture, $\sim 10^{-3}$ c, are quite large compared to the velocity of the Earth around the sun, $\sim 10^{-4}$ c [226]. This suggests that a straight-line approximation is acceptable for the time measurement we considered.

With that, the Poisson equation can be transformed by using time as the variable,

$$\frac{\ddot{\phi}(t)}{\dot{r}(t)^2} + \frac{2\dot{\phi}(t)}{\dot{r}(t)r(t)} - \frac{\ddot{r(t)}\dot{\phi}(t)}{\dot{r}(t)^3} = 4\pi G\rho(t). \tag{3.64}$$

To reconstruct the axion-photon coupling, we extract $\phi_{\text{out}}(t_i)$ and $(g^2_{a\gamma\gamma}\rho(t_i))_{\text{out}}$, from the power spectral density and power, respectively, at N different measurement times i (corresponding to N different locations in the cluster). We also determine the velocity v of the AMC from the power spectral density. Now, by using the Poisson equation in the form of Eq. (3.64), we define the function which returns $g^2_{a\gamma\gamma}\rho(r)$ when the impact parameter, the radius, and the gravitational potential are known. Concretely, the functional $\mathcal{F}(b, R, g_{a\gamma\gamma}; t_i)$ models the axion field dynamics within the

[7]We assume here that $R = r(0)$.

[8]Note, again, that a realistic description of the Earth's motion should account for its orbit around the sun. In this more realistic picture, the trajectory would therefore no longer be a straight line.

gravitational potential of the axion miniclusters, accounting for the position and velocity of the AMC at time t_i.

$$\mathcal{F}(b, R, g_{a\gamma\gamma}; t_i) = \frac{g_{a\gamma\gamma}^2}{4\pi G}\left(\frac{\ddot{\phi}(t_i)}{\dot{r}(t_i)^2} + \frac{2\dot{\phi}(t_i)}{\dot{r}(t_i)r(t_i)} - \frac{r(\ddot{t}_i)\dot{\phi}(t_i)}{\dot{r}(t_i)^3}\right). \tag{3.65}$$

Finally, the parameters b, R and $g_{a\gamma\gamma}$ are reconstructed by maximizing a function, that by no means is unique and different choices may alter the reconstruction of the parameters. The one that we have used, based on its simplicity is,

$$\mathcal{L}(b, R, g_{a\gamma\gamma}) = \sum_i \log\left(\frac{(g_{a\gamma\gamma}^2\rho(t_i))_{\text{out}}}{|(g_{a\gamma\gamma}^2\rho(t_i))_{\text{out}} - \mathcal{F}(b, R, g_{a\gamma\gamma}; t_i)|}\right). \tag{3.66}$$

One can identify some important error sources when reconstructing the coupling. First, in the reconstruction, there are inevitable statistical fluctuations in the axion field. Indeed, the random phases in the AMC wave function generate granule fluctuations for a specific realization of the phases, as anticipated in Sec 3.2.1. The granules, nonetheless, do not affect the width of the power spectral density, but they translate into fluctuations in the power. Hence, using the formalism constructed in this section, the granule structures affect the quantity $(g_{a\gamma\gamma}^2\rho)_{\text{out}}$ extracted from the power measurement and those statistical fluctuations will also impact on the reconstruction of the axion-photon coupling via the maximization of Eq. (3.66).

The width of the power spectral density is not affected by the statistics of the axion field; instead, it is inherently influenced by errors arising from the finite frequency bin size $\Delta\omega = 2\pi/T$, as discussed in Sec. 3.2.3. Consequently, determining the signal width, crucial for reconstructing the potential $m_a\phi_{\text{out}}$, introduces an uncertainty proportional to $\Delta\omega$. This uncertainty extends to the first and second derivatives of the potential, which are essential for computing the function $\mathcal{F}(b, R, g_{a\gamma\gamma})$. Thus, the reconstruction of the axion-photon coupling applying Eq. (3.66) suffers from a systematic error that gets stronger as the ratio of $\Delta\omega$ over the signal width increases. In other words, we require $\Delta\omega/(2m_a v_c\sqrt{-2\phi(r)}) \ll 1$. Besides the error from finite binning, noise, and background also impact the determination of the signal width and, consequently, the reconstruction of the gravitational potential. Moving forward, only the values of $S(\omega_d)$ that exceed the noise/background level are considered. While this does not significantly impact potential reconstruction, it can lead to a degradation in signal width measurement when dealing with lighter clusters.

Furthermore, the number N of time data points t_i is expected to provide another source of systematic error. Indeed, in the limit of small N, the potential is only reconstructed at a few locations, and, similarly to before, its first and second derivatives get less accurately reconstructed, leading to the same conclusion.

3.3.2 Application to Simulated Data

To test the method described, we simulate an encounter with an axion minicluster (AMC) with a detector on Earth. For simplicity, we assume that an AMC features an NFW profile and that the impact parameter and the velocity of the AMC are unknown parameters.

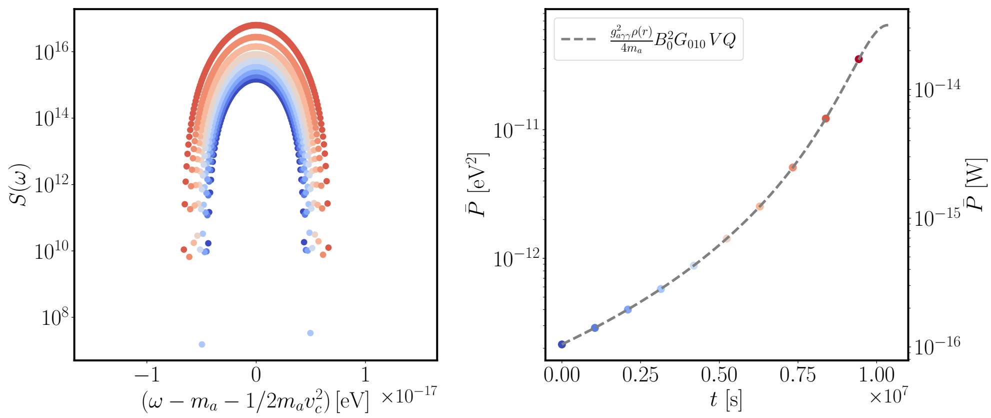

Figure 3.1. Averaged signal of an NFW profile axion minicluster crossing the Earth. For this example we consider a mass $M = 10^{-10}\,M_\odot$, radius $R = 10^{-5}$ pc and concentration $c = 10$. The velocity of the AMC is $v = 10^{-4}c$ and we are crossing it with an impact parameter $b = 10^{-6}$ pc. We assume that each measurement period is $T = 5 \times 10^4$ s. *Left*: Averaged power spectral density at each measurement location (from blue to red as we are moving toward the cluster center). The dots are showing the power in each frequency bin. *Right*: Averaged power as a function of time. Each dot represents the power calculated from the spectral power at a different location.

We follow the probability distribution in Eq. (3.50) to simulate the spectral power, $S(\omega)$, induced by the AMC, at each measurement location inside the cluster corresponding to measurement times t_i. Here, the bin width of the spectral power is defined by the period of the measurement T. The induced power is calculated according to Eq. (3.59) for each simulated spectral power. The data are at the end composed of N successive measurements of $\{S(\omega; t_i), P(t_i)\}$ for $i = 0, ...N$.

In Fig. 3.1, we show for a simulated cluster with mass $M = 10^{-10} M_\odot$, radius $R = 10^{-5}$ pc and concentration $c = 10$[9], the reconstruction of the gravitational energy $(m_a \phi(t_i))_{\text{out}}$ and $(g_{a\gamma\gamma}^2 \rho(t_i))_{\text{out}}$. As before, the impact parameter and the cluster velocity are $b = 10^{-6}$ pc and $v = 10^{-4}c$. At each location, the measurements are taken during $T = 2 \times 10^5$s, and we collect data at a total of $N = 40$ locations. The input axion mass and coupling were taken as $m_a = 5 \times 10^{-5}$eV, and $g_{a\gamma\gamma} = 10^{-15}\text{GeV}^{-1}$. For the experiment parameters we took, $B_0 = 8$T, $V = 220$l, $Q = 10^5$, $\mathcal{G} = 0.69$ (TM_{010} mode) and $\omega_c = m_a$.

As already pointed out, the important parameter controlling the accuracy of the reconstruction is $\Delta\omega/(m_a \phi)$. In this example, the AMC parameters have been chosen in order to have the ratio $\Delta\omega/(m_a \phi) \sim \mathcal{O}(10^{-2})$. This choice leads to a reasonable reconstruction of the gravitational energy, but some fluctuations are already visible in $g_{a\gamma\gamma}^2 \rho$.

In order to illustrate the sensitivity of the construction on $\Delta\omega/(m_a \phi)$, we show in the left panel of Fig. 3.2 the ratio between the reconstructed coupling, g_{out}, and the input one, g_{in}, as a function

[9] The concentration parameter is a key input that defines the ratio between the halo's virial radius and its scale radius, R_{vir}/R_s. This parameter is needed when calculating the initial halo density, which we assume follows the NFW profile.

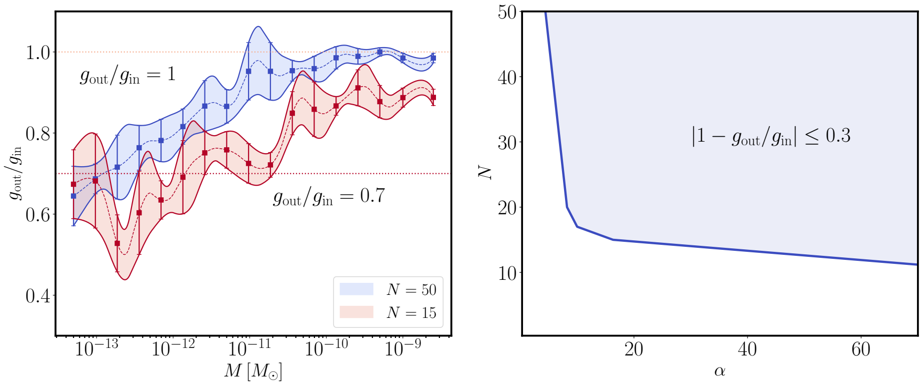

Figure 3.2. *Left*: Reconstruction of the axion-photon coupling as a function of the mass for $N = 40$ and $N = 20$ data points. The shaded region shows the dispersion of the reconstruction over 10 simulated reconstructions, the dashed lines the average. For both curves, the radius is set to $R = 10^{-5}$ pc, the AMC velocity to $v = 10^{-4}$c and the measurement time to $T = 10^5$s. *Right*: Sensitivity of the coupling reconstruction as a function of the number of time data points $N \approx 2R/(vT)\sqrt{1-(b/R)^2}$ and the averaged ratio $\Delta\omega/(m_a\phi) \approx [TGm_aM/(2\pi)]^{-1}\,(\log(R/b)/(R-b))$. The blue shaded region shows the region where the axion-photon coupling is reconstructed with an error less than 30%. The dashed orange lines show the rectangle approximations used to infer the rate of encounters in Sec. 3.3.3.

of the AMC mass. The other parameters (v, R, b, T) are fixed to be $\left(10^{-4}c, 10^{-5}\text{pc}, 10^{-6}\text{pc}, 10^5\text{s}\right)$, respectively. We have simulated 10 signal realizations for each mass and reconstructed the coupling for each of them. The dashed lines show the average reconstructed coupling, and the solid upper and lower lines show the variance of the reconstruction. As the mass decreases, the ratio $\Delta\omega/(m_a\phi)$ diminishes, indicating that the gravitational potential's reconstruction is increasingly affected by larger deviations stemming from the bin width $\Delta\omega$. The reconstruction process through the Poisson equation becomes inefficient under these conditions. This inefficiency results in a systematic error that grows more pronounced in the left panel of Fig. 3.2, where there is a general deviation from $g_{\text{out}}/g_{\text{in}} = 1$ towards smaller values. This trend can be attributed to larger fluctuations in the reconstructed gravitational potential. Since density values cannot be negative, the Poisson equation tends to overestimate density, resulting in a systematic underestimation of the coupling to align with the reconstructed $(g^2_{a\gamma\gamma}\rho(t_i))_{\text{out}}$. Furthermore, the power experiences significant statistical fluctuations, leading to an observable increase in variance as we move towards lower mass values. Finally, the red and blue curves show how the number of location data points alters the reconstruction. In particular, the red and blue lines have been simulated for $N = 15$ and $N = 50$ points, respectively. Note that the choice of the maximizing function in Eq.(3.66) is expected to impact how the reconstructed coupling deviates from the input one.

Since the primary influence on the reconstruction is coming from the ratio $\Delta\omega/(m_a\phi)$ and the number of location data points N, we show in the right panel of Fig. 3.2, the region of those parameters that returns a reasonable reconstruction with precision $|1 - g_{\text{out}}/g_{\text{in}}| \leq 0.3$. The number of data points in this particular context we determine by the ratio of the total distance covered to the distance covered per measurement, $N = 2R\sqrt{1-(b/R)^2}/(vT)$, where we assume that each point can be taken after having measured at a location during a period T. Moreover, since the quantity $\Delta\omega/(m_a\phi)$ depends on the location where the measurement is performed, we use in Fig. 3.2 the potential averaged over the path of the Earth throughout the AMC. The resolution of the gravitational potential will therefore be approximated as $\Delta\omega/m_a\phi \sim m_a vT\sqrt{GM\frac{\log(R/b)}{(R-b)}}$.

3.3.3 Rate of Encountering Suitable AMCs

Here, we estimate the rate at which we may encounter an AMC with parameters that allow for a reasonable reconstruction of the axion-photon coupling (see blue region in the right panel of Fig. 3.2). Our approach is simplistic. We assume that all axion miniclusters are spherically symmetric, with the same size, and have the same mass[10]. The rate is then given by,

$$\Gamma = n_{\text{AMC}}(r)\langle\sigma v\rangle, \tag{3.67}$$

where the axion minicluster number density is,

$$n_{\text{AMC}}(r) = f_{\text{AMC}}\frac{\rho_{\text{DM}}(r)}{M}, \tag{3.68}$$

and f_{AMC} is the fraction of the total dark matter density in AMCs and M is the AMC mass.

The local density of dark matter is modeled by an NFW profile evaluated at $r = 8.33$ kpc,

$$\rho_{\text{DM}}(r) = \frac{\rho_s}{(r/r_s)(1+r/r_s)^2}, \tag{3.69}$$

with $\rho_s = 0.014\text{M}_\odot\text{pc}^{-3}$, $r_s = 16.1$ kpc [230], so that the local dark matter density is $\rho_{\text{DM}} = 0.45\,\text{GeV/cm}^3$.

Concerning the minicluster fraction, f_{AMC}, Refs. [197, 229, 231] for example, find from numerical simulations that the fraction of axions bound in AMCs is ~ 0.75 at redshift around $z \sim 100$. However, it is quite uncertain how this evolves until today. In any case, the numerical values in our figures show rates divided by f_{AMC}. But to give rough and optimistic numbers we assume $f_{\text{AMC}} \sim 1$.

The geometrical cross section to encounter an AMC with impact parameter less than b and a relative velocity between v_i and v_f, is given by $\sigma(b) = \pi b^2$ and the differential rate becomes,

$$\frac{d\Gamma}{db} = n_{\text{AMC}}(r)\left\langle v\frac{d\sigma}{db}\right\rangle = n_{\text{AMC}}(r)\int_{v_i}^{v_f} vf(v)\frac{d\sigma}{db}dv, \tag{3.70}$$

where $f(v)$ is the velocity distribution. We consider the distribution in the laboratory frame from [225] adapting the conventional Standard Halo Model (SHM) that yields to a Maxwell-Boltzmann distribution in the galactic frame,

$$f_{\text{gal}}(v) = 4\pi\frac{1}{\pi\sqrt{\pi}}\frac{v^2}{v_0^3}e^{-v^2/v_0^2}, \tag{3.71}$$

where $v_0 \sim 220\,\text{km/s}$ is the velocity dispersion [232, 233], some papers give slightly different velocities, e.g. Ref. [99] has a value of $\sim 270\text{km/s}$. We have checked that this does not drastically

[10] A better estimate for the rate should consider a more realistic mass distribution for the AMCs. See, for instance, Ref. [229]. In light of our relatively crude approximations for several other effects, we neglect this effect.

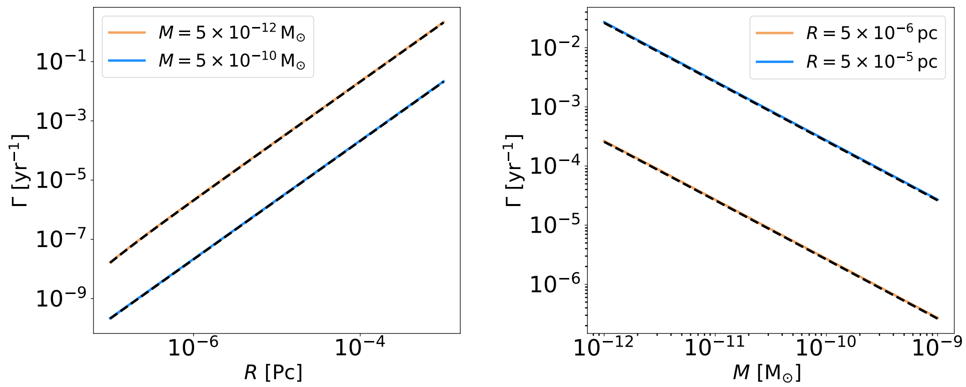

Figure 3.3. *Left*: Detection rate as a function of the radius for two AMC masses. *Right*: Detection rate as a function of the mass for two AMC radius. In both panels, the rate is normalized with the axion fraction bound in AMCs, f_{AMC}. The black dashed lines represent the detection rate for same parameters for $v_0 = 270$ km$/s$

alter the rate, as the dashed lines show in Fig 3.3. Note that, the velocity distribution is expected to be additionally cut-off beyond the escape velocity $v_{\mathrm{esc}} \sim 544\,\mathrm{km/s}$ [234].

Performing the transformation to the detector rest frame [234] as $\mathbf{v} \to \mathbf{v} - \mathbf{v}_{\mathrm{lab}}(t)$, and averaging over the spatial angles yields to the detector frame speed distribution [235],

$$\begin{cases} \dfrac{2v}{\sqrt{\pi} v_0 v_{\mathrm{lab}}} e^{-v_{\mathrm{lab}}^2/v_0^2} \sinh\left(\dfrac{2v_{\mathrm{lab}}}{v_0^2} v\right) e^{-v^2/v_0^2} & |\mathbf{v} + \mathbf{v_s}| < v_{esc}, \\ 0 & |\mathbf{v} + \mathbf{v_s}| > v_{esc}, \end{cases} \tag{3.72}$$

where $v_{\mathrm{lab}} \sim 235\,\mathrm{km/s}$ is the laboratory velocity relative to the galactic frame [236] and v_s is the Sun's velocity relative to the galactic frame. We can indeed use an angular averaged distribution, as does not matter from which direction we encounter our (spherically symmetric) AMCs.

According to Fig. 3.2, we estimate that a reasonable axion-photon coupling reconstruction is possible if

$$\alpha_{\mathrm{min}} \leq m_a v \frac{T}{\pi} \sqrt{2GM \frac{\log{(R/b)}}{(R-b)}}, \tag{3.73}$$

$$N_{\mathrm{min}} \leq \frac{2R}{vT} \sqrt{1 - (b/R)^2}, \tag{3.74}$$

with $\alpha_{\mathrm{min}} \approx 19$ and $N_{\mathrm{min}} \approx 17$ (these values are obtained from approximating the blue shaded region in Fig. 3.2 as a rectangle). These constraints come from imposing a sufficiently good resolution of the gravitational potential and on enough of data points, as given by the blue region in the right panel of

Fig. 3.2[11]. We furthermore define $\kappa \equiv b/R$, and the maximum measurement time as $T_{\text{max}}(R, b, v) = 2\sqrt{R^2 - b^2}/(vN_{\text{min}})$, such that the two previous equations now become,

$$\alpha_{\text{min}} N_{\text{min}} \leq 2m_a/\pi\sqrt{2MGR}\sqrt{-(1+\kappa)\log(\kappa)}. \tag{3.75}$$

Solving this last equation numerically gives the maximal impact parameter - radius ratio, $\kappa_{\text{max}}(M, R)$, as a function of the AMC mass and radius. Note that the reconstructible impact parameters do not depend on the relative velocity. We can therefore use the full available range of velocities from 0 to v_{esc}. Finally, using Eq. (4.32) we obtain that the rate of AMC encounters that allows for a reasonable reconstruction of the axion-photon coupling is given by,

$$\Gamma(M, R) = n_{\text{AMC}}(r)\pi R^2 \kappa_{\text{max}}(M, R)^2 \int_0^{v_{esc}} vf(v)dv. \tag{3.76}$$

We show in Fig. 3.3 the resulting rate as a function of the radius (left panel) and the mass (right panel). We observe that the rate typically increases as we go to larger radius. On the other hand, increasing the mass decreases the rate since in that case the number density of miniclusters decreases. Taking the full shape of the blue shaded region in Fig. 3.2 into account (and not the rectangle approximation considered above) would increase the rate compared to what we are presenting here. An example of this case we have calculated the rate for the conservative limits illustrated in Fig 3.2, $\Gamma(M = 10^{18}\text{kg}, R = 10^{-3}\text{pc}) \sim$ and $\Gamma^{'}(M = 10^{18}\text{kg}, R = 10^{-3}\text{pc}) \sim$ for a region outside the region.

In Fig. 3.4, we show the rate of the AMC encounters for which a reasonable reconstruction is possible as a function of both the mass and the radius (left panel). As the mass decreases, the reconstruction becomes less efficient. However, the number density of miniclusters increases even faster, and the overall rate increases. We also observe that larger AMCs have the best chances of detection, leading to a good axion-photon coupling reconstruction. Nonetheless, as shown in recent works (see Refs. [204,237–240]), AMCs might be strongly affected by tidal interactions with galactic stars.[12] Although the survival of the AMCs depends on their density profile shape (NFW, power law, among others), it has been argued that their survival is directly proportional to the mean density of the cluster. For this reason, even if encounters with larger AMCs are frequent, their survival should be more strongly affected compared to smaller AMCs. We show on the right panel of Fig. 3.4 the AMC encounter rate weighted by the survival probability. Note, however, that the survival probability has been extracted from the results of Ref. [204] for a Lane-Emden profile (see, for instance, Ref. [241]). However, it has also been argued in Ref. [204] that clusters with density profiles similar to NFW should be more resistant to stellar interactions. It is also important to consider the disruption effects that can be produced by the Earth and by the Sun. To get an estimate, let us consider the energy

[11]Note, again that his "rectangular" approximation provides an easy-to-handle approximation of the blue shaded region in the left panel of Fig. 3.2. This makes it simple to obtain a first estimate for the rate. Considering the exact shape of this surface is expected to not alter the results drastically and would lead an increase of the encounter rate

[12]Here, we are concerned with potential destructive encounters with stars other than the Sun before the AMC is in our vicinity.

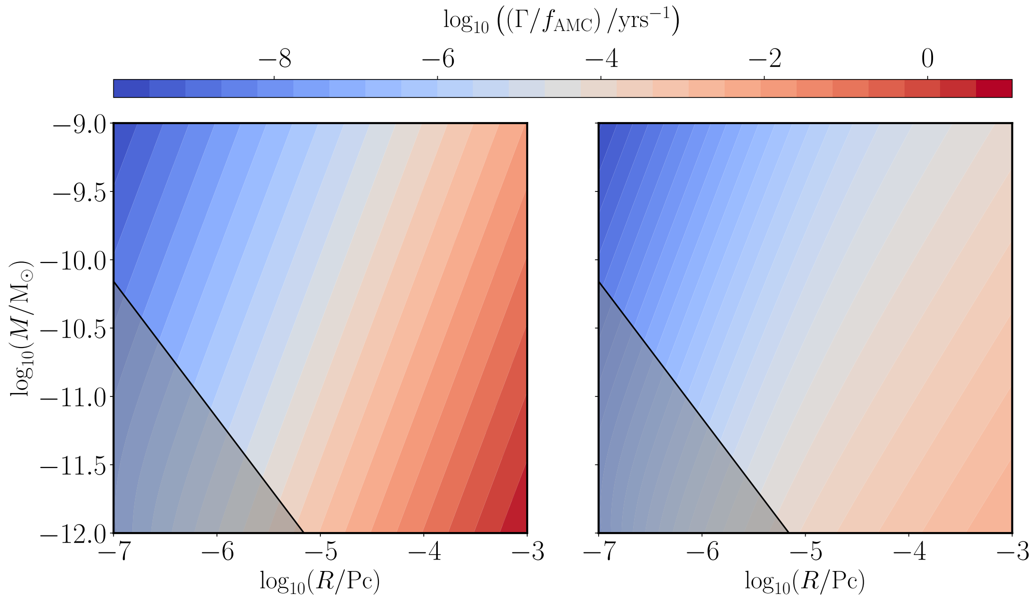

Figure 3.4. *Left*: Rate of AMC encounters (normalized by the DM fraction in AMC $f_{\rm AMC}$) that allow for a reconstruction of the axion-photon coupling. *Right*: Rate accounting for the survival probability decreasing with the mean density $\sim M/R^3$ (given in Ref. [204]). The gray shaded region corresponds to the parameter space where ou formalism does not hold, see Eq.(3.36).

injection generated by an interaction with an astrophysical object, [237]

$$\Delta E \approx \left(\frac{2GM_d}{b^2 V_d}\right)^2 \frac{M\langle R^2\rangle}{3}, \tag{3.77}$$

where M_d and V_d are the mass and the relative velocity of the disturber interacting with the minicluster with mass M. b is the impact parameter and $\langle R^2\rangle$ is the mean squared radius of the minicluster.

In practice, the energy needed to destroy the minicluster is around $\Delta E \sim E_b$, with E_b the binding energy of the system. For the disruption caused by the Sun, we find that all of the parameter space shown in Fig. 3.4, will suffer from tidal disruption due to the Sun. This effect should be smaller only at higher masses and relatively small radii. As an example, for a minicluster of radius $R \sim 3 \times 10^{-6}$ pc the minimum mass to survive the Sun disruption is $M \sim 10^{-4}{\rm M}_\odot$. These parameters, however, correspond to $\Gamma \sim 10^{-13}$/yr, an exceedingly rare event. This implies the need for numerical simulations that account for the non-trivial changes in the cluster structure due to the interaction with the solar system. The tidal interaction caused by the Earth leaves the cluster relatively intact. The quadratic dependence on the disturber mass causes this. Nevertheless, we expect that the crossing of the Earth in the cluster will induce changes in the local structure, for example, some turbulence around the Earth's location. This would affect the signal, and this effect should be studied via some numerical simulations as well.

Finally, from Eq. (3.75), we can also see that a larger axion mass allows for a higher rate because the same value of κ can be achieved for a smaller mass of the AMC. Keeping the other parameters fixed gives a linear increase in the rate due to the higher number density of the AMCs. However, this increase is constrained by the axion dark matter mass range and the range over which spectrally resolved detection is feasible. Specifically, the axion mass range limits the effectiveness of increasing the encounter rate because, at certain mass ranges, the interaction dynamics of axions with other particles become less favorable for enhancing the rate. In the second case, as we have discussed in Sec 2.1.4, spectrally resolved detection involves identifying and characterizing signals based on their distinct spectral properties, the mass range being one of the most relevant since the spectral features of axions or their interactions with AMCs become convoluted or challenging to differentiate from background noise or other astrophysical signals.

3.3.4 Discussion

Axion haloscopes are only sensitive to the product of coupling and density, $g^2_{a\gamma\gamma}\rho$. However, we argue that in the case of an encounter with an AMC, the energy/frequency spectrum of the power provides additional information on its gravitational potential. Using the precise energy spectrum measurements in haloscope experiments, we can trace the gravitational potential of an AMC as the Earth traverses it. Subsequently, we employ the Poisson equation to establish a link between the derived gravitational potential and the cluster's density. We can disentangle the axion-photon coupling by combining the density information with the power extracted from the haloscope cavity ($P \sim g^2_{a\gamma\gamma}\rho$).

To demonstrate the effectiveness of our method, we applied it to simulated haloscope signals encountered by an AMC. This has been done assuming a self-consistent wave function for the miniclusters [204,210], as well as incorporating the axion field statistics [225,226]. Based on our simulations, we have determined the precision of reconstructing the axion-photon coupling by considering a number of data points and the AMC parameters. We find that denser miniclusters allow for a better coupling reconstruction because they possess a higher concentration of axion dark matter particles, resulting in a stronger gravitational potential within the cluster. The stronger gravitational pull enhances the interaction between axions and photons, making the coupling signal easier to detect and, therefore, clearer and more distinct spectral features present in the signal, making it easier to identify and analyze the axion-photon coupling signal accurately. Furthermore, we observe that denser AMCs exhibit reduced relative statistical fluctuations in power, contributing to more stable measurements.

Of course, we have to ask how likely it is to encounter a suitable AMC for which we can indeed reconstruct the axion-photon coupling. Unfortunately, the average rate to cross such an AMC is relatively low. If the AMC and axion parameters are of a favorable size, the rate can be of the order of one per $10^2 - 10^3$ years[13]. However, it can be much lower. The scaling can be inferred from Fig. 3.3 and Eq. (3.75). Finally, we stress that for our estimates, we used a rather simplistic model of a minicluster that encountered the detector in a straight line without being perturbed by the gravitational fields of the Earth and the Sun. In regions with sizable rates this should be a large

[13] Larger masses of the axions, or more generally axion-like particles, may allow for an increase in the rate beyond this point, because the reconstruction may be possible for lower minicluster masses that can be more abundant, cf. Eq. (3.75). That said, achieving a sufficient spectral resolution might be difficult at the correspondingly higher frequencies.

effect [204, 237]. A more careful analysis of the rate should be done, including a detailed simulation of the changes of the minicluster due to its interaction with the solar system and the effects this has on the signal. In light of this, our investigation should be undertaken as an indicative pilot study.

Let us finally return to whether we can tell whether axions are a dominant contribution to dark matter. As discussed, we know the coupling after an encounter with a minicluster. Then, from the measurement of the homogeneous (non-minicluster) dark matter signal[14] we can measure this part of the density. If this measurement yields a value similar to the expected density at our location, it is at least suggestive that axions constitute a significant component of dark matter.

3.4 Understanding Axion Quantum States

As discussed in Chap. 2.1.3, axion states for dark matter must have extremely high occupation numbers [165, 242]. This, together with a small velocity spread suggest that axions behave as coherent, macroscopic waves rather than discrete particles. This wave-like behavior arises because low-mass axions, with their long de Broglie wavelengths and consequently high occupation numbers, fill the universe in a way that is effectively indistinguishable from a classical field [243, 244]. For this reason, axions are often treated as classical coherent waves, which approximates a coherent quantum states as we discuss below. However, the exact nature of their quantum state and if they form a Bose-Einstein condensate or if they exhibit other forms of collective behavior, remains unclear. Therefore, one may wonder how axions being in different quantum states might influence observables.

As mentioned earlier, axions in a classical coherent state exhibit spatial coherence, meaning that the phase relationship remains approximately constant over large spatial regions. This is a characteristic common to a single-frequency classical wave. This coherence corresponds to a delocalized wave-like behavior consistent with a classical field description. These states are temporally stable, exhibiting minimal fluctuations in certain physical quantities, such as the energy density while maintaining coherence in their phase over time [245–247]. This behavior can be compared to the idea of a coherent state in quantum mechanics. Specifically, a quantum mechanical coherent state $|\alpha\rangle$ is an eigenstate of the annihilation operator, $\hat{a}$, satisfying $\hat{a}|\alpha\rangle = \alpha|\alpha\rangle$, where α is a complex number. This is a coherent superposition of different energy eigenstates of the harmonic oscillator, which evolve in time as simple oscillations while maintaining their overall shape with minimal spreading[15]. The quantum coherent state for a single spatial mode is the closest analog to a single spatial mode classical wave, with stable phase and amplitude coherence. Therefore, a simple example to make this comparison is to consider a classical coherent state confined to a single spatial mode, representing a specific configuration, such as a localized overdensity (e.g., a minicluster). While a classical oscillating state, such as one described by a harmonic potential, have no intrinsic uncertainties in its dynamics, a quantum coherent state is subject to quantum fluctuations. This refers to the fact that

[14] Estimating the fraction contained in miniclusters is more complex, as we do not expect to encounter more than once during a reasonable amount of time. Therefore, we cannot obtain a statistically significant result.

[15] Superpositions of coherent states, such as $|\alpha\rangle+|\beta\rangle$, which can produce interference patterns depending on their relative phases and amplitudes, are also possible. This extends the classical analogy to include coherence from overlapping states.

it does not correspond to a fixed particle number but to a state with a well-defined average particle number, i.e., the expectation value of the particle number operator [248–250]. This distinction is important. A coherent state, being a superposition of energy eigenstates, involves multiple particle number states. When the particle number is well-defined and conserved, the energy eigenstates are associated with distinct particle number states, which are governed by the number operator $\hat{N} = \hat{a}^\dagger \hat{a}$. Due to their wave-like nature, axions can exist in superpositions of these energy eigenstates, allowing them to occupy multiple energy states simultaneously. The exact nature of this superposition may have effects on observables and experimental signatures [56]. Thereby, hopefully one can get insights into their dynamics.

As a further motivation, looking at the quantum mechanical description can provide some perspective on axion structures. While structures like axion miniclusters or compact axion stars are typically studied using a classical wave description, as we did in Sec. 3.2, the formation of such axion structures could also affect the quantum state. For example, as the structure forms, internal energy and particle distribution reconfigure the spatial arrangement and it is also plausible that the quantum state may be affected as well. Thus, is important to see whether the quantum mechanical stat is relevant for experimental detection.

Building on this, we are interested in how different frequencies arising from axion-spin interactions manifest in quantum observables. Furthermore, we aim to explore how the quantum state of axions influences measurements within experimental settings, providing a clearer view of the dynamics of axions as a fundamental component of dark matter and their detectability in experimental setups such as the Cosmic Axion Spin Precession Experiment (CASPEr) [56]. Approaching fundamental aspects of the axion, in our case, by exploring the coupling with nucleons, could provide insights into how axions distribute among different energy levels and give some understanding of how these dynamics could impact measurements in DM detection experiments.

In what follows, we will attempt to understand energy eigenstates and, subsequently, simple superposition of axion states in a direct detection setups. Our goal is to study how the quantum mechanical nature of axions, specifically in scenarios where they are bound by Earth's gravitational field, impacts experiments aimed at detecting these particles, such as CASPEr. We look into how different frequencies related to axion-spin interactions manifest in quantum observables and how the quantum state of axions influences measurements in these experiments. The goal is to improve our understanding of axion behavior in experimental setups.

The following subsections are based on Ref. [2]. This work was done in collaboration with Cedric Quint, Joerg Jaeckel and Valentina Montoya. I was involved in performing the model description and inspecting the simple case of a single spin together with Cedric Quint. I also contributed to describing and discussing suitable measurement procedures for oscillations with the axion mass. Some sections of the complete article were excluded due to their irrelevance to this thesis. Some additional explanations and complementary sections where included in this thesis for the sake of clarity. All the results presented in this thesis are used with permission from all researchers involved.

3.4.1 A Quantum Perspective on Oscillation Frequencies in Axion Dark Matter Experiments

We propose exploring the coupling with nucleons to contribute to discussing the dynamics of the axion field from a quantum perspective. Concretely, we aim to explore how the quantum mechanical nature of axions, specifically in scenarios where Earth's gravitational field binds them, impacts experiments aimed at detecting these particles, such as the (CASPEr). This scenario is challenging since detecting axions bound to Earth's gravity is extremely difficult due to their subtle interactions. While most axions are not expected to be bound to Earth, exploring the scenario of bound axion states can still provide insights that may apply to more general cases. So, studying the time evolution of signals in axion dark matter experiments from a quantum perspective is an initial step into comprehending axion dynamics and anticipates potential signals arising from interactions.

In the specific scenario under consideration, where dark matter is conventionally treated as a classical field in experiments [163, 226], obtaining a better understanding from the quantum mechanical perspective becomes also relevant, particularly in the context of the discussion above. That said, we study how the oscillation frequencies that are the basis of resonant detection methods arise in a quantum mechanical setting and how the experimental measurements depend on the quantum state of the setup.

As our goal is to understand the oscillation frequencies of the axion from a quantum perspective, frequencies that are typically treated classically, we will first review the quantum analogue of the classical treatment of oscillatory systems through the Jaynes-Cummings model (JCM) [251]. The interactions between axions and spins in the experiments are analogous to the interactions modeled in the JCM. The quantum states of axions and their influence on observable frequencies and measurements can be effectively described in the same way the JCM describes the dynamics of a quantum system interacting with a quantized field, as we will detail in the following section. Our aim here is to describe the basic framework we will apply to the case of axion detection experiments.

3.4.2 The Jaynes-Cummings model analogy

The JCM [251], introduced in 1963 by Edwin Jaynes and Fred Cummings, studies the quantum mechanical interactions between an atom and a single-mode radiation field that is quantized, see Fig 3.5. It is used to study the classical aspects of spontaneous emission and plays a key role in revealing the existence of Rabi oscillations in atomic excitation probabilities for fields with defined energy/ photon number. In this model, the atom and the radiation field exchange a quanta of energy: the atom can either absorb a photon and transition to an excited state or emit a photon and return to the ground.

The JCM Hamiltonian

While the physical systems of axions and the Jaynes-Cummings model are distinct, the mathematical formalism used in the JCM, such as the representation of the Hamiltonian of the system, the

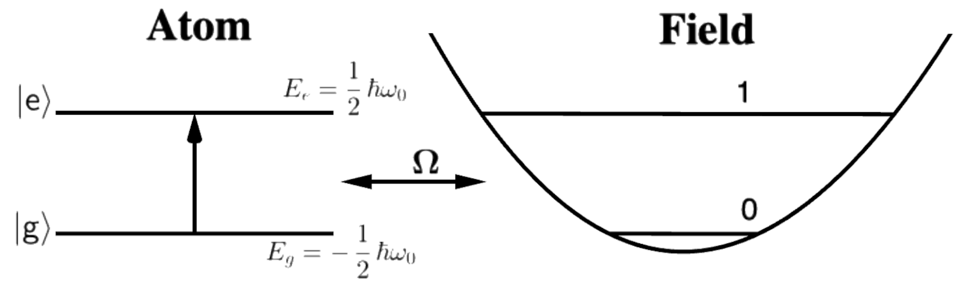

Figure 3.5. Representation of the Jaynes-Cummings model. Here, the atom is a two-level system coupled to a quantized single-mode field, represented by a harmonic oscillator. The coupling between the atom and the field is characterized by Ω, the Rabi frequency. Illustration inspired by [252].

description of state transitions, and the calculation of observable quantities, can be adapted and applied to our study of axions and their effects on observable phenomena. In both cases, the evolution of the quantum states of the system is influenced by the interaction with the respective quantized fields. Therefore, by making parallels between these systems, some good insights can be gained into the quantum perspective of oscillation frequencies in axion dark matter experiments through the well-understood dynamics of the Jaynes-Cummings model.

Since we want to describe the interaction between a two-level quantum system and a quantized harmonic oscillator field, the interaction Hamiltonian couples the atomic transition operators to the electromagnetic field dipole operators. Let us fist consider an atom, with levels $|g\rangle$ (ground state) and $|e\rangle$ (excited state), interacting with a single-mode cavity field with an arbitrary oriented polarization vector $\mathbf{e}$,

$$\hat{\mathbf{E}} = \mathbf{e}\left(\frac{\hbar\omega}{\epsilon_o V}\right)^{1/2} \sin{(kz)}(\hat{a} + \hat{a}^\dagger), \tag{3.78}$$

where a and $a^\dagger$ are annihilation and creation operators. The interaction Hamiltonian is [252],

$$\hat{H}_{\mathrm{I}} = -\hat{\mathbf{g}} \cdot \hat{\mathbf{E}} = -\hat{d}\left(\frac{\hbar\omega}{\epsilon_o V}\right)^{1/2} \sin{(kz)}(\hat{a} + \hat{a}^\dagger), \tag{3.79}$$

where the dipole moment operator, $\hat{d}$, can be expressed as the dot product of the atomic dipole operator $\hat{\mathbf{d}}$ with the polarization vector $\mathbf{e}$, i.e., $\hat{d} = \hat{\mathbf{d}} \cdot \mathbf{e}$. To obtain the dipole operator in the context of a two-level system, we can introduce transition operators obeying Pauli spin algebra, such that,

$$\begin{aligned}
&\hat{\sigma}_+ = |e\rangle\langle g|, \quad \hat{\sigma}_- = |g\rangle\langle e| = \hat{\sigma}_+^\dagger, \quad \hat{\sigma}_3 = |e\rangle\langle e| - |g\rangle\langle g|, \\
&[\hat{\sigma}_+, \hat{\sigma}_-] = \hat{\sigma}_3, \quad [\hat{\sigma}_3, \hat{\sigma}_\pm] = 2\hat{\sigma}_\pm,
\end{aligned}$$

where $\hat{\sigma}_3$ represents the inversion operator. These transition operators correspond to the creation and annihilation of excitations within the system, representing photon absorption and emission or transitions between quantum states. They are associated with the induced dipole moment, as quantum transitions inherently involve changes in the charge distribution, generating an electric dipole moment. From here we can rewrite the dipole operator as,

$$\hat{d} = d|g\rangle\langle e| + d^*|e\rangle\langle g| = d\hat{\sigma}_- + d^*\hat{\sigma}_+ = d(\hat{\sigma}_+ + \hat{\sigma}_-),$$

where we have used the fact that, due to parity symmetry, $\langle e|d|e\rangle = 0 = \langle g|d|g\rangle$.

The interaction Hamiltonian can be written as,

$$\hat{H}_{\mathrm{I}} = \hbar\lambda(\hat{\sigma}_+ + \hat{\sigma}_-)(\hat{a} + \hat{a}^\dagger), \tag{3.80}$$

where $\lambda = gd/\hbar$.

Continuing with the construction of the total Hamiltonian of the model, let us obtain now the free atomic Hamiltonian. Here, the zero level of the energy between $|g\rangle$ and $|e\rangle$, is taken halfway between the two levels, as shown in Fig. 3.5. This midpoint choice creates a symmetric energy scale that simplifies calculations for analyzing the system's energy dynamics. The atomic Hamiltonian can be written as,

$$\hat{H}_{\mathrm{A}} = \frac{1}{2}(E_e - E_g)\hat{\sigma}_3 = \frac{1}{2}\hbar\omega_0\hat{\sigma}_3, \tag{3.81}$$

where $E_e = -E_g = 1/2\hbar\omega_0$.

The free-field Hamiltonian,

$$\hat{H}_{\mathrm{F}} = \hbar\omega\hat{a}^\dagger\hat{a}. \tag{3.82}$$

Now, we can write the full Hamiltonian of the model,,

$$\hat{H} = \hat{H}_{\mathrm{A}} + \hat{H}_{\mathrm{F}} + \hat{H}_{\mathrm{I}}, \tag{3.83}$$

$$= \frac{1}{2}\hbar\omega_0\hat{\sigma}_3 + \hbar\omega\hat{a}^\dagger\hat{a} + \hbar\lambda(\hat{\sigma}_+ + \hat{\sigma}_-)(\hat{a} + \hat{a}^\dagger). \tag{3.84}$$

In the free-field and the free-atomic case, the operators involved evolve in a similar way,

$$\hat{a}(t) = \hat{a}(0)e^{-i\omega t}, \quad \hat{a}^\dagger(t) = \hat{a}^\dagger(0)e^{i\omega t} \tag{3.85}$$

$$\hat{\sigma}_\pm = \hat{\sigma}_\pm(0)e^{\pm\omega_0 t}. \tag{3.86}$$

The dependency of the operators can be approximated as,

$$\begin{aligned}
\hat{\sigma}_+\hat{a} &\sim e^{i(\omega_0-\omega)t}, \\
\hat{\sigma}_-\hat{a}^\dagger &\sim e^{-i(\omega_0-\omega)t}, \\
\hat{\sigma}_+\hat{a}^\dagger &\sim e^{i(\omega_0+\omega)t}, \\
\hat{\sigma}_-\hat{a} &\sim e^{-i(\omega_0+\omega)t}.
\end{aligned}$$

When the atomic transition frequency is close to the field frequency, $\omega_0 \sim \omega$, rapid oscillations occur in the last two terms of the Hamiltonian. These rapid variations can lead to a complicate and more careful analysis. More specifically, the terms $\hat{\sigma}_+\hat{a}^\dagger$ and $\hat{\sigma}_-\hat{a}$, do not conserve energy in a straightforward sense. By applying the rotating wave approximation (RWA), that is, by omitting these non-energy-conserving terms, the Hamiltonian simplifies to,

$$\hat{H} = \frac{1}{2}\hbar\omega_0\hat{\sigma}_3 + \hbar\omega\hat{a}^\dagger\hat{a} + \hbar\lambda(\hat{\sigma}_+\hat{a} + \hat{\sigma}_-\hat{a}^\dagger). \tag{3.87}$$

The model has the following constants of motion that are worth mentioning. First, we have the excitation number,

$$\hat{N}_e = \hat{a}^\dagger\hat{a} + |e\rangle\langle e|, \quad [\hat{H}, \hat{N}_e] = 0, \tag{3.88}$$

and second we have the electron number,

$$\hat{P}_e = |e\rangle\langle e| + |g\rangle\langle g| = 1, \quad [\hat{H}, \hat{P}_e] = 0, \tag{3.89}$$

this is valid when no other atomic states can become populated.

As we explain, for the JCM the number of electrons is unchanged[16]. Instead, the relevant operators would destroy the excited electron state and create a lower energy electron state. Importantly, while the state of the electrons in the atom changes, the total number of electrons is unchanged. Hence, the energy available for creating the photon is only the difference in the binding energies. These are key characteristics that will allow us to make, later in Sec. 3.4.2, a straightforward analogy between this photon emission from an excited atom case and our case of axion dark matter experiment, which we make explicitly later in the next subsection.

Now, let us take a look into the stationary states of the JCM. Consider once again the Hamiltonian in Eq. (3.87). Analyzing the possible transitions in terms of photon (field) number states, where each state $|n\rangle$ represents a fixed number of photons, we observe that the allowed transitions are [253],

$$|e\rangle|n\rangle \longleftrightarrow |g\rangle|n+1\rangle, \quad |e\rangle|n-1\rangle \longleftrightarrow |g\rangle|n\rangle. \tag{3.90}$$

The whole dynamic of the system will be confined to this transition configuration. When considering the transitions between the ground and exited states, the key transitions involve changes in the photon number by ± 1 coupled with the atomic state change. By defining the product states in Eq. (3.90), the matrix elements of the Hamiltonian in this context are calculated within a 2×2 subspace. This restriction to a 2×2 matrix arises from the fact that the dynamics of the system primarily involve transitions that change the photon number by ± 1,

$$\mathbf{H}^{(n)} = \omega_c \begin{pmatrix} n\omega + \frac{1}{2}\hbar\omega_0 & \hbar\lambda\sqrt{n+1} \\ \hbar\lambda\sqrt{n+1} & (n+1)\omega - \frac{1}{2}\hbar\omega_0 \end{pmatrix}. \tag{3.91}$$

This matrix form applies on a basis where the two states involved are orthogonal, corresponding to the atomic states (ground and excited) combined with photon numbers n and $n+1$. The energy eigenvalues of the Hamiltonian are,

$$E_\pm(n) = \left(\frac{1}{2} + n\right)\hbar\omega \pm \hbar\Omega_n(\Delta), \tag{3.92}$$

[16]This is already required by lepton number conservation.

where Ω_n is the Rabi frequency which quantifies how rapidly the system oscillates between energy states, and $\Delta = \omega_0 - \omega$. The eigenstates associated are,

$$|n,+\rangle = (\cos(\phi_n/2)|\psi_{1n}\rangle + \sin(\phi_n/2)|\psi_{2n}\rangle), \tag{3.93}$$

$$|n,-\rangle = (-\sin(\phi_n/2)|\psi_{1n}\rangle + \cos(\phi_n/2)|\psi_{2n}\rangle), \tag{3.94}$$

where $\phi_n = \tan^{-1}(\frac{2\lambda\sqrt{n+1}}{\Delta})$.

The description above of the stationary states are helpful when describing the dynamics for rather general initial states, for example, superpositions.The study of these superpositions will be of great help in understanding possible state superpositions in dark matter experiments, as presented in Sec 3.4.5. For now, to have a clear idea, let us look into a concrete example where the initial state is a superposition of states for the JCM,

$$|\psi_f(0)\rangle = \sum_n C_n|n\rangle. \tag{3.95}$$

An atom prepared in a state $|e\rangle$, then introduced into the field, so that the initial state of the system is,

$$\begin{aligned}|\psi_{af}(0)\rangle &= \sum_n C_n|n\rangle|e\rangle = \sum_n C_n|\psi_{1n}\rangle,\\ &= \sum_n C_n(\cos(\phi_n/2)|n,+\rangle - \sin(\phi_n/2)|n,-\rangle).\end{aligned}$$

For $t > 0$ the state vector goes as,

$$|\psi_{af}(t)\rangle = \exp\left(-\frac{i}{\hbar}\hat{H}t\right)|\psi_{af}(0)\rangle. \tag{3.96}$$

This time evolution introduces oscillatory dynamics between the atomic and field states, where the oscillation frequency for each component depends on n and the coupling parameter λ. These oscillations are significant when studying transition rates in the JCM, insights that will be relevant to our discussion of superpositions in dark matter experiments later in this Chapter.

Linking Axion Dark Matter description in Fock Space to the Jaynes-Cummings Model

We can make a straightforward analogy between the photon emission from an excited atom case and our case of the axion dark matter experiment. We can compare the electron states to the spin states and the photon to the axion, as shown in Fig. 3.6. In the DM experiment case, the total number of spins is conserved, and the energy difference is only given by the binding energy in the magnetic field, very similar to the case of the electrons in the atom. In contrast, neither axion nor photon numbers are conserved, and their full energy is required/available in the process.

We describe the axion field using creation and annihilation operators, establishing a formalism that mirrors the treatment of quantum systems in the JCM. Additionally, we assume that the field can be represented in terms of energy eigenfunctions that are normalizable solutions of the Klein-Gordon equation for the axion field[17]. In the JCM, the interaction between a two-level quantum system and

[17] We neglect self-interactions of the axion field.

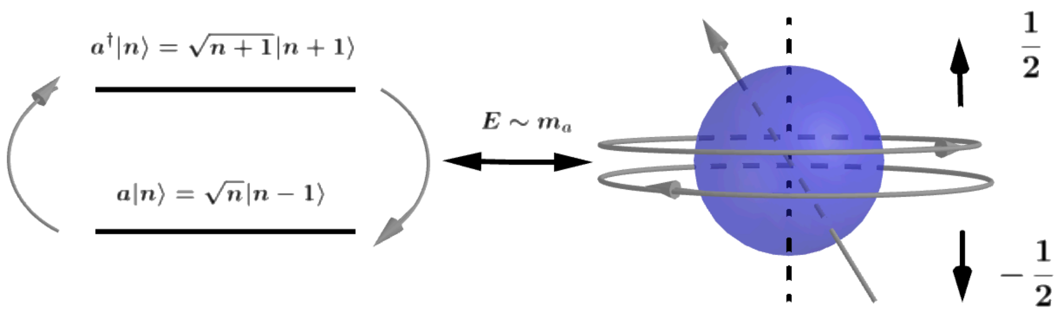

Figure 3.6. Illustration of the axion-spin system. A Single spin up state, flips it into a down state by $E \approx m_a \approx \omega_L$. This is compensated by the operator a "destroying" one axion of energy. And vice versa.

a quantized field mode is characterized by energy eigenstates and operators representing transitions between these states, similar to the eigenfunctions we consider for the axion field. We express the field operator in the interaction picture as [18],

$$\phi(t,x) = \sum_n \frac{1}{\sqrt{2E_n}} \left[\phi_n(x) a_n \exp(-iE_n t) + \phi_n(x) a_n^\dagger \exp(+iE_n t)\right], \tag{3.97}$$

where a_n and $a_n^\dagger$ are the annihilation and creation operators for axions and E_n represents the energy eigenvalues of the eigenstates described by the wave functions $\phi_n(x)$.

Expanding on the comparison to the JCM Hamiltonian in Eq.(3.85), here, the total Hamiltonian of the system is presented as a sum of an interaction term H_{int}, the experimental Hamiltonian in the absence of axions, H_{exp} and the term corresponding to the axion field, H_{ax},

$$\begin{aligned} H &= H_{ax} + H_{int} + H_{exp} \\ &= \int d^3x \, \frac{1}{2}\left[(\dot{\phi}(x))^2 + (\nabla\phi(x))^2 + m_a^2\phi^2\right] + H_{int} + H_{exp} \\ &= \sum_n E_n \left(a_n^\dagger a_n + \frac{1}{2}\right) + H_{int} + H_{exp}. \end{aligned} \tag{3.98}$$

In the context of axions confined within Earth's gravitational potential, each energy level E_n includes the full relativistic energy of state n, accounting for the axion rest mass and additional contributions from gravitational binding. Since the gravitational binding energy is much smaller than the axion mass, we can approximate the total energy as $E_n \approx m_a +$ small correction.

This description focuses on experiments like CASPEr, which target axion-nuclear spin interactions. We make some simplifying assumptions to adapt the analysis to this experimental framework. Specifically, we treat the system as a collection of stationary, non-self-interacting spin-$1/2$ states located near $x = 0$. These spins are exposed to a magnetic field along the z-axis, resulting in an energy splitting determined by the Larmor frequency [19]. This simplified description captures the essential

[18] We choose the $\phi_n(x)$ to be real and normalize $\int_x \phi_n \phi_m = \delta_{nm}$.

[19] The Larmor frequency characterizes the precession rate of a magnetic moment around an external magnetic field, depending on the field strength and the particle's gyromagnetic ratio.

two-level dynamics of the axion system and aligns with the structured energy interactions modeled by the JCM, as described in Sec. 3.4.2.

The corresponding Hamiltonian in this case, can be written as,

$$H_{exp} = -\frac{\omega_L}{2} \sum_{i=1}^{N_s} \sum_{s,s'=\uparrow,\downarrow} \left[b_s^\dagger \left(\sigma_z\right)_{ss'} b_{s'} \right]_i , \tag{3.99}$$

where $b_{s,i}^\dagger$ and $b_{s,i}$ represent the creation and annihilation operators for the spin state s of the i-th nucleon, and $\vec{\sigma} = (\sigma_x, \sigma_y, \sigma_z)$ are the Pauli matrices.

It is important to mention another assumption we make regarding the dissipation/relaxation terms that are usually included, c.f., e.g. [254–256]. Here, we neglect these effects because we assume the relevant time scales to be very large ($T_2 \to \infty$). This claim, however, should be approached with caution. It is true that in experimental setups like CASPEr [173], the impact of dissipation and relaxation effects might be minimized or controlled to a great extent; good enough for our assumption to hold, nevertheless, stating that these effects are entirely neglected is potentially misleading. We, therefore, acknowledge that while the dissipation/relaxation terms are assumed to have minimal impact in our context due to long time scales, their potential influence on the system in a more general description should not be entirely disregarded and should be properly studied. But this is beyond the present work.

Finally, we described the interaction with an axion-induced electric dipole operator, cf. [257],

$$H_{int} = -\int d^3x \mathcal{L}_{int} = \int d^3x \frac{i}{2} g_d \phi(x) F_{\mu\nu} \bar{\psi} \sigma^{\mu\nu} \gamma^5 \psi. \tag{3.100}$$

In our approach, the electromagnetic field is represented by a fixed external electric field $\vec{E}$ and, as already mentioned, the matter fields ψ as a set of N_s non-moving and non-interacting spins located (close) to $x = 0$,

$$\psi \approx \sum_{i=1}^{N} \sum_{s=\uparrow,\downarrow} \sqrt{\delta(x)} \exp(-i\epsilon_0 t - i\epsilon_s t) u_s b_{s,i}, \tag{3.101}$$

where we neglect the antiparticle contributions, which corresponds to a non-relativistic situation.

The matter field operator, which embeds the creation operators for the spin-up and spin-down states at a specific location, $b_{s,i}$, interacts with specific spin energies along with a spin-independent energy component. This characterization parallels the free atomic Hamiltonian, which establishes the energy baseline between the $|g\rangle$ and $|e\rangle$ states, illustrated in Fig. 3.5. The spinors and spin-state energies are given by

$$\begin{aligned} u_\uparrow &= (1,0,0,0)^T, \qquad \epsilon_\uparrow = -\frac{1}{2}\omega_L, \\ u_\downarrow &= (0,1,0,0)^T, \qquad \epsilon_\downarrow = \frac{1}{2}\omega_L. \end{aligned} \tag{3.102}$$

This Ansatz simplifies the interaction term as (see, e.g. [258])

$$\frac{i}{2} F_{\mu\nu} \bar{\psi} \sigma^{\mu\nu} \gamma^5 \psi = 2\vec{E}\hat{\vec{S}}\delta(x). \tag{3.103}$$

Here, $\hat{\vec{S}}$ is the spin operator for the full set of spins that can be expressed as [259]

$$\hat{\vec{S}}(t) = \frac{1}{2}\sum_{i=1}^{N_s}\sum_{s,u=\uparrow,\downarrow} b^\dagger_{s,i}(\vec{\sigma})_{su}b_{u,i}\exp(i(\epsilon_s - \epsilon_u)t). \tag{3.104}$$

Now, let us focus on the experimental situation where the electric field aligns with the x-direction. In this case, the spin component along this direction can be described using the spin creation and annihilation operators as,

$$\hat{S}_x(t) = \frac{1}{2}\sum_{i=1}^{N_s}\sigma_{x,i}(t) = \frac{1}{2}\sum_{i=1}^{N_s}\left[b^\dagger_{\uparrow,i}b_{\downarrow,i}\exp(-i\omega_L t) + b^\dagger_{\downarrow,i}b_{\uparrow,i}\exp(+i\omega_L t)\right]. \tag{3.105}$$

Putting everything together we have,

$$\begin{aligned} H_{int}(t) &= g_d E_x(0)\sum_n \frac{1}{\sqrt{2E_n}}\phi_n(0)\sum_{i=1}^{N_s}\Big[a_n b^\dagger_{\downarrow,i}b_{\uparrow,i}\exp(-i(E_n-\omega_L)t) \\ &\qquad + a^\dagger_n b^\dagger_{\uparrow,i}b_{\downarrow,i}\exp(+i(E_n-\omega_L)t)\Big]. \end{aligned} \tag{3.106}$$

The time dependence arises from the respective states/operators, $\hat{a}(t) = a_n e^{-iE_n t}$, $\hat{a}^\dagger(t) = a^\dagger_n e^{iE_n t}$. Here, integrating over an infinite time, we would give us a δ-function in energy. As in the previous JCM case, we apply the so-called rotating wave approximation (RWA) (cf., e.g., [260,261]). So we leave aside the terms with $\sim \exp(\pm i(E_n + \omega_L)$ that oscillate very fast.

This scenario can be simplified by assuming that all axions occupy the same spatial state, which implies that there is only one energy state E with wave function φ occupied. However, this configuration does not uniquely define the quantum state of the axion field, since a variable number of axions can populate this spatial state due to the bosonic characteristics of axions. Furthermore, we chose the magnetic field such that the Larmor frequency aligns with the energy of the single axion by setting $\omega_L = E \approx m_a$, ensuring resonance between the Larmor frequency and the energy associated with an individual axion. In this case the interaction simplifies to,

$$H_{int} = \frac{g_d E_x(0)}{\sqrt{2E_n}}\varphi(0)\sum_{i=1}^{N_s}\left[ab^\dagger_{\downarrow,i}b_{\uparrow,i} + a^\dagger b^\dagger_{\uparrow,i}b_{\downarrow,i}\right]. \tag{3.107}$$

Energy conservation in this scenario can be understood as follows. The operator $b^\dagger_{\downarrow,i}b_{\uparrow,i}$ takes a single spin up state and flips it into a down state. This costs an energy ω_L. This is compensated by the operator a "destroying" one axion of energy $E \approx m_a \approx \omega_L$. Then the energy is conserved. Here as in the two-level atom system, the energy cost associated with the spin transformation (this also being a two level system) corresponds to the energy required for transitions between atomic levels in the JCM.

Finally, let us now look at a state in Fock space that contains N_a axions and where $N_\uparrow$ spins are up and $N_\downarrow$ spins are down,

$$|N_a, N_\uparrow, N_\downarrow\rangle. \tag{3.108}$$

The effect of the interaction Hamiltonian can be seen structurally as,

$$H_{int}|N_a, N_\uparrow, N_\downarrow\rangle = A|N_a - 1, N_\uparrow - 1, N_\downarrow + 1\rangle + B|N_a + 1, N_\uparrow + 1, N_\downarrow - 1\rangle, \tag{3.109}$$

with some constants A, B.

Essentially, it is the annihilation of an axion that provides the energy for the spin flip. Consequently, the full relativistic energy, including the rest mass energy, is available for this process. We stress one final time that the energy exchange mechanism described as the annihilation of an axion providing the energy for spin changes evidently resembles JCM energy transitions between atomic and field states. More specifically, the annihilation of axions serves as the energy source for inducing spin changes, just as photons facilitate transitions in the JCM by exchanging energy between the atomic and field states.

3.4.3 Energy eigenstate

With the framework in place, we can study the behavior of the system by focusing on energy eigenstates, particularly those without the dipole interaction component. The simplest initial state is an energy eigenstate of $H_{ax} + H_{exp}$.

This strategy allows us to consider scenarios in which external influences, such as switching off the electric field before starting the experiment, can be taken into account, the traceability of the analysis system. Furthermore, we can facilitate the analysis of the dynamics of the system even more by treating the axion interaction as a small perturbation due to its weak influence on the experiment. More specifically, we consider a situation where we start with an axion number eigenstate with N_a axions and all spins parallel to the magnetic field $N_\uparrow = N_s$ and $N_\downarrow = 0$,

$$|N_a, N_s, 0\rangle. \tag{3.110}$$

This simplified initial state presents a minimum uncertainty, simplifies the dynamics of the system, and facilitates the study of its evolution over time. Starting from a state with these characteristics lays the foundation for a subsequent examination of the properties and behavior of the coherent states within the quantum system under study.

In the absence of interactions, there is a set of degenerated energy eigenstates with the above state,

$$|N_a - N_\downarrow, N_s - N_\downarrow, N_\downarrow\rangle, \qquad N_\downarrow = 0, \ldots, N_s. \tag{3.111}$$

Hence, we can narrow our analysis to this degenerate subspace by adhering to the principles of degenerate perturbation theory in the presence of weak interactions. This targeted approach allows a more detailed exploration of how these weak interactions influence spin dynamics, especially when the system is initially set in superposition states that are not energy eigenstates, as we will see later in Sec 3.4.4.

The number of degenerate states is 2^{N_s}. Yet, the interaction Hamiltonian meets the condition $[H_{int}, S^2] = 0$; this ensures that S^2 is conserved. Consequently, we can focus on the subspace characterized by the identical total spin as the initial state described in Equation (3.110). Thus, the dimension of the relevant Fock-space is $N_s + 1$.

Single spin case, $N_s = 1$

The simplest case we can analyze is $N_s = 1$. Here, we have only two degenerate states,

$$|N_a, 1, 0\rangle, \quad |N_a - 1, 0, 1\rangle. \tag{3.112}$$

In this subspace, our interaction Hamiltonian is given by,

$$H_{\text{int}} = \omega_c \begin{pmatrix} 0 & \sqrt{N_a} \\ \sqrt{N_a} & 0 \end{pmatrix}. \tag{3.113}$$

In this scenario, a direct connection to JCM can be established based on the interaction Hamiltonian. This form of the interaction Hamiltonian closely resembles the Hamiltonian in the two-level atom approximation where the atom and field states are represented by a two-dimensional Hilbert space, as shown in Eq. (3.91). The off-diagonal $\sqrt{N_a}$ terms in the Hamiltonian mirror the coupling strength between the two states, in analogy to the coupling between the atom and the field in the JCM.

Furthermore, the effective coupling frequency, ω_c, as defined in Equation (3.114), leads to a direct connection to the Rabi-frequency in the JCM. In this context, the effective coupling frequency is expressed as,

$$\omega_c \sqrt{N_a} = \frac{g_d E_x(0)}{\sqrt{2E_n}} \varphi(0) \sqrt{N_a} = \frac{g_d E_x(0)}{\sqrt{2E_n}} \sqrt{2\rho_a/m_a}, \tag{3.114}$$

where ρ_a is the axion energy density and accordingly ρ_a/m_a is the number density. Here, $\varphi^2(0)$ gives the probability density for an axion to be located in the vicinity of $x = 0$, when only a single axion is present. This increases by the number of axions, N_a, occupying the same state. Hence, both the coupling frequency ω_c and the Rabi-frequency, as discussed in [262], serve an equivalent role in their respective contexts (recall that the Rabi frequency characterizes the coupling strength g between the atom and the field in the JCM, $\Omega_{\text{Rabi}} = 2g$). Some other similarities can be drawn when comparing the energy eigenvalues of both models.

Now, we can study the time evolution in the interacting picture starting from the initial state $(1, 0)^T$. In this picture, the oscillation $\sim E = \omega_L$ from the non-interacting parts H_{ax} and H_{exp} are factored out. So that,

$$\Psi(t)_I = \left(\cos(\sqrt{N_a}\omega_c t), -i\sin(\sqrt{N_a}\omega_c t)\right)^T. \tag{3.115}$$

We can already see that the time scale of the evolution is only fixed by the coupling frequency ω_c, which is suppressed by the small coupling g_d. Here, the time evolution of the system in the interaction picture shows oscillations that are determined only by the coupling frequency. The axion energy/mass and the Larmor frequency do not appear explicitly. Whether these observations are artifacts of the interaction picture is a valid question. However, in the interaction picture, the oscillations induced by the interaction are uniform across all relevant states, resulting in a predictable and uniform effect on the observables. Consequently, this uniform oscillation does not alter the value of the expectation of the observables, $\langle S_z \rangle$, $\langle S_y \rangle$, since it affects all relevant states equivalently, as shown in Fig. 3.7 for an example with $N_a = 5$.

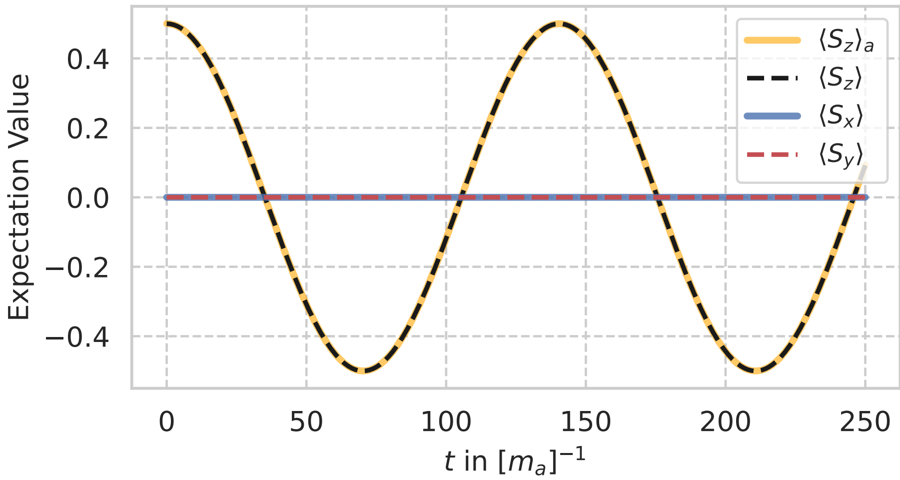

Figure 3.7. Time evolution of the expectation values of the spin operator for the state $|5,1,0\rangle$ with coupling frequency $\omega_c = .01\,[m_a]$, $m_a = 1\,[m_a]$. $\langle S_z \rangle_a$ denotes the analytical result for the z-direction given by equation (3.115). The other expectation values, and further numerical results in this note were obtained using the Qutip library [263, 264]. Everything is kept in units of the axion mass, such that the result is invariant under rescalings. We see an oscillation only for the expectation value $\langle S_z \rangle$. Also note that the oscillation frequency in this signal is given by twice the coupling frequency $\sqrt{N_a}\omega_c$ as the expectation value depends on $\cos^2(\sqrt{N_a}\omega_c t) - \sin^2(\sqrt{N_a}\omega_c t)$.

We can explain the absence of an oscillation with the Larmor frequency easily, since we started from an energy eigenstate, which are stationary (i.e., expectation values involving them do not depend on time). The only real-time dependence here, arises from the fact that the interaction Hamiltonian slightly changes the energy eigenstates and eigenvalues. The time evolution arises due to this small frequency splitting $\sim \omega_c$. However, one must be careful because the sensitive observable measured in CASPEr is supposed to be the transverse magnetization rotating with the Larmor frequency; this should correspond to $\langle S_y \rangle(t)$. As we discuss in detail in Sec. 3.4.4, this absence is an artifact of the special initial state we have taken and the specific quantity we have chosen to measure. For now, in an energy eigenstate, the expectation value of the field operator, which, in the classical approximation, we would want to identify with the classical field value, vanishes. The non-vanishing energy is essentially stored in the expectation value of the square of the field value[20]. In this sense, no proper classical field drives the expectation values of $S_{x,y}$.

Multiple spin case, $N_s > 1$

In the case of more than one spin, in the absence of interactions, we can write the interaction Hamiltonian in the degenerate subspace Eq. (3.111) spanned by

[20]The vanishing expectation value can be understood as follows. Energy eigenstates are stationary, i.e., the phases $\exp(-iEt)$ from their time evolution drop out when calculating expectation values. Therefore, the expectation value of the field operator is time-independent. As we do not have a situation with spontaneous symmetry breaking, the constant value must indeed be zero.

$|N_a - N_\downarrow, N_s - N_\downarrow, N_\downarrow\rangle$, where $0 \le N_\downarrow \le N_s$,

$$\begin{aligned}(H_{int})_{ij} &= \langle N_a - i + 1, N_s - i + 1, i - 1|H_{int}|N_a - j + 1, N_s - j + 1, j - 1\rangle \\ &= \omega_c(\delta_{j,i+1} + \delta_{j+1,i})\sqrt{(\min(i,j))(N_s - \min(i,j) - 1)}\sqrt{N_a - \min(i,j) - 1}.\end{aligned}$$

Explicitly, the matrix representation of the interaction Hamiltonian is schematically given by

$$H_{int} = \omega_c \begin{pmatrix} 0 & \sqrt{N_a N_s} & 0 & \dots & \dots & 0 \\ \sqrt{N_a N_s} & 0 & \sqrt{2(N_s-1)(N_a-1)} & 0 & \dots & 0 \\ \vdots & \ddots & \ddots & \ddots & \vdots & \vdots \end{pmatrix}. \tag{3.116}$$

The matrix structure in Eq. (3.116) can be derived from the interaction Hamiltonian, resulting in a symmetric band matrix with non-zero entries solely on the first sub- and superdiagonals. This structural pattern arises from the nature of the interaction Hamiltonian, which, when acting on any energy eigentate, eases the inversion of a spin while creating or annihilating an axion. This interaction mechanism adjusts the energy content of the system, by providing the necessary energy or by absorbing the excess energy in the axion field.

To compute the elements of this matrix, we can use the normalization of the degenerate energy eigenstates and the combinatorics arising when applying the interaction Hamiltonian. A state $|N_a - N_\downarrow, N_s - N_\downarrow, N_\downarrow\rangle$ corresponds to the tensor product of an axion number state with a superposition of spin product states containing the correct quantity of spin-up and spin-down states. Ensuring the orthonormality of such states needs accounting for the number of feasible product states containing $N_\downarrow$ down- and $N_s - N_\downarrow$ up-states. This is the same as counting the subsets with $N_\downarrow$ elements within a set of N_s elements. Therefore, the normalization is given by,

$$|N_a - N_\downarrow, N_s - N_\downarrow, N_\downarrow\rangle = \binom{N_s}{N_\downarrow}^{-1/2}\left(|N_a - N_\downarrow\rangle \otimes \sum_i |S(N_\downarrow)_i\rangle\right). \tag{3.117}$$

Here, the states $|S(N_\downarrow)_i\rangle$ are the product states with the correct number of up- and down-spins. When applying the interaction Hamiltonian, the number of possible flips that can occur when projecting onto another state has to be accounted. Consider the part of the interaction that projects the state $|N_a - (N_\downarrow + 1), N_s - (N_\downarrow + 1), N_\downarrow + 1\rangle$ onto $|N_a - N_\downarrow, N_s - N_\downarrow, N_\downarrow\rangle$. For every product state, $N_\downarrow + 1$ possible flips are to be carried out. However, since the resulting state has fewer spins in the down position, redundancy will be present in the resulting superposition. This redundancy shows up in the interaction as the number of product states within the initial state,

$$\begin{aligned}(H_{int})_{N_\downarrow - 1, N_\downarrow} &= \sqrt{N_a - N_\downarrow}\left(\binom{N_s}{N_\downarrow}\binom{N_s}{N_\downarrow + 1}\right)^{-1/2} \cdot (N_\downarrow + 1)\binom{N_s}{N_\downarrow + 1}, \\ &= \sqrt{(N_a - N_\downarrow)(N_\downarrow + 1)(N_s - N_\downarrow)}.\end{aligned} \tag{3.118}$$

The first two factors besides the axion number arise from the normalization, whereas the factors after are from the application of the interaction, as already discussed above. The elements on the subdiagonal can be obtained in the same way.

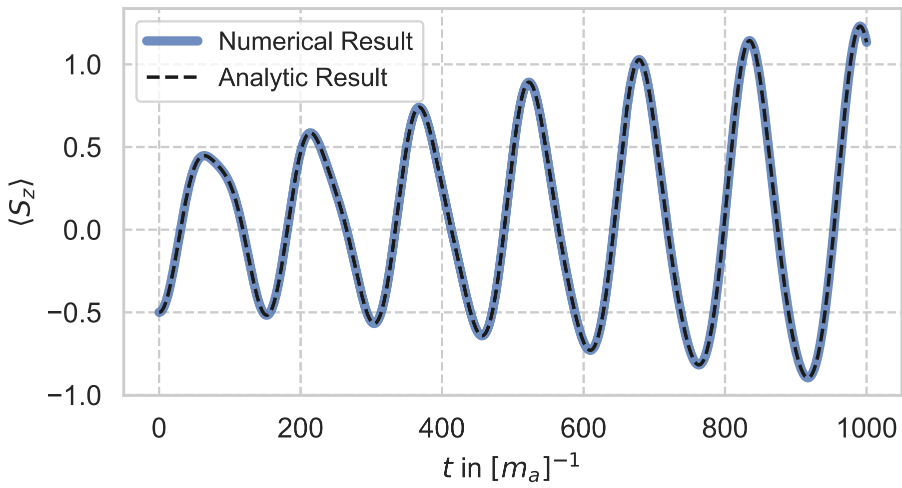

Figure 3.8. Expectation values $\langle S_z \rangle$ for the initial energy eigenstate $|5, 1, 2\rangle$. The axion mass in this computation was taken as $m_a = 1\,[m_a]$, and the coupling frequency given via $\omega_c = 0.01\,[m_a]$. As a check we show a numerical result obtained via Qutip [263, 264] (black, dashed), and an analytical one (obtained with Sympy [265]) from the interaction Hamiltonian in Eq. (3.116) (blue, solid).

Using the above interaction Hamiltonian, we can compute the evolution of an original energy eigenstate. An example is shown in Fig. 3.8. However, as before, we find that no oscillation with the Larmor frequency appears for $\langle S_x \rangle$ and $\langle S_y \rangle$. Both keep vanishing. This can be understood from the fact that the energy splittings in the degenerate subspace are all proportional to the small frequency ω_c. Therefore, no oscillation with the Larmor frequency appears. More technically, we can see that the application of the spin operators in the x- or y- direction raises or lowers the spin in each state by one unit. If we leave the axion state unchanged as in a pure spin measurement, the resulting state is a combination of states whose energy differs from the original energy by one unit of the Larmor frequency. These states are thus orthogonal to the original state, and the expectation value vanishes. That said, it is clear that this can be remedied if the initial state already contains a combination of energy eigenstates with energies differing by one unit of ω_L. We go into more detail on this matter in the following subsection.

3.4.4 The appearance of oscillations with the axion mass and suitable measurement procedures

In the previous section, we noted that for particle number eigenstates, the expectation value of spin does not exhibit oscillations with the Larmor frequency, contrary to what is typically expected in experiments. A simple argument is that the axion field is unlikely to exist in a particle number eigenstate. Instead, it is often suggested that a coherent or Glauber state [245], might be a more suitable assumption for describing the axion field [266].

Coherent states are superpositions of Fock states and exhibit both coherence and quantum superposition properties. In contrast to Fock states, which have a fixed particle number, coherent states allow particle number fluctuations, making them well-suited for systems like the axion field, where

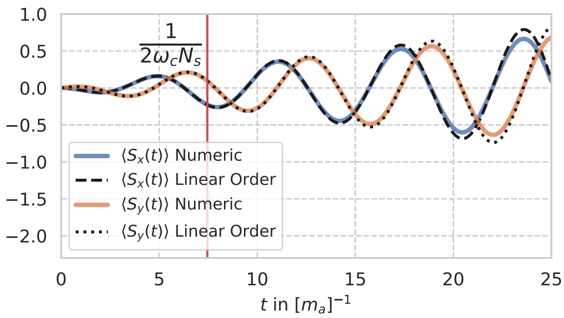

Figure 3.9. Time evolution of the spin expectation values in the directions transverse to the magnetic field. The chosen initial state is $\frac{1}{\sqrt{2}}(|5\rangle + |4\rangle)|3,0\rangle$. The coupling frequency and axion mass/Larmor frequency are given by $\omega_c = .01\,[m_a]$ and $m_a = 1\,[m_a]$. As expected we observe an oscillating signal with a frequency m_a. Also as expected we find good agreement between the linear order result Eq. (3.124) and the numerical result obtained with Qutip [263, 264].

particle number is not conserved. Consequently, modeling the axion field as a coherent or Glauber state may offer a more precise and flexible representation of its quantum behavior. In such a case, relaxation processes may bring us closer to a particle number state, particularly for axions trapped in some potential, causing no signal to be detected. Fortunately, small modifications away from the pure axion number state give rise to an oscillating signal with an amplitude close to the classical expectation, as shown in the following subsection. This means that the initial state would have to be rather close to the number eigenstate to suppress the signal by orders of magnitude, which is unlikely since no strong processes force the system into a number eigenstate. Now, if the system is in an exact number eigenstate, the experimental procedure can always be adapted so the system is modified away from an energy eigenstate into a state where oscillations with $\omega_L = E \approx m_a$ will occur. In the following, we present explicit yet crude examples that closely relate to JCM superposition of excitation number states, known as dressed states, as described in Sec. 3.4.2. While a more comprehensive examination of measurement procedures and their practical implementations in CASPEr would be beneficial, such an in-depth analysis falls outside the scope of our work (we make some additional comments on the effects of measurements in Appendix C.1).

3.4.5 A simple initial state oscillating with frequency $\omega_L = E \approx m_a$

We can consider one of the simplest non-axion particle number eigenstates as,

$$|\Psi_0\rangle = \frac{1}{\sqrt{2}}\left(|N_a\rangle + |N_a - 1\rangle\right) \otimes |N_s \uparrow, 0 \downarrow\rangle. \tag{3.119}$$

As shown in Fig. 3.9 this already produces the desired oscillation with ω_L.

A priori this is just an example of one of the most straightforward superposition states, leading to a suitable time-dependence. In the next subsection (as well as in Appendix C.1), we discuss how we can obtain such a state starting from an energy eigenstate.

To make sure that we are not dealing with a special feature of the state in Eq. (3.119), we analyze the signal for a more general initial state denoted as $|\Psi_0\rangle$. In order to achieve this, we use a first-order approximation in the interacting Hamiltonian, specifically in the small frequency ω_c, to derive the linearized time evolution. This approach exploits the smallness of the effective coupling frequency. We examine the time evolution of the proposed initial state within the interaction picture and subsequently linearize it,

$$|\Psi_I(t)\rangle = e^{iH_0t}e^{-iHt}|\Psi_0\rangle = (1 - i(H - H_0)t + \mathcal{O}(t^2))|\Psi_0\rangle. \tag{3.120}$$

The time evolution of the spin operators (acting on the ith spin) in the interaction picture is given by,

$$\begin{aligned} \frac{1}{2}e^{iH_0t}\sigma_{i,x}e^{-iH_0t} &= \frac{1}{2}\left[e^{im_at}\sigma_i^- + e^{-im_at}\sigma_i^+\right], \\ \frac{1}{2}e^{iH_0t}\sigma_{i,y}e^{-iH_0t} &= \frac{1}{2}\left[ie^{im_at}\sigma_i^- - ie^{-im_at}\sigma_i^+\right], \end{aligned} \tag{3.121}$$

where, we simplified our notation for the spin-flip operators to be $b^\dagger_{i,\downarrow}b_{i,\uparrow} = \sigma_i^-$ and $b^\dagger_{i,\uparrow}b_{i,\downarrow} = \sigma_i^+$.

Putting everything together, we obtain the expectation values

$$\begin{aligned} \langle S_x\rangle &= \sum_{i=1}^{N_s}\frac{1}{2}\langle\Psi_0|(1 + iH_{\text{int}}t)(e^{im_at}\sigma_i^- + e^{-im_at}\sigma_i^+)(1 - iH_{\text{int}}t)|\Psi_0\rangle \\ &\approx \sum_{i=1}^{N_s}\langle\Psi_0|\frac{\omega_c}{2}\Big[e^{im_at}(\sigma_i^- + ia^\dagger\sigma_i^+\sigma_i^-t + ia\sigma_i^-\sigma_i^-t) \\ &\qquad + e^{-im_at}(\sigma_i^+ + ia\sigma_i^+\sigma_i^-t + ia^\dagger\sigma_i^+\sigma_i^+t)\Big]|\Psi_0\rangle \end{aligned} \tag{3.122}$$

$$\begin{aligned} \langle S_y\rangle &= \sum_{i=1}^{N_s}\frac{1}{2}\langle\Psi_0|(1 + iH_{\text{int}}t)i(e^{im_at}\sigma_i^- - e^{-im_at}\sigma_i^+)(1 - iH_{\text{int}}t)|\Psi_0\rangle \\ &\approx \sum_{i=1}^{N_s}\langle\Psi_0|\frac{i\omega_c}{2}\Big[e^{im_at}(\sigma_i^- + ia^\dagger\sigma_i^+\sigma^-it + ia\sigma_i^-\sigma_i^-t) \\ &\qquad - e^{-im_at}(\sigma_i^+ + ia\sigma_i^+\sigma_i^-t + ia^\dagger\sigma_i^+\sigma_i^+t)\Big]|\Psi_0\rangle. \end{aligned} \tag{3.123}$$

Given that there is consistently either a single spin change operator or an axion number changing operator in the system, it becomes apparent that in linear order, the state $|\Psi_0\rangle$ has to be a superposition. This necessity arises because the states must display some mismatch in their spin or axion number for the expectation value to avoid being projected to zero.

This can be explicitly seen for the example state Eq. (3.119),

$$\begin{aligned} \langle S_x\rangle &= \sum_{i=1}^{N_s} i\omega_ct\left(\frac{e^{im_at}}{2}\langle\Psi_0|a^\dagger\sigma_i^+\sigma_i^-|\Psi_0\rangle - \frac{e^{-im_at}}{2}\langle\Psi_0|\sigma_i^+\sigma_i^-a|\Psi_0\rangle\right) \\ &= \frac{\omega_c\sqrt{N_a}N_st}{2}\sin(m_at), \\ \langle S_y\rangle &= \sum_{i=1}^{N_s} -\omega_ct\left(\frac{e^{im_at}}{2}\langle\Psi_0|a^\dagger\sigma_i^+\sigma_i^-|\Psi_0\rangle + \frac{e^{-im_at}}{2}\langle\Psi_0|\sigma_i^+\sigma_i^-a|\Psi_0\rangle\right) \\ &= -\frac{\omega_c\sqrt{N_a}N_st}{2}\cos(m_at)\,. \end{aligned} \tag{3.124}$$

When calculating the expectation values at linear order in time, the only components that contribute are states where the axion numbers differ by 1. Consequently, it becomes evident that even with a straightforward alteration of an energy eigenstate, specifically, one comprising states with axion numbers differing by 1, we will observe oscillations of the transverse magnetization at the Larmor frequency. Note that the amplitude of the oscillations in Eq. (3.124) exhibits the scaling $\sim \sqrt{N_a} N_s$ that we expect in the classical approximation.

3.4.6 Using the experiment to change the state away from an axion number eigenstate

We have shown that even a slight deviation from the energy eigenstate enables observing an oscillating spin expectation value. Now, we will explore how such a modification can be achieved by appropriately manipulating the experimental setup.

Let us focus on the simplest case of only one spin for the calculation. We will comment on the case with more spins later. Using the initial state $|N_a, 1, 0\rangle$, we can take the result for the time evolved state, Eq. (3.115), explicitly writing the state vectors,

$$|\Psi(t)\rangle = \cos\left(\sqrt{N_a}\omega_c t\right)|N_a\rangle \otimes |\uparrow\rangle + i\sin\left(\sqrt{N_a}\omega_c t\right)|N_a - 1\rangle \otimes |\downarrow\rangle \,. \tag{3.125}$$

Now, we can switch off the experiment after some time t_{stop}. For example, we could do this by disconnecting the electric field, but we will discuss more efficient ways.

After switching off the experiment the state would continue to evolve with the "free" Hamiltonian. If we wait longer, spin relaxation plays a role (not included in our simple Hamiltonian). In particular, if we wait longer than the spin relaxation time, the spins return to their position aligned with the magnetic field. However, the axion field, being much more weakly coupled, is not affected by this,

$$\begin{aligned}
|\Psi(t)\rangle &= \cos\left(\sqrt{N_a}\omega_c t_{stop}\right)\exp(i\delta_\uparrow)|N_a\rangle \otimes |\uparrow\rangle + \sin\left(\sqrt{N_a}\omega_c t_{stop}\right)\exp(i\delta_\downarrow)|N_a - 1\rangle \otimes |\uparrow\rangle \\
&= \left[\cos\left(\sqrt{N_a}\omega_c t_{stop}\right)\exp(i\delta_\uparrow)|N_a\rangle + \sin\left(\sqrt{N_a}\omega_c t_{stop}\right)\exp(i\delta_\downarrow)|N_a - 1\rangle\right] \otimes |\uparrow\rangle.
\end{aligned}$$

Here, the phases $\delta_\uparrow$, $\delta_\downarrow$ between the two different eigenstates depends on the relaxation process.

Nevertheless, Eq. (3.126) combines states with different energy, similar to Eq. (3.119). Therefore, if we switch the experiment on again, we will typically find an oscillating spin transverse to the magnetic field.

In Fig. 3.10, we show the transverse spin expectation values for states of the form, Eq. (3.126) after switching on the interaction again. For illustration, we do not show the time during which the relaxation takes place but continue directly after t_{stop}. An explicit formula for the expectation value of S_y is given by,

$$\langle S_y\rangle = \frac{1}{\sqrt{2}}\sin\left(2\sqrt{N_a}\omega_c t_{stop}\right)\sin\left(\sqrt{N_a}\omega_c t\right)\cos\left(\sqrt{N_a - 1}\omega_c t\right)\cos\left(\delta_\uparrow - \delta_\downarrow - m_a t\right). \tag{3.126}$$

As we can see, the maximum amplitude of subsequent oscillations in the spin expectation value is determined by the contribution amplitude of the $|N_a - 1\rangle$ axion state. To achieve an amplitude of about ~ 1, waiting for a time approximately of the order of $1/(\sqrt{N_a}\omega_c)$ is necessary for a significant spin flip in the initial phase. In a more realistic scenario with a large number of spins N_s, flipping

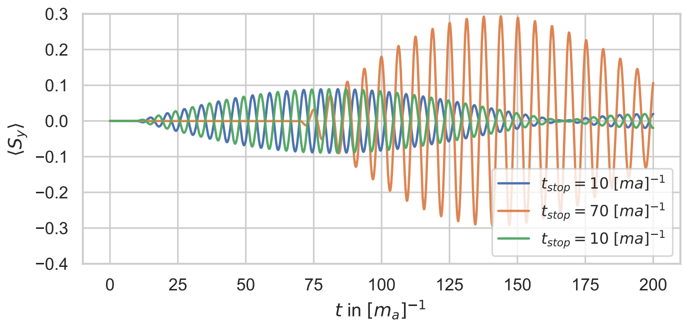

Figure 3.10. Evolution of the spin expectation value in the y-direction before and after stopping the experiment to allow for spin relaxation or flushing of the spins (the time during the interruption of the measurement is not shown). The blue line corresponds to $t_{stop} = 10\,[m_a]^{-1}$ and the orange one to $t_{stop} = 70\,[m_a]^{-1}$ with phase $\delta = \delta_{\uparrow} - \delta_{\downarrow} = -1.5$ and the green line corresponds a $t_{stop} = 10\,[m_a]^{-1}$ and $\delta = 1.5$.

just one spin suffices, reducing the initial phase requirement by roughly a factor of $\sqrt{N_s}$, as evident from the general Hamiltonian Eq. (3.116).

Given the long coherence times present in experiments like CASPEr, the relaxation of the spins may take a long time, surpassing typical measurement times, as CASPEr is specifically designed to minimize relaxation effects. This seems more efficient. Another practical alternative involves removing the polarized nuclei (or, more accurately, the corresponding atoms) from the system and replacing them with a freshly polarized sample. Essentially, this action “renews” the spins and provides a notably efficient resolution.

Replacing the samples to renew the spins can be considered inefficient, particularly since it involves discarding mostly unused spins. A more practical and resourceful method involves adjusting the magnetic field to alter the Larmor frequency, thereby exploring a different axion mass. By selecting an appropriate time t_{stop}, a single spin sample can be used to“prime” the axion state to encompass a spectrum of masses. Following this priming process, the measurement can continue as usual. In addition, this method increases efficiency by allowing a single spin sample to be used to explore a broader range of axion masses without the need for frequent sample replacements. Also, the experimental setup can maintain a consistent starting point across different measurements by priming the axion state in advance for various masses. This can reduce variability in the initial states and improve the reproducibility of results.

3.4.7 Discussion

Throughout this section, we have focused on classical and quantum coherent states in the context of axions. We emphasized the characteristics of the quantum coherent state and how they can be linked to their energy eigenstates. When the number of particles is fixed and conserved, the energy eigenstates become associated with distinct particle number states governed by the operator $\hat{N}$. Axions, as quantum particles with wave-like behavior, can exist in superpositions of these energy eigenstates, allowing them to occupy several energy states simultaneously.

By examining coherent states and their relationship with energy eigenstates, we gain insights into the fundamental physics behind astrophysical phenomena like axion stars and miniclusters. While understanding the formation and stability of axion stars and their potential fragmentation into mini-clusters is an important motivation, our primary focus is not on these structures. Instead, we explored the dynamics of axions as dark matter and their impact on experimental outcomes. This approach provides context for understanding quantum states of axions, and their implications in various settings, but the main emphasis of our study was on their role in dark matter experiments.

We have addressed a fundamental aspect from a quantum mechanical perspective: the origin of oscillation frequencies relevant to axion dark matter experiments. By studying the quantum nature of the axion field, we have elucidated underlying mechanisms that give rise to these frequencies. Beginning with a setup where axions are coupled to spins as probed by CASPEr [56], we clarified this connection by demonstrating that the initial quantum field theoretical model and the experimental context can be effectively approximated using a Jaynes-Cummings type model [251]. Our discussion also includes suitable observables, focusing on the specific case of axion experiments without introducing new elements to the general discussion of the Jaynes-Cummings model or the quantum/classical connection.

In experimental setups like the CASPEr experiment, three base frequencies are significant: the axion energy $E \approx m_a$, the Larmor frequency $\omega_L = g\mu_N B$, and the coupling frequency due to the electric dipole moment. In a resonant configuration, experimental parameters are intentionally set such that $\omega_L = E \approx m_a$. The central question of interest is how this setup leads to the magnetization signal oscillating with the Larmor=axion frequency. In classical field theory calculations, this oscillation primarily arises from the axion field oscillations at this frequency resonating with spin precession, resulting in the oscillation of magnetization with m_a. From a quantum mechanical standpoint, we can consider energy/axion number eigenstates with a given spin value in the direction of the magnetic field, such as $|N_a, N_s \uparrow, 0 \downarrow\rangle$. The interaction Hamiltonian provides the flipping of one spin at the expense of one axion, transitioning to $|N_a - 1, (N_s - 1) \uparrow, 1 \downarrow\rangle$. This process conserves energy as the absorption of one axion balances the energy required to flip a spin at ω_L. Axion number conservation is not preserved in this interaction, and the symmetry of the interaction concerning axion absorption and emission is complete. The inclination towards absorption comes from the chosen initial configuration, where all spins reside in the lower-energy state, predisposing them to absorb an axion with energy $m_a = \omega_L$. Transitions are still possible but suppressed if the resonance condition is not met. Energy conservation remains valid, which can be understood from $|N_a, N_s \uparrow, 0 \downarrow\rangle$ not being an energy eigenstate of the Hamiltonian, including the dipole interaction.

Starting from an energy eigenstate, we observe a spin expectation value oscillation aligned with the magnetic field, determined by a coupling frequency around ω_c. This slow oscillation arises from the dipole interaction splitting the previously degenerate set of eigenstates $|N_a, (N_s - N_d) \uparrow, N_d \downarrow\rangle$ by amounts $\sim \omega_c$. Once the interaction is present, an initial state like $|N_a, N_s \uparrow, 0 \downarrow\rangle$ becomes a superposition of states with different energies of the full Hamiltonian, causing time evolution with a frequency $\sim \omega_c$. Starting from an initial energy/axion number eigenstate does not result in an oscillating spin expectation value perpendicular to the magnetic field. While processes that would favor the creation of an axion number eigenstate are not currently apparent, they are not ruled out. Therefore, it is important to investigate observables that remain valid in this scenario, as they could serve as the desired observables for axion dark matter detection. This issue is rectified by starting with states that are not energy eigenstates of the Hamiltonian without interactions. Even simple superpositions lead to perpendicular spin oscillations. This deviation from the energy eigenstates shows the possibility of detecting axion dark matter through observable phenomena such as these spin transverse oscillations. The oscillation frequency $\omega_L \approx m_a$ arises because it corresponds to the level spacing between different energy eigenstates of the Hamiltonian without the interaction, as categorized by axion number (level spacing set by m_a) and spin in the magnetic field direction (level spacing by ω_L).

Chapter 4

Detecting Very Small Dark Matter Local Structure of Weakly Interacting Particles

In this chapter, we explore the detection of very small local dark matter structures, i.e., in the solar system neighborhood, through the lens of WIMPs. We specifically focus on particle-like dark matter and in particular WIMPs as defined in Sec. 2.1.1. We will use a simple description of particles that have lead to clicks in a ground-based detector to explore the detectability of such small structures. Subsequently, we will compare this simplified depiction with the detection capabilities of the most recent direct detection projections [53, 109, 114, 116–119, 267] . By using direct detection methods, our objective is to establish a minimum detection time for detecting these tiny dark matter structures.

Inspired by the Standard Halo Model (SHM), which describes DM distribution in the Milky Way, we focus on small-scale structures within the DM halo, though much smaller than those considered in SHM. The SHM, for instance, postulates the presence of sub-halos or minihalos around the Galactic Center; these structures are hard to observe due to their diffuse nature. Our study extends this idea to the Solar System scale, approximately $\sim \mathcal{O}(1)$ light-year, where even smaller structures may exist. While it remains unclear if such small structures should exist, our approach allows us to test for their presence and explore their potential impact on the DM distribution, offering insights into the finer details of halo structure.

Models and simulations are useful tools for understanding the localized distribution of dark matter (DM), but their accuracy is often limited by the scarcity of observational data for comparison [268–270]. This gap between theoretical predictions and observational evidence requires cautious interpretation of simulation results and careful extrapolation to real-world scenarios. While small structures may have a minimal impact on the overall dynamics of the DM halo, they can influence local density and velocity distributions [271–273]. In our work, we focus on very small DM structures and test their detectability through direct detection experiments. These structures could also play a role in indirect detection via annihilation signals, as their density enhances the likelihood of DM particle interactions. We aim to characterize these detectable clumps in noisy environments, distinguishing potential DM signals from background noise [274–276]. By studying their effects, we hope to gain insights into their role in the local DM distribution.

In this context, we search for clustering of events in the time domain as a potential indicator of underlying structure, since this could reveal patterns or correlations. To do so, we conduct a model-independent analysis describing particle detection from a ground-based detector using a Poisson process (PP) description; we will detail how this process serves our purpose in sec 4.1. To simplify for now, since we will go into detail later, we describe the smooth background as having a steady detection rate under the Poisson process (PP), similar to a uniform process. Conversely, we describe the substructure as the cases in which a higher number of events occur in a shorter period than the mean detection time, always following a Poisson process. This way, we can perform the spectral analysis of the signals in the frequency domain and perform statistical tests to spot how to distinguish the excess on top of the smooth background (where the excess represents the sub-structure we want to detect). Such an approach can be studied within the context of dark matter candidates like WIMPs [42] or FIMPs [89, 277]. We make use of the projection curves of experiments like XENON1T [267] and DARWIN [53] to estimate the number of events and detection time to obtain a distinction between smooth background and over-density (sub-structure).

This chapter is organized as follows. In Sec. 4.1, we present a simple statistical approach to describe a local density accounting for inhomogeneities such as particle clusters, which may contribute to an event detection signal. In our simplistic picture, DM local density can be studied spatially, i.e., the velocity distribution and its evolution in time is neglected[1]. We also make an analytical estimate for the sensitivity to sub-structure in our picture. In Sec. 4.1.4, we perform a numerical simulation and analyze the spectral densities and the ability to distinguish detection excess. In Sec. 4.2, we contrast our simulation with real parameters and estimate detection time and event for DD experiments. Finally, in Sec. 4.3 we discuss the results and some prospects.

4.1 Signal Modeling of DM Substructure in the Solar System: From Homogeneous Distributions to Clumpy Scenarios

As mentioned, DM sub-structure in our Solar System, $\sim \mathcal{O}(10^{-3})$ly or smaller, has not been extensively studied, although the understanding of such substructure (density and velocity) is essential for terrestrial direct detection experiments [274–276].

One simple way to begin inquiring about these sub-structures in our locality is by pointing to the fact that the event rates in DM experiments involving WIMPs are given by the phase space distribution function (DF) of such particles in the Solar System [278]. That said, we analyze first two opposing scenarios: one in which the local dark matter density is completely uniform and one in which it is highly clustered. Once these extremes are established, we study an intermediate point in which the distribution contains a mixture of homogeneous regions and clusters.

[1] The velocity of the clumps is not meant to change drastically in the locality, therefore the imprint of some overdensities, if they exist, should behave similarly.

In our initial approach, we model non-interacting particles that are homogeneously distributed in space without assuming any preferred position. A detector is placed in this setup, which registers events or ”clicks” when a particle reaches it. In the left panel of Fig. 4.1a, we show the signal generated by this homogeneous distribution (bottom section) as a function of time. The middle section presents the number of particles detected per time bin, revealing minor fluctuations and some degree of random clumping. The top section shows the initial input for the simulation, which is overall homogeneous, as depicted in the left panel. In real-world experiments, signals are likely to deviate from perfect homogeneity due to random clumping of dark matter. This is illustrated in the right panel of Fig. 4.1, where we observe a larger degree of clumping, which becomes more pronounced than the fluctuations seen in the homogeneous case. By introducing this clumped distribution (top section of right panel), we can simulate a transition between a purely homogeneous distribution and one with increasingly frequent clump encounters. This approach allows us to model the potential presence of localized overdensities in the dark matter distribution, providing a more realistic representation of the system.

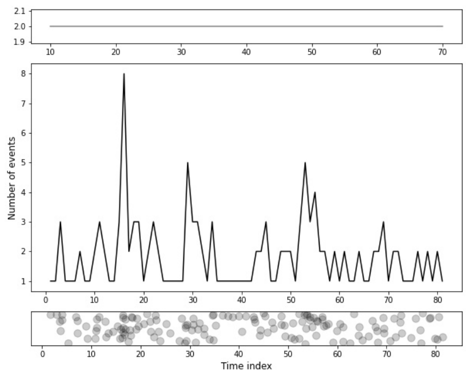

(a) Signal and flux of DM generated by a homogeneous stochastic process.

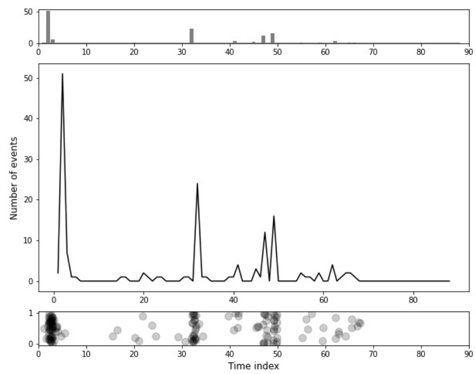

(b) Signal and flux of clumpy DM generated under the same conditions as 4.1a.

Figure 4.1. Statistical approach to signal imprint and flux for different extreme distributions.

4.1.1 Modeling the Signal with a Filtered Poisson Process

To model the signal analitically, we adapted the filtered Poisson process described in Ref. [279]. For simplicity and mathematical tractability, we chose an exponential form to describe the overdensities. This exponential choice provides a simple representation of short-duration, intense particle accumulations, which are theoretically plausible for dark matter clumping events[2].

In this framework, the signal is represented as the sum of K arrivals at the detector,

$$\eta_K(t) = \eta_{h,k}(t) + \eta_{o,k'}(t), \tag{4.1}$$

[2]Another possible description, and perhaps more physical, that can give similar results consist on considering a clump of rectangular size instead of spikes.

where $\eta_{h,k}(t)$ gives account of the homogeneous arrivals as,

$$\eta_{h,k}(t) = \sum_{k=1}^{K} A_k(t), \tag{4.2}$$

and A_k is described by an exponential distribution,

$$P_A(A; \langle A \rangle) = \frac{1}{\langle A \rangle} e^{-\frac{A}{\langle A \rangle}}. \tag{4.3}$$

Here the amplitudes A, are taken to be always positive and, $\langle A \rangle$ is the average over all random variables.

The overdensities $\eta_{o,k'}(t)$ are modeled as,

$$\eta_{o,k'}(t) = \sum_{k'=1}^{K'(T)} B_{k'} \psi \left(\frac{t - ik'\omega_o t}{\tau_d} \right), \tag{4.4}$$

where τ_d is the duration in time of the overdensity, i.e., the size measured in terms of how long it takes for the detector to cross the clump[3], $B_{k'}$ is the amplitude of the overdensity that also follows an exponential function and whose amplitude is taken to be positive[4]. Finally, ψ represents the function describing the shape of the clumps, that in our case was chosen for simplicity as an exponential function of the form, $\psi(\nu) = \Theta(\nu)e^{-\nu}$, where Θ represents a Heaviside function and ν is dimensionless variable, which in our case is $\left(\frac{t-ik'\omega_o t}{\tau_d}\right)$. The overdensities/clumps arrive according to a Poisson distribution,

$$P_{\hat{K}}(\hat{K}; T, \tau_w) = \frac{1}{K!} \left(\frac{T}{\tau_w} \right)^{\hat{K}} e^{\frac{T}{\tau_w}}, \tag{4.5}$$

where τ_w is the mean value of the exponential distribution describing the arrival times. The mean number of arrivals in this Poisson distribution is given by $\langle K \rangle = T/\tau_k$, where T is the total measurement time.

To further analyze the impact of these clumps, we introduce the intermittency parameter $\gamma = \tau_d/\tau_w$ [280]. This parameter accounts for the varying frequency of clump encounters at the detector over time, so it effectively accounts for the average fraction of time spent inside clumps. It compares the time scales of two different processes: the mean waiting time between events and the characteristic time of the clumps. For $\gamma < 1$, overdensities arrive rarely, resulting in a strongly intermittent signal. For $\gamma > 1$, overdensities overlap, and the signal begins to resemble random and symmetric fluctuations.

In the fig. 4.2, we have illustrated the intermittency parameter's effect. Here, we present two signals with different γ parameters, and we can observe that in the case where the parameter has larger values, the peaks above the average are more prominent. So, the intermittency parameter accounts for clump arrivals at the detector over time. We will review this parameter again later in the next subsection. The figure also illustrates the exponential shape of the clumps, where it is more

[3] We assume the clump's crossing time is shorter than the detection time for differentiation. If the crossing time matches or exceeds the detection time, the spectrum resembles a homogeneous distribution making detection more challenging.

[4] It is also possible to produce under densities and detect them, see Appendix D.1

evident that the particle accumulations follow a rapid rise and fall in intensity, consistent with the transient nature of dark matter clumping events that may be expected. This behavior highlights the short-lived, localized nature of the overdensities, with the signal peaking quickly and decaying exponentially, aligning with theoretical expectations for such phenomena. This exponential form is also advantageous in spectral analysis: it produces a characteristic frequency distribution with a distinct decay pattern that aligns with theoretical expectations for inhomogeneous signals produced by intense clumping events. Specifically, the exponential decay in the B_k amplitudes leads to a broadband spectrum with identifiable peaks corresponding to the arrival rate of overdensities. This spectral behavior offers an interpretable signature for detecting and distinguishing clumping structures within a signal.

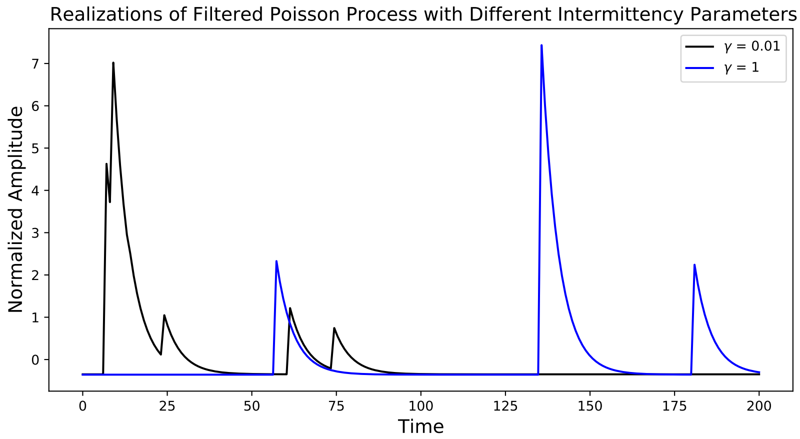

Figure 4.2. Realization of the filter Poisson process we have adapted to describe the overdensities. We present two examples of different intermittency parameters.

In our toy model, we use parameters that allow us to adjust the probability of finding these clumps as we transition from a completely smooth density distribution to an extremely clumped one. In the following subsections, we will first in Sec. 4.1.2 describe our model analytically, define the relevant variables, and characterize the spectra. Second, in Sec. 4.1.4, we will describe our numerical approach, and we will finally perform statistical tests in order to, in a simple way, get an idea of the conditions necessary to distinguish overdensities in case of detection.

4.1.2 Analytical estimate for the sensitivity

The Fourier power spectrum, $P(\mathrm{K})$, is a powerful tool to study density variations and, generally, analyze cosmic mass density fields. The power spectrum provides information about signal power distribution at different frequencies. In the context of studying overdensities, it helps to identify dominant frequencies where the signal exhibits significant variations or peaks, indicating possible overdensities. So, while it does not provide detailed positional analysis, it effectively reveals patterns and details at smaller scales that might otherwise be obscured by large density fluctuations. Therefore, we will employ power spectral analysis to study the density fluctuations in the signal we are modeling.

To determine the power spectral density (PSD) of the process described by Eq. (4.1), we analyze each contribution separately and sum them later [279,281,282]. For $\eta_{h,k}(t)$: we perform the Fourier transform

$$\mathcal{F}_T[\eta_{h,k}(t)](\omega) = \frac{1}{\sqrt{T}} \int_0^T dt \sum_{k=1}^{K} A_k e^{-i\omega t}, \tag{4.6}$$

when multiplying by the complex conjugate and taking an average overall random variables,

$$\langle |\mathcal{F}_T[\eta_{h,k}(t)](\omega)|^2 \rangle = \frac{2\langle A\rangle^2}{T\omega^2}(1-\cos(\omega T)), \tag{4.7}$$

the second term in the equation resembles a Delta function taking the limit:

$$\begin{aligned}\lim_{T\to\infty} \langle |\mathcal{F}_T[\eta_{h,k}(t)](\omega)|^2 \rangle &= 2\langle A\rangle^2 \lim_{T\to\infty} \frac{(1-\cos(\omega T))}{T\omega^2} \\ &= 2\langle A\rangle^2 \pi\delta(\omega). \end{aligned} \tag{4.8}$$

With normalization, $\int_{-\infty}^{\infty} d\omega\delta(\omega) = 1$.

For $\eta_{o,k'}(t)$: we rewrite the contribution as a stochastic differential equation,

$$\tau_d \frac{d}{dt}\eta_{o,k'}(t) = -\eta_{o,k'}(t) + \sum_{k=1}^{K} A_k \delta\left(\frac{t-t_k}{\tau_d}\right), \tag{4.9}$$

defining the linear operator $\mathcal{L}[u(t)] = f(t)$, then,

$$\mathcal{L}\eta_{o,k'}(t) = f_k(t),$$

with a Fourier transform for solution of Eq.(4.9):

$$\mathcal{F}_T[\eta_{o,k'}(t)](\omega) = \int_{-\infty}^{\infty} ds'\Theta(s')e^{-i\frac{2\pi}{T_o}s'+s'}e^{-i\omega s'}\frac{1}{\sqrt{T}}\int_0^T du' f_{k'}(u')e^{-i\omega u'},$$

such that the contribution to the PSD is,

$$\mathcal{S}_{\eta_o}(\omega) = 2\gamma^{'}\langle B\rangle^2 \frac{\tau_d}{1+\tau_d^2(\omega-\omega_0)^2}, \tag{4.10}$$

where the intermittency parameter can be then identified has the overall clump rate multiplied by the observation time $\gamma^{'} = \Gamma_c$T, so that $\gamma^{'}$ will account for the total number of clumps and $\langle B\rangle$ will account for the total number of events within a single clump. The detailed calculation of the power spectra is found in Appendix D.1. Then, the PSD of the process of the process described by Eq. (4.1) is,

$$\mathcal{S}_{\eta_{Tot}}(\omega) = 2\pi\langle A^{'}\rangle^2\delta(\omega) + 2(\Gamma_c T)\langle B\rangle^2 \frac{\tau_d}{1+\tau_d^2(\omega-\omega_0)^2}. \tag{4.11}$$

Eq. (4.11) breaks down the PSD into two main components. The first component is a Dirac delta function at $\omega = 0$, denoted by $\delta(\omega)$. This component is associated with the average squared amplitude A' of the process, accounting for the homogenous contributions to the power spectrum.

The second component is a Lorentzian function, which is characterized by a peak centered at $\omega = \omega_0$ and has a specific width determined by τ_d, a characteristic time constant that in our case represents the length of the overdensity in time,i.e., the size of the clump. This Lorentzian function is related to the squared amplitude B and the number of total clumps/overdensities, $\Gamma_c T$ and represents the contributions of the overdensities to the power spectrum. In practical experiments conducted over a finite time period, the homogeneous contribution, represented by the Dirac delta function in an ideal case, is not perfectly sharp. Instead, it is expected to exhibit a broader behavior resembling a Lorentzian function centered around $\omega_0 = 0$, similar to a Cauchy distribution. This adjustment accounts for the finite measurement time in realistic setups, leading to a smoothed-out behavior in the power spectrum.

At this point, let us clarify some general vital points concerning a Lorentzian function that models a power spectrum. Understanding such aspects will help us identify crucial parameters for signal analysis based on the number of events, enabling us to recognize various structural scenarios we need to consider when aiming to detect some structure.

In general, the size of the power spectrum scales with the number of events since the amplitude of the spectrum directly depends on the number of events (or some power of the number of events). If the number of events increases, the statistical fluctuations in the power spectrum may decrease. This is because, with more events, the statistical noise tends to average out, leading to smoother and more stable power spectrum estimates. The width (or Full Width at Half Maximum, FWHM) of the Lorentzian function, which characterizes the fluctuations in the spectrum, may remain constant with an increase in the number of events. We can easily see this by assuming that the power spectrum estimate is subject to additive white noise, such that,

$$\mathcal{S}(\omega) = \mathcal{S}_{\text{true}}(\omega) + \epsilon(\omega),$$

where $\mathcal{S}(\omega)$ is power spectrum estimate at frequency ω, $\mathcal{S}_{\text{true}}(\omega)$ the true underlying power spectrum and $\epsilon(\omega)$ is the noise, which, in our case, is attributed to shot noise arising from statistical fluctuations in the discrete detection of events. Note that here, we have not yet considered a specific normalization of the noise, and this might influence the estimation accuracy and how increasing the number of events can enhance the reliability and robustness of the estimated power spectrum; we will go into detail about this normalization in the next subsections, for now let us set the ground on a very general case.

The variance of the noise term can quantify the statistical fluctuations in the estimated power spectrum, $\text{Var}[\epsilon(\omega)]$. As the number of events N increases, we can model the noise term as a sum of independent noise contributions from each event, $\epsilon(\omega) = \sum_i^N \epsilon_i(\omega)$. By the properties of independent random variables, the variance of the sum of independent random variables is the sum of their variances. Therefore, the variance of the noise term in the power spectrum estimate scales with the number of events.

$$\text{Var}[\epsilon(\omega)] = N\text{Var}[\epsilon_i(\omega)].$$

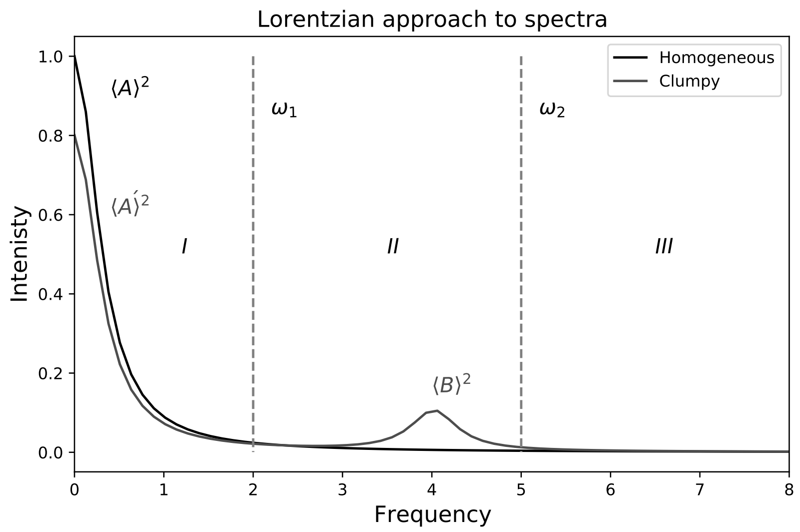

Figure 4.3. Analytical PSDs for a homogeneous signal (black solid line) and a signal containing clumps (grey solid lines). We have divided the space of frequencies into three regions, I,II, and III, which represent the regions where we can calculate the power to tell if one can distinguish between both signals. Region I was delimited at a frequency in which the homogeneous spectrum has decay at a 80% and the second cutting frequency was selected just ensuring the clump contribution was entirely contained within region II.

As N grows, the sum of these noise contributions tends to average out. Consequently, the variance of the noise in the power spectrum decreases with the number of events, leading to smoother and more stable power spectrum estimates. However, the principles discussed about how noise variance scales with the number of events and tends to average out with more events can also be relevant in understanding aspects of shot noise, especially in scenarios involving discrete event arrivals and fluctuations. This is because both share randomness, flat power spectra, no temporal correlation, and additive properties. The distinction is that shot noise is signal-dependent, while white noise is not. More precisely, shot noise arises from discrete random events (such as the arrival) and its magnitude scales with the signal strength. In contrast, white noise refers to any random signal with a flat spectral density, typically used as a theoretical model in signal processing. Thus, taking into account the caveat about its origin, shot noise that can be classified for our purposes as a type of white noise. We refer to this noise as *observational noise*, later on.

4.1.3 Analytical signal analysis

To analyze signals effectively, particularly when identifying clusters or clumps within them, it is important to define the minimum conditions required for this differentiation using analytical methods. We assume the existence of a small overdensity in the signal and we look for the conditions to distinguish them from a signal that does not contain overdensities.

One simple way is to obtain the power of the signal containing clumps by integrating Eq. (4.11) and comparing it to the power of a signal without clump contributions, integrating Eq. (4.8), across diverse frequency ranges. In Fig. 4.3, we present the Lorentzian PSDs for a homogeneous signal (black solid line) and a signal containing clumps (gray solid line). In the figure, we have divided the space of frequencies into three regions, I, II, and III, which represent the three integration limits that we will take to calculate the power of each contribution and to make a comparison of the rate between the power of each one in the intervals indicated by each region. It should be acknowledged that the parameter selection for generating the clump-inclusive signal, so far, is arbitrary and up until this point is used for illustration purposes, later however is not arbitrary and quite relevant. The characteristic frequency of the clump could, depending on the observation time, fall into a different region than the one indicated in Fig. 4.3, depending on the case.

In general, the power of the homogeneous contribution, P_h is,

$$P_h = \int_{\Delta\omega_R} \frac{1}{\pi}\langle A\rangle^2 \frac{T}{1+T^2\omega^2} d\omega, \tag{4.12}$$

where we have approximated the delta function to a Lorentzian function and $\Delta\omega_R$ represents the range of frequencies depending on the region R, we are in, and T is the duration of the process, i.e., observation time. For the homogeneous Poisson process the average amplitude is proportional to the total number of events, so that $\langle A\rangle = N$, therefore,

$$P_h = \frac{N_t^2}{\pi}\tan^{-1}(T\omega)|_R. \tag{4.13}$$

On the other hand, following the same reasoning, the power of the signal containing clumps, P_c can be written as,

$$\begin{aligned} P_c &= \int_{\Delta\omega_R} \frac{1}{\pi}\langle A^{'}\rangle^2 \frac{T}{1+T^2\omega^2} d\omega + \int_{\Delta\omega_R} 2\gamma^{'}\langle B\rangle^2 \frac{\tau_d}{1+\tau_d^2(\omega-\omega_0)^2} d\omega, && (4.14)\\ &= \frac{N_h^2}{\pi}\tan^{-1}(T\omega) + N_c n_o^2 \tan^{-1}(\tau_d(\omega-\omega_0))|_R, && (4.15)\end{aligned}$$

where N_h represents the number of events classified as homogeneous contributions withing the signal, N_c is the number of clumps and n_o is the number of events within a single clump.

For a Poisson process, the number of events is given by the product of the rate parameter (which represents the average number of events per unit time, typically in years) and the total observation time. This relation is expressed as $N = \Gamma T$, where:

- Γ: Rate of events
- T: Total observation time

In our case, we define each variable as follows:

- $N_h = \Gamma_h T$: Number of homogeneous events, where Γ_h is the rate of homogeneous events.
- $N_c = \Gamma_c T$: Number of clumps, where Γ_c is the rate of clump events.

- $n_o = \lambda_c T_c$: Number of events in a single clump, where T_c is the fixed time duration of the clumps, and λ_c represents the event rate inside clumps.

Additionally, we define an overdensity parameter, λ, as a dimensionless quantity representing the true overdensity (excluding background contributions). It is given by,

$$\lambda = \frac{\lambda_c}{\Gamma_h}.$$

Therefore, we can express λ_c as:

$$\lambda_c = \lambda\, \gamma_c\, T_c,$$

where γ_c represents a specific rate associated with clump events[5] In table 4.1 there is a summary of the variables we used in this analysis.

Symbol	**Description**
N_h	Number of homogeneous events in the signal
N_c	Number of clumps
n_o	Number of events within a single clump
Γ	Rate of events
T	Total observation time
Γ_h	Rate of homogeneous events
Γ_c	Rate of clump events
T_c	Fixed time duration of each clump
λ_c	Event rate within clumps
λ	Dimensionless overdensity parameter
γ_c	Specific rate associated with clump events

Table 4.1. Summary of variables used in the analysis.

Now, over specific frequency ranges as shown in Fig. 4.3 we can compare the total power in each signal, that is to calculate a ratio, R_P, between the powers. This can provide a quantitative measure of the differences between the two PSDs such that,

$$\begin{aligned} R_P = \frac{P_c}{P_h} &= \frac{N_h^2(\tan^{-1}(T\omega_f) - \tan^{-1}(T\omega_i))}{N_t^2(\tan^{-1}(T\omega_f) - \tan^{-1}(T\omega_i))} \\ &\quad + \frac{\pi N_c n_o^2(\tan^{-1}(\tau_d(\omega_f - \omega_0)) - \tan^{-1}(\tau_d(\omega_i - \omega_0))}{N_t^2(\tan^{-1}(T\omega_f) - \tan^{-1}(T\omega_i))}\Bigg|_R . \end{aligned} \tag{4.16}$$

Before interpreting the power ratios, we note that this PSD treatment assumes a consistent detection time and similar observational conditions for both signals. While the exact event counts may vary, the total detection time and sensitivity are fixed and equal, providing a basis for meaningful PSD comparison.

[5] In more complex models, the expression for λ_c may involve additional factors, such as the impact parameter or other characteristics of the clump traversal.

For the analysis, we will consider, in principle, that the noise can be neglected due to a large number of detections. When the number of events is small, the noise within the signal becomes significant, especially in the spectral region where the signal is present; we will consider this case later in the analysis. Therefore, unless explicitly stated, we generally assume a large number of events for our analysis.

Region I :$\omega_i = 0$ $\omega_f = \omega_1$

Let us look at what is happening in this region regarding the extent of a purely homogeneous process. Within this region, we must select our cutoff frequency based on the idea that the contribution of the process should be almost entirely contained there. The peak generated by a purely homogeneous process after a some detection time should be entirely contained in this region. The spectrum, as we already shown in Eq. (4.12), is a Lorentzian function, which is characterized by a peak at zero frequency and a gradual decrease in amplitude as frequency increases. The cutoff frequency can be determined by finding the frequency at which the spectrum drops to a certain percentage P_{cutoff} (e.g., half) of its peak value. For a Lorentzian function, the cutoff frequency can be found by setting the denominator equal to the desire percentage of its peak value,

$$\begin{aligned} \frac{T}{1 + T^2\omega_{\text{cutoff}}^2} &= P_{\text{cutoff}}, \\ \omega_{\text{cutoff}} &= \sqrt{\frac{\frac{T}{P_{\text{cutoff}}} - 1}{T^2}}. \end{aligned} \tag{4.17}$$

The relevant contribution in this region comes from the first term in Eq. (4.16), where the homogeneous contribution is. In the hypothetical case in which no clumps were present, $Nh = N_t$ and $Nh = N_t$, the ratio would be equal to unity. In the presence of clumps, the number of detections $Nh < N_t$ would automatically leave the ratio between the powers below unity.

In a broader view, we can also examine the second term of Eq. (4.16). Here, the inverse tangents are affected by how close the integration frequencies are to the clump's frequency. In our case, both ω_i and ω_f are below the clump's characteristic frequency, which negatively impacts the ratio. This means the ratio in this range is typically around unity or less, as the first term of the equation contributes more strongly. Analyzing this part of the spectrum alone is useful but not sufficient to determine if the clump is distinguishable. Only in rare cases, such as a very dense clump with a duration smaller than the observation window, might there be a noticeable feature in this region (or if the clump's frequency lies in this part of the spectrum, which is not the case here).

Region II: $\omega_i = \omega_1$ $\omega_f = \omega_2$

In this region, we focus on the behavior of the frequency range between ω_i and ω_f, which must be close to the characteristic frequency ω_0 of the cluster. Specifically, ω_i is the lower cutoff frequency, and ω_f must contain the cluster almost entirely. To calculate the value for ω_f, we can follow a procedure similar to that in Eq. (4.17).

The goal here is to analyze the ratio between the contribution from the clumps and the total power in the spectrum. The second term of Eq. (4.16) is central to this. When the frequency differences

$(\omega_f - \omega_0)$ and $(\omega_i - \omega_0)$ are small, we can approximate the inverse tangents as $\tan^{-1}(\Delta\omega) \approx \Delta\omega$, where $\Delta\omega$ is the frequency difference.

This simplification leads us to the following expression for the ratio, R_P:

$$R_P \approx \frac{N_c n_o^2 \tau_d(\omega_f - \omega_i)}{N_t^2(\tan^{-1}(T\omega_f) - \tan^{-1}(T\omega_i))}. \tag{4.18}$$

Here, R_P depends on several factors, including N_c, the number of clumps. In the next section, we will discuss how N_c is influenced by the probability of encountering a clump, the observation time, and the size of the clumps in the time domain. These factors allow us to derive a condition for a significant contribution from the clumps.

We can rearrange the expression to obtain an inequality that ensures the clump contribution is substantial, i.e., $R_P \geq 1$:

$$\begin{aligned}
&\frac{\pi N_c n_o^2 \tau_d(\omega_f - \omega_i)}{N_t^2(\tan^{-1}(T\omega_f) - \tan^{-1}(T\omega_i))} \geq 1, \\
&N_c n_o^2 \pi \tau_d(\omega_f - \omega_i) \geq N_t^2(\tan^{-1}(T\omega_f) - \tan^{-1}(T\omega_i)), \\
&N_c n_o^2 \pi \geq \frac{(\tan^{-1}(T\omega_f) - \tan^{-1}(T\omega_i))}{(\omega_f - \omega_i)} \frac{N_t^2 \omega_0}{2\pi}.
\end{aligned} \tag{4.19}$$

We define $\tau_d = 2\pi/\omega_0$, and note that since the difference between ω_f and ω_i is large compared to the inverse tangents, the fraction is less than 1. Thus, we arrive at the final form,

$$N_c \geq \tan^{-1}\left(\frac{T(\omega_f - \omega_i)}{1 + T^2\omega_f\omega_i}\right) \frac{\omega_0}{(\omega_f - \omega_i)\pi} \frac{N_t}{n_a^2}. \tag{4.20}$$

This inequality indicates that a ratio greater than or equal to one, $R_P \sim 1$, is more likely to occur with fewer, larger clumps. Larger clumps require fewer events to distinguish them, resulting in a more pronounced ratio. On the other hand, smaller clumps require a significant increase in the number of clumps to achieve the same ratio. The dependence of N_c on the eigenfrequency ω_0 is important. Specifically, Eq. (4.20), shows that a lower eigenfrequency requires fewer events for a significant contribution due to higher intensity. This relationship aligns with the behavior described by the Poisson distribution: when the probability is fixed, the intensity of the events can be adjusted inversely with the number of events to maintain the same probability.

Distinguishing a clump in noisy environments

Moving forward, discussing the analysis in scenarios with limited events is essential, as it aligns more closely with realistic situations. Until now, our focus has been on scenarios with many events where the intrinsic noise of the processes was disregarded, as previously discussed. However, this noise factor becomes significant in realistic scenarios with fewer events.

In this scenario, we can deal with two types of additional noise terms: observational (Ω_n) or dynamical (Δ_n) noise. Observational noise or shot noise, as we defined in more detail in Sec. 4.1.2, refers to noise disconnected from the overdensity contribution; that is , the number of clumps and the amplitude of the process play no role, while the dynamical noise is added as random forcing in the stochastic process that accounts for the clumps. For our purposes, we will deal with observational noise only. This noise is, therefore, simply added to the process described in Eq. (4.1),

$$\Omega_n(t) = \eta(t) + \sigma\mathcal{N}(t),$$

where $\mathcal{N}(t)$ represents a normally distributed process with a mean that vanishes to zero and a standard deviation of one unit, and σ is essentially the standard deviation of the noise process. Here, for simplicity of notation, the subscript K was eliminated.

To ensure that $N(t)$ represents a dimensionless variable we can construct it using integrated increments of the Wiener process [279],

$$\mathcal{N}(t) = \frac{1}{\Delta_t^{1/2}} \int_t^{t+\Delta_t} dW(s). \tag{4.21}$$

Here, Δ_t denotes the sampling time, where each sample $N[n] = N(n\Delta_t)$, where $n = 0, 1, 2, \dots$ is normally and independently distributed with zero mean and standard deviation equal to the unity. The power spectral density can be directly obtained through the auto-correlation function (see App. D.2)),

$$R_{\mathcal{N}}(t) = \left(1 - \frac{|t|}{\Delta_t}\right)\Theta(\Delta_t - |t|), \tag{4.22}$$

so that,

$$\mathcal{S}_{\mathcal{N}}(\omega) = \int_{-\infty}^{\infty} dte^{-i\omega t} R_{\mathcal{N}}(t) = 2\frac{1 - \cos{(\Delta_t\omega)}}{\Delta_t\omega^2}. \tag{4.23}$$

As the time resolution is important for the noise processes, we also introduce the normalized time step $\tilde{t} = \delta_t/T$, so that

$$\mathcal{S}_{\mathcal{N}}(\omega) = 2\frac{T}{\tilde{t}}\frac{1 - \cos{(\tilde{t}T\omega)}}{T^2\omega^2}. \tag{4.24}$$

For small values of $\tilde{t}$, we can make an expansion of the cosine around zero, and we have,

$$\lim_{\tilde{t}\to 0} \frac{\mathcal{S}_{\mathcal{N}}(\omega)}{T\tilde{t}} = 1. \tag{4.25}$$

In the limit where $\tilde{t} \to 0$, $\mathcal{N}(t)$ approaches white noise, that is, a flat power spectrum. This means that the total power of $\mathcal{N}$ is divided among a more significant number of frequencies, reducing the power per frequency, as we already stated in a more general framework in Sec. 4.1.2.

With this clarified, let us take a look to the signal to noise ratio (SNR) between the power of the clump only and the noise,

$$\text{SNR} = \frac{N_c n_a^2 \pi(\tan^{-1}(\tau_d(\omega_f - \omega_0)) - \tan^{-1}(\tau_d(\omega_i - \omega_0))}{\text{Var}[\epsilon(\omega_i)]}, \tag{4.26}$$

where we assumed that here we are assuming that the homogeneous process is negligible. The variance of the white noise, we can treat as $\text{Var}[\epsilon(\omega)] = \sigma^2 = N_t$, where σ is the standard deviation of the process generating the noise; therefore,

$$\begin{aligned} \text{SNR} &\approx \frac{N_c n_a^2 \pi(\tan^{-1}(\tau_d(\omega_f - \omega_0)) - \tan^{-1}(\tau_d(\omega_i - \omega_0))}{N_t}, \\ &\approx \text{C}(\lambda_c T_c)^2 \frac{N_c}{N_t}, \end{aligned} \tag{4.27}$$

we have included all frequency-dependent values in C. When considering the whole process, i.e., with the homogeneous detections, the signal-to-noise ratio will behave exactly as in Eq. (4.27), but the parameter will be adjusted to,

$$C' = \frac{\pi(\tan^{-1}(\tau_d(\omega_f - \omega_0)) - \tan^{-1}(\tau_d(\omega_i - \omega_0))}{(\tan^{-1}(T\omega_f) - \tan^{-1}(T\omega_i)) + 1}. \tag{4.28}$$

We have shown in Eq. (4.27) that the SNR depends directly on the clump parameters, implying that the SNR value will not increase over time. It is important to note that while extending the detection time may increase the number of detections, the scaling of the number of events within the clump (where λ_c represents the number of events inside the clump per unit time) also occurs. This scaling factor impacts the signal-to-noise ratio, potentially leading to limited improvement despite the increase in the number of detections. This suggests that we must find another way to optimize the information contained in the signal to maximize the signal-to-noise ratio with few events.

One strategy we propose is to focus on the cluster region and make cuts, i.e., analyze the spectrum in small sections in time where the noise content can be averaged and thus reduce fluctuations; then, we average the power spectrum and perform the power ratio/ SNR. In this way, we would have a better chance of distinguishing a clump, even if we have multiple clumps that are not very dense. In the range of interest, we make M cuts and analyze them in portions. In the case of white noise, the fluctuations are similar across different cuts, and the SNR calculation considers the average power of the signal relative to the fluctuations in the noise power across the cuts. Accounting for fluctuations enhances signal detection and extraction, especially when the signal may be weak. When we divide a noise signal into segments of equal length and then average these segments, the resulting power spectrum of the noise signal will likely have reduced variance compared to the original power spectrum of the noise signal.

To calculate the SNR using the fluctuations of the white noise signal, we can define it as the ratio of the average power of the signal to the fluctuations of the noise,

$$\text{SNR} = \frac{\frac{1}{M}\sum_1^M P_{avg,sig}}{\sqrt{\frac{1}{M}\sum_i^M P_{avg,noise}}} = \frac{\sum_1^M P_{avg,sig}}{N_t}\sqrt{M}. \tag{4.29}$$

As seen from Eq. (4.29), the signal-to-noise ratio can grow proportionally to the square root of the number of cuts in the region where the clumps are located. Thus giving us more chance of detection even when the signal is weak.

Now, let us explore the parameter space determined by the fraction of dark matter contained in clumps, Ω, and the clump radius, R_c. The fraction of dark matter is defined as, $\Omega = N_c M_c/M_t$, where N_c is the number of clumps, M_c is the mass of a single clump, and M_t is the total mass of dark matter. This analysis aims to determine the region of the parameter space (Ω, R_c) in which it would be possible to detect a clump after a certain observation time. Specifically, we aim to identify the conditions under which a clump can be detected with 2000 events and a SNR of ≥ 3, based on our simplified model.

In Sec.4.2, we will elaborate on how this parameter space is explored in more detail. The relevant region of the parameter space (Ω, R_c) for clump detection is illustrated in Fig. 4.4, which shows the conditions for detecting a clump under these observational constraints.

In this example, we illustrate the case of an overdensity of $\lambda_c = 50$ and an observation time, $T_{0b} =$ 2yrs. In Fig. 4.4 , we show a blue region for clump detection with the reliability of $SNR \geq 3$, delimitated by a blue line that represents SNR in the absence of homogeneous contributions, that is, the SNR presented in Eq. (4.27). Moreover, we compute the SNR by adding the homogeneous contribution, as in Eq. (4.28), represented by the dashed blue line. Here, the contribution of the homogeneous distribution significantly reduces the detectable region, which is expected since the power spectrum of such contribution is a flat, Eq. (4.11), just white noise, Eq. (4.24). The gray shaded region represents the part of the analysis that corresponds to environments with noise or few events. Here, we have established, in theory, how our simplified model gains significance only by making signal cuts and averaging, as shown in Eq. (4.29). We have taken M=10, and as shown in Fig. 4.4, the analysis, indeed, expands the parameter space for detection.

It is important to clarify that to ensure that the analysis of the slices really gives more information about the signal, it is necessary to impose that at least in each of the slices, a clump is totally or partially contained. We will get back to this result (Fig. 4.4) in Sec. 4.2. Finally, Fig. 4.4 shows three limits; the first one is the limit imposed by the observation time, presented as a gray vertical shaded region. This limit indicates that for a given observation time (which translates into a certain distance traveled by the detector), a maximum clump size can be detected and can not exceed the distance traveled by the detector. This means that if the clump is larger than the distance traveled by the detector, we will always be inside the clump and unable to discern if we are inside it. The second limit we impose regards the minimum number of events inside a clump that must be detected. We have set such a limit as two events and represented it as a vertical black dashed line. Finally, an additional limit is represented by a tilted black dashed line. This limit represents a minimum of one clump detection as we can see, in this particular case, such line lays outside the confidence region, meaning that we have more than one clump detection over the $SNR \sim 3$. This may not be true for all the cases, so it is important to check in every case just as a consistency check.

Region III : $\omega_i = \omega_2 \; \omega_f = \omega_{lim}$

Defining the value of our limiting frequency in this region is important. This frequency limit should not be excessively high, as discriminating a cluster at higher frequencies demands an excellent resolution. To determine the highest frequency that can be resolved based on the measurement time (represented by τ), one can use the FWHM as the measure of resolution. A Lorentzian function's Full Width at Half Maximum (FWHM) is 2τ, which indicates the range of frequencies where the peak's contribution reduces to half of its maximum value. Thus, the highest frequency that can be

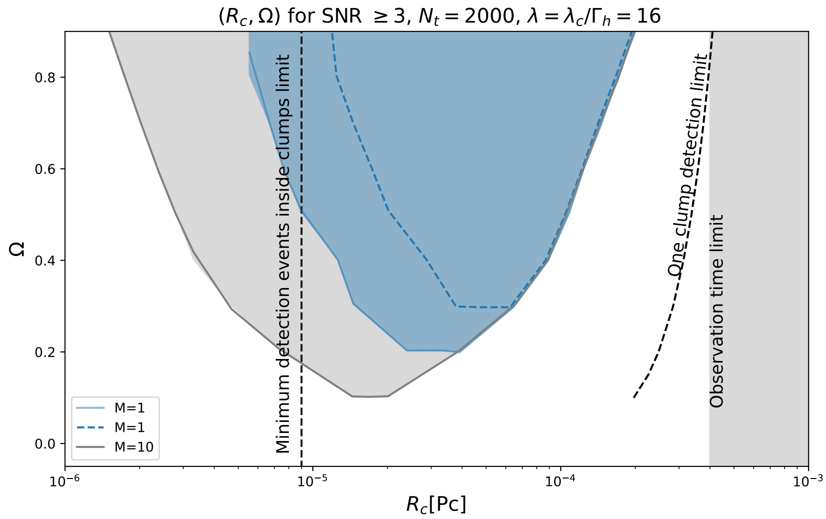

Figure 4.4. Region of the parameter space (Ω, R_c) in which with 2000 total events it would be possible to detect a clump with a reliability of $SNR \geq 3$. In this example we illustrate the case of an overdensity of $\lambda = 16$ on average. The gray shaded region represents the SNR analysis by making cuts in the signal, in this case $M = 10$.

resolved based on the measurement time in the spectrum is determined by it. Both parts of Eq. (4.16) hold significance in this frequency spectrum segment. The first term, representing the homogeneous contributions, will stay consistent. Meanwhile, the frequency ω_f will be significantly higher than the characteristic frequency of the clumps so that,

$$R_P \approx \frac{N_h^2}{N_t^2} + \frac{N_c^2(\tan^{-1}(\tau_d\omega_f) - \tan^{-1}(\tau_d(\omega_i - \omega_0)))}{N_t^2(\tan^{-1}(\omega_f) - \tan^{-1}(\omega_i))}\Bigg|_{III}. \tag{4.30}$$

For sufficiently large frequencies, the inverse tangent function approaches a constant value $\pi/2$, so that,

$$R_P \approx \frac{N_h^2}{N_t^2} + \frac{N_c^2\tan^{-1}(\tau_d(\omega_i - \omega_0))}{N_t^2\tan^{-1}(\omega_i)}\Bigg|_{III}, \tag{4.31}$$

unless τ_d is significant, Eq. (4.31) will stabilize closely to unity in the large frequency range limit. It is important to note that analyzing just this frequency region does not provide definitive confirmation of a clump's presence. The behavior of the power ratio in this range helps us understand how the clump might manifest in the spectrum, but a comprehensive analysis of the entire spectrum is needed to conclusively detect the clump.

In conclusion, this analytical approach simplifies the problem, offering a useful framework for a first approach to the study. However, it only partially accounts for the effects of fluctuations arising from a finite number of events, leaving some complexities unresolved. These aspects would require further exploration in a more realistic and comprehensive scenario. From our analysis of the different regions, we can draw several conclusions. First, the contribution from the homogeneous process will be significant unless it is well-understood and can be effectively removed from the spectrum. In most cases, the signal is dominated by homogeneous events, where the power ratio stays close to unity. While high fluxes of weak clumps could contribute to the signal, we emphasize that this is an unlikely scenario and not the focus of this analysis. Second, assuming the power ratio exceeds a value of 2, we can predict a minimum probability, based on the total number of detections, that a clump may be present in the signal. Finally, this analysis can also be applied in reverse, to assess the likelihood of detecting a clump under specific conditions.

Finally, all these analyses were done under the condition that clump detections were available. It is important to have a clearer idea of the possible encounter rate in order to make the whole analysis possible. Since the particle representation studied in this chapter is compatible with direct detection experiments, let us stop for a moment to get insights into the encounter rates. Here, we will consider the fraction of dark matter Ω that we will explore in more detail in Sec. 4.2, for different clump radii and masses to check, as a first attempt, the parameters that make it possible to have at least one encounter per year. To do so, we have used same assumptions about the velocity distribution stated in Chap 3.3.3, eqs. (3.71), (3.72). Therefore

$$\begin{aligned} \frac{d\Gamma_e}{dR} &= n_{\text{clump}} \left\langle v \frac{d\sigma}{dR} \right\rangle, \\ &= n_{\text{clump}} \int_{v_i}^{v_f} v f(v) \frac{d\sigma}{dR} dv, \end{aligned} \tag{4.32}$$

where we have assumed hard sphere approximation for the cross section.

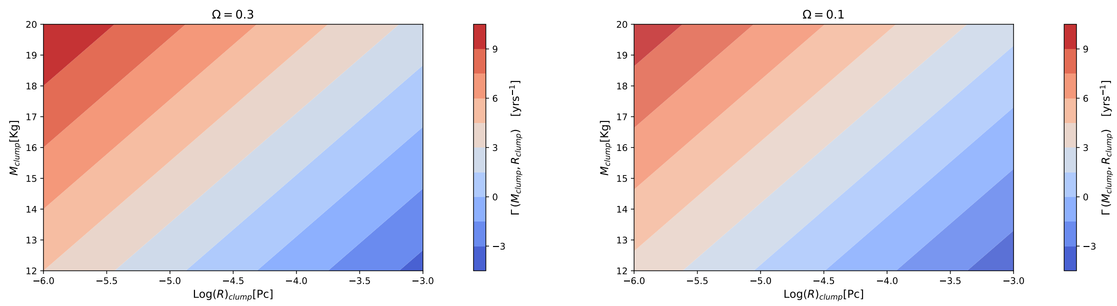

(a) Encounter rate for fixed density ratio $\Omega = 0.3$.

(b) Encounter rate for fixed density ratio $\Omega = 0.1$.

Figure 4.5. Encounter rates for fixed density ratio. Here, we have considered a range of input masses based on the results of Sec 4.1.4. We have considered a velocity distribution in the detector frame of reference.

In Figure 4.5b, we have estimated the encountering rate for $\Omega = (0.3, 0.1)$. Very naively one possible clump characteristic that is potentially detectable are $M \sim 10^{15}$kg and $R = 10^{-4.5}$pc for an overdensity of $\lambda = 16$. For such values, $\Gamma_e \sim 1\text{yr}^{-1}$ which represents a very optimistic possibility of encountering in relatively short time scales. The plot shows that, in principle, less massive clumps result in higher detection rates. This is because smaller clumps, while less dense individually, tend to appear more frequently due to their abundance in the dark matter distribution. As clump mass decreases, the frequency of potential encounters or interactions with the detector increases, leading to an elevated event rate. Consequently, more massive clumps are less likely and contribute fewer events despite their higher individual density.

4.1.4 Numerical approach

This section details how we simulate the signal and obtain the power spectrum of the random process discussed in 4.1.2. Implementing a numerical approach, we gain several advantages. For instance, the simulation allows us to model clumps flexibly, adjusting parameters like clump size, density, and frequency to test different scenarios. Additionally, the simulation provides a more comprehensive treatment of finite event number fluctuations, which is one of the key aspects of this study. It can also account for complex features in the signal, such as overlapping clumps, that are challenging to address analytically. Finally, the numerical power spectrum analysis offers a practical means to test and validate analytical approximations.

We begin by looking into the representation of the baseline or smooth background through a Poisson process. A Poisson Process (PP) is a sequence of events where the number of arrivals N in a time interval (a, b) follows a Poisson distribution with shape parameter Λ,

$$\Pr(N = k) = \frac{(\Lambda)^k}{k!} e^{-\Lambda}, \tag{4.33}$$

where $T = b - a$ and $\Lambda = \lambda T$ [283,284]. Here, λ represents the arrival rate, assumed constant for our purposes. In our approach, we model the signal arrivals as a Poisson process, where the frequency of arrivals within any given time frame follows a Poisson distribution. To simulate overdensities, we extend this to a non-homogeneous Poisson process where the arrival rate/intensity varies over time to represent clumps. This variation is achieved by introducing stochastic fluctuations in the arrival rate, creating intervals with higher event densities to simulate these over-dense regions.

We generate these density fluctuations by defining a probability P of observing a clump within each interval of time T. For a total signal duration T_o, we define a certain number of attempts as $n = \text{int}(T_o/T_c)$, where T_c is the size of the clump in time. Now, within each interval T, we simulate a "dice roll" (a draw from a binomial distribution) to determine whether a clump occurs. When a clump is chosen in an interval (illustrated as green dots in Fig. 4.6), a random density spike is generated with a rate that exceeds the average rate of the background distribution. This setup ensures that clumps are stochastically generated with counts higher than the expected background level, simulating regions of overdensity contrasting with the low-event background.

We defined our parameter space as the probability of encountering a clump P (to randomize the rate), the frequency of the overdensity/clump $\nu_{\text{od}} \propto 1/T$, the number of total events N and the arrival average rate of the overdensity λ_{od}.

We focus on generating overdensities and studying their statistical likelihood in the following. All the details on how we generate the baseline can be found in Appendix D.3. We use a uniformly spaced time grid to introduce additional event counts in the signal. Within each time bin, we drew a sample from a binomial distribution. Based on whether the obtained value is above or below a predefined probability (P), we then drew a sample from either a low fixed intensity λ (representing the smooth background) or a high-intensity λ_{od} (representing the clump). This approach ensures

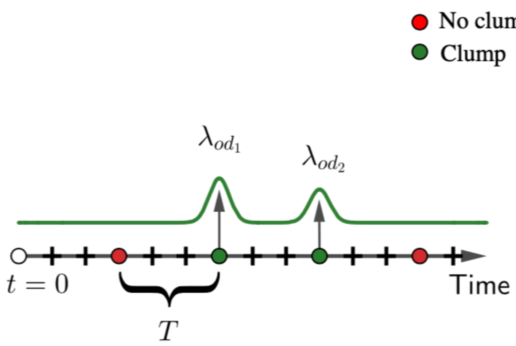

Figure 4.6. Illustration of how the over densities are introduced. T represents the period of the clumps, and red and green indicators are determined randomly by a binomial distribution. The rate detection of the over-density is also randomized.

that the overall process exhibits a random arrival rate/intensity, with background and clump events contributing to the signal.

Fixed Parameters non-homogeneous case	
Parameter	Value
λ_{od}	20
T	3
P	10%

Table 4.2. Parameters for over densities. T represents the period on average for which the binomial distribution can randomly create higher counts, see Fig 4.6, P represents the probability of the over density to occur/success.

We generate around ~ 1000, number of events to see if the signal was distinguishable visually in the power spectrum following the parameters in Table 4.2. Until this point, we do not allow the clumps to overlap, and they all have, on average, the same size.

Just to clearly differentiate in this case the signal, we averaged segments of the simulated signals to assign more accurate power to the correct frequencies and reduce noise-induced fluctuations in power. As expected, the power shows an additional peak at $\omega_o = 2.1$ corresponding to the power associated with the overdensities in this example case. We calculate the peak-to-noise ratio (signal excess) on the region of interest as [285–287],

$$\text{SE} = \frac{\text{Power of the peak - mean power}}{\text{std}}. \tag{4.34}$$

In addition, as the homogeneous contribution of the random Poisson process and the noise factor appear at every frequency, we calculate the probability associated with the chance of one of those random contributions to actually reach the same power of the peak of interest [288]:

$$P(\text{false alarm}) = 1 - (1 - e^{-S_p})^{N_\nu}, \tag{4.35}$$

here S_p is the power of signal peak and N_ν represents the number of independent frequencies of the band of interest, for our case $N_\nu = 2$. We also established a relation between the fit parameters and the simulation parameters for localized cases, see Appendix D.4. In Fig 4.7, two individual runs for the same parameters were performed for one case where the localized overdensity can be fully distinguished and another where it is more challenging to distinguish. The total number of events in both cases was set to 1000. For each case, it can be seen in the figure that there are two realizations marked as red and black lines; this gives an intuition of how the individual runs fluctuate. In addition, we have a dashed gray line representing the average value of a run without clumps, i.e., of the background. For each case we have also included an estimate of the false alarm probability.

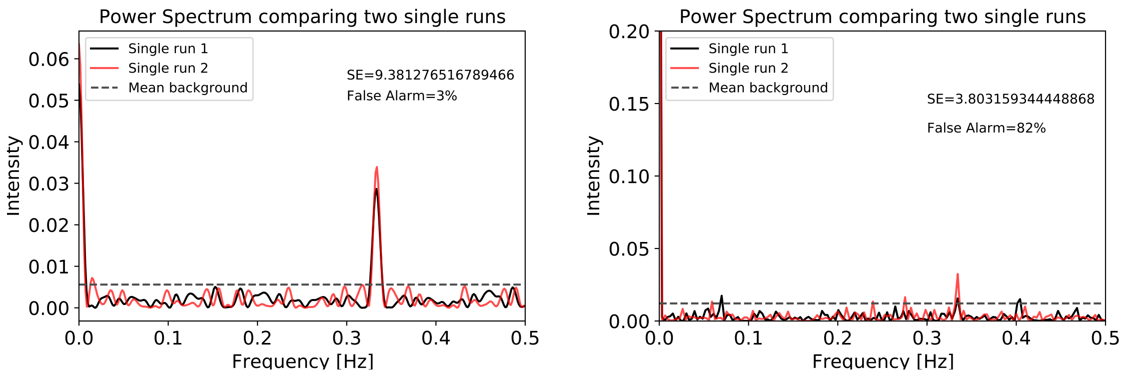

Figure 4.7. Power spectrum for two different cases and two different realizations. Here we illustrate two extreme cases where the localized overdensity can be either fully distinguished or fully mixed with the background.

In a realistic scenario, clumps may overlap and vary in size or frequency. To incorporate this into our simulation, we define a set of possible clump sizes. When a clump appears in an interval, its intensity is randomly selected from this predefined list of sizes. We also impose a restriction to ensure that no clump exceeds the overall measurement duration. In this case, we performed a Lorentz fit to a signal containing nonlocalized clumps, i.e., combinations of different characteristic clump sizes/frequencies, to test both numerical and analytical setups. In Fig. 4.8, we show the numerical averaged spectrum (gray dotted line) including superposition of overdensities with $\nu_{\text{od}} = [1.88, 2.01]$, $P = 0.3$, $N = 150$, and $\lambda_{\text{od}} = 40$. For such spectrum, we make the fit this the analytical result obtained in Eq. (4.11) (red solid line) for fitting parameters $\langle A \rangle^2 = 0.04$, $\tau = 34$ and $\gamma' = 0.08$, $\langle B \rangle^2 = 0.02$, $\tau_d = 37$, $\omega_0 = 2.1$. We show the overall noise by a black dashed line that compared differs from the analytical stimation of the noise by ~ 0.0025 . It is important to mention that for this illustrative plot we have only shown the contribution of the white noise for frequencies higher than zero, but in general terms white noise also contributes to the peak centered ar zero frequency. In the subplot of Fig. 4.8 we make a cut on the frequency range to concerning only the clump contribution of the spectrum for both, numerical and analytical parts.

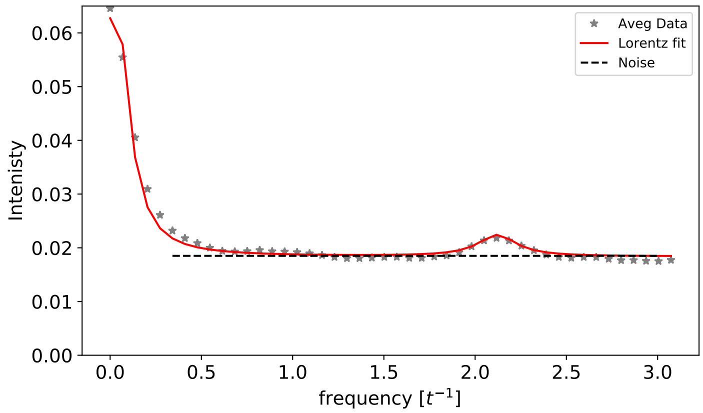

Figure 4.8. Eq. (4.11) fit for the numerical power spectrum including superposition of overdensities with $\nu_{\rm od} = [1.88, 2.01]$, $P = 0.3$, $N = 150$, and $\lambda_{\rm od} = 40$. For the complete spectrum the fit results were $\langle A\rangle^2 = 0.06$, $\tau = 34$ and for the clump fitting parameters $\gamma' = 0.08$, $\langle B\rangle^2 = 0.026$, $\tau_d = 37$, $\omega_0 = 2.1$, plus an overall noise factor represented by the dashed black line.

Distinguishable Over-densities numerical analysis

To distinguish structure in the detection, we perform a statistical test to estimate the significance of the numerical signal containing some clumps; we later in Sec. 4.2 apply this test to signals where the clumps are identified as dark matter small structures under appropriate and realistic conditions. To do so, we define the null and alternative hypotheses as,

$\mathcal{H}_0$: *the power spectrum of the signal corresponds to white noise, i.s flat spectrum for* $f \neq 0$.
$\mathcal{H}_1$: *the power spectrum is not flat.*

We tested the hypothesis under the standard *t-test* [289, 290] and the nonparametric Mann-Whitney U test [291, 292], see Appendix D.5. Additionally, in Appendix D.6, we have expanded about the testing of the numerical parameters under the null hypothesis using the Mann-Whitney U test.

It is essential to establish a clear connection between the simulated parameters and the physical phenomena they represent. This connection forms the basis for the applicability of simulation results to practical scenarios. In the following section we bridge the gap between the simulated parameters and their physical analogs, the simulation becomes relevant and provides knowledge that can be extrapolated to real-world situations.

4.2 Exploring Dark Matter Clumps: Physical Characteristics and Signal Analysis

In an approximation to a realistic measure of dark matter clumps, we assume the detector is moving as the Earth goes through a cubic volume of 1 ly^3, see Fig. 4.9, with a constant velocity of $v = 220\,\mathrm{km/s}$.

Let us consider an example to clarify the concept. Suppose we detect signals over one year. In this scenario, we have traveled through a cube with a size of $x(t_o) = vt_o$, where t_o is the detection time. Within the trajectory of at least 2×10^{-4} pc that we can cover in a year, we can traverse the clump partially or completely. In this case, we can detect a clump even with a non-central crossing, meaning we do not need to pass through its full radius to identify it.

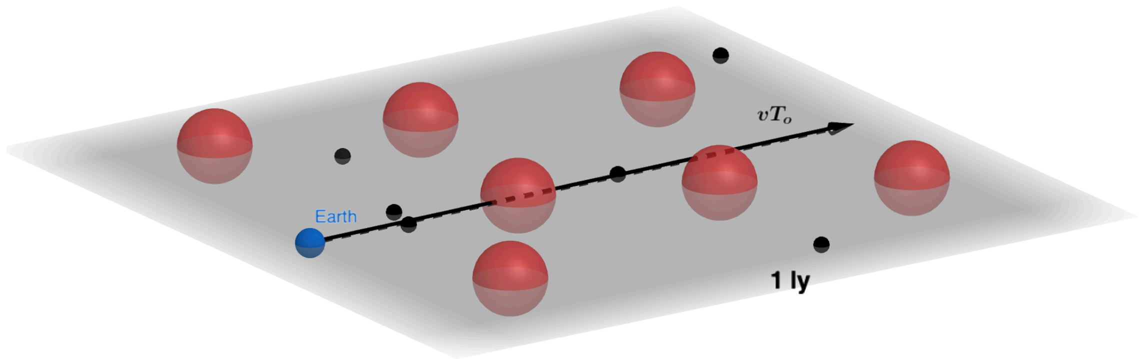

Figure 4.9. Scenario for dark matter detection. The Earth acts as a detector in a cubic volume of 1 ly^3. The black dots represent dark matter particles and the red spheres represent DM clumps. We illustrate the possibilities of traversing the clumps partially or completely.

Let us simplify our picture considering that all clumps are same size and have the same mass,

$$m_c = \frac{4}{3}\pi R_c^3 \rho_c, \tag{4.36}$$

where ρ_c and R_c are the density and the radius of the clump, respectively. The density of the clump ρ_c can be linked to the average DM density at our current location ρ_{DM}, along with the overdensity λ and fraction contained in clumps f, as follows,

$$\rho_{\rm DM} = \rho_h + f\rho_c. \tag{4.37}$$

Here, the average density will consist of the density from our uniform detection process plus a specific portion attributed to the clump structure. The overdensity is then $\lambda_c = \rho_c/\rho_h$, so that,

$$m_c = \frac{4}{3}\pi R_c^3 \rho_{\rm DM} \left(\frac{\lambda_c}{1+\lambda_c f}\right). \tag{4.38}$$

Now, for a given mass m_c, and therefore, a given radius R_c there will always be a corresponding fraction of dark matter,

$$\Omega = N_c \frac{m_{\rm c}}{M_{\rm DM}}, \tag{4.39}$$

where $M_{\rm DM}$ is the total DM mass and N_c the number of clumps. In our case, we have taken the total mass as the one contained in the detector's trajectory.

In our study, we use the physical characteristics of clumps such as the clump mass, its radius, and the number of clumps (from the overall dark matter fraction Ω), (M_c, R_c, N_c), to determine the specific parameters (λ_c, f, N_c) needed to define our numerical signal. This signal is then subjected to the test outlined in sec. 4.1.4, providing us with the confidence to ascertain whether this clump can be distinguished after a fixed observation time.

Our numerical analysis comprises variable clump radii and different total fractions of clumps accounting for dark matter. As already mentioned, these physical parameters define the parameters in our simulation. More specifically, we have generated the corresponding signal for each parameter space point (Ω, R_c) and applied the null hypothesis test with respect to the expected average signal for a homogeneous distribution. In Fig. 4.10, the black crosses represent the clumps that we can distinguish with a reliability of more than 3σ in 95% of the 100 times we generated the signal and applied the test. Contrasting the analytical distinguish-ability analysis, we have included our numerical result with the corresponding SNR presented in the Eq. (4.27). In Fig. 4.10, the analytical counterpart is shown as black curves. We have also illustrated the graph as crosses and gray curves from analyzing a few accounts. The analytical part is based on Eq. (4.29). For the numerical part, we have proceeded analogously to that already described in the sec. 4.1.3. As seen in each case we have tested, the numerical and analytical results are in good agreement for different number of events and different overdensity.

Finally, we want to make an observation regarding a limitation of our method. When the overdensity is small, the number of clumps increases considerably, which allows us to describe clumps with smaller sizes. However, in this case, the spectrum generated by the signal is more difficult to distinguish because of its similarity to the homogeneous case. Moreover, each clump may have on avergae very few events making it difficult to distinguish them due to the possible large fluctuations. So, the higher the overdensity, the higher the probability of distinguishing the clump.

In the following, we are going to roughly estimate the time required for upcoming experiments to detect the distinguishable small structure based on the minimum number of events we have found.

Estimation of Clump Detection Time for Direct Detection

Taking the statistical analysis results for the sensitivity projections we have presented earlier in Chap. 2.1.2, specifically in Fig. 2.3 of XENONnT [267] and DARWIN [53], for different DM masses and spin-independent cross-sections, we can estimate the observation time required for these experiments to see the curves in Fig D.4a, i.e., the time that will take to distinguish clumps with such characteristics using the number of events we find in your analysis, see Table 4.3. Here, we have considered that the efficiency of the detectors along the detection time is constant. We have made a linear interpolation of the number of events each collaboration expects in a short time. In Fig 4.11 (left panel), we have represented the physical characteristics of a clump that could be detected with the data found in the Table 4.3. As the number of events is very small, simulating a clump that can be detected with a good level of reliability is difficult. Although we have reduced the reliability level for the numerical estimation to 85%, we do not find with our method that a clump can be detected

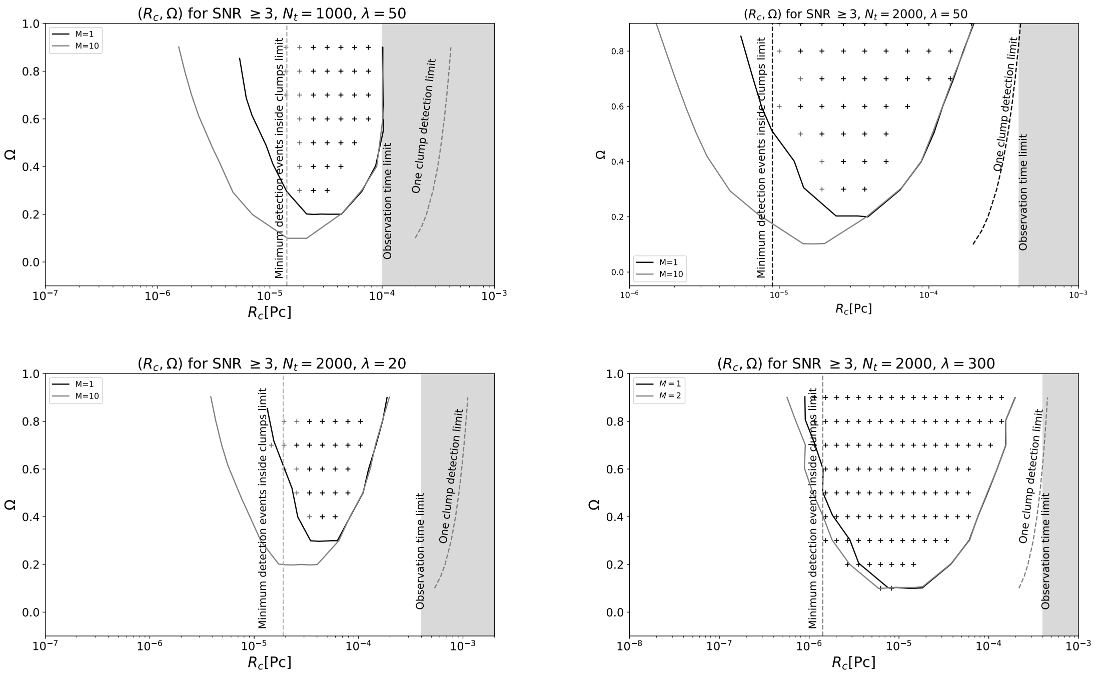

Figure 4.10. In the different panels shown the parameter space generating distinguishable clumps with a $SNR \geq 3$. For each case we have contrasted the numerical results (crosses) and the analytical results (curves) for different observation times, number of events and overdensities, as indicated in each panel at the top, here the background is negligible ~ 1 event per unit time. The vertical lines represent a minimum limit of detections within the clump of 2 and the gray shaded areas are the upper limit imposed by the observation time.

with only 100 events. The choice of $\lambda_c = 20$ was convenient because we know that these are the minimum overdensities we can detect. So, in a slightly more refined analysis, it might be possible to improve the estimates, but in our simplistic model only the parameter space is very small.

Additionally, with the improved sensitivity projected for DARWIN, we can estimate the number of events using the same ratio of events to cross-section as in the case presented in Table 4.3. Based on this, the expected number of events for WIMP masses of $20\mathrm{GeV}/c^2$ and $100\mathrm{GeV}/c^2$ at the improved sensitivity level of $1.5 \times 10^{-49}\mathrm{cm}^2$ and a $500\mathrm{t} \times \mathrm{y}$ exposure would be approximately: ~ 480 events for $20\mathrm{GeV}/c^2$ and ~ 535 events for $100\mathrm{GeV}/c^2$. In Fig. 4.11 (right panel), we show the most optimistic approximation for greater exposure to demonstrate how the clump parameter space changes. Moreover, to detect 1000 events with DARWIN and compare them with regions like the one shown in the top left panel of Fig. 4.10, an exposure time of approximately 935 ton-years would be required, given the improved sensitivity of $1.5 \times 10^{-49}\mathrm{cm}^2$ and a 500 ton-year exposure. Alternatively, the number of events could be increased by either enhancing the detector's sensitivity or adjusting the WIMP mass to optimize detection within the same exposure time.

Observation time [yrs]					
Experiment	Mass [GeV/c^2]	$\sigma_{\rm SI}$[cm^2]	50 events	100 events	200 events
XENONnT	6	3×10^{-44}	13.1	26.3	52.6
XENONnT	50	5×10^{-47}	2.8	5.6	11.3
DARWIN	20	2×10^{-47}	1.6	3.2	6.4
DARWIN	100	2×10^{-47}	1.1	2.2	4.4

Table 4.3. Observation time for experiments to distinguish small dark matter structure. The projection of these times take into account the exposure time of each experiment, the fiducial volume and the statistical prediction of events during the exposure time for different masses and cross sections given by each collaboration.

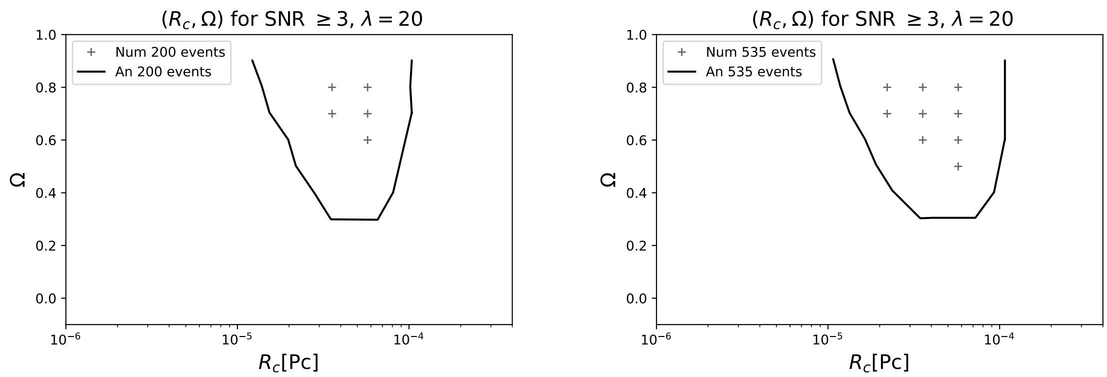

Figure 4.11. In the left panel we show the clump dimensions projected from Table 4.3. The numerical estimative was obtained with 85% of confidence level. In the right panel we show the same but for an approximate number of events at the improved sensitivity level of 1.5×10^{-49}cm^2 and $500t \times y$ exposure for DARWIN. Both cases we consider a negligible background ~ 1 event per unit time

Clump contribution to the matter power spectrum of the Universe

We aim to compare the contribution of clumps to the matter power spectrum alongside other known density fluctuations. To do so, we start by analyzing the linear power spectrum from Eq (4.10). By transforming this into k-space, with the relations $\omega = vk$ and $\tau_d = x_d/v$, we can express the one-dimensional power spectrum $P(k)_{\rm 1D}$ as follows,

$$P(k)_{\rm 1D} = 2(\Gamma_c T)\langle B\rangle^2 \frac{x_d}{v}\frac{1}{1 + x_d^2(k - k_0)^2}. \tag{4.40}$$

Analyzing the linear power spectrum provides a baseline for understanding the contribution of clumps to the overall matter distribution in the universe. It isolates how clumps, as density fluctuations, behave, allowing for a simple way to distinguish their behavior before extrapolating the analysis in three-dimensional space. In the left panel of Fig 4.12, we have illustrated the linear power spectrum of two clusters over different observing times. The clusters have a characteristic size of $1, 5 \times 10^{-3}$pc, and 8×10^{-4}pc as indicated above each peak. We have taken different observing times to naively estimate the time needed to resolve the clump or observe the clump completely. We note that the contributions of both clumps are similar and that in both cases, after a comparable period of time, the contribution can be fully resolved. However, we would like to mention that even if the clump is not completely resolved after a shorter time of observation $\sim$ 2yrs, the maximum peak can begin to be distinguished, which in a very rough way could give us indications in a short time of the contribution of these structures. It should be noted that we have taken examples where a remarkable contribution is attained. We take such examples in order to understand the behavior of the contribution to the spectrum.

Based on the linear power spectrum, we can get an insight into the possible contribution of these clumps into the matter power spectrum of the Universe. To do this, we first assume isotropy and we apply the radial Fourier transform to the power spectral density in Eq. (4.10),

$$\mathcal{F}^{-1}[\tilde{\mathcal{S}(\omega)}] = f(\vec{x}) = \frac{1}{(2\pi)^3}\int_{-\infty}^{\infty} \mathcal{S}(\omega) e^{-i\vec{\omega}\cdot\vec{x}} d^3\omega, \tag{4.41}$$

subsequently, in momentum space, we derive the contribution of the clumps as,

$$P(k) = \int_{-\infty}^{\infty} f(x) e^{i(\omega t - \vec{k}\cdot\vec{x})} d^4x. \tag{4.42}$$

This approach enables us to incorporate the contribution that a representative case of the clumps could generate into the matter power spectrum.

To get a clearer visual of the scale to which we contribute, we reproduce the primordial inflationary spectrum with the present distribution in galactic scales through a Harrison-Zeldovich spectrum [293]. This power spectrum is represented by the gray solid line in Fig 4.12. We have taken the example of the two clumps in the left panel of Fig 4.12, more specifically, the parameters to reproduce those peaks. We take these examples to evaluate the Eq. (4.42). In particular, the contribution is observed at $k \sim 10^{10}\text{Mpc}^{-1}$, much smaller and different scales than the scales modeled by the Harrison-Zeldovich spectrum, that have already some testing, e.i., some observational data [294].

It is important to note that the impact on the power spectrum can vary considerably due to the diverse nature of detectable clumps in our study. We may encounter a high flux of small clumps or a smaller flux of denser clumps. The variability of these contributions is due to the different cluster encounter probabilities, which can vary from medium to low, which means how probable each of these scenarios is and the time required to identify peaks in the spectrum. As a result, the contributions to the power spectrum exhibit notable fluctuations. It is important to note that our toy model parameters are intentionally simplified for ease of analysis. Therefore, a more detailed investigation could refine the values we have determined here, providing a more nuanced understanding of the contributions to the power spectrum.

4.3 Discussion

We have studied small dark matter structures on scales comparable to the size of the solar system, focusing on their potential spectral signatures in ground-based experiments compatible with WIMP

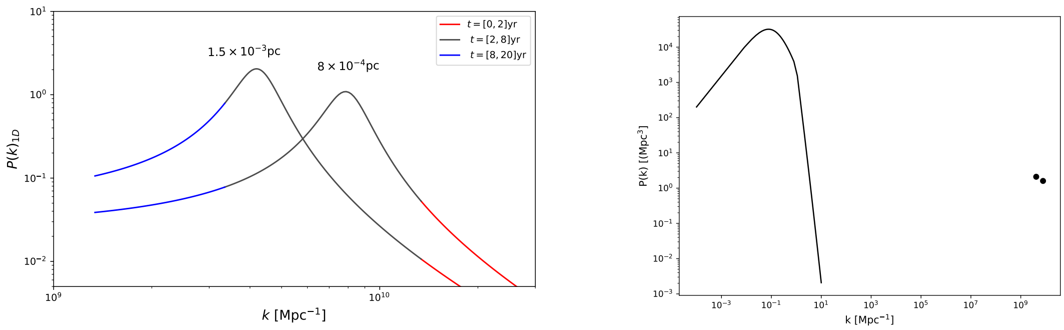

Figure 4.12. On the left-hand side, we show the clump linear power spectrum locally for $v = 220$ km/s. On the right we show the matter power spectrum of the universe including two example cases of clump contributions.

searches, such as XENONnT, and future extensions like DARWIN. Specifically, we analyzed the spectral fingerprints these structures might leave if they pass through an Earth based detector.

Our simplified model assumes a smooth background representing homogeneously distributed dark matter in our local region. We contrast this with a scenario in which dark matter is distributed differently, specifically localized in clumps rather than spread evenly. In this clumped model, certain areas are denser than others, even though the average dark matter density in the locality remains unchanged. These over dense regions, or ”clumps,” are modeled as agglomerations of dark matter particles. If encountered, such clumps would generate a significantly higher number of detection events than expected from the background alone. We have modeled the encounters with dark matter particles analytically and numerically to explore these distributions.

In the analytical approach, we adapted a filtered Poisson process to account for clumps, or over-densities, within a generally homogeneous signal. For the numerical model, we simulated a homogeneous Poisson process to represent a smooth background and a non-homogeneous Poisson process to simulate clumped dark matter. In both cases, we analyzed the resulting signals in the frequency domain using Fourier analysis and found that the power spectra from both methods showed similar trends. During this analysis, we noted that the analytical model could be further refined. For example, replacing the current peak-shaped clump model with a rectangular-shaped clump could improve alignment with the numerical model, even as an approximation. This refinement is left for future work.

Continuing with the spectral analysis, we characterized the spectral density in the homogeneous and over dense cases and compared the two spectra using statistical tests that accepted or did not accept the null hypothesis for the numerical simulation.

In our study, we tested the null hypothesis using conventional tests like the *t-test* and alternative methods like the non-parametric Mann-Whitney (MW) test. Both tests were capable of evaluating our hypothesis. Initially, the non-parametric test appeared to detect signals with greater clarity and efficiency. However, upon closer examination, we observed that it provided results that were overly optimistic, surpassing the expected outcomes derived from analytical signal-to-noise ratio analysis, which are considered ideal. Consequently, in our analysis, we opted for the *t-test* since the results were more conservative and aligned more closely with our expectations.

From our analysis, we could infer some parameters characterizing the clumps that, in principle, we could detect, such as how dense they are and what their size is, as shown in Fig. 4.10. We have found that for a small number of events, $N_t \sim 1000 - 2000$ clumps with radius in the range $(10^{-6}, 10^{-4})$ can be detected with a good level of confidence. In addition, we included sensitivity projections of direct detection experiments, specifically in the context of WIMPs. Our results indicate that with the advent of the new generation of detectors, there is a potential to detect some small DM structures.

Based on our simplistic analysis, a minimum exposure time of at least 1.1 years would be required to achieve this distinction in experiments like DARWIN. We tested the potential characteristics of the clumps that DARWIN could potentially test, Table 4.3, and found that the parameter space allowed is slim for such a realistic case. In Fig. 4.11, we show that with 200 detections at a sensitivity level of $\sigma_{\rm SI} = 2 \times 10^{-47}$ cm^2, and by extrapolating to improved sensitivity of $\sigma_{\rm SI} = 1.5 \times 10^{-49}$ cm^2 with an exposure of 500 t$\times$yr, yielding approximately 535 detections, there is an 85

Finally, we made a first step to illustrate the contribution of small clumps to the universe's matter power spectrum. To do so, we have taken our linear approximation (Eq. (4.10)) and estimated the full-dimensional contribution (4.42). In our example case, the contribution is observed at $k \sim 10^{10}$Mpc^{-1}. We note that the impact on the power spectrum can vary considerably due to the diverse nature of detectable clumps in our study. We may encounter a high flux of small clumps or a smaller flux of denser clumps. The variability of these contributions is due to the different cluster encounter probabilities, which can vary from medium to low, which means how probable each of these scenarios is and the time required to identify peaks in the spectrum. As a result, the contributions to the power spectrum exhibit notable fluctuations.

It is important to note that our toy model parameters are intentionally simplified for ease of analysis. Therefore, this work represents a first step towards understanding the delectability of very small structures locally, and a more detailed investigation could refine the values we have determined here, providing a more nuanced understanding of small local structures.

Chapter 5

Heating DM: core-cusp inner density profiles for Halos

The following work is based on a joint project with Prof. Laura Covi.

ΛCDM describes to a good extent the large-scale structure of the Universe, i.e., at distances larger than $\mathcal{O}$(Mpc). As we have mentioned, to study smaller (medium) scales, N-body simulations have been the main tool so far. Several DM-only simulations can be obtained to understand the structure and abundance of CDM halos and their substructure [295,296]. However, it remains unclear whether these predictions are confirmed in nature. In particular, there are some points already established with some clarity where CDM simulations disagree with observations [297–299], and therefore a more detailed study including simulations with baryonic matter and additional interactions, among other aspects are needed [300,301].

This chapter addresses the core-cusp problem, which refers to observed density profiles in small galaxies and their discrepancy with predictions based on CDM simulations. To do so, we study a DM candidate capable of undergoing exothermic processes. These exothermic processes heat the medium, producing an increase in the volume, which can explain the expected cored density profile in the central dense regions of small galaxies and, at the same time, agree with CDM predictions on larger scales. We use the gravothermal fluid description [302,303] to study the heating effect on the halo.

In the following, we describe the core-cusp problem and define the framework in which the discrepancy between simulations and observations can, in principle, be resolved using dark matter capable of carrying out exothermic processes.

The mass density profile for collisionless CDM halos increases towards the center in the simulations. This can be model in the central region as $\rho_{\rm DM} \propto r^{-1}$ [23,61,304], and it is well described by a Navarro-Frenk-White (NFW) profile [305],

$$\rho_{\rm DM}(r) = \frac{\rho_s}{(r/r_s)(1+r/r_s)^2}, \tag{5.1}$$

where ρ_s and r_s are characteristic density and scale radius of the halo. Nevertheless, observations of rotation curves of disk galaxies show a linearly rising circular velocity of stars in the inner regions, resulting in constant "cored" density profiles modeled by $\rho_{\text{DM}} \propto r^0$ [61, 306]. This discrepancy between the observed profiles and those expected based on the simulations is the so-called core-cusp problem. The issue becomes very relevant when studying dwarf and low-surface brightness galaxies because they are expected to have a high DM content. These galaxies have low luminosity and surface brightness, are less influenced by baryonic processes, such as star formation, which could potentially modify the DM distribution due to baryon-dark matter interaction processes. These galaxies are therefore, in practice, easier to simulate because their matter content is dominated by the dark matter component and therefore they are an appealing place to test CDM [307, 308].

The discrepancies between the standard CDM prediction and the observations in small-scale structures may indicate that DM is not completely collisionless. Self-interacting DM (SIDM) has been a popular proposal to explain the central mass deficit in halos [309]. In this scenario, DM particles perform elastic scatterings with each other through $2 \to 2$ interactions [36, 310, 311]. At sufficiently large radii, the collision rate is negligible, and therefore, SIDM halos have the same structure as CDM halos. This is because the scattering rate between SIDM particles is proportional to the density of the dark matter. The local collision rate is given by [312],

$$R_{\text{scatt}} = \frac{\sigma}{m} v_{\text{rel}} \rho_{\text{DM}} \approx 0.1\text{Gyr}^{-1} \left(\frac{\rho_{\text{DM}}}{0.1\text{M}_{\odot}/\text{pc}^3}\right) \left(\frac{v_{\text{rel}}}{50\text{km/s}}\right) \left(\frac{\sigma/m}{1\text{cm}^2/\text{g}}\right), \tag{5.2}$$

where the DM density ρ_{DM}, and the value of the averaged relative velocity between particles, v_{rel}[1], are compared with the values of a typical dwarf galaxy towards the central region [313]. The cross-section per unit mass must be at least $\sigma/m \sim 1\text{cm}^2/\text{g}$ to have one scattering per particle over 10 Gyr, as shown in eq. (5.2), and therefore have an effect on the halo. For $\sigma/m \sim 1\text{cm}^2/\text{g}$, the mean free path of DM particles exceeds the core radius of the halo. This implies that the ratio of the mean free path to a characteristic length scale—specifically, the core radius of the halo—becomes larger than unity. This ratio, known as the *Knudsen number*, indicates that when it exceeds one, heat conduction becomes effective in the inner halo [312]. Here, heat conduction refers to the transfer of thermal energy from higher to lower temperature regions. For this value of σ/m, the scattering radius R_{scatt} becomes insignificant during the early stages of structure formation. Therefore, for a constant σ/m, the impact of self-interactions on the structure of halos occurs primarily at later times and on smaller scales within the dense inner regions. Self-interactions can also dramatically affect sub-structures through evaporation or tidal disruptions, so the cross sections for these processes become very constrained [309].

Self-interactions transport heat. The net heat gained contributes to an increase in the velocity dispersion of the DM particles and leads to a decrease in the mass density by expanding the volume occupied by DM. As a result, the velocity dispersion, which indicates the temperature of the DM particles, is not constant throughout the halo; it increases towards the center of the inner halo. Another scale-dependent effect here is that the impact of the energy released is more pronounced at smaller

[1]In a typical dwarf galaxy, the velocity follows a Maxwell-Boltzmann distribution

scales, where the injected energy self-heats the DM particles and enhances core formation in smaller halos [2] [315, 316]. There have been studies probing that such a process in the elastic regime can describe the core formation effect from DM self-heating and that it is indeed sharply escalated for halos smaller than a certain mass [38, 312].

Here, we study an exothermic model in isolated halos involving processes such as $3 \to 2$ scatterings, so unlike normal scatterings, energy is released or given off to the surroundings. We adopt the gravothermal fluid formalism to study the density profile and its velocity dispersion, and we discuss the possible astrophysical imprints that the process can enhance.

5.1 Describing self-heating Dark Matter

It is convenient to treat DM as an ideal gas to study the effect of the self-interactions in the halo. In the presence of an efficient heat conduction mechanism, the dynamics of a spherical halo can be described by the gravothermal fluid evolution [302, 303]. The formalism approximates the DM particles as an ideal fluid that is described by their mass density ρ and fluid pressure p. We are going to describe the gravothermal evolution of a pure SIDM as proposed in Refs [317–320], and add a heat injection term that models the DM self-heating following Refs [36, 38, 302, 321].

In the context presented, it is assumed that the self-interaction and self-heating mechanisms of DM become significant only after the formation of the halo [38].

Let us define the 1-D velocity dispersion $\nu = \sqrt{p(r,t)/\rho(r,t)}$, to state the equations of evolution of the gravothermal fluid as:

$$\frac{\partial \rho \nu^2}{\partial r} + \frac{GM\rho}{r^2} - V_r \frac{\partial V_r}{\partial r} = 0, \tag{5.3}$$

$$\frac{\partial M}{\partial r} - 4\pi r^2 \rho = 0, \tag{5.4}$$

$$\frac{3}{\nu}\left(\frac{\partial \nu}{\partial t}\right)_M - \frac{1}{\rho}\left(\frac{\partial \rho}{\partial t}\right)_M = \frac{1}{\nu^2}\frac{\partial u}{\partial t}, \tag{5.5}$$

where G is the Newton constant, M represents the enclosed fluid mass within radius r and $(\partial_t)_M = \partial_t + \vec{V} \cdot \vec{\nabla}$, where $\vec{V}$ is the fluid bulk velocity. This last term describes modifications in characteristics like temperature, pressure, density, and internal energy that arise from heating processes within the fluid. Simultaneously, its location changes as the fluid element moves within its environment, so $(\partial_t)_M$, specifically refers to changes within the fluid element as it changes its state and location. The set of equations describes the evolution of the mass density, where the nature of a SIDM model is manifested by the heat conductivity term present in the first equation of thermodynamics. In Sec. 5.2, we will describe this process in more detail.

To properly describe the process, we need the evolution of the bulk velocity as well. For that, we

[2] This effect can be estimated analytically and tested through N-body simulations, as shown in Ref. [314].

use the continuity equation,

$$\partial_t\rho\rho + \vec{\nabla}\cdot(\rho\vec{V}) = 0$$
$$\partial_t\rho + \frac{\rho}{r}\left(V_r + r\frac{\partial V_r}{\partial r}\right) + \frac{1}{r}\left(\rho + r\frac{\partial\rho}{\partial r}\right)V_r = 0$$

taking the stationary solution $\partial_t\rho = 0$ we get for the bulk velocity:

$$\frac{\partial V_r}{\partial r} - \frac{V_r}{r}\left(\frac{r}{\rho}\frac{\partial\rho}{\partial r} - 2\right) = 0. \tag{5.6}$$

The bulk velocity effects in the fluid momentum conservation equation are assumed to be negligible since we required the halo to be in quasi-static equilibrium.

On the other hand, velocity dispersion due to self heating is obtained form eq (5.5) as,

$$\frac{3}{\nu}(\partial_t\nu + \vec{V}\cdot\vec{\nabla}\nu) - \frac{1}{\rho}(\partial_t\rho + \vec{V}\cdot\vec{\nabla}\rho) = \frac{1}{\nu^2}\frac{\partial u}{\partial t},$$

with the stationary solution,

$$\frac{\partial\nu}{\partial r} - \frac{r}{3V_r\nu}\frac{\delta u}{\delta t} - \frac{\nu}{3\rho}\left(\frac{\partial\rho}{\partial r}\right) = 0. \tag{5.7}$$

Taking (5.6) to rewrite $(\partial\rho/\partial r)$ in terms of V_r, we can rewrite,

$$\frac{1}{r^2}\frac{\partial}{\partial r}(r^2V_r) + \frac{3}{\nu}\left(V_r\frac{\partial\nu}{\partial r}\right) - \frac{1}{\nu^2}\frac{\delta u}{\delta t} = 0 \tag{5.8}$$

Here again, we have considered the stationary solution. The details of the calculations are presented in Appendix E.1.

The heat conduction is modeled by heat diffusion given by,

$$\frac{\delta u}{\delta t} = \frac{m}{\rho}\Delta\cdot(\kappa\Delta\nu^2), \tag{5.9}$$

where u is the specific energy per unit mass and κ is the thermal conductivity. The heat gain is used to increase the velocity dispersion of the particles, and as the volume expands, the mass density decreases as well.

Finally, the set of differential equations to numerically solve is:

$$\frac{\partial(\rho\nu^2)}{\partial r} + \frac{GM\rho}{r^2} + V_r\frac{\partial V_r}{\partial r} = 0, \tag{5.10}$$
$$\frac{\partial M}{\partial r} - 4\pi r^2\rho = 0, \tag{5.11}$$
$$\frac{\partial V_r}{\partial r} - \frac{V_r}{r}\left(\frac{r}{\rho}\frac{\partial\rho}{\partial r} - 2\right) = 0, \tag{5.12}$$
$$\frac{1}{r^2}\frac{\partial}{\partial r}(r^2V_r) + \frac{3}{\nu}\left(V_r\frac{\partial\nu}{\partial r}\right) - \frac{1}{\nu^2}\frac{\delta u}{\delta t} = 0. \tag{5.13}$$

Equations (5.10) to (5.13), are the final set of equations to be solved. We discuss in the following sections,in the framework of the above equations, how the exothermic processes affect the density profile and velocity dispersion.

5.2 Heat Conduction

As stated earlier in eq (5.9), the heat conduction is modeled by a heat diffusion equation. In the context of standard heat diffusion, which assumes that the distance between collisions is shorter than the size of the system, the flux can be expressed as,

$$\frac{L(r,t)}{4\pi r^2} = -\kappa m \frac{\partial \nu^2}{\partial r}, \tag{5.14}$$

where the luminosity $L(r, t)$ represents the rate of energy that crosses a sphere of a radius r and it is related to the gradient of temperature. To calculate the heat conductivity κ, one needs to parametrize the distribution perturbations due to collisions that generate small deviation from a local equilibrium Maxwellian space-phase distribution f. To do so, the perturbations δf can be parametrized as $\delta f = (\overline{f}/T)\mathbf{g} \cdot \Delta T(\mathbf{r}, \mathbf{t})$, where $\overline{f}$ represents the average value of the distribution, T is the temperature and **g** is a vector function that represents the deviations from a local equilibrium distribution caused by collisions in a system [322]. The conductivity is obtained as,

$$\kappa = -\frac{1}{3T} \int d^3 \frac{v^2}{2} \mathbf{v} \cdot \mathbf{g}\overline{f}. \tag{5.15}$$

The calculation of κ from eq. (5.15) is highly non trivial . As an alternative, it is possible to estimate κ in the limit where the mean free path of DM particles is either much shorter (SMFP regime) or much longer (LMFP regime) than the size of the halo. In this case, we assume that the free streaming length λ is shorter than the physical size of the system, $H = \sqrt{\nu^2/4\pi G\rho}$, as we mentioned before. One can derive the heat flux from the Boltzmann set (5.3), so that,

$$\kappa_{\text{SMFP}} = \frac{75\sqrt{\pi}}{64} \frac{\rho \lambda^2}{a m t_{\text{self}}}, \tag{5.16}$$

where t_{self} is the self-interaction time scale and $a = \sqrt{16/\pi}$ is a coefficient relevant for the hard-sphere scattering of particles with a Maxwell-Boltzmann velocity distribution [320]. This, together with the rate of specific heat gain for a fluid element,

$$\frac{\partial u_{\text{cond}}}{\partial t} = -\frac{1}{4\pi r^2 \rho} \frac{\partial L}{\partial r}, \tag{5.17}$$

where u is the energy per DM particle, account for the heat conduction in this picture.

For illustration, let us review the case of $2 \to 2$ annihilation processes. In this case, an important effect for self heating DM (SHDM) comes with DM semi-annihilations, DM + DM $\to$ DM + χ, where χ is a light particle, assuming a constant $\langle \sigma_{semi} v_{rel} \rangle$. For SHDM, a small portion of the DM particles that are enhanced in kinetic energy due to semi-annihilations are trapped within the halo instead of escaping through DM self-interactions (assuming the escaped particles have no impact on halo evolution). The boosted DM particle carries a high kinetic energy of $\partial E = m/4$, which is the energy injection that subsequently is redistributed to the other DM particles, causing self-heating. This self-heating can be effectively described as injecting heat into the local DM fluid element at a given rate,

$$\frac{\partial u_{semi}}{\partial t} = \rho \frac{\langle \sigma_{semi} v_{rel} \rangle}{m} \xi \frac{\partial E}{m}, \tag{5.18}$$

here, ξ is a dimensionless coefficient determining the efficiency of the process. References [37, 38, 323] have shown that, in general, DM undergoing $2 \to 2$ processes can solve the core-cusp problem as they generate volume expansion due to heat transfer, thus preventing the nucleus from developing a cusp. However, the core formation resulting from self-heating seems more efficient for smaller halos [37, 38], which seems inconsistent with observations (and the bounds coming from them) and thus casts doubt on the feasibility of SHDM. Therefore, alternatives such as the $3 \to 2$ exothermic processes are an attractive option to study because the conduction dynamics are the same, so they can generate the redistribution of the energy density under the same considerations of the $2 \to 2$ case, with the only difference being the process that produces the heat conduction.

In Fig 5.2, we have reproduced the results presented in [38] where the evolution of the density profile is shown for a SHDM with DM mass $m_\chi = 0.9$MeV, $\sigma_{sel}/m_\chi = 0.1\text{cm}^2/g$ and $\langle \sigma_{semi} v_{rel} \rangle = 6 \times 10^{-26}\text{cm}^3/s$. For this case, we have solved the set of equations (5.10) to (5.13) (we explain the step by step the procedure in Sec 5.2.1) using the heat conduction term as indicated in eq.(5.18), with $\partial E = 1/2m$, the efficiency ξ was fixed motivated by N-body simulations [38]. We detail the value of this parameter more carefully in the following subsection, see Sec 5.2.1. The virial mass of the halo determines the density evolution. Very briefly, the virial mass is defined as a concept to estimate the mass of a galaxy based on the dynamics of its components, like dark matter and stars. Such virial mass comes from considering a state of dynamical equilibrium where the kinetic energy of its components balances the gravitational potential energy of a bound system through the so-called virial theorem [23, 324]. In Fig 5.2, the solid lines represent the checks we have done for the core formation for virial masses of $M = 10^9\text{M}_\odot$ and $M = 10^{10}\text{M}_\odot$ corresponding to typical masses for satellite galaxies and dwarf galaxies, respectively, which turns out to be more efficient towards smaller halos, as was already pointed out in Refs [37, 38]. Nevertheless, step-wise core formation is expected to remain a common feature among SHDM scenarios, prompting the exploration of alternative frameworks. In what follows, we will test another exothermic process that can be adapted to the modeling of the heat injection described before.

5.2.1 Self-heating process $3 \to 2$

We consider a heating process for DM through self-annihilation DM DM DM $\to$ DM DM [73, 325]. In addition to possibly explaining the core-cusp profile, these annihilations can inject additional kinetic energy into the boosted particles when altering the number density of particles, Fig. 5.1b. Since the exothermic annihilation process generates additional energy, which raises the temperature of the surrounding medium for both baryonic and DM components, the temperature of the neutral hydrogen within the subhalo increases. This leads to a higher thermal excitation of the neutral hydrogen atoms, which enhances the intensity of the 21-cm line, for example [326].

Some DM candidates can address dark matter self-annihilation. SIMPs [37, 327, 328] serve as viable candidates for dark matter in this case, as they are thermal relics whose current density can be determined by the cross-section interactions between DM and SM particles and also self-interactions. Elastically Decoupling Relics (ELDERs) [39] are also DM candidates that behave similarly. In both cases, it is possible to consider $3 \to 2$ cannibalization processes. Specifically, in the case of ELDERs, their decoupling from the plasma takes place before their freeze-out, resulting in ongoing changes to their number density through cannibalization processes (refer to Fig 5.1a). In contrast, for SIMPs, the $3 \to 2$ process decouples prior to the $2 \to 2$ process, as illustrated in Fig 5.1b. This distinction between SIMPs and ELDERs is the reason why we have chosen to focus on describing the ELDER scenario in our description[3]. Further details on this topic are provided in Appendix E.2.

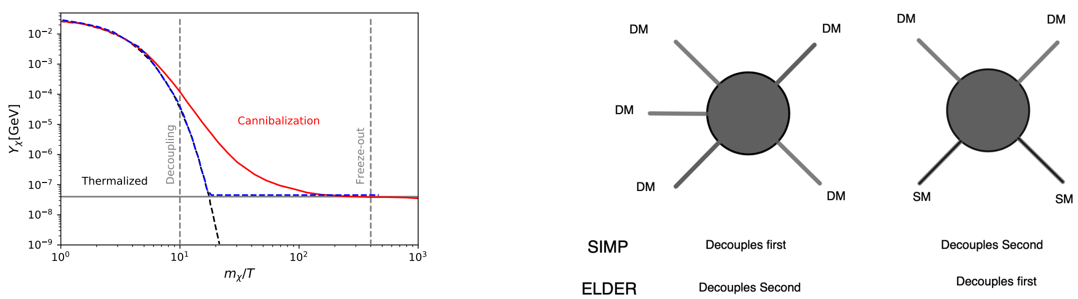

(a) Dark matter yield as a function of temperature T with $m_\chi = 10$MeV.

(b) SIMPs vs ELDERs.

Figure 5.1. Cannibalization process. On the right-hand side, we illustrate DM yield as a function of temperature T with $m_\chi = 10$MeV. The black dotted line represents the equilibrium distribution, and the bred line represents the ELDER evolution undergoing the cannibalization process and the blue dotted line is an illustration of the standard freeze-out process. On the left side, we contrast SIMPs vs ELDERs. Both candidates undergo $2 \to 2$ and $3 \to 2$ processes, but in general, for ELDERs, the cannibalization process decouples last.

As the framework stands, to effectively describe the heat injection to the local DM fluid element as,

$$\frac{\partial u}{\partial t} = \Gamma_{3\to 2}\xi \frac{\partial E}{m}, \tag{5.19}$$

where $\Gamma = \eta^2 \langle \sigma_{3\to 2} v^2 \rangle$, η is the number density, ∂E is the kinetic energy of the captured boosted DM particle so is taken as $\propto m$. The efficiency ξ is challenging to model, and it usually involves a more careful treatment that is beyond the scope of this thesis. Therefore, we use a simplified assumption in which the efficiency is uniform,

$$\xi = b\frac{r}{\lambda}, \tag{5.20}$$

where b is a fudge factor (or correction coefficient) set to 3. This choice is motivated from the N-body simulation result for the inelastic SIDM [38], and $\lambda = 1/(\rho\sigma_{self}/m)$ is the mean streaming length of DM. The conduction term goes as [82]:

[3] ELDER is a Cold Dark Matter (CDM) candidate consistent with observations from CMB and structure formation [39].

$$\frac{\partial u}{\partial t} = \eta^2 \langle \sigma_{3\to 2} v^2 \rangle \frac{br}{\lambda} \frac{\partial E}{m} \tag{5.21}$$

$$= \left(\frac{\rho}{m}\right)^2 \frac{\alpha^3}{m^5} \frac{br}{\lambda} \frac{\partial E}{m}, \tag{5.22}$$

where m is the mass of the DM particle, and α is the strength of the number-changing self-annihilation process for the $3 \to 2$ process. Here, we have taken the parametrization of the the self-annihilation cross-sections in the non-relativistic limit, assuming that the same annihilation cross-section that determined the decoupling of ELDERs in the early universe is still applicable to exothermal processes later,

$$\lim_{T\to 0} (\langle \sigma_{3\to 2} v^2 \rangle) = \frac{\alpha^3}{m_\chi^5}, \tag{5.23}$$

see Section 2.1.1 and Appendix E.2, for more details. In general, for any process that converts DM mass deficit into kinetic energy, the rate per unit mass at which the DM halo is heated will be characterized by the self-annihilation process, the energy injection, and the number density of the particles involved. The density of particles involved in the heating process needs to be small so that high heating rates are avoided.

Numerical solution method

We solve numerically the set of equations (5.10) to (5.13) using the corresponding heat conduction term for ELDERs, eq. (5.22). We show the core formation generated by the exothermal processes in Fig. 5.2. We first assume a constant and uniform velocity dispersion ν to solve the equations. In this way, we solve first eq. (5.12) and eq. (5.13) to have an initial solution for the density ρ and V_r. We take those solutions to solve eq. (5.10) and eq. (5.11) to obtain a solution for ν. Finally, we solve again eq. (5.12) and eq. (5.13) with the updated value of ν. We solve the equations iteratively until they converge. This procedure was first followed in references [320, 323].

Is important to highlight that our description, as detailed in Sec. 5.1 is stationary because we assume that DM self-interaction and DM self-heating are unimportant during the halo formation process. Some works include a non-stationary treatment of the gravothermal equations, as in Ref [38]. In this work, a comparison has been made between the stationary solution and the one that includes a complete time dependence, and it has been found that they are compatible. We have compared our results for the $2 \to 2$ process (see Fig. 5.2 solid lines) with those proposed in that paper and found that the solution for the energy density agrees in both cases.

5.3 Discussion

In figure 5.2, we show the core formation for an ELDER (dotted red lines), following similar parameters used in the SHDM evolution (solid lines). We take the same mass for the DM as in the previous

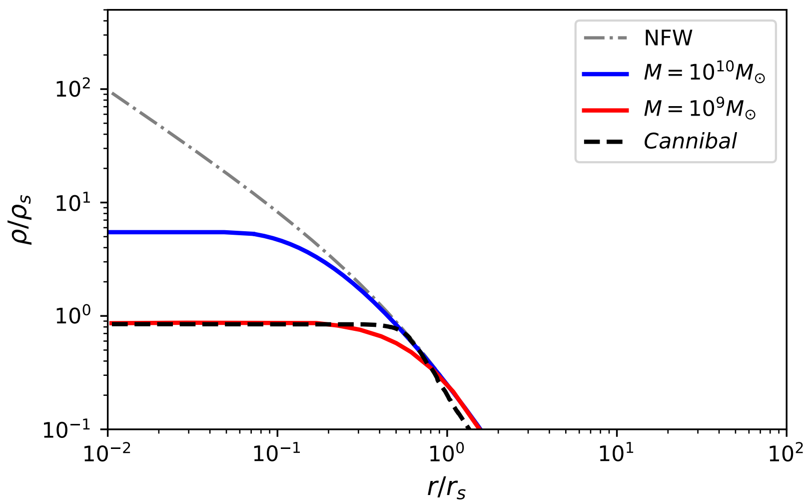

Figure 5.2. Density profiles for $2 \to 2$ (solid lines) for $\langle \sigma v \rangle = 6 \times 10^{-26}\text{cm}^3/s$ and the cannibalization process (dashed lines) for $\alpha = 5 \times 10^2$. Here the evolution of the density is determined by the virial halo mass M as indicated in the plot. For this plot we have fixed $m_\chi = 0.9$ MeV. Here the density and the radius are compared to $\rho_s \approx 0.011\text{M}_\odot/\text{pc}^3(10^{10}\text{M}_\odot/M_{\text{halo}})^{0.24}$ and $r_s = 3.43\text{kpc}(M_{\text{halo}}/10^{10}\text{M}_\odot)^{0.44}$, coming from the virial halo description.

case and calculate the coupling for the process to $\alpha = 5 \times 10^2$ MeV and $\nu_i = 10km/s$. The α value presented in figure 5.2 resulted from numerically matching the cross sections of the $2 \to 2$ process in the new framework of the $3 \to 2$ process. We tested the exothermal process only for small masses of galaxies because, for such scales, the $2 \to 2$ becomes very restricted since the core formation becomes very efficient. It has been shown that the self-interactions do not play an important role in larger virial masses [36, 38] . As shown in Fig. 5.2, for a low mass galaxy, $M = 10^9 M_\odot$ the cannibalization process generates a core inner profile with a more extended plateau that decreases faster than that generated by the $2 \to 2$ process. The interpretation of this behavior may be related to the exothermal process displacing the particles by modifying the density distribution due to the energy injection. As seen in Fig. 5.2, the density profile for cannibal shows a discrepancy w.r.t the NFW profile in the outer parts of the halo. This could be due to the redistribution of the energy density being too efficient for the particular set of conditions we have chosen.

One way to test if this process could give better fitting results for a given final galaxy is by exploring different initial conditions set (M_i, ν_o), where M_i is the initial mass of the halo, and ν_o is the initial constant value for the velocity dispersion; as well imposing more robust restrictions on the cross-section so the process is more suppressed. In Fig. 4.10, we have computed the mass function and the density distribution of a galaxy with viral mass $M_{200} = 10^9\text{M}_\odot$, undergoing cannibal processes with different coupling strength as well as different initial conditions, (M_i, ν_o). From the evolution of the mass and density functions performed in the graph, one of the most relevant aspects is that the initial velocity dispersion is crucial in the evolution of the halo. A higher initial velocity dispersion corresponds to a greater mass deficit. This observation aligns with expectations, as a higher velocity dispersion implies increased energy transfer within the medium, enhancing the efficiency of the cannibalization process. Now, the value of the coupling found empirically by comparison with the case already studied in the literature of the $2 \to 2$ process [38], fits more optimally the conditions to recreate the final halo, slight variations in the coupling are not drastic in the final result. Moreover, there are notable numerical challenges that need addressing. The evolution of the mass function highlights significant numerical limitations. In the right panels of Fig. 5.3, truncations of the function occur beyond a certain scale due to erratic behavior. This highlight the need for a more sophisticated numerical treatment to enhance the accuracy of model testing. This avenue for improvement is a potential direction for future research in this topic.

However, it is notable that a mass deficit persists in both exothermal processes, disfavoring their suitability for analyzing small galaxies. This finding marks an initial phase for further studies of these processes. As a prospective endeavor, we suggest delving deeper into the parameter space encompassing dark matter mass and coupling. It is also important to test the model with a broader mass galaxy range and contrast it with observations to conclude whether this exothermal process successfully solves the problem. Another working point to ELDERs that needs further testing is that the numerical evolution of the density is not entirely consistent with the NFW profile in the outer regions for all couplings, i.e., it does not provide a perfect fit due to numerical limitations. Moreover, it is important to note that some studies have shown that the NFW profile is perhaps not the best profile to describe such small galaxies [329–331] and further testing with other self-consistent profiles will be necessary to test the viability of the model.

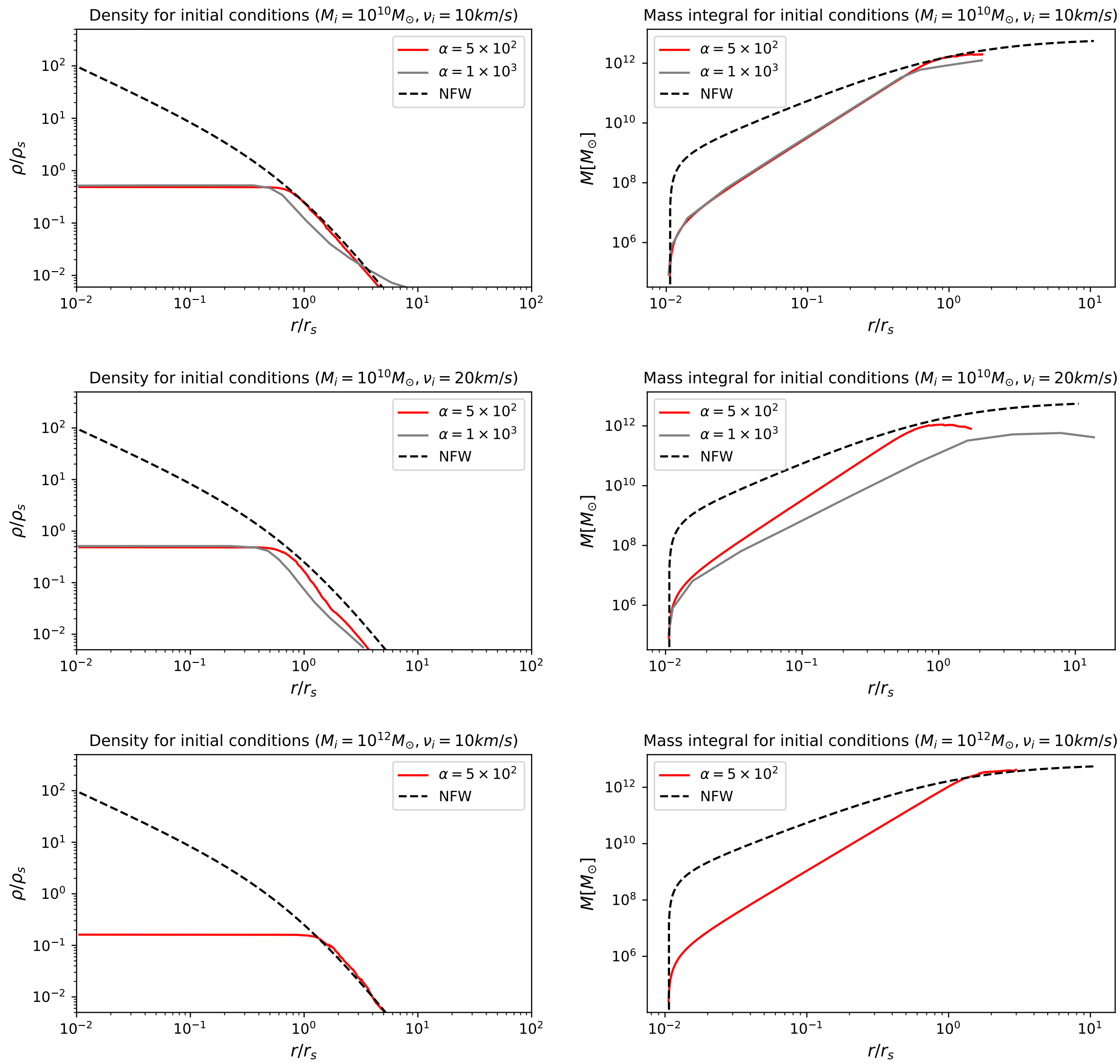

Figure 5.3. Density and mass functions for cannibals. We have tested two couplings $\alpha = 5 \times 10^2$ (red solid lines) and $\alpha = 1 \times 10^3$ (grey solid lines), for different sets of initial conditions as is indicated on each subplot. Here the density and the radius are compared to $\rho_s \approx 0.011\mathrm{M}_\odot/\mathrm{pc}^3(10^{10}\mathrm{M}_\odot/M_{\mathrm{halo}})^{0.24}$ and $r_s = 3.43\mathrm{kpc}(M_{\mathrm{halo}}/10^{10}\mathrm{M}_\odot)^{0.44}$, coming from the virial halo description. For all of the cases $M_{200} = 10^9\mathrm{M}_\odot$.

Chapter 6

Summary and Outlook

This thesis studies small-scale dark matter structures, focusing on two main aspects: the phenomenology of very small dark matter structures at local scales (about one light-year or less) and the behavior of small dark matter halo density profiles.

The dark matter puzzle has been a central question in cosmology for decades, and while the λ-CDM model has successfully explained large-scale structures in the Universe, its limitations on smaller scales motivate further investigation. In Chap. 1, we explore the origins of this puzzle and the need to address these limitations, setting the stage for the present work. After this, we reviewed in Chapter 2, the general properties of dark matter and focused on two primary candidates: WIMPs and axions. For WIMPs (Secs. 2.1.1 to2.1.2), we review their potential origins and how they might have been produced in the early Universe. We also discuss strategies for their direct detection, considering experiments like XENON1T and DARWIN. Similarly, we explore the properties of axions in Secs 2.1.3 to 2.1.3, including their cosmological origins, interactions with the Standard Model, and the detection methods designed for them. We also discuss experiments like ADMX and CASPEr, where the developments presented in this thesis could play a significant role. Through this review of both candidates, we set the preliminaries and the stage for our study, addressing the questions surrounding dark matter and highlighting the various approaches to which this thesis can contribute.

A big part of this work, detailed in Chapter 3, explores axions as dark matter and how local direct detection can provide insights into their distribution and nature. We begin by reviewing axion cosmology and setting the stage for a detailed study of axion miniclusters, including their general characteristics, Secs. (3.1 to 3.2.2). Focusing on detecting axion minicluster structures, we investigate how the spectral information obtained from haloscope experiments can be used to determine the gravitational potential and density of an axion minicluster. All from a single detection, Secs. (3.2.3 to 3.3.3). This approach takes advantage of the high accuracy of energy spectrum measurements in haloscope experiments. More in detail, applying Poisson's equation, we establish a relationship between the extracted gravitational potential and the density of the axion minicluster as the Earth passes through it. Finally, we combine the information on the minicluster's density with the extracted power from the haloscope cavity, successfully disentangling the axion-photon coupling and providing some insights into the local axion dark matter density.

Following our study of axions, axion structures, and their detectability, we focus on the quantum nature of axion dark matter and its relevance to dark matter experiments. We begin by reviewing axions in the context of quantum states, distinguishing between classical and quantum descriptions in Sec. 3.4. We then focused on the characteristics of different quantum states and its connection to energy eigenstates, briefly exploring differences between particle number states and coherent states. Our main contribution to the discussion of quantum states, presented from Sec. 3.4.1 to Sec. 3.4.6, was to address an essential aspect from a quantum mechanical perspective: the origin of the oscillation frequencies relevant to axion dark matter experiments. By examining the quantum nature of the axion field, we have shed light on the underlying mechanisms that give rise to these frequencies. To do so, we started from a scenario in which axions are coupled to spins. We show that a Jaynes-Cummings-type model can effectively approximate the original quantum field theoretical model and the experimental situation well. Finally, we identify the most suitable observables for probing these frequencies in experiments.

Beyond axions, Chapter 4 considers WIMP-based dark matter structures. Specifically, we consider the possibility that they are concentrated in overdense clumps on small scales. Our goal was to test their detectability by studying the time structure of the signal and the spectral signature of these small structures as they traverse the Earth in light of current and future ground-based experiments. We began by modeling a smooth background representing the homogeneously distributed dark matter in our locality, contrasting it with a scenario where dark matter is redistributed into denser clumps while maintaining the same average density. We identified these clumps as overdensities, or agglomerations of dark matter particles, which, in the case of detection, would generate a significantly larger number of events than expected. We used DARWIN sensitivity projections to determine how long it would take to detect these clumps. From our analysis, we were able to infer some parameters that characterize the clusters that, in principle, we could detect, such as how dense they are and what their size is. We also established a comparison illustrating the possible contribution of the clumps to the total mass spectrum compared to known contributions.

In the final chapter, Chap. 5, we address the cusp-core density problem, which concerns the steep density profiles predicted for dark matter halos versus the observed flat cores in some small galaxies. Our goal was to explore potential resolutions to this discrepancy. We began by using the gravothermal formalism in Sec. 5.1, to describe small dark matter halos, where annihilation or cannibalization processes could occur in the halo's inner and denser parts. These processes are exothermic, meaning that the energy released during annihilation dissipates into the medium, increasing the velocity of the dark matter particles and generating a redistribution of matter in the halo; we describe the heat conduction responsible for this phenomenon in Sec. 5.2. This redistribution could explain why the density profiles in some small galaxies are flat in the center, in contrast to the steep cusp profile expected according to initial predictions. Our study concluded in Sec. 5.2.1 that exothermic cannibalization processes can generate an effective redistribution of the energy density in the dark matter halo. Although this study represents only a first step in understanding the exothermic reactions of dark matter in halo centers and more detailed research is required to draw more solid and feasible conclusions, this thesis has contributed to understanding and exploring the exothermic process held by cannibalization processes.

In summary, this thesis has contributed to understanding small-scale dark matter structures, particularly in axions and WIMPs. Our analyses provide interpretations of the possible detection of these structures in the context of current and future dark matter detection experiments. By examining the theoretical and experimental aspects of small dark matter clusters, axion mini-clusters, and possible interactions, this work has helped lay the groundwork for interpreting direct detection results.

Appendix A

Preliminaries

This appendix introduces the QCD axion, a theoretical particle proposed to resolve the strong CP problem, a major question in particle physics regarding CP symmetry violation in Quantum Chromodynamics (QCD). Section A.1.1, begins with an overview of the θ-term in QCD, which leads to the CP problem, followed by Section A.2, which presents the Peccei-Quinn solution. The appendix includes derivations and discussions on the QCD vacuum structure, axion model formulations, and the significance of *invisible axion* models such as DFSZ and KSVZ, which allow the axion to interact minimally with Standard Model particles. This appendix thus establishes the basis for subsequent discussions of axions in the main text.

A.1 QCD Axion Genesis

In the following we are gong to introduce the the QCD axion through the strong CP problem and the Peccei-Quinn solution.

A.1.1 θ-term of QCD and the strong CP problem

Quantum chromodynamics is a SM sector defined as a SU(3) gauge theory sufficient to explain the known interactions between quarks and gluons [332,333]. One can argue that, as in every Yang-Mills theory, QCD generically breaks CP symmetry via the so called θ-term [334,335]. More specifically, when imposing local gauge symmetries, global symmetries and the particle content, the sum of all renormalizable hermitian operators that can be constructed under such frame should be included in the Lagrangian of the theory. The θ-term in QCD, $\sim \theta G\tilde{G}$, where G is the gluon field strength tensor, is invariant under all the SM gauge symmetries, since G and $\tilde{G}$ transform in the adjoint representation of SU(3). Therefore, the complete QCD Lagrangian reads as,

$$\mathcal{L}_{QCD} = -\frac{1}{2}\mathrm{Tr}G_{\mu\nu}G^{\mu\nu} + \overline{q}(i\not{D} - M_q)q + \theta\frac{g_s}{16\pi^2}\mathrm{Tr}G_{\mu\nu}\tilde{G}^{\mu\nu}, \tag{A.1}$$

where $G_{\mu\nu} = G^a_{\mu\nu}T^a$, q are the quark fields, D is the covariant derivative, M_q are the quark masses, g_s is the strong coupling constant and $\tilde{G}_{\mu\nu} = \epsilon_{\mu\nu\rho\sigma}G^{\rho\sigma}/2$.

The θ-term is also consistent with the vacuum structure of QCD [336, 337]. The baseline lays in the field equations in Euclidean space,

$$D_\mu G_{\mu\nu} = 0. \tag{A.2}$$

To find solutions with finite action, the field strength needs to tend to zero at infinity so the gauge fields asymptotically approach to a pure gauge. This solutions are called instantons, and have been widely studied since the 1970's [338–340]. The boundary condition satisfying the above requirement is

$$E \propto \frac{1}{2}\int d^4x \mathrm{Tr} G_{\mu\nu}\tilde{G}_{\mu\nu} \geq 8\pi^2|q|, \tag{A.3}$$

where q is the Pontryagain index or winding number. The minimum for the energy above happens for self-dual (or anti-self-dual) Yang-Mills configurations $G_{\mu\nu} = \tilde{G}_{\mu\nu}$, (or $G_{\mu\nu} = -\tilde{G}_{\mu\nu}$). Attempting to solve this configurations in a simple way implies imposing a spherically symmetric Ansatz, [337],

$$\mathcal{A}_\mu = \frac{ir^2}{r^2+\rho^2} g^{-1}(x)\partial_\mu g(x), \tag{A.4}$$

$$G_{\mu\nu} = \frac{4\rho^2}{(r^2+\rho^2)^2}\sigma_{\mu\nu}, \tag{A.5}$$

where $g(x) = -(i/r)x_\mu\sigma_\mu$ and $\sigma_{ab} = \frac{1}{4i}[\sigma_a, \sigma_b]$. As shown in eq. (A.5), the field strength tensor vanishes as $r \to \infty$, this corresponds to the BPST instanton solution that carries winding number $q = 1$ (or $q = -1$). The instanton solution depends strongly on the choice of the matrix $g(x)$. In particular, if the matrix $g(x)$ is the identity, one finds the trivial solution $\mathcal{A}_\mu = 0$ which is the classical vacuum carrying $q = 0$. In general, each vacuum can be classified by its Pontryagain index so that the $|n\rangle$ configuration has index $q = n$.

To construct a proper vacuum, a linear combination of vacua is considered, $\Psi(\mathcal{A})$[1] [341,342]. For a transformation , T_1, (where T_n, denote the gauge transformations corresponding to the n homotopy class), the observables remain invariable. In particular, it commutes with the Hamiltonian and has an eigenvalue $e^{-i\theta}$, so that,

$$T_n\Psi(\mathcal{A}) = (T_1)^n\Psi(\mathcal{A}) = e^{-in\theta}\Psi(\mathcal{A}), \tag{A.6}$$

where $T_1|n\rangle = |n+1\rangle$. Now, in the above formulation one can see that the transformations $T_0, T_1, \ldots T_n$ do not bring $\Psi(\mathcal{A})$ into another vacuum, and that such vacuum is characterized by one eigenvalue θ of T_1, therefore,

$$\Psi(\mathcal{A}) = \sum_{n=-\infty}^{\infty} e^{in\theta+i\alpha}|n\rangle. \tag{A.7}$$

[1] When a vacuum $|n\rangle$ is considered and a transformation T_1 is applied, the vacuum changes. This is because the vacuum is not invariant under all possible gauge transformations and therefore the vacuum is not properly defined.

The θ vacuum is usually defined with $\alpha = 0$, and its importance lays in the fact that the θ angle is an observable parameter. To investigate its properties and the physical consequences, we can write down the transition amplitude between θ vacua as [343],

$$\langle\theta^{'}|e^{-Ht}|\theta\rangle = \delta(\theta^{'} - \theta)\int[d\mathcal{A}_\mu]\exp\left(-\int d^4x(\mathcal{L} + \mathcal{L}_\theta)\right), \tag{A.8}$$

where $\mathcal{A}_\mu$ are pure gauge fields and $\mathcal{L}_\theta = i\theta q$. In Minkowski space the effective interaction is,

$$\mathcal{L}_\theta = \theta q = \theta\frac{g_s^2}{32\pi^2}G^{a,\mu\nu}\tilde{G}^a_{\mu\nu}. \tag{A.9}$$

The above term is a total divergence, but since the contribution to the action from this term is coming from the instanton solutions, it cannot be neglected. This also states that any physical consequence of the θ-term are caused by non-perturbative effects. Another important remark on this term is that $G\tilde{G}$ is a pseudo-tensor of rank 0 in 4- dimensional space-time, so it changes the sign for the reflection of one coordinate. For $\theta \neq 0, \pi$ it violates P and T invariance,

$$G^{a,\mu\nu}\tilde{G}^a_{\mu\nu} \sim \vec{E}\cdot\vec{B} \xrightarrow{CP} \vec{E}\cdot(-\vec{B}) \sim -G^{a,\mu\nu}\tilde{G}^a_{\mu\nu}. \tag{A.10}$$

By the CPT theorem , it violates CP invariance. Such effect coming from eq. (A.9) are expected to be large except for very small values of θ. To have an estimate of θ, one can take a look to the electric dipole moment of the neutron (nEDM), d_n. The upper bound of d_n [125, 344–347] is currently,

$$|d_n| < 1.8\times10^{-26}e.\text{cm}. \tag{A.11}$$

which corresponds to a θ [126, 337],

$$\theta < 10^{-10}. \tag{A.12}$$

The estimation of the θ-term is both significant and puzzling, as all dimensionless parameters, including θ, are expected to be of order one. In fact, up until now, all other parameters have been of this order. This raises a naturalness problem, which leads to the so-called CP problem.

The effective interaction $\mathcal{L}_\theta$ has been studied within the context of massless quarks. However, in a more realistic scenario where quarks have mass, they also contribute to the θ-term. It is important to note that the value of θ can only be constrained when all quarks are massive; otherwise, the term remains unobservable. To explore this further, let us look into a Lagrangian that includes massive quarks and strong interactions,

$$\mathcal{L} = -\frac{1}{2}\text{Tr}G_{\mu\nu}G^{\mu\nu} + \overline{\psi}(i\not{D} + m_q)\psi. \tag{A.13}$$

When performing a chiral transformation, the mass term picks up a phase, $\psi_L \to e^{i\theta_q/2}\psi_L$, $\psi_R \to e^{-i\theta_q/2}\psi_R$. Moreover, the Lagrangian gets and additional topological term since the fermionic path integral is not invariant,

$$\mathcal{L} = -\frac{1}{2}\text{Tr}G_{\mu\nu}G^{\mu\nu} + \overline{\psi}(i\not{D} + m_q e^{i\theta_q})\psi - \theta_q\frac{g_s^2}{16\pi^2}\text{Tr}G_{\mu\nu}\tilde{G}^{\mu\nu}. \tag{A.14}$$

The Lagrangian ends up with a contribution to the $G\tilde{G}$ term due to the anomalous character of the transformation performed [127]. Now, the physical relevant parameter should included not only the irremovable phases in the quark mass matrix caused by the changing neutral currents, but the full electroweak sector of the SM, so that,

$$\overline{\theta} = \theta + \text{ArgDet } M_q, \tag{A.15}$$

implying that $\overline{\theta} < 2.5 \times 10^{-10}$ to explain the nEDM. [124–127].

A.2 Peccei-Quinn solution

There are a catalog of different possible solutions to the CP problem, one of the simplest is just considering vanishing quark masses, [348]. Nevertheless, in terms of the ratio between the lightest quarks making a zero mass up quark is rather improbable.

The most accepted method so far for explaining the smallness of $\overline{\theta}$, was provided by Peccei and Quinn in 1977 [121, 132]. Their idea was to consider a dynamical $\overline{\theta}$ parameter which eventually should settle in a CP conserving state. To achieve this, they demonstrated that if an extended QCD Lagrangian includes an axial $U(1)PQ$ (Peccei-Quinn) symmetry, which is broken by an axial anomaly, CP conservation can be satisfied. However, to make $\overline{\theta}$ dynamical, additional fields and degrees of freedom must be introduced beyond the Standard Model. A straightforward extension involves adding a complex scalar field that spontaneously breaks the $U(1)PQ$ symmetry by acquiring a vacuum expectation value. The formal formulation would be to consider the new field acting as another Higgs doublet, and so, one chooses a potential for the Higgs fields such as the Lagrangian is symmetrical under chiral rotations of the quark fields and introduces a shift to the vacuum angle to have a true symmetrical description, $\theta = \theta - \theta_q$. After the breaking of both, electroweak symmetry and Peccei-Quinn symmetry, the neutral components of the Higgs doublets acquire their vevs and the phases become Nambu-Goldstons. The surviving combination becomes a massless field, called the axion ϕ, which has a remaining shift symmetry, $\phi \to \phi + 2\pi n f_\phi$. For such field, the kinetic term and the interaction,

$$\mathcal{L} = \frac{1}{2}(\partial_\mu \phi)(\partial^\mu \phi) - \frac{g_s^2}{16\pi^2}\left(\overline{\theta} + \frac{\phi}{f_\phi}\right) \text{Tr} G_{\mu\nu}\tilde{G}^{\mu\nu}. \tag{A.16}$$

Is important to notice that the axion-gluon coupling is model independent. Removing the axion-quark coupling more interactions can arise like the axion-photon term. As state before, $\overline{\theta}$ eventually should settle in a CP conserving state. The Vafa and Witten theorem states that with no more sources of CP violation, the QCD vacuum energy is minimized at a CP symmetric state. The potential could be written using non perturbative effects of QCD[2] as,

$$V_{inst}(\phi) = m_\pi^2 f_\pi^2 \frac{m_u m_d}{(m_u^2 + m_d^2)}\left[1 - \cos\left(\frac{\phi}{f_\phi}\right)\right]. \tag{A.17}$$

[2] One can also derive the potential in chiral perturbation theory.

The prediction for th axion mass is then [133, 139],

$$m_\phi^2 = \left.\frac{\partial^2 V}{\partial \phi^2}\right|_{min} = \frac{m_\pi^2 f_\pi^2}{f_\phi^2}\frac{m_u m_d}{(m_u + m_d)^2} \tag{A.18}$$

The axion potential can also be written in terms of the topological susceptibility of QCD, leading to
,

$$m_\phi(T) = \frac{\sqrt{\chi_{\rm QCD}(T)}}{f_\phi}. \tag{A.19}$$

The original Peccei-Quinn model features an f_ϕ of the order of the electroweak scale, resulting in heavy axions and strong couplings to the Standard Model, which were soon ruled out. However, by adding additional degrees of freedom to this model, it is possible to produce light axions with very weak interactions, leading to the so-called invisible axion models. This approach is realized in the DFSZ [349] and KSVZ models [350].

The mechanism for solving the CP problem, opens up also some experimental possibilities to probe axions. For instance, is of our interest the coupling of axions to the neutron electric dipole moment and the axion to photon coupling, which we will study more closely in Sec 2.1.3.

Appendix B

Experimental Axion Searches

This appendix provides a detailed derivation of the equations and formalism necessary for modeling axion field interactions with electromagnetic cavities, specifically in the context where we have used axion miniclusters (AMCs).

The first section B.1, derives the theoretical model for axion field interactions with cavity modes, treating the axion field as a Gaussian random field. This section lays the groundwork for understanding how axions couple to electromagnetic fields. Here, a simplified calculation of mode coefficients and spectral power densities under the assumption of small cavity sizes is also provided, giving a practical approach to detecting axion signals. Section B.2, introduces a random phase model for the density fluctuations of axion miniclusters. Finally, the section B.3,calculates the spectral power resulting from the interaction of axions with electromagnetic cavities, incorporating the properties of AMCs.

B.1 Extraction Information on the Axion Field in a Rectangular Cavity

B.1.1 Axion Field as a Gaussian Random Field

If the axion field is a Gaussian random field, we can rewrite it in terms of a random phase,

$$a(\boldsymbol{k}) = n(\boldsymbol{k}) e^{i\phi_{\boldsymbol{k}}}. \tag{B.1}$$

From the last section we can calculate the spectrum density of the TE_{101} mode on the resonant frequency.
By definition,

$$\begin{aligned}
\boldsymbol{E}_{101} &= E_y(x,z)\boldsymbol{e_y}, \\
E_y(x,z) &= \frac{\pi}{2\sqrt{L_x L_y L_z}} \sin\left(\frac{\pi x}{L_x}\right) \sin\left(\frac{\pi z}{L_z}\right), \\
\omega_{101} &= \sqrt{\left(\frac{\pi}{L_x}\right)^2 + \left(\frac{\pi}{L_z}\right)^2},
\end{aligned} \tag{B.2}$$

with L_i the length of the cavity in the x, y, z direction.
With that the geometric factor is ,

$$\mathcal{G}_{101}(\boldsymbol{k}) = gB_y \frac{\pi}{2\sqrt{L_x L_y L_z}} \int_0^{L_x} dx \sin\left(\frac{\pi x}{L_x}\right) e^{-ik_x x} \int_0^{L_y} dy e^{-ik_y y} \int_0^{L_z} dz \sin\left(\frac{\pi z}{L_z}\right) e^{-ik_z z}$$
$$\mathcal{G}^*_{101}(\boldsymbol{k}) = gB_y \frac{\pi}{2\sqrt{L_x L_y L_z}} \int_0^{L_x} dx \sin\left(\frac{\pi x}{L_x}\right) e^{ik_x x} \int_0^{L_y} dy e^{ik_y y} \int_0^{L_z} dz \sin\left(\frac{\pi z}{L_z}\right) e^{ik_z z} \tag{B.3}$$

Using that result we can calculate the coefficient of this mode as,

$$\alpha_{101}(t) = \int \frac{d^3k}{(2\pi)^3} \left(a(\boldsymbol{k}) \omega^2(\boldsymbol{k}) \frac{\mathcal{G}_{101}(\boldsymbol{k})}{(\omega_{101}^2 - \omega(\boldsymbol{k})^2)} e^{i\omega(\boldsymbol{k})t} + c.c. \right), \tag{B.4}$$

Integrating this last expression over $\int dt\, e^{-i\omega t}$ to get the time Fourier transform. Only the first term in the parenthesis will be kept. Indeed each terms will lead to a delta function, the first one to $\delta(\omega(\boldsymbol{k}) - \omega)$ and the second to $\delta(\omega(\boldsymbol{k}) + \omega)$. The first delta therefore impose $\omega(\boldsymbol{k}) = \omega$ and the second $\omega(\boldsymbol{k}) = -\omega$. If we are looking for positive ω, the second term cancels.

$$\alpha_{101}(\omega) = \frac{\omega^2}{(\omega_{101}^2 - \omega^2)} \int \frac{d^3k}{(2\pi)^3} a(\boldsymbol{k})\, \mathcal{G}_{101}(\boldsymbol{k})\, \delta(\omega(\boldsymbol{k}) - \omega). \tag{B.5}$$

Let's finally add the quality factor $\mathcal{Q}$ of the cavity

$$\alpha_{101}(\omega) = \frac{\omega^2}{(\omega_{101}^2 - \omega^2 - i\frac{\omega_{101}\omega}{\mathcal{Q}})} \int \frac{d^3k}{(2\pi)^3} a(\boldsymbol{k})\, \mathcal{G}_{101}(\boldsymbol{k})\, \delta(\omega(\boldsymbol{k}) - \omega), \tag{B.6}$$

such that at the frequency ω_{101}, the signal is resonant and it leads to

$$\alpha_{101}(\omega_{101}) = iQ \int \frac{d^3k}{(2\pi)^3} a(\boldsymbol{k})\, \mathcal{G}_{101}(\boldsymbol{k})\, \delta(\omega(\boldsymbol{k}) - \omega_{101}), \tag{B.7}$$

Small Cavity

Assuming that the cavity is small enough such that the axion field is constant inside it, the geometric factor will be constant and given by,

$$\mathcal{G}_{101} = gB_y \frac{2}{\pi} \sqrt{L_x L_y L_z}. \tag{B.8}$$

The mode coefficient at resonance will be,

$$\alpha_{101}(\omega_{101}) = gQB_y \frac{2}{\pi} \sqrt{L_x L_y L_z} \int \frac{d^3k}{(2\pi)^3} a(\boldsymbol{k})\, \delta(\omega(\boldsymbol{k}) - \omega_{101}). \tag{B.9}$$

Using the random phases encoded inside $a(\boldsymbol{k})$, we can calculate the averaged value of the spectral power density of the photon signal as,

$$\begin{aligned} S(\omega_{101}) &= |\alpha_{101}(\omega_{101})|^2, \\ &= g^2 \mathcal{Q}^2 B_y^2 \frac{4V}{\pi^2} \int \frac{d^3k}{(2\pi)^3} |n(\boldsymbol{k})|^2\, \delta(\omega(\boldsymbol{k}) - \omega_{101}), \\ &= g^2 \mathcal{Q}^2 B_y^2 \frac{4V}{\pi^2} |n(\omega_{101})|^2. \end{aligned} \tag{B.10}$$

As expected, in such a case, no directional information could be extracted from the SPD $S(\omega_{101})$.

B.2 General Formalism and Random Phase Model For axion miniclusters

In the non-relativistic and low-density regime, axions are effectively described by the Schrödinger equation. Specifically, for self-gravitating systems of moderate density, such as Axion Miniclusters (AMCs), the dynamics are governed by a complex scalar field $\psi(\boldsymbol{x}, t)$ obeying the Schroedinger-Poisson (SP) equations [211],

$$\begin{aligned} i\partial_t\psi &= -\frac{\nabla^2}{2m_a}\psi + m_a\phi\psi, \\ \nabla^2\phi &= 4\pi G m_a|\psi|^2 = 4\pi G\rho, \end{aligned} \tag{B.11}$$

where ϕ is the gravitational potential and m_a the axion mass. The density in the non-relativistic approximation of the axion field is $\rho = m_a|\psi|^2$.

Importantly, the typical de Broglie wavelength is expected to exceed the inter-particle separation usually by a significant margin. In other words, the typical occupation numbers are very large such that ψ can be viewed as a classical field describing a large number of axions [80, 163].

This equation has been solved extensively with numerical simulations [351–355]. However, analytical approximations have been developed to reduce the computational cost while still retaining a good description of the system [204, 211, 212, 226, 356]. One approach [204, 211–213] is to decompose the wave function into energy eigenmodes of the Schroedinger equation,

$$\begin{aligned} \psi(\boldsymbol{x}, t) &= \sum_i a_i\psi_i(\boldsymbol{x})e^{-iE_it}, \\ \left(-\frac{\nabla^2}{2m_a} + m_a\phi(\boldsymbol{x})\right)\psi_i(\boldsymbol{x}) &= E_i\psi_i(\boldsymbol{x}), \end{aligned} \tag{B.12}$$

where ψ_i are the modes with E_i their corresponding energy. The coefficients a_i are complex and can be found by solving the Poisson equation,

$$\begin{aligned} \nabla^2\phi(\boldsymbol{x}) &= 4\pi G m_a|\psi(\boldsymbol{x}, t)|^2 \\ &= 4\pi G m_a\sum_i|a_i|^2|\psi_i(\boldsymbol{x})|^2 + m_a\sum_{i\neq j}a_ia_j^*\psi_i(\boldsymbol{x})\psi_j^*(\boldsymbol{x})e^{-i(E_i-E_j)t}. \end{aligned} \tag{B.13}$$

The interference between different modes on the right hand side of Eq. (B.13) is time dependent. This makes it difficult to solve the Poisson equation. To overcome this issue, one usually assumes that each coefficient a_i, carries a different random phase [211]. As a simplification, we can solve the Poisson equation on average to obtain a fully time-independent system,

$$\begin{aligned} \left(-\frac{\nabla^2}{2m_a} + m_a\phi(\boldsymbol{x})\right)\psi_i(\boldsymbol{x}) &= E_i\psi_i(\boldsymbol{x}), \\ \nabla^2\phi(\boldsymbol{x}) = 4\pi G m_a\langle|\psi(\boldsymbol{x}, t)|^2\rangle &= 4\pi G m_a\sum_i|a_i|^2|\psi_i(\boldsymbol{x})|^2. \end{aligned} \tag{B.14}$$

The average performed is an ensemble average. In this sense, an individual minicluster will still carry a density featuring (time-dependent) fluctuations due to the interference terms,

$$\rho = m_a|\psi(\boldsymbol{x}, t)|^2 = m_a\sum_i|a_i|^2|\psi_i(\boldsymbol{x})|^2 + m_a\sum_{i\neq j}a_ia_j^*\psi_i(\boldsymbol{x})\psi_j^*(\boldsymbol{x})e^{-i(E_i-E_j)t}, \tag{B.15}$$

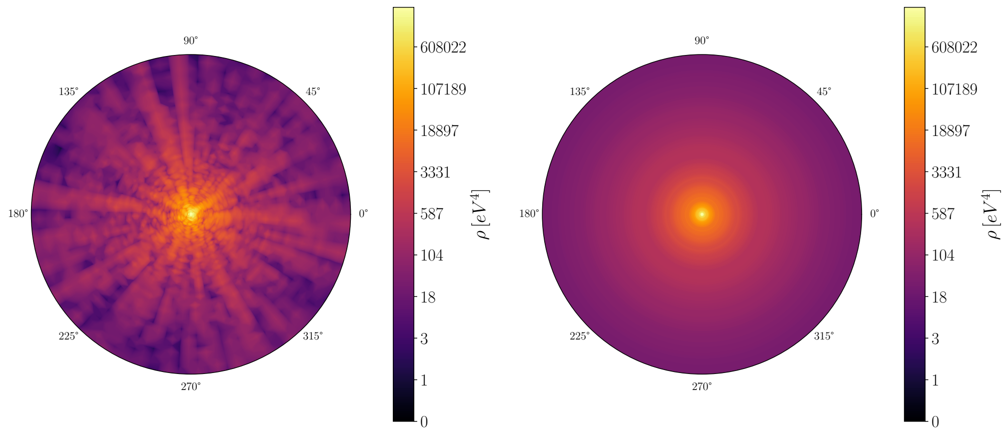

Figure B.1. *Left*: Single realization of the density profile of an NFW [23] AMC with mass $M = 10^{-13}\,M_\odot$, radius $R = 10^{-8}$ pc and concentration $c = 10$. *Right*: Density profile averaged over the random phases. Note that the radial features in the left panel are numerical artifacts. Increasing the grid as well as the number of angular momentum modes is expected to remove them but also drastically increases the computational effort required.

where the fluctuations in the AMC density profile appear in the second term of the right hand side. These "granules" have a characteristic length scale of the order of the de Broglie wavelength,

$$\ell_{\text{gran}} \sim \lambda_{\text{dB}} \sim 1/(m_a v), \tag{B.16}$$

and a characteristic time scale

$$T_{\text{gran.}} \sim 1/(m_a v^2), \tag{B.17}$$

where v is the typical velocity dispersion of the cluster [208–210]. An example of a realization obtained by selecting random phases is shown in Fig. B.1 and clearly shows this non-uniform nature. Such features are also observed in numerical simulations [353, 357, 358].

For our purposes the granules are important, because they correspond to fluctuations in the density that limit the precision with which the coupling can be measured, cf. Sec. 3.3.1.

B.3 Axion minicluster Power Spectral Density

In this appendix, we derive the spectral power for the axion field given in Eq. (3.33). We start by solving the differential equation (3.47) for the electric field amplitude $\alpha_j(t)$ and then calculate its discrete Fourier transform for a measurement period T. We follow the same steps as in Refs. [225, 226] to obtain the spectral power,

$$
\begin{aligned}
S(\omega_d) &= \frac{(\Delta t)^2}{T} |\sum_{nlm} C_{nlm} \sum_{n=0}^{N_T-1} e^{i\omega_d n\Delta t} \left(a_{nlm}\psi_{nlm}(\boldsymbol{x}) e^{-i\omega_{nlm} n\Delta t} + c.c.\right)|^2, \\
&= \frac{1}{T} |\sum_{nlm} C_{nlm} \sum_{n=0}^{N_T-1} \Delta t\, e^{i\omega_d n\Delta t} \left(a_{nlm}\psi_{nlm}(\boldsymbol{x}) e^{-i\omega_{nlm} n\Delta t} + c.c.\right)|^2, \\
&\approx \frac{1}{T} |\sum_{nlm} C_{nlm} \int_{-T/2}^{T/2} dt\, e^{i\omega_d t} \left(a_{nlm}\psi_{nlm}(\boldsymbol{x}) e^{-i\omega_{nlm} t} + c.c.\right)|^2,
\end{aligned}
\tag{B.18}
$$

where $\Delta t = T/N_T$ and we have introduced the coefficients C_{nlm} as

$$
C_{nlm} = \sqrt{(g_{a\gamma\gamma}B_0)^2\, \mathcal{G}_j\, V} \frac{\omega_{nlm}^2}{\sqrt{2m_a}\left(\omega_j^2 - \omega_{nlm}^2 - i\omega_j\omega_{nlm}/Q\right)}. \tag{B.19}
$$

In this last equation, $\mathcal{G}_j$ is the usual form factor and is of the order $\mathcal{O}(1)$, V is the cavity volume and ω_{nlm} is the mode energy. Note that the wave functions $\psi_{nlm}(\boldsymbol{x})$ depend on the location $\boldsymbol{x}$ (in a frame centered at the origin of the cluster) at which we are doing the measurement in the cluster. We assumed in the main text that the cluster is moving slowly enough so that its motion is neglected during the measurement period T.

The time integral can be solved easily by noting that

$$
\frac{1}{T}\int_{-T/2}^{T/2} dt e^{i\omega_d t} e^{-i\omega_{nlm} t} = \text{sinc}\left((\omega_{nlm} - \omega_d)\,\frac{T}{2}\right). \tag{B.20}
$$

With this, Eq. (B.26) becomes,

$$
S(\omega_d) \approx T |\sum_{nlm} C_{nlm} a_{nlm} \psi_{nlm}(\boldsymbol{x})\, \text{sinc}\left((\omega_{nlm} - \omega_d)\,\frac{T}{2}\right)|^2. \tag{B.21}
$$

The average value of the power spectral density is obtained by taking the average over the random phases, leading to,

$$
\begin{aligned}
\bar{S}(\omega_d) &= T \langle |\sum_{nlm} C_{nlm} a_{nlm} \psi_{nlm}(\boldsymbol{x})\, \text{sinc}\left((\omega_{nlm} - \omega_d)\,\frac{T}{2}\right)|^2 \rangle, \\
&= T \sum_{nlm} |C_{nlm} a_{nlm} \psi_{nlm}(\boldsymbol{x})|^2\, \text{sinc}^2\left((\omega_{nlm} - \omega_d)\,\frac{T}{2}\right).
\end{aligned}
\tag{B.22}
$$

With the definition of the coefficients a_{nlm} given in Eq. (3.35), we get

$$
\bar{S}(\omega_d) = 4\pi m_a T \int dE\, f(E) |C(E)|^2 \sqrt{(2m_a\,(E - m_a\phi(r)))}\, \text{sinc}^2\left((E + m_a + \omega_{\text{amc}} - \omega_d)\,\frac{T}{2}\right), \tag{B.23}
$$

where with the use of the density of states $g(E)$, we have transformed the sum into an integral such that in the continuous limit,

$$
C(E) = \sqrt{(g_{a\gamma\gamma}B_0)^2\, \mathcal{G}_j\, V} \frac{(E + m_a + \omega_{\text{amc}})^2}{\sqrt{2m_a}\left(\omega_j^2 - (E + m_a + \omega_{\text{amc}})^2 - i\omega_j\,(E + m_a + \omega_{\text{amc}})\,/Q\right)}. \tag{B.24}
$$

However, the energy distribution function obtained in Sec. 3.2.2 is valid in a frame located at the center of the cluster. Since we are here analyzing the signal in the laboratory frame, the minicluster velocity should be carefully subtracted when the energy is defined. Interpreting Eq. (B.23) in a particle picture, we have that the velocities would be shifted as $\boldsymbol{v} \to \boldsymbol{v} + \boldsymbol{v_c}$, where $\boldsymbol{v_c}$ is the cluster velocity. With this, Eq. (B.23) becomes,

$$\begin{aligned}\bar{S}(\omega_d) &= m_a^3 T \int d^3\tilde{\boldsymbol{v}}\, f(|\,\tilde{\boldsymbol{v}} - \boldsymbol{v_c}\,|)|C(|\,\tilde{\boldsymbol{v}} - \boldsymbol{v_c}\,|)|^2 \,\mathrm{sinc}^2\left(\left(m_a + m_a\phi(r) + m_a\tilde{v}^2/2 - \omega_d\right)\frac{T}{2}\right), \\ &= m_a^3 T \int d\Omega \int_{v\in[0,\sqrt{-2\phi(r)}]} d\tilde{v}\,\tilde{v}^2\, f(|\,\tilde{\boldsymbol{v}} - \boldsymbol{v_c}\,|)|C(|\,\tilde{\boldsymbol{v}} - \boldsymbol{v_c}\,|)|^2 \\ &\qquad\qquad \times \mathrm{sinc}^2\left(\left(m_a + m_a\phi(r) + m_a\tilde{v}^2/2 - \omega_d\right)\frac{T}{2}\right),\end{aligned} \tag{B.25}$$

where we define $\tilde{\boldsymbol{v}} = \boldsymbol{v} + \boldsymbol{v_c}$ and express the distribution $f(E)$ as a function of the velocity rather than the energy, $E = m_a + m_a\phi(r) + m_a v^2/2$, and include an appropriate transformation of the integration measure. Finally, the integral runs only over laboratory velocities that return velocity in the cluster frame smaller than the escape velocities $v_{\text{max}} = \sqrt{-2\phi(r)}$.
A further simplification can be made if we assume that the distribution function $f(v)$ is constant over the width of the sinc. In this limit,

$$\begin{aligned}\bar{S}(\omega_d) = 4\pi^2 m_a^2 \tilde{v}_d \int d\theta \sin(\theta)\, f(\tilde{v}_d^2 + v_c^2 - 2\tilde{v}_d v_c\cos(\theta))|C(\tilde{v}_d^2 + v_c^2 - 2\tilde{v}_d v_c\cos(\theta))|^2 \\ \times \Theta\left(\sqrt{-2\phi(r)} - (\tilde{v}_d^2 + v_c^2 - 2\tilde{v}_d v_c\cos(\theta))\right)\Theta\left(\tilde{v}_d^2 + v_c^2 - 2\tilde{v}_d v_c\cos(\theta)\right),\end{aligned} \tag{B.26}$$

where the velocity $\tilde{v}_d$ returns an energy ω_d, $\tilde{v}_d = \sqrt{2/m_a\,(\omega_d - m_a\phi(r) - m_a)}$, θ is the angle between $\tilde{\boldsymbol{v}}_d$ and $\boldsymbol{v_c}$ and the Heaviside functions ensure that no velocity exceeds the escape velocity.

While the final angular integral typically requires numerical evaluation, the key characteristics of the spectrum can still be deduced. The presence of Heaviside functions clearly indicates that the signal will be centered around the kinetic energy of the cluster, $\omega_d = m_a v_c^2/2$. Furthermore, the signal will be contained in the frequency range,

$$\frac{m_a}{2}v_c^2 + m_a - m_a\sqrt{-2\phi(r)}v_c \leq \omega_d \leq \frac{m_a}{2}v_c^2 + m_a + m_a\sqrt{-2\phi(r)}v_c. \tag{B.27}$$

Appendix C

Effects of Measurements on the Quantum State

This appendix explores the impact of different measurement procedures on the quantum state and its subsequent evolution, particularly in the context of systems like those studied in CASPEr experiments. The goal is to complement the main discussion by collecting a couple of examples and remarks on the influence of the measurement process on the system and its time evolution after the measurement.

In section C.1.1, discusses the effects of a full measurement of the spin in a given direction. This section highlights how such a measurement can disrupt the system's state, pushing it away from an energy eigenstate and leading to observable spin oscillations. It also examines how the expectation value of the spin behaves after the measurement, showing that classical-like evolution may not be immediately evident. Finally section C.1.2, introduces the concept of weak or non-demolition measurements, which have less destructive effects on the system's state. This section shows how these measurements still induce oscillations in the spin expectation value, albeit at smaller amplitudes. It emphasizes the difficulty in obtaining a classical-like evolution for the system, even under weak measurements.

C.1 Comments on effects of measurements on the state

Very generally, measuring the spin in the x- or y-direction, as done in an experiment like CASPEr, affects the state of the system [2]. This is evident from the non-vanishing commutator

$$[H, S_y] = im_a S_x + 2\omega_c S_z(a^\dagger + a), \tag{C.1}$$

that ensures that simultaneous eigenstates do not exist. This holds even in the absence of interactions $\sim \omega_c$.

In particular, starting from an energy eigenstate, a measurement typically drives the system into a state that is no longer an energy eigenstate but instead includes contributions from states with energy differences on the order of $\sim m_a = \omega_L$.[1] This scenario already aligns with the conditions required to produce observable spin expectation values oscillating at the frequency ω_L. However, the measurement process alone does not necessarily guarantee that the expectation value of the field exhibits behavior akin to a "close to classical" state.

In the following, we will provide two explicit examples of the side effects of different measurement procedures. Investigating what occurs in a more realistic modeling of the measurement procedure, as implemented in CASPEr, would be an interesting direction for future study but is beyond the scope of the present work.

C.1.1 Complete spin measurement

The most basic way to implement a measurement in quantum mechanics is to perform a full measurement of a Hermitian operator. This process returns an eigenvalue of the operator, and after the measurement, the system collapses into the corresponding eigenstate.

Let us now do this for the simplest case of only one spin. Using the initial state $|N_a, 1, 0\rangle$ we can simply use the result for the time evolved state Eq. (3.115) explicitly writing the state vectors,

$$|\Psi(t)\rangle = \cos\left(\sqrt{N_a}\omega_c t\right)|N_a\rangle \otimes |\uparrow\rangle + i\sin\left(\sqrt{N_a}\omega_c t\right)|N_a - 1\rangle \otimes |\downarrow\rangle\,. \tag{C.2}$$

We can rewrite this into the spin states in the y-direction (or alternatively x-direction) using,

$$\begin{aligned} |\uparrow\rangle &= \frac{1}{\sqrt{2}}(|\rightarrow\rangle + |\leftarrow\rangle) \\ |\downarrow\rangle &= -\frac{i}{\sqrt{2}}(|\rightarrow\rangle - |\leftarrow\rangle) \end{aligned} \tag{C.3}$$

such that

$$\begin{aligned} |\Psi(t)\rangle = &\frac{1}{\sqrt{2}}(\cos\left(\sqrt{N_a}\omega_c t\right)|N_a\rangle + \sin\left(\sqrt{N_a}\omega_c t\right)|N_a - 1\rangle) \otimes |\rightarrow\rangle \\ &+ \frac{1}{\sqrt{2}}(\cos\left(\sqrt{N_a}\omega_c t\right)|N_a\rangle - \sin\left(\sqrt{N_a}\omega_c t\right)|N_a - 1\rangle) \otimes |\leftarrow\rangle. \end{aligned} \tag{C.4}$$

At time t_{meas}, a measurement of the spin in the y-direction is performed. As a result, the system collapses into an eigenstate of the spin operator in the y-direction. For instance, consider the case where the spin is aligned along the positive y-axis. To describe the state after the measurement, we project the system onto this eigenstate using the appropriate projection operator,

$$P_y^{\rightarrow} = |\rightarrow\rangle\langle\rightarrow|. \tag{C.5}$$

This yields

$$P_y^{+}|\Psi(t_{meas})\rangle = \frac{1}{\sqrt{2}}(\cos\left(\sqrt{N_a}\omega_c t_{meas}\right)|N_a, \rightarrow\rangle + \frac{1}{\sqrt{2}}(\sin\left(\sqrt{N_a}\omega_c t_{meas}\right)|N_a - 1, \rightarrow\rangle. \tag{C.6}$$

A simple projection results in a state that is not yet normalized. However, this is straightforward to address since, immediately following the measurement of a spin in the positive direction, there is a

[1]This remains true even in the absence of interactions, i.e., for $\omega_c = 0$.

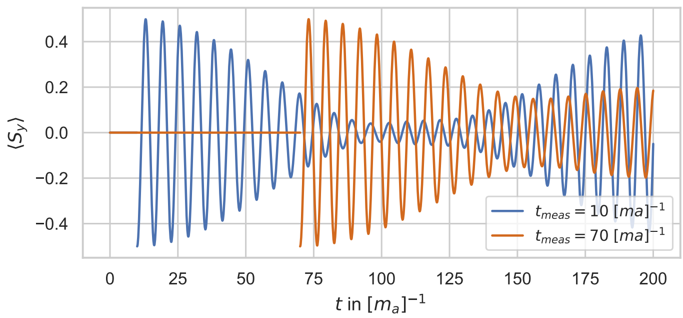

Figure C.1. Evolution of the expectation value in y-direction of the spin before and after the measurement, for $N_s = 1$ and $N_a = 2$. The blue line corresponds to $t_{meas} = 10\,[m_a]^{-1}$ and the orange one to $t_{meas} = 70\,[m_a]^{-1}$.

100% probability of being in this state. Thus, normalization to 1 can be applied directly,

$$\begin{aligned} |\Psi_{\text{new}}\rangle &= \frac{1}{\sqrt{1/2}} P_y^+ |\Psi(t_{meas})\rangle \\ &= (\cos\left(\sqrt{N_a}\omega_c t_{meas}\right) |N_a, \rightarrow\rangle + (\sin\left(\sqrt{N_a}\omega_c t_{meas}\right) |N_a - 1, \rightarrow\rangle. \end{aligned} \tag{C.7}$$

To determine the outcome of subsequent measurements at later times, we can perform a time evolution of the new state $|\Psi_{\text{new}}\rangle$. This involves returning to the original basis to evolve the state forward in time,

$$\begin{aligned} |\Psi_{\text{new}}\rangle = &\frac{1}{\sqrt{2}}(\cos\left(\sqrt{N_a}\omega_c t_{meas}\right) (|N_a, \uparrow\rangle + i|N_a, \downarrow\rangle) \\ &- \frac{i}{\sqrt{2}}(\sin\left(\sqrt{N_a}\omega_c t_{meas}\right) (|N_a - 1, \uparrow\rangle - i|N_a - 1, \downarrow\rangle). \end{aligned} \tag{C.8}$$

At this point, it is clear that the state is not an energy eigenstate of the Hamiltonian without the dipole interaction. Therefore, we expect the system to exhibit non-trivial evolution with the axion/Larmor frequency, as discussed in Sec. 3.4.5. The oscillations can be seen in Fig. C.1 where we plot the time evolution of the spin expectation value following the measurement. This is the positive outcome.

However, as we can also see from Fig. C.1, the magnitude of the initial oscillation is independent of the time of the measurement. This occurs because the measured spin value in the y-direction now corresponds to the expectation value $\langle S_y \rangle$, which (approximately) evolves according to the classical evolution equation. As a result, the axion effect does not immediately influence the initial amplitude of the oscillations in the expectation value.

One might question whether this behavior is specific to the single spin system and the measurement of a non-zero spin in the y-direction. However, even in systems with more than one spin, such a measurement can have undesirable effects. For instance, in the case of an even number of spins, it is possible to measure zero spin in the y-direction. Yet, when considering the subsequent time evolution of the expectation value $\langle S_y \rangle$, the axion effect is still not manifested in the classical sense. The reason for this is that in this case, the expectation value $\langle S_z \rangle$ of the spin in the z-direction vanishes. To support this argument, we found the general discussion of higher spin representations in [359] to

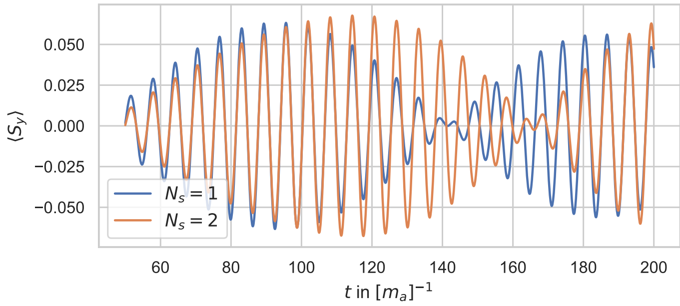

Figure C.2. Time evolution of the expectation value of $\langle S_y \rangle$ after weak measurement (C.9) at time $t_{meas} = 50\,[m_a]^{-1}$ for one (blue line) and two spins (orange line)

be particularly useful. Classically, it is $\langle S_z \rangle$ that governs the leading-order evolution of the spin into the transverse plane.

C.1.2 Weak/Non-demolition Measurement of spin

As we have seen, in the standard approach to measurement, performing a complete measurement of the spin in a particular direction can significantly alter the state during the measurement process. For instance, it can destroy the initial $\langle S_z \rangle$, which would naively drive the classical evolution. As a result, the evolution after such a measurement is often influenced more by the measurement outcome itself than by the axion-induced evolution that occurred prior to the measurement [2].

An alternative is to perform a so-called non-demolition (cf., e.g., [253]) or weak measurement (cf., e.g., [360]) of the spin,

$$|\Psi_{\text{after measurement}}\rangle = e^{-i\epsilon S_y}|\Psi\rangle. \tag{C.9}$$

In Fig. C.2 we plot the time evolution of the expectation value of $\langle S_y \rangle$ after such a weak measurement for an initial energy eigenstate. As noted, a similar problem arises in the multi-spin case as in the single-spin measurement scenario. The measurement induces an oscillation, although smaller, which is not directly associated with the axion effect. This oscillation also appears when a measurement is made immediately after starting the experiment, where the axion effect should be negligible. Even more worryingly, the maximum amplitude of the oscillation is often related to the intensity of the measurement itself.

This problem may be due in part to the performance of a single weak measurement and the use of a small number of spins. However, the two example measurement procedures demonstrate that, when considering only the single expectation value of the field, it is not trivial to achieve a quasi-classical evolution for an energy eigen-state by simply performing spin measurements on the system.

Appendix D

Particle-like Clumpy DM

This appendix explores the methodology and mathematical derivation of power spectral density (PSD) in the context of our study of signals containing overdensities, along with its theoretical background and practical application. Here we also expand on the numerical process we implemented to simulate the detection of single particles and clumps. Specifically, the appendix includes two major parts. First, it presents a detailed analysis of PSD calculation based on a filtered Poisson process. This part enables the quantification of contributions from both homogeneous and clumpy signals, offering insight into their spectral characteristics. We also include a brief overview of the Wiener-Khinchin theorem, a foundational result connecting the autocorrelation function of a signal with its spectral density, which supports the PSD analysis used in this work. Second, the appendix outlines a detailed guide to numerically generate homogeneous detections or backgrounds and how to include localized clumps and superposition of clumps into the signal. We include some insights about the non-parametric test that, at some point, we used to test the null hypothesis when comparing the numerical signals. We added some extra numerical tests to the simulation to distinguish small clumps.

The structure of the appendix is as follows: Section D.1 details the mathematical approach to PSD for mixed-density particle detections, incorporating both homogeneous and structured overdensity contribution to the signals. Section D.2 provides a concise derivation of the Wiener-Khinchin theorem to underscore the theoretical framework behind the spectral analysis. Section D.3 describes the baseline simulation setup for homogeneous particle detections using a Poisson process, specifying the parameters and statistical approach used to generate representative PSD data. In Section D.4, we describe how to include in the numerical simulation overdensities. In Section D.5 we briefly explain how the non-parametric Mann-Whitney U test tests the null hypothesis and, finally, in Section D.6 we include some tests on the simulation when distinguishing small clumps.

D.1 Power spectral density

We adapt the procedure for filter Poisson process described Ref. [279], to describe the process involving over-densities as $\eta_{\hat{K}}(t) = \eta_{H,K}(t) + \eta_{O,K'}(t)$, where $\eta_{H,K}(t)$ describe the signal coming form particles distributed homogeneously and $\eta_{O,K'}(t)$ describe the small structure.

Following (4.1.2), we can treat each process separately and sum up afterwards.

For $\eta_{H,K}(t)$: We can consider the homogeneous solution as the sum over the amplitudes without describing time,

$$\eta_{H,K}(t) = \sum_{k=1}^{K} A_k(t), \tag{D.1}$$

where $A_k(t)$ is also described by eq. (4.3). To have find the contribution of this process to the power spectral density we perform the Fourier transform as follows,

$$\mathcal{F}_T[\eta_{H,K}(t)](\omega) = \frac{1}{\sqrt{T}} \int_0^T dt \sum_{k=1}^{K} A_k e^{-i\omega t}, \tag{D.2}$$

multiplying for its complex conjugate and averaging over all random variables,

$$|\mathcal{F}_T[\eta_{H,K}(t)](\omega)|^2 = \frac{1}{T} \int_0^T dt_l \int_0^T dt_m \sum_{l=1}^{K} \sum_{m=1}^{K} A_l A_m e^{-i\omega(t_m - t_l)}, \tag{D.3}$$

solving the amplitude squared, we get,

$$\begin{aligned} |\mathcal{F}_T[\eta_{H,K}(t)](\omega)|^2 &= \frac{1}{T\omega^2} \sum_{l=1}^{K} \sum_{m=1}^{K} A_l A_m \left(e^{i\omega t}\right)_0^T \left(e^{-i\omega t'}\right)_0^T \\ &= \frac{2}{T\omega^2} \sum_{l=1}^{K} \sum_{m=1}^{K} A_l A_m (1 - \cos(\omega T)), \end{aligned} \tag{D.4}$$

therefore,

$$\langle |\mathcal{F}_T[\eta_{H,K}(t)](\omega)|^2 \rangle = \frac{2\langle A \rangle^2}{T\omega^2} (1 - \cos(\omega T)). \tag{D.5}$$

The second term in the equation above resembles a Delta function taking the limit,

$$\begin{aligned} \lim_{T\to\infty} \langle |\mathcal{F}_T[\eta_{H,K}(t)](\omega)|^2 \rangle &= 2\langle A \rangle^2 \lim_{T\to\infty} \frac{(1 - \cos(\omega T))}{T\omega^2} \\ &= 2\langle A \rangle^2 \pi \delta(\omega). \end{aligned} \tag{D.6}$$

With normalization, $\int_{-\infty}^{\infty} d\omega \delta(\omega) = 1$.

For $\eta_{O,K'}(t)$:

$$\eta_{O,K'}(t) = \sum_{k'=1}^{K'(T)} B_{k'} \psi\left(t - ik'\omega_o t\right), \tag{D.7}$$

holding the condition $\tau_d = 1$, where $B_{k'}$ is the amplitude of the over density also following an exponential function and t is now random and represents the times in which each clump arrives. We hold the structure of the homogeneous case but we need to make additional considerations. For instance, the over densities are introduced into the process by a period that depends on a random factor so it does not occurs always. This randomness is modeled by a binomial distribution that will measure the arrivals of the clumps given a probability of success p and a number of attempts $n = \text{int}(T/T_o)$, defined as the total length of the signal over period of the over densities. Therefore, the intermittent parameter $\gamma^{'} = \tau_d/\tau w^{'} = 1/(n(1-p))$.

Even though $t_{k'}$ is in this case a random variable it is described with by a Bionomial distribution, so the process described in eq. (4.4) holds. Therefore we can write,

$$\mathcal{F}_T[\eta_{O,k'}(t)](\omega) = \int_{-\infty}^{\infty} ds'\Theta(s')e^{-i\frac{2\pi}{T_o}s'+s'}e^{-i\omega s'}\frac{1}{\sqrt{T}}\int_0^T du' f_{k'}(u')e^{-i\omega u'}.$$

To get the expression:

$$\mathcal{F}_T[\eta_{O,k'}(t)](\omega) = \left(\frac{1}{1+i(\omega-\omega_0)}\right)\left(\frac{1}{\sqrt{T}}\sum_{k'=1}^{K'} B_{k'}e^{-it_{k'}\omega}\right), \tag{D.8}$$

where ω_0 is the fundamental frequency of the over densities.

The PSD of the process we are describing is defined as,

$$\mathcal{S}_{\phi'} = \lim_{T\longrightarrow\infty}\langle|\mathcal{F}_T[\eta_{O,k'}(t)](\omega)|^2\rangle,$$

then we get,

$$\mathcal{S}_{\phi'}(\omega) = \frac{1}{1+(\omega-\omega_0)^2}\lim_{T\longrightarrow\infty}\left\langle\frac{1}{T}\sum_{m'=1}^{K'}\sum_{l'=1}^{K'} B_m B_l e^{-i\omega(t_{l'}-t_{m'})}\right\rangle.$$

Now, taking the average over the random variables,

$$\begin{aligned}\left\langle\frac{1}{T}\sum_{m'=1}^{K'}\sum_{l'=1}^{K'} B_m B_l e^{-i\omega(t_{l'}-t_{m'})}\right\rangle &= \sum_{K'=0}^{\infty} P_{K'}(K';T,\tau_w^{'})\frac{1}{T}\sum_{m'=1}^{K}\sum_{l'=1}^{K}\int_0^T dt_1 g(t_1)\ldots\int_0^T dt_{K'}g(t_{K'})\\ &\times\int_0^\infty dB_1 P(B_1)\ldots\int_0^\infty dB_{K'}P(B_{K'})B_{m'}B_{l'}e^{-i\omega(t_{l'}-t_{m'})},\end{aligned}$$

where $g(t)$ is the Binomial distribution describing time.

When $m^{'} = l^{'}$,

$$\sum_{K'=0}^{\infty} P_{K'}(K';T,\tau_w^{'})\frac{K'}{T}G(T)^{K'}\times\int_0^\infty dB_1 P(B_1)\ldots\int_0^\infty dAB_{K'}P(B_{K'})B^2$$
$$\sum_{K'=0}^{\infty} P_{K'}(K';T,\tau_w^{'})\frac{K'}{T}G(T)^{K'}\langle B^2\rangle = \sum_{K'=0}^{\infty} P_{K'}(K';T,\tau_w^{'})G(T)^{K'}\frac{K'}{T}2\langle B\rangle^2,$$

where $\lim_{T\longrightarrow\infty} G(T) = 1$.

When $m^{'} \neq l^{'}$,

$$\sum_{K'=0}^{\infty} P_{K'}(K';T,\tau_w^{'})\frac{K^{'}(K^{'}-1)}{T}G(T)^{K'-2}\int_0^T dt g(t)\int_0^T ds\langle B\rangle^2 g(s)e^{-i\omega(t-s)}$$
$$\sum_{K'=0}^{\infty} P_{K'}(K';T,\tau_w^{'})\frac{K^{'}(K^{'}-1)}{T}\langle B\rangle^2 G(T)^{K'-1}\int_0^T dt g(t)e^{-i\omega t(1-i\omega_o k)},$$

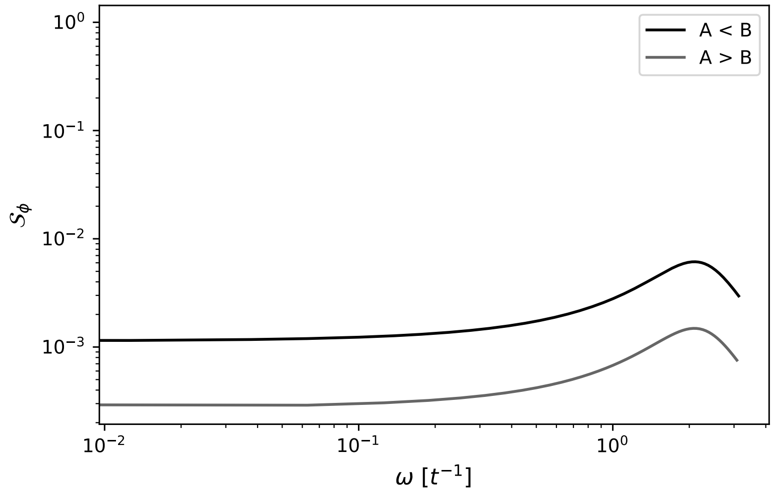

Figure D.1. Power spectral density. We show two cases that can be obtained form the analytical expression in Eq. (D.12). The black line represents the case in each we obtain an overdensity and the gray line represents the case for an underdensity. In both cases the imprint behaves similar as expected, the overall contribution to the spectral density is the crucial factor to distinguish both cases.

the integral $F(t) = \int_0^T dtg(t)e^{-i\omega t}$ when $T \longrightarrow \infty$ is the Fourier transform of a Gaussian distribution which is constant with respect to t. Then we have:

$$\sum_{K'=0}^{\infty} P_{K'}(K';T,\tau_w^{'})\frac{K^{'}(K^{'}-1)}{T}\langle B\rangle^2 e^{-i\hat{\omega}T} = \frac{T}{\tau_w^2}G(T)^{k-1}F(T)\langle B\rangle^2 e^{-i\omega_o K'},$$

$$\lim_{T\longrightarrow\infty}\left\langle \frac{1}{T}\sum_{m'=1}^{K'}\sum_{l'=1}^{K'} B_m B_l e^{-i\omega(t_{l'}-t_{m'})}\right\rangle = 2\gamma^{'}\langle B\rangle^2. \tag{D.9}$$

Finally,

$$\boxed{\mathcal{S}_{\phi'}(\omega) = \frac{2\gamma^{'}\langle B\rangle^2}{1+(\omega-\omega_0)^2}}. \tag{D.10}$$

Summing the above result with the contribution for the over/under densities we get,

$$\boxed{\mathcal{S}_{\phi_{Tot}}(\omega) = 2\pi\langle A\rangle^2\delta(\omega) + 2\gamma^{'}\langle B\rangle^2\frac{\tau_d}{1+\tau_d^2(\omega-\omega_0)^2}}. \tag{D.11}$$

We can rewrite the power spectrum as follows to perform the fit:

$$\mathcal{S}_{\phi_{Tot}}(\omega) = \hat{\mathcal{A}} + 2\gamma^{'}\langle B\rangle^2\frac{1/\tau_d}{1/\tau_d^2+(\omega-\omega_0)^2} \tag{D.12}$$

D.2 The Wiener–Khinchin theorem

The Wiener-Khinchin theorem [361, 362] states that the auto-correlation function of a stationary random process has a spectral decomposition given by the power spectral density of that process.

Let us consider a signal in time $x(t)$. In the case of a continuous-time process, the auto-correlation function (ACF) is defined as,

$$G(\tau) = \lim_{T\to\infty} \frac{1}{T} \int_0^T x(t)x(t+\tau)dx. \tag{D.13}$$

This theorem relates the Fourier transform of the signal $x(t)$ with its ACF. The forward Fourier transform of $x(t)$ is given by,

$$\hat{x}(\omega) = \int_0^T dte^{-i\omega t}x(t), \tag{D.14}$$

from which we can define, as we have done before, the power spectral density as,

$$\mathcal{S}(\omega) = \lim_{T\to\infty} \frac{1}{2\pi T}|\hat{x}(\omega)|^2. \tag{D.15}$$

Now to relate $G(\tau)$ with $S(\omega)$,

$$\begin{aligned}\mathcal{S}(\omega) &= \lim_{T\to\infty} \frac{1}{2\pi T} \int_0^T dte^{-i\omega t}x(t) \int_0^T dt'e^{-i\omega t'}x^*(t') \\ &= \{(t,t') \to (t', \tau = (t-t'))\},\end{aligned} \tag{D.16}$$

$$\begin{aligned}\mathcal{S}(\omega) &= \lim_{T\to\infty} \frac{1}{2\pi T} \left(\int_0^T d\tau e^{-i\omega\tau} \int_0^{T-\tau} dt'x(t')x^*(t+\tau) \right. \\ &\quad \left. + \int_{-T}^0 d\tau e^{-i\omega\tau} \int_{-\tau}^T dt'x(t')x^*(t+\tau) \right) \\ \mathcal{S}(\omega) &= \frac{1}{2\pi T} \left(\int_{-T}^0 d\tau e^{-i\omega\tau}(TG(\tau) + \mathcal{O}(1/T) \right. \\ &\quad \left. + \int_0^T d\tau e^{-i\omega\tau}(TG(\tau) + \mathcal{O}(1/T) \right), \\ &= \frac{1}{2\pi} \lim_{T\to\infty} \int_{-T}^T d\tau e^{-i\omega\tau}G(\tau).\end{aligned} \tag{D.17}$$

Since the ACF is an even function,

$$\begin{aligned}\mathcal{S}(\omega) &= \frac{1}{2\pi} \int_{-\infty}^{\infty} d\tau e^{\pm i\omega\tau}G(\tau) \\ &= \frac{1}{\pi} \int_0^{\infty} d\tau G(\tau)\cos(\omega\tau)\end{aligned} \tag{D.18}$$

using $\delta(x) = 1/2\pi \int_{-\infty}^{\infty} e^{\pm i\omega x}d\omega$, one can conclude [363],

$$G(\tau) = \int_{-\infty}^{\infty} e^{i\omega\tau} \mathcal{S}(\omega) d\omega. \tag{D.19}$$

For the discrete case,

$$\mathcal{S} = \frac{1}{2\pi} \sum_{k=-\infty}^{\infty} r_{xx}(k) e^{-i\omega t}, \tag{D.20}$$

where r_{xx} represents the discrete auto-correlation function, and $\omega = 2\pi f$. For a a discrete-time sequence, the spectral density is periodic in the frequency domain,

$$r_{xx}(\tau) = \int_{-\pi}^{\pi} \mathcal{S}(\omega) e^{i\omega\tau} d\omega. \tag{D.21}$$

D.3 Power spectrum baseline

To simulate the case of a detection of particles homogeneously distributed in space we perform a random process indexed by time [364, 365]. In the following we show as an example one particular case to illustrate how we simulate the homogeneous detections.

D.3.1 Set up

We take a Poisson process to model the number of detections of certain particles during some period of time. We assume at first the average occurrence of those detections. See Table D.1.

Fixed Parameters homogeneous case	
Parameter	Value
λ	2
N	1000
N_s	1000

Table D.1. Parameters used to perform the Poisson process. N_s represent the number of times the simulation was performed and N the number of total events.

To do so, a sequence of random variables is made up from the same Poisson distribution, given by the probability mass function (PMF) :

$$P_x(k) = \frac{e^{-\lambda}\lambda^k}{k!}, \tag{D.22}$$

where λ represents the average occurrence rate per unit time and k represents the occurrences.

To know the likelihood of k particles arriving to the detector in t units of time, the Poisson process is modeled with a rate (λt):

$$P_x(k) = \frac{e^{-\lambda t}(\lambda t)^k}{k!} \,. \tag{D.23}$$

To model the times between consecutive events we can consider an exponential distribution, so if $X_1, X_2, ..X_n$ are random variables, then: $X_1 =$ the interval of time between the start of the process and the first detection. $X_2 =$ the inter time between the first and the second detection, and so on :$X_k = e^{\lambda}$,

The probability distribution function (PDF) and the cumulative distribution function (CDF) goes as follows:

$$P_X(t) = \lambda e^{-\lambda t} \,, \tag{D.24}$$

$$CDF = F_x(t) = P(X < +t) = \int_0^t \lambda e^{-\lambda t} = 1 - e^{-\lambda t}. \tag{D.25}$$

To simulate the inter times, the inverse function of the CDF is constructed (Inverse CDF technique) by feeding it with different probability values from a uniform distribution $uniform(0,1)$. This will give back the corresponding inter times for the respective probabilities.

$$F_x^{-1}(t) = -\frac{\ln(1-t)}{\lambda} \,. \tag{D.26}$$

Finally the arrival times, will be just linear combinations of those inter arrival times. This process above is understood in our case like a time-domain signal representing particle detections, Fig D.2a.

To analyze the signal we consider the Fourier transform of a stochastic process even though it does not exist, eq. (D.27).

$$\begin{aligned} \mathcal{X}_T(t) &= \left\{ \begin{array}{ll} X(t) & \text{if } |t| \leq T/2 \\ 0 & \text{if } |t| > T/2 \end{array} \right\} = X(t)\text{rect}(t/T). \\ \mathcal{F}(\mathcal{X}_T(t)) &= \int_{-\infty}^{\infty} X_T(t) e^{-i2\pi f t} df, \quad T < \infty, \end{aligned} \tag{D.27}$$

using Parseval's theorem:

$$\begin{aligned} \int_{-T/2}^{T/2} |\mathcal{X}_T(t)|^2 dt &= \int_{-\infty}^{\infty} |\mathcal{F}(\mathcal{X}_T(t))|^2 df \\ \frac{1}{T}\int_{-T/2}^{T/2} \mathcal{X}_T^2(t) dt &= \frac{1}{T}\int_{-\infty}^{\infty} |\mathcal{F}(\mathcal{X}_T(t))|^2 df, \end{aligned} \tag{D.28}$$

we obtain the average power over all time. In eq. (D.28) we have that the right side does not exist, but its expectation value does, then:

$$\begin{aligned} \mathrm{E}\left(\frac{1}{T}\int_{-T/2}^{T/2} \mathcal{X}_T^2(t) dt\right) &= \mathrm{E}\left(\frac{1}{T}\int_{-\infty}^{\infty} |\mathcal{F}(\mathcal{X}_T(t))|^2 df\right) \\ T &\longrightarrow \infty \\ \langle \mathrm{E}[X]^2 \rangle &= \int_{-\infty}^{\infty} \lim_{t \longrightarrow \infty} \mathrm{E}\left[\frac{|\mathcal{F}(\mathcal{X}_T(t))|^2}{T}\right] df \end{aligned} \tag{D.29}$$

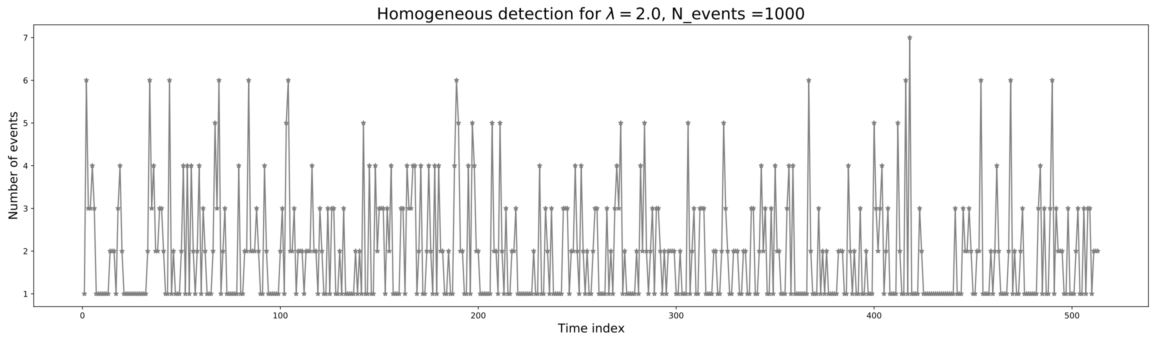

(a) Signal generated from one homogeneous Poisson process.

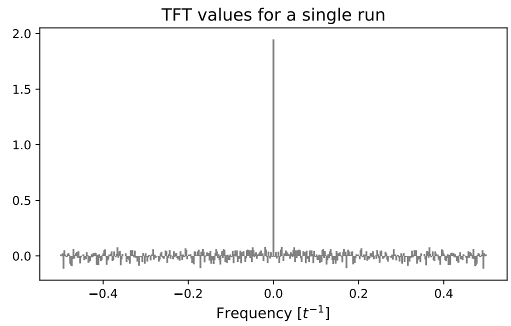

(b) FFT for one single run of the random process.

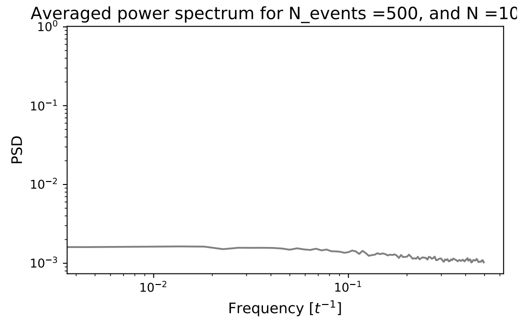

(c) Average power spectrum for 1000 detection samples.

Figure D.2. Homogeneous signal analysis.

In Fig D.2c, we can see that the process behaves as a form of Gaussian white noise which is expected due to the fact that the magnitude of the signal at all frequencies, even arbitrary large ones, is equal to its rate.

D.4 Characterization of localized clump peak

As shown in Fig 4.1b, the power spectrum shape for clumps is represented by a single peak that can be model as a Lorentz function $\mathbf{L}(x; q_i)$ centered at the fixed frequency for the clumps, [366, 367], then,

$$\mathbf{L}(x; q_i) = q_0 + \frac{q_1}{\pi}\left[\frac{q_3}{(x-q_2)^2 + q_3^2}\right], \tag{D.30}$$

where x represents the array of frequencies in which the function is evaluated and q_i are all the parameters of shape, i.e, q_0 represents the base line (flat background), q_1 is the amplitude, q_2 is the center position of the peak and q_3 is the width. Here we neglect higher modes that might appear in some cases.

To obtain and expression for the spectrum including the homogeneous contributions, we consider an additional Lorentz function $\mathbf{L}(x; q_i, q_j) = \mathbf{L}(x; q_i)_{cp} + \mathbf{L}(x; q_j)_h$, see Fig D.3a. In Fig D.3a, we took the power spectrum generated by the simulation with poor statistics and allowed a Lorentzian fit

Power spectrum parameters equivalence	
Shape Parameter	Simulation parameter
q_0	0.0
q_1	$C_3\lambda_{over}^3 + C_2\lambda_{over}^2 + C_1(P^{(2)})\lambda_{over} + C_0(P^{(1)})$
q_2	$1/T$
q_3	$B_1 \exp(B_2 N_e)$
q_0^h, q_2^h	0.0

Table D.2. Shape Parameters from the fit related to simulation parameters. We neglected variations on the parameters for which STD < 0.01, i.e the simulation parameters considered here contribute considerably to the shape of the fitting function. The constant values are presented in Table D.3

using *python-numpy* for the data, the fitted function recognized both peaks, nevertheless the widths are not accurate mostly because the background is not averaged enough and interfered with the signal, which mostly represents a latent limitation in real life experiments.

We know that in the absence of structure and for an infinite time, the power of the central peak is determined by a delta function which amplitude depends on the average rate of the homogeneous detection process. Now, when we introduce clumps, see Fig D.3b, we kept mostly the same parameters as in Table D.2 except for clump-specific parameters, such as self-frequency of the clump, overdensity and encounter probability. That is, we kept the same parameters that describe the background in the case there are also clumps involved. Nevertheless, such narrow peak is not very realistic, because it may be the case, that we measure a convolution of peaks much less intense, so we can expect a broader peak representing a combination of very small clumps. This case was already mentioned in Section 4.1.4.

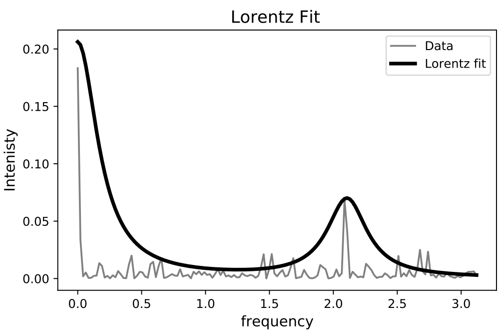

(a) Lorentz fit for complete spectrum with $q_1^h = 0.4$, $q_2^h = 10^{-17}$, $q_3^h = 0.06$ and $q_0 = 9.3 \times 10^{32}$, $q_1 = 0.2$, $q_2 = 0.33$, $q_3 = 0.06$

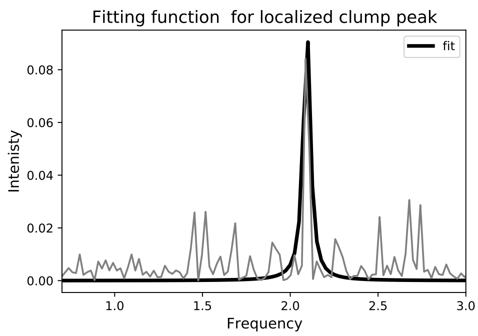

(b) Lorentz function vs data for parameters obtained by fitting each shape parameter to the general Lorentz function, Table D.3.

Figure D.3. Lorentz fit for a signal with $(\lambda_{od} = 30, P = 30\%, T = 3.0)$

Fit Parameters values	
Parameter	Value
C_3	$1.5 \times 10^{-5} \pm 3.38 \times 10^{-6}$
C_2	-0.0029 ± 0.0005
$C_1(P^{(1)})$	$(-1.542 \pm 0.333)P^2 + (1.547 \pm 0.307)P - (0.07 \pm 0.06)$
$C_0(P^{(2)})$	$(2.765 \pm 0.500)P - (0.987 \pm 0.252)$
B_1	$\exp(-2.861 \pm 0.159)$
B_2	-0.0047 ± 0.0004

Table D.3. Values for the constant and variable parameters for the power spectrum fit of the clump peak.

D.5 Statistic Test

The Mann-Whitney U test is a non parametric test of the null hypothesis between two independent groups. This test checks the difference between the samples by assigning ranks and summing, and does not required that the samples are normally distributed or follow any particular distribution curve [292, 368–371].

The general assumptions the date should meet to be analyzed by this test are:

- All the observations from both groups are independent of each other.
- The responses are ordinal or continuous.
- Under the null hypothesis H_0, the distributions of both populations must be equal.
- The alternative hypothesis must consist in that the distributions are not equal.

To perform the test it is required to calculate a statistic, denoted U and is the smaller value of U_1 and U_2, as defined below:

$$\begin{aligned} U_1 &= n_1 n_2 + n_1 \frac{(n_1+1)}{2} - R_1, \\ U_2 &= n_1 n_2 + n_2 \frac{(n_2+1)}{2} - R_2, \end{aligned} \tag{D.31}$$

where n_1 and n_2 are the sample sizes for sample 1 and 2 respectively, and R_1 and R_2 are the sum of the ranks for the samples. The smallest value between U_1 and U_2 is then used to consulting significance table [372] which will reject or not the null hypothesis based on the significance value established to perform the test.

D.6 Statistic test on numerical parameters

We have defined as free parameters λ_{od}, P, N so we have tested the null hypothesis by running (λ_{od}, P, N) for a fixed detection time and an approximately equal number of events (of course, due to the stochastic nature of the process it is not possible to ensure that the same number of events is always present, only events on average). We obtain the power spectrum for each case and test the null hypothesis in order to scan the behavior of the p-value.

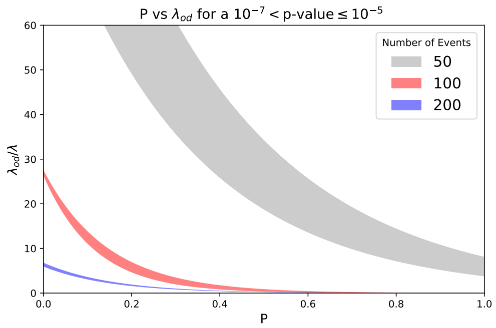

(a) Pairs of (λ_{od}, P) for different number of events capable of generating a significance level of order 5σ. The statistics for this scan was taken form $N = 100$ samples of each spectrum.

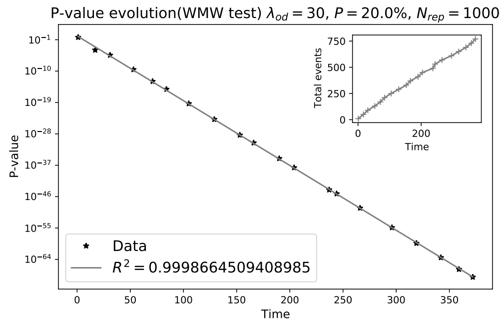

(b) Time evolution of the p-value for$(\lambda_{od} = 30, P = 20\%)$. Dots represent the data and the solid line represent the exponential fit. In the upper side the relation of number of events and time is shown.

Figure D.4. Parameters to obtain a 5σ signal.

In Fig D.4a, we show which values for the parameter space defined by (λ_{ob}, P) can reject the null hypotheses. We perform the analysis for different number of events on average. Our numerical analysis shows that it is possible to distinguish tiny DM structures with at least 100 events, here is important to stress that physical parameters regarding clumps are not yet explored, we will do so in the following sections. In Fig D.4a there are some regions, nonetheless, that can not be resolved with such a small data set (see purple and red regions around $P = 0.3$). We can estimate how many events would be needed to resolve the pink and purple lines in Fig D.4a. First, we fix the over-density value to a small value, e.g., $\lambda_{od} = 5$, and we increase the signal time or, equivalently, the number of events, as we are interested in events with the low rate with respect to the smooth background and low probability. With these signals, we perform a two-sample Z test [373, 374] to determine if it is possible to distinguish them from the smooth background. We found that sample size needed distinguish small over-densities $\lambda_{od} = 5$ with $P = (0.02, 0.1)$ lays around $N \sim 3000$.

Appendix E

Core-Cusp Problem

This appendix provides a detailed derivation of the base equations and formalism necessary for modeling self-interacting dark matter (SIDM) and self-heating dark matter (SHDM) in a gravothermal fluid framework. These derivations allow us to quantify the thermal and dynamic evolution of dark matter within halos. The first section, Gravothermal Fluid Formalism, E.1, derives the differential equations governing heat transport, density evolution, and the gravitational influence within the halo, enabling a rigorous description of core formation under self-healing mechanisms. This formalism is crucial for understanding SIDM's behavior in dense regions of dark matter halos. In the second section, ELDERs, E.2, we explore models of dark matter that involve significant self-interactions and elastic scattering with standard model particles, focusing on the thermal relic scenario. This short review provides necessary insights for addressing the core-cusp problem in dark matter distribution. The derivations in this appendix set the basis for the main analysis and offer a foundation for further computational modeling.

E.1 Gravothermal Fluid formalism

In the following, we are going to derive in detail the set of differential equation needed to describe SIDM and SHDM through the gravothermal formalism.

Let us define the 1-D velocity dispersion $\nu = \sqrt{p(r,t)/\rho(r,t)}$, to state the equations of evolution of the gravothermal fluid as:

$$\frac{\delta \rho \nu^2}{\delta r} + \frac{GM\rho}{r^2} = 0, \tag{E.1}$$

$$\frac{\delta M}{\delta r} - 4\pi r^2 \rho = 0, \tag{E.2}$$

$$\frac{3}{\nu}\left(\frac{\delta \nu}{\delta t}\right)_M - \frac{1}{\rho}\left(\frac{\delta \rho}{\delta t}\right)_M = \frac{1}{\nu^2}\frac{\delta u}{\delta t}, \tag{E.3}$$

where G is the Newton constant and M represents the enclosed fluid mass within radius r. Using the definition of the velocity dispersion we have,

$$\frac{\delta P(r,t)}{\delta r} + \frac{GM\rho}{r^2} = 0, \tag{E.4}$$

and the equation describing the enclosed mass per unit radios. Until this point we have a description of evolution of the pressure and density. The last equation of the set in eq. (E.1) is the first law of thermodynamics and represents the evolution of the self heating process. To make a proper description of it, we need to define the Lagrangian time derivative as,

$$(\delta_t)_M = \delta_t + \vec{V} \cdot \vec{\nabla},$$

where $\vec{V}$ represents the fluid bulk which is determined by the continuity equation,

$$\begin{aligned}
\delta_t \rho\rho + \vec{\nabla} \cdot (\rho \vec{V}) &= 0 \\
\delta_t \rho + \rho(\vec{\nabla}\vec{V}) + (\vec{\nabla}\rho)\vec{V} &= 0 \\
\delta_t \rho + \rho \frac{1}{r}\frac{\delta r V_r}{\delta r} + \frac{1}{r}\frac{\delta}{\delta r}(r\rho)V_r &= 0 \\
\delta_t \rho + \frac{\rho}{r}\left(V_r + r\frac{\delta V_r}{\delta r}\right) + \frac{1}{r}\left(\rho + r\frac{\delta \rho}{\delta r}\right)V_r &= 0,
\end{aligned}$$

taking the stationary solution, $\delta_t \rho = 0$ we get for the bulk velocity:

$$\frac{\delta V_r}{\delta r} - \frac{V_r}{r}\left(\frac{r}{\rho}\frac{\delta \rho}{\delta r} - 2\right) = 0. \tag{E.5}$$

The velocity dispersion due to self heating becomes,

$$\begin{aligned}
\frac{3}{\nu}\left(\frac{\delta \nu}{\delta t}\right)_M - \frac{1}{\rho}\left(\frac{\delta \rho}{\delta t}\right)_M &= \frac{1}{\nu^2}\frac{\delta u}{\delta t} \\
\frac{3}{\nu}(\delta_t \nu + \vec{V} \cdot \vec{\nabla}\nu) - \frac{1}{\rho}(\delta_t \rho + \vec{V} \cdot \vec{\nabla}\rho) &= \frac{1}{\nu^2}\frac{\delta u}{\delta t},
\end{aligned}$$

now, taking stationary solution we get,

$$\frac{3}{\nu}\left[\frac{V_r}{r}\left(\frac{\delta \nu}{\delta r}\right)\right] - \frac{1}{\rho}\left[\frac{V_r}{r}\left(\frac{\delta \rho}{\delta r}\right)\right] = \frac{1}{\nu^2}\frac{\delta u}{\delta t}$$

$$\frac{\delta \nu}{\delta r} - \frac{r}{3V_r \nu}\frac{\delta u}{\delta t} - \frac{\nu}{3\rho}\left(\frac{\delta \rho}{\delta r}\right) = 0 \tag{E.6}$$

where the heat conduction is modeled by a heat diffusion,

$$\frac{\delta u}{\delta t} = \frac{m}{\rho}\Delta \cdot (\kappa \Delta \nu^2), \tag{E.7}$$

where u is the specific energy per unit mass and κ is the thermal conductivity.

In the SHDM scenario, a small portion of the DM particles, which are enhanced through DM semi-annihilations, are captured within the halo instead of escaping due to DM self-interactions. This process can be effectively described as injecting heat into the local DM fluid element at a given rate,

$$\frac{\delta u}{\delta t} = \rho \frac{\langle \sigma_{semi} v_{rel} \rangle}{m} \xi \frac{\partial E}{m}, \tag{E.8}$$

here ξ is the efficiency to capture a boosted DM particle and is a difficult task to model it. We adopt the constant treatment provided in Ref. [38] as,

$$\xi = b\frac{r}{\lambda}, \tag{E.9}$$

where b is the fudge factor set to 3 based on N-body simulations, and $\lambda = 1/(\rho\sigma_{self}/m)$ is the mean streaming length of DM.

The set of differential equations to solve becomes:

$$\frac{\delta P(r,t)}{\delta r} + \frac{GM\rho}{r^2} = 0, \tag{E.10}$$

$$\frac{\delta M}{\delta r} - 4\pi r^2\rho = 0, \tag{E.11}$$

$$\frac{\delta V_r}{\delta r} - \frac{V_r}{r}\left(\frac{r}{\rho}\frac{\delta\rho}{\delta r} - 2\right) = 0, \tag{E.12}$$

$$\frac{\delta\nu}{\delta r} - \frac{r}{3V_r\nu}\frac{\delta u}{\delta t} - \frac{\nu}{3\rho}\left(\frac{\delta\rho}{\delta r}\right) = 0, \tag{E.13}$$

taking into account the state equation of the process, then we obtain for solving the system,

$$\begin{aligned} \rho &= \frac{P}{\nu^2} \\ \frac{\delta\rho}{\delta r} &= \frac{1}{\nu^2}\frac{\delta P}{\delta r} - \frac{2P}{\nu^3}\frac{\delta\nu}{\delta r} \end{aligned} \tag{E.14}$$

This is finally the set of equation that solved numerically can account for the evolution of SHDM inside the halo.

E.2 ELDERs

Some models in which dark matter particles have strong number-changing self-interactions are attractive and are of interest to our study the core-cusp problem. When dark matter (DM) is considered as a thermal relic, its present-day density can be determined by either the cross section of number-changing self-interactions, as observed in the scenario of Strongly-Interacting Massive Particles (SIMP) [375], or by the cross section of elastic scattering between DM and the Standard Model (SM) particles, as seen in the Elastically Decoupling Relic scenario (ELDER) [82]. Both scenarios offer valuable insights for studying the nature of DM and its implications for the core-cusp problem.

In the following we briefly look into the viability of the ELDER scenario without considering a specific model of either the dark sector or the portal connecting it to the SM. Instead, we adopt a simple parametrization for the cross sections associated with both the number-changing self-scattering of dark matter (DM) and the elastic scattering between DM and SM particles. This approach allows us to assess the viability of the ELDER scenario in a more general framework, encompassing a range of possible scenarios without being limited to specific models.

E.2.1 Brief thermal history

ELDER DM, χ, can undergo the following processes [39],

- Elastic scattering: $\chi + SM \Leftrightarrow \chi + SM$.

- Annihilations to SM: $\chi + \chi \Leftrightarrow SM + SM$.

- Self-Annihilations: $\chi\chi\chi \Leftrightarrow \chi\chi$

- Elastic Self-Scattering: $\chi\chi \Leftrightarrow \chi\chi$

At high temperatures, when the dark matter particle is relativistic, it remains in thermal and chemical equilibrium with the plasma and the fourth reactions above are active. As the universe cools, the temperature eventually drops below the mass of DM leading to two significant events in its thermal history. First the ”decoupling” occurs when the rate of elastic scattering between dark matter and SM particles becomes insufficient to maintain thermal equilibrium. Then ”freeze-out” happens when the rate of self-annihilation within the dark matter sector can not maintain chemical equilibrium. At this stage, the comoving density of dark matter becomes fixed. Between decoupling and freeze-out, chemical equilibrium within the dark matter sector is still maintained through self-annihilations. However, the temperature of the dark matter gas T', is no longer equal to the temperature of the SM sector T. In this regime, ”cannibalization” takes place, where $3 \to 2$ self-annihilations reduce the number density of dark matter particles but simultaneously inject kinetic energy into the remaining gas. As the dark matter gas cannot exchange entropy with the SM sector during this time, its comoving entropy density remains constant as the universe expands,

$$a^3 s'_\chi = a^3 \frac{m_\chi n_\chi}{T'} = \text{cte} \tag{E.15}$$

$$\Longrightarrow (T')^{1/2} e^{-m_\chi/T'} \propto T^3, \tag{E.16}$$

where $a \propto T^{-1}$ is the FRW scale-factor. This results in T', decreasing slower than T, therefore the number density during the cannibalization changes slowly, as shown in Fig. 5.1a.

The DM number density at freeze-out is given by,

$$n_f = \frac{\rho'_f}{m_\chi} = \frac{s'_f T'_f}{m_\chi}. \tag{E.17}$$

To determine the temperatures at decoupling and freeze-out, one needs to parametrize the scattering and the self-annihilation cross sections in the non relativistic limit. We show the latter which is the relevant for us,

$$\lim_{T\to 0} (\langle \sigma_{3\to 2} v^2 \rangle) = \frac{\alpha^3}{m_\chi^5}, \tag{E.18}$$

the ELDER mechanism requires the self-annihilation process to maintain the DM gas in chemical equilibrium until at least the decoupling temperature, conditions that translates into [39],

$$\alpha \approx 0.015 \mathrm{m}_{\chi \mathrm{MeV}} (1 + 0.16 \log (\mathrm{m}_{\chi \mathrm{MeV}})). \tag{E.19}$$

Eqs. (E.18), and (E.19) are crucial for the estimation of the heat conduction in Sec 5.2.1.

E.2.2 The Boltzmann equation

The microscopic Boltzmann equation for the phase-space density of the DM particles can be described as,

$$\frac{d\eta_\chi}{dt} + 3H\eta_\chi = -\langle \sigma_{3\to 2} v^2 \rangle (\eta_\chi^3 - \eta_\chi^2 \eta_\chi^{equi}) + \dots \tag{E.20}$$

During the cannibalization stage, the yield of dark matter evolves at a slow pace primarily because of the gradual change in the dark matter temperature. This slow evolution leads to an interesting outcome: the final abundance of dark matter becomes approximately independent of the specific timing of freeze-out and, consequently, the self-annihilation cross-section.

Bibliography

[1] Virgile Dandoy, Joerg Jaeckel, and Valentina Montoya. Using Axion Miniclusters to Disentangle the Axion-photon Coupling and the Dark Matter Density. 7 2023.

[2] Joerg Jaeckel, Valentina Montoya, and Cedric Quint. A Quantum Perspective on Oscillation Frequencies in Axion Dark Matter Experiments. 4 2023.

[3] Matthias Bartelmann. The dark universe. *Rev. Mod. Phys.*, 82:331–382, Feb 2010.

[4] F. Zwicky. On the Masses of Nebulae and of Clusters of Nebulae. *The Astrophysical Journal*, 86:217, October 1937.

[5] Vera C. Rubin and W. Kent Ford, Jr. Rotation of the Andromeda Nebula from a Spectroscopic Survey of Emission Regions. *Astrophys. J.*, 159:379–403, 1970.

[6] M. S. Roberts and R. N. Whitehurst. The rotation curve and geometry of M31 at large galactocentric distances. *The Astrophysical Journal*, 201:327–346, October 1975.

[7] V. C. Rubin, Jr. Ford, W. K., and N. Thonnard. Rotational properties of 21 SC galaxies with a large range of luminosities and radii, from NGC 4605 (R=4kpc) to UGC 2885 (R=122kpc). *The Astrophysical Journal*, 238:471–487, June 1980.

[8] P. A. R. Ade et al. Planck 2015 results. XIII. Cosmological parameters. 2015.

[9] Edward W. Kolb. Particle physics and cosmology, 1994.

[10] E. R. Harrison. Standard model of the early universe. *Ann. Rev. Astron. Astrophys.*, 11:155–186, 1973.

[11] Robin W. Tucker and Charles Wang. Dark matter gravitational interactions. *Class. Quant. Grav.*, 15:933–954, 1998.

[12] Rodrigo Calderón, Arman Shafieloo, Dhiraj Kumar Hazra, and Wuhyun Sohn. On the consistency of ΛCDM with CMB measurements in light of the latest Planck, ACT and SPT data. *JCAP*, 08:059, 2023.

[13] Lavinia Heisenberg, Hector Villarrubia-Rojo, and Jann Zosso. Can late-time extensions solve the H0 and $\sigma 8$ tensions? *Phys. Rev. D*, 106(4):043503, 2022.

[14] Vivian Poulin, Tristan L. Smith, Tanvi Karwal, and Marc Kamionkowski. Early Dark Energy Can Resolve The Hubble Tension. *Phys. Rev. Lett.*, 122(22):221301, 2019.

[15] Rodrigo Calderón, Radouane Gannouji, Benjamin L'Huillier, and David Polarski. Negative cosmological constant in the dark sector? *Phys. Rev. D*, 103(2):023526, 2021.

[16] Alain Coc and Elisabeth Vangioni. Primordial nucleosynthesis. *Int. J. Mod. Phys. E*, 26(08):1741002, 2017.

[17] Andreea S. Font, Kathryn V. Johnston, James S. Bullock, and Brant Robertson. Chemical abundance distributions of Galactic halos and their satellite systems in a lambda-CDM Universe. *Astrophys. J.*, 638:585–595, 2006.

[18] Nathalie Deruelle, Jean-Philippe Uzan, and Patricia de Forcrand-Millard. *Relativity in Modern Physics*. Oxford University Press, 08 2018.

[19] William H. Press and Paul Schechter. Formation of galaxies and clusters of galaxies by self-similar gravitational condensation. *Astrophys. J.*, 187:425–438, 1974.

[20] P. J. E. Peebles. *The Large-Scale Structure of the Universe*. 1981.

[21] George O. Abell. The Distribution of rich clusters of galaxies. *Astrophys. J. Suppl.*, 3:211, 1958.

[22] Simon D. M. White and M. J. Rees. Core condensation in heavy halos: A Two stage theory for galaxy formation and clusters. *Mon. Not. Roy. Astron. Soc.*, 183:341–358, 1978.

[23] Julio F. Navarro, Carlos S. Frenk, and Simon D. M. White. The Structure of cold dark matter halos. *Astrophys. J.*, 462:563–575, 1996.

[24] Asantha Cooray and Ravi K. Sheth. Halo Models of Large Scale Structure. *Phys. Rept.*, 372:1–129, 2002.

[25] Leandros Perivolaropoulos and Foteini Skara. Challenges for ΛCDM: An update. *New Astron. Rev.*, 95:101659, 2022.

[26] B. Moore, S. Ghigna, F. Governato, G. Lake, Thomas R. Quinn, J. Stadel, and P. Tozzi. Dark matter substructure within galactic halos. *Astrophys. J. Lett.*, 524:L19–L22, 1999.

[27] David H. Weinberg, James S. Bullock, Fabio Governato, Rachel Kuzio de Naray, and Annika H. G. Peter. Cold dark matter: controversies on small scales. *Proc. Nat. Acad. Sci.*, 112:12249–12255, 2015.

[28] Pierre Boldrini. The Cusp–Core Problem in Gas-Poor Dwarf Spheroidal Galaxies. *Galaxies*, 10(1):5, 2021.

[29] B. Moore, S. Ghigna, F. Governato, G. Lake, Thomas R. Quinn, J. Stadel, and P. Tozzi. Dark matter substructure within galactic halos. *Astrophys. J. Lett.*, 524:L19–L22, 1999.

[30] V. Springel, J. Wang, M. Vogelsberger, A. Ludlow, A. Jenkins, A. Helmi, J. F. Navarro, C. S. Frenk, and S. D. M. White. The Aquarius Project: the subhaloes of galactic haloes. *Monthly Notices of the Royal Astronomical Society*, 391(4):1685–1711, December 2008.

[31] Jeremy L. Tinker, Brant E. Robertson, Andrey V. Kravtsov, Anatoly Klypin, Michael S. Warren, Gustavo Yepes, and Stefan Gottlöber. The Large-scale Bias of Dark Matter Halos: Numerical Calibration and Model Tests. *The Astrophysical Journal*, 724(2):878–886, December 2010.

[32] Ravi K. Sheth and Giuseppe Tormen. Large-scale bias and the peak background split. *Monthly Notices of the Royal Astronomical Society*, 308(1):119–126, September 1999.

[33] Wayne Hu, Rennan Barkana, and Andrei Gruzinov. Cold and fuzzy dark matter. *Phys. Rev. Lett.*, 85:1158–1161, 2000.

[34] Jens C. Niemeyer. Small-scale structure of fuzzy and axion-like dark matter. *Progress in Particle and Nuclear Physics*, 113:103787, 2020.

[35] Luis A. Anchordoqui, Ignatios Antoniadis, and Dieter Lust. Fuzzy dark matter and the dark dimension. *Eur. Phys. J. C*, 84(3):273, 2024.

[36] Ayuki Kamada, Hee Jung Kim, Hyungjin Kim, and Toyokazu Sekiguchi. Self-Heating Dark Matter via Semiannihilation. *Phys. Rev. Lett.*, 120(13):131802, 2018.

[37] Ayuki Kamada, Hee Jung Kim, and Hyungjin Kim. Self-heating of Strongly Interacting Massive Particles. *Phys. Rev. D*, 98(2):023509, 2018.

[38] Ayuki Kamada and Hee Jung Kim. Escalating core formation with dark matter self-heating. *Phys. Rev. D*, 102(4):043009, 2020.

[39] Eric Kuflik, Maxim Perelstein, Nicolas Rey-Le Lorier, and Yu-Dai Tsai. Elastically Decoupling Dark Matter. *Phys. Rev. Lett.*, 116(22):221302, 2016.

[40] Nicolas Bernal, Xiaoyong Chu, Camilo Garcia-Cely, Thomas Hambye, and Bryan Zaldivar. Production Regimes for Self-Interacting Dark Matter. *JCAP*, 03:018, 2016.

[41] Hiroyuki Kase, Junichiro Makino, and Yoko Funato. Missing dwarf problem in galaxy clusters. *Publ. Astron. Soc. Jap.*, 59:1071, 2007.

[42] Leszek Roszkowski, Enrico Maria Sessolo, and Sebastian Trojanowski. WIMP dark matter candidates and searches—current status and future prospects. *Rept. Prog. Phys.*, 81(6):066201, 2018.

[43] C. B. Adams et al. Axion Dark Matter. In *Snowmass 2021*, 3 2022.

[44] David Ellis, David J. E. Marsh, Benedikt Eggemeier, Jens Niemeyer, Javier Redondo, and Klaus Dolag. Structure of axion miniclusters. *Phys. Rev. D*, 106(10):103514, 2022.

[45] Benedikt Eggemeier, Ananthu Krishnan Anilkumar, and Klaus Dolag. Evidence for axion miniclusters with an increased central density. *Phys. Rev. D*, 110(4):043530, 2024.

[46] Ciaran A. J. O'Hare, Giovanni Pierobon, and Javier Redondo. Axion Minicluster Streams in the Solar Neighborhood. *Phys. Rev. Lett.*, 133(8):081001, 2024.

[47] Huangyu Xiao, Liang Dai, and Matthew McQuinn. Detecting dark matter substructures on small scales with fast radio bursts. *Phys. Rev. D*, 110(2):023516, 2024.

[48] Benjamin W. Lee and Steven Weinberg. Cosmological lower bound on heavy-neutrino masses. *Phys. Rev. Lett.*, 39:165–168, Jul 1977.

[49] B. H. J. McKellar and S. Pakvasa. Cosmological Bounds on Heavy Neutrinos Through the Decays Neutrino $(H) \to 3$ Neutrino (L) and Neutrino $(H) \to$ Neutrino (L) γ. *Phys. Lett. B*, 122:33–36, 1983.

[50] S. Baek, D. G. Cerdeno, Y. G. Kim, P. Ko, and C. Munoz. Direct detection of neutralino dark matter in supergravity. *JHEP*, 06:017, 2005.

[51] Elham Aldufeery and Maien Binjonaid. Dark matter constraints and the neutralino sector of the scNMSSM. *Universe*, 7(2):31, 2021.

[52] James M. Cline, Pat Scott, Kimmo Kainulainen, and Christoph Weniger. Update on scalar singlet dark matter. *Phys. Rev. D*, 88:055025, Sep 2013.

[53] J. Aalbers et al. DARWIN: towards the ultimate dark matter detector. *JCAP*, 11:017, 2016.

[54] N. Du et al. A Search for Invisible Axion Dark Matter with the Axion Dark Matter Experiment. *Phys. Rev. Lett.*, 120(15):151301, 2018.

[55] Ciaran A. J. O'Hare and Anne M. Green. Axion astronomy with microwave cavity experiments. *Phys. Rev. D*, 95(6):063017, 2017.

[56] Dmitry Budker, Peter W. Graham, Micah Ledbetter, Surjeet Rajendran, and Alex Sushkov. Proposal for a Cosmic Axion Spin Precession Experiment (CASPEr). *Phys. Rev. X*, 4(2):021030, 2014.

[57] Yonit Hochberg, Tongyan Lin, and Kathryn M. Zurek. Detecting ultralight bosonic dark matter via absorption in superconductors. *Phys. Rev. D*, 94:015019, Jul 2016.

[58] N. Aghanim et al. Planck 2018 results. VI. Cosmological parameters. *Astron. Astrophys.*, 641:A6, 2020. [Erratum: Astron.Astrophys. 652, C4 (2021)].

[59] D. N. Spergel et al. First year Wilkinson Microwave Anisotropy Probe (WMAP) observations: Determination of cosmological parameters. *Astrophys. J. Suppl.*, 148:175–194, 2003.

[60] K. A. Olive et al. Review of Particle Physics. *Chin. Phys. C*, 38:090001, 2014.

[61] Julio F. Navarro, Carlos S. Frenk, and Simon D. M. White. A Universal density profile from hierarchical clustering. *Astrophys. J.*, 490:493–508, 1997.

[62] Naoki Seto and Asantha Cooray. Search for small-mass black-hole dark matter with space-based gravitational wave detectors. *Physical Review D*, 70(6), Sep 2004.

[63] E. R. Siegel, M. P. Hertzberg, and J. N. Fry. Probing dark matter substructure with pulsar timing. *Monthly Notices of the Royal Astronomical Society*, 382(2):879–885, Dec 2007.

[64] V. I. Dokuchaev, Yu. N. Eroshenko, and I. I. Tkachev. Destruction of axion miniclusters in the galaxy. *Journal of Experimental and Theoretical Physics*, 125(3):434–442, Sep 2017.

[65] Joerg Jaeckel, Sebastian Schenk, and Michael Spannowsky. Probing dark matter clumps, strings and domain walls with gravitational wave detectors, 2020.

[66] V S Berezinsky, V I Dokuchaev, and Yu N Eroshenko. Small-scale clumps of dark matter. *Physics-Uspekhi*, 57(1):1–36, Jan 2014.

[67] Martin Bucher and David Spergel. Is the dark matter a solid? *Physical Review D*, 60(4), Jul 1999.

[68] David E Kaplan, Gordan Z Krnjaic, Keith R Rehermann, and Christopher M Wells. Atomic dark matter. *Journal of Cosmology and Astroparticle Physics*, 2010(05):021–021, May 2010.

[69] Nayara Fonseca, Enrico Morgante, Ryosuke Sato, and Géraldine Servant. Axion fragmentation, 2020.

[70] A. D. Dolgov, S. L. Dubovsky, G. I. Rubtsov, and I. I. Tkachev. Constraints on millicharged particles from Planck data. *Phys. Rev. D*, 88(11):117701, 2013.

[71] Chris Kouvaris. Composite Millicharged Dark Matter. *Phys. Rev. D*, 88(1):015001, 2013.

[72] Samuel D. McDermott, Hai-Bo Yu, and Kathryn M. Zurek. Turning off the Lights: How Dark is Dark Matter? *Phys. Rev. D*, 83:063509, 2011.

[73] Eric D. Carlson, Marie E. Machacek, and Lawrence J. Hall. Self-interacting Dark Matter. *The Astrophysical Journal*, 398:43, October 1992.

[74] Eric D. Carlson, Marie E. Machacek, and Lawrence J. Hall. Self-interacting dark matter. *Astrophys. J.*, 398:43–52, 1992.

[75] John Kormendy and G. R. Knapp, editors. *Dark matter in the universe*, volume 117 of *IAU Symposium*, January 1987.

[76] J. Silk et al. *Particle Dark Matter: Observations, Models and Searches*. Cambridge Univ. Press, Cambridge, 2010.

[77] J. Diemand, M. Kuhlen, P. Madau, M. Zemp, B. Moore, D. Potter, and J. Stadel. Clumps and streams in the local dark matter distribution. *Nature*, 454:735–738, 2008.

[78] Nilanjan Banik, Gianfranco Bertone, Jo Bovy, and Nassim Bozorgnia. Probing the nature of dark matter particles with stellar streams. *JCAP*, 07:061, 2018.

[79] Peter Coles and Francesco Lucchin. *Cosmology: The origin and evolution of cosmic structure*. John Wiley & Sons, 2003.

[80] Lam Hui. Wave Dark Matter. *Ann. Rev. Astron. Astrophys.*, 59:247–289, 2021.

[81] Gianfranco Bertone, Dan Hooper, and Joseph Silk. Particle dark matter: Evidence, candidates and constraints. *Phys. Rept.*, 405:279–390, 2005.

[82] Eric Kuflik, Maxim Perelstein, Nicolas Rey-Le Lorier, and Yu-Dai Tsai. Phenomenology of ELDER Dark Matter. *JHEP*, 08:078, 2017.

[83] Carlos E. Yaguna. The Singlet Scalar as FIMP Dark Matter. *JHEP*, 08:060, 2011.

[84] B. Ryden. *Introduction to cosmology*. Cambridge University Press, 1970.

[85] P. S. Bhupal Dev, Anupam Mazumdar, and Saleh Qutub. Constraining Non-thermal and Thermal properties of Dark Matter. *Front. in Phys.*, 2:26, 2014.

[86] Gary Steigman, Basudeb Dasgupta, and John F. Beacom. Precise Relic WIMP Abundance and its Impact on Searches for Dark Matter Annihilation. *Phys. Rev. D*, 86:023506, 2012.

[87] Howard Baer, Ki-Young Choi, Jihn E. Kim, and Leszek Roszkowski. Dark matter production in the early Universe: beyond the thermal WIMP paradigm. *Phys. Rept.*, 555:1–60, 2015.

[88] Giorgio Arcadi, Maíra Dutra, Pradipta Ghosh, Manfred Lindner, Yann Mambrini, Mathias Pierre, Stefano Profumo, and Farinaldo S. Queiroz. The waning of the WIMP? A review of models, searches, and constraints. *Eur. Phys. J. C*, 78(3):203, 2018.

[89] Lawrence J. Hall, Karsten Jedamzik, John March-Russell, and Stephen M. West. Freeze-In Production of FIMP Dark Matter. *JHEP*, 03:080, 2010.

[90] Pasquale Dario Serpico and Dan Hooper. Gamma-rays from Dark Matter Annihilation in the Central Region of the Galaxy. *New J. Phys.*, 11:105010, 2009.

[91] A. Albert et al. Search for dark matter towards the Galactic Centre with 11 years of ANTARES data. *Phys. Lett. B*, 805:135439, 2020.

[92] Nhan Thien Chau et al. Indirect dark matter search in the Galactic Centre with IceCube. *PoS*, ICRC2023:1394, 2023.

[93] David G. Cerdeno and Anne M. Green. Direct detection of WIMPs. pages 347–369, 2 2010.

[94] G. Arcadi, C. Döring, C. Hasterok, and S. Vogl. Inelastic dark matter nucleus scattering. *JCAP*, 12:053, 2019.

[95] Jodi Cooley. Dark Matter direct detection of classical WIMPs. *SciPost Phys. Lect. Notes*, 55:1, 2022.

[96] J. Rich. DIRECT DETECTION OF PARTICLE DARK MATTER. In *23rd Rencontres de Moriond: Astronomy: Detection of Dark Matter*, pages 43–53, 1988.

[97] Thomas Lacroix, Arturo Núñez Castiñeyra, Martin Stref, Julien Lavalle, and Emmanuel Nezri. Predicting the dark matter velocity distribution in galactic structures: tests against hydrodynamic cosmological simulations. *JCAP*, 10:031, 2020.

[98] Katharena Christy, Jason Kumar, and Louis E. Strigari. Dark matter velocity distributions: Comparing numerical simulations to analytic results. *Phys. Rev. D*, 109(6):063016, 2024.

[99] K. Choi, Carsten Rott, and Yoshitaka Itow. Impact of the dark matter velocity distribution on capture rates in the Sun. *JCAP*, 05:049, 2014.

[100] Pijushpani Bhattacharjee, Soumini Chaudhury, Susmita Kundu, and Subhabrata Majumdar. Sizing-up the WIMPs of Milky Way : Deriving the velocity distribution of Galactic Dark Matter particles from the rotation curve data. *Phys. Rev. D*, 87:083525, 2013.

[101] Marcin Misiaszek and Nicola Rossi. Direct Detection of Dark Matter: A Critical Review. *Symmetry*, 16(2):201, 2024.

[102] A. Liam Fitzpatrick, Wick Haxton, Emanuel Katz, Nicholas Lubbers, and Yiming Xu. The Effective Field Theory of Dark Matter Direct Detection. *JCAP*, 02:004, 2013.

[103] F. Mayet et al. A review of the discovery reach of directional Dark Matter detection. *Phys. Rept.*, 627:1–49, 2016.

[104] Martin Hoferichter, Philipp Klos, Javier Menéndez, and Achim Schwenk. Analysis strategies for general spin-independent WIMP-nucleus scattering. *Phys. Rev. D*, 94(6):063505, 2016.

[105] Mark W. Goodman and Edward Witten. Detectability of Certain Dark Matter Candidates. *Phys. Rev. D*, 31:3059, 1985.

[106] Fady Bishara, Joachim Brod, Benjamin Grinstein, and Jure Zupan. From quarks to nucleons in dark matter direct detection. *JHEP*, 11:059, 2017.

[107] G. Angloher et al. Light dark matter search using a diamond cryogenic detector. *Eur. Phys. J. C*, 84(3):324, 2024.

[108] Laura Baudis. Wimp dark matter direct-detection searches in noble gases. *Physics of the Dark Universe*, 4:50–59, 2014. DARK TAUP2013.

[109] E. Aprile et al. The XENONnT Dark Matter Experiment. 2 2024.

[110] Sergey Maiorov and R Golyatina. Ionization cross section of noble gas atoms by electron impact. *Physical Sciences and Technology*, 9, 06 2022.

[111] Rusudan Golyatina and S. Maiorov. Analytical cross section approximation for electron impact ionization of alkali and other metals, inert gases and hydrogen atoms. *Atoms*, 9:90, 10 2021.

[112] J. Aalbers et al. A next-generation liquid xenon observatory for dark matter and neutrino physics. *J. Phys. G*, 50(1):013001, 2023.

[113] Marc Schumann. Dark Matter Search with liquid Noble Gases. 6 2012.

[114] J. Angle et al. First Results from the XENON10 Dark Matter Experiment at the Gran Sasso National Laboratory. *Phys. Rev. Lett.*, 100:021303, 2008.

[115] The xenon100 dark matter experiment. *Astroparticle Physics*, 35(9):573–590, April 2012.

[116] E. Aprile et al. XENON100 Dark Matter Results from a Combination of 477 Live Days. *Phys. Rev. D*, 94(12):122001, 2016.

[117] F. Agostini et al. Sensitivity of the DARWIN observatory to the neutrinoless double beta decay of ^{136}Xe. *Eur. Phys. J. C*, 80(9):808, 2020. [Erratum: Eur.Phys.J.C 83, 996 (2023)].

[118] J. Aalbers et al. Solar neutrino detection sensitivity in DARWIN via electron scattering. *Eur. Phys. J. C*, 80(12):1133, 2020.

[119] D. S. Akerib et al. Results from a search for dark matter in the complete LUX exposure. *Phys. Rev. Lett.*, 118(2):021303, 2017.

[120] D. S. Akerib et al. The LUX-ZEPLIN (LZ) Experiment. *Nucl. Instrum. Meth. A*, 953:163047, 2020.

[121] R. D. Peccei and Helen R. Quinn. CP conservation in the presence of pseudoparticles. *Phys. Rev. Lett.*, 38:1440–1443, Jun 1977.

[122] Frank Wilczek. Problem of Strong P and T Invariance in the Presence of Instantons. *Phys. Rev. Lett.*, 40:279–282, 1978.

[123] R.J. Crewther, P. Di Vecchia, G. Veneziano, and E. Witten. Chiral estimate of the electric dipole moment of the neutron in quantum chromodynamics. *Physics Letters B*, 88(1):123–127, 1979.

[124] C. A. Baker et al. An Improved experimental limit on the electric dipole moment of the neutron. *Phys. Rev. Lett.*, 97:131801, 2006.

[125] J. M. Pendlebury et al. Revised experimental upper limit on the electric dipole moment of the neutron. *Phys. Rev. D*, 92(9):092003, 2015.

[126] C. Abel et al. Measurement of the Permanent Electric Dipole Moment of the Neutron. *Phys. Rev. Lett.*, 124(8):081803, 2020.

[127] R. D. Peccei. The Strong CP problem and axions. *Lect. Notes Phys.*, 741:3–17, 2008.

[128] Gerrit Schierholz. Dynamical solution of the strong CP problem within QCD? *EPJ Web Conf.*, 274:01009, 2022.

[129] Y. Nakamura and G. Schierholz. The strong CP problem solved by itself due to long-distance vacuum effects. *Nucl. Phys. B*, 986:116063, 2023.

[130] Gerrit Schierholz. Absence of strong CP violation. 3 2024.

[131] Gerrit Schierholz. Repercussions of the Peccei-Quinn axion on QCD. 7 2023.

[132] R. D. Peccei and Helen R. Quinn. Constraints imposed by CP conservation in the presence of pseudoparticles. *Phys. Rev. D*, 16:1791–1797, Sep 1977.

[133] Steven Weinberg. A new light boson? *Phys. Rev. Lett.*, 40:223–226, Jan 1978.

[134] F. Wilczek. Problem of strong p and t invariance in the presence of instantons. *Phys. Rev. Lett.*, 40:279–282, Jan 1978.

[135] Claude Amsler et al. Review of Particle Physics. *Phys. Lett. B*, 667:1–1340, 2008.

[136] David B. Kaplan. Opening the Axion Window. *Nucl. Phys. B*, 260:215–226, 1985.

[137] Joerg Jaeckel and Andreas Ringwald. The Low-Energy Frontier of Particle Physics. *Ann. Rev. Nucl. Part. Sci.*, 60:405–437, 2010.

[138] Igor G. Irastorza and Javier Redondo. New experimental approaches in the search for axion-like particles. *Prog. Part. Nucl. Phys.*, 102:89–159, 2018.

[139] Giovanni Grilli di Cortona, Edward Hardy, Javier Pardo Vega, and Giovanni Villadoro. The QCD axion, precisely. *JHEP*, 01:034, 2016.

[140] A. Ringwald. Photon Regeneration Plans. In *6th International Workshop on the Identification of Dark Matter*, pages 388–395, 12 2006.

[141] R. Cameron et al. Search for nearly massless, weakly coupled particles by optical techniques. *Phys. Rev. D*, 47:3707–3725, 1993.

[142] F. Brandi et al. Optical production and detection of dark matter candidates. *Nucl. Instrum. Meth. A*, 461:329–331, 2001.

[143] Javier Redondo and Andreas Ringwald. Light shining through walls. *Contemp. Phys.*, 52:211–236, 2011.

[144] P. Sikivie. Experimental tests of the ”invisible” axion. *Phys. Rev. Lett.*, 51:1415–1417, Oct 1983.

[145] S. J. Asztalos, G. Carosi, C. Hagmann, D. Kinion, K. van Bibber, M. Hotz, L. J Rosenberg, G. Rybka, J. Hoskins, J. Hwang, P. Sikivie, D. B. Tanner, R. Bradley, and J. Clarke. Squid-based microwave cavity search for dark-matter axions. *Physical Review Letters*, 104(4), January 2010.

[146] Ian P. Stern. Axion Dark Matter Searches. *AIP Conf. Proc.*, 1604(1):456–461, 2015.

[147] C. Bartram et al. Search for Invisible Axion Dark Matter in the 3.3–4.2 μeV Mass Range. *Phys. Rev. Lett.*, 127(26):261803, 2021.

[148] I. Stern. ADMX Status. *PoS*, ICHEP2016:198, 2016.

[149] Adam Burrows, Michael S. Turner, and R. P. Brinkmann. Axions and sn 1987a. *Phys. Rev. D*, 39:1020–1028, Feb 1989.

[150] Ron Mayle, James R. Wilson, John Ellis, Keith Olive, David N. Schramm, and Gary Steigman. Constraints on axions from sn 1987a. *Physics Letters B*, 203(1):188–196, 1988.

[151] Jochen Keller and Armen Sedrakian. Axions from cooling compact stars. *Nucl. Phys. A*, 897:62–69, 2013.

[152] Armen Sedrakian. Axion cooling of neutron stars. *Phys. Rev. D*, 93(6):065044, 2016.

[153] Mikhail V. Beznogov, Ermal Rrapaj, Dany Page, and Sanjay Reddy. Constraints on Axion-like Particles and Nucleon Pairing in Dense Matter from the Hot Neutron Star in HESS J1731-347. *Phys. Rev. C*, 98(3):035802, 2018.

[154] Michael S. Turner. Axions from SN 1987a. *Phys. Rev. Lett.*, 60:1797, 1988.

[155] Luca Di Luzio et al. Probing the axion–nucleon coupling with the next generation of axion helioscopes. *Eur. Phys. J. C*, 82(2):120, 2022.

[156] Armen Sedrakian. Axion cooling of neutron stars. *Phys. Rev. D*, 93:065044, Mar 2016.

[157] Antoine Garcon et al. The cosmic axion spin precession experiment (CASPEr): a dark-matter search with nuclear magnetic resonance. *Quantum Sci. Technol.*, 3(1):014008, 2017.

[158] S. J. Asztalos et al. A SQUID-based microwave cavity search for dark-matter axions. *Phys. Rev. Lett.*, 104:041301, 2010.

[159] T. Nitta et al. Search for the Cosmic Axion Background with ADMX. 3 2023.

[160] Ben T. McAllister, Graeme Flower, Justin Kruger, Eugene N. Ivanov, Maxim Goryachev, Jeremy Bourhill, and Michael E. Tobar. The ORGAN Experiment: An axion haloscope above 15 GHz. *Phys. Dark Univ.*, 18:67–72, 2017.

[161] D. Alesini et al. Galactic axions search with a superconducting resonant cavity. *Phys. Rev. D*, 99(10):101101, 2019.

[162] S. Lee, S. Ahn, J. Choi, B. R. Ko, and Y. K. Semertzidis. Axion Dark Matter Search around 6.7 μeV. *Phys. Rev. Lett.*, 124(10):101802, 2020.

[163] P. Sikivie. Experimental Tests of the Invisible Axion. *Phys. Rev. Lett.*, 51:1415–1417, 1983. [Erratum: Phys.Rev.Lett. 52, 695 (1984)].

[164] Frank Wilczek. Two Applications of Axion Electrodynamics. *Phys. Rev. Lett.*, 58:1799, 1987.

[165] David J. E. Marsh. Axion Cosmology. *Phys. Rept.*, 643:1–79, 2016.

[166] Pierre Sikivie. Invisible Axion Search Methods. *Rev. Mod. Phys.*, 93(1):015004, 2021.

[167] Adrian Constantin. *References*, page 343–348. London Mathematical Society Student Texts. Cambridge University Press, 2016.

[168] Leanne D. Duffy, P. Sikivie, D. B. Tanner, Stephen J. Asztalos, C. Hagmann, D. Kinion, L. J Rosenberg, K. van Bibber, D. B. Yu, and R. F. Bradley. A high resolution search for dark-matter axions. *Phys. Rev. D*, 74:012006, 2006.

[169] Gray Rybka and ADMX Collaboration. Direct detection searches for axion dark matter. *Physics of the Dark Universe*, 4:14–16, September 2014.

[170] Deniz Aybas et al. Search for Axionlike Dark Matter Using Solid-State Nuclear Magnetic Resonance. *Phys. Rev. Lett.*, 126(14):141802, 2021.

[171] Budker Group. Casper, 2016.

[172] Deniz Aybas, Hendrik Bekker, John W. Blanchard, Dmitry Budker, Gary P. Centers, Nataniel L. Figueroa, Alexander V. Gramolin, Derek F. Jackson Kimball, Arne Wickenbrock, and Alexander O. Sushkov. Quantum sensitivity limits of nuclear magnetic resonance experiments searching for new fundamental physics. *Quantum Sci. Technol.*, 6(3):034007, 2021.

[173] D. F. Jackson Kimball, S. Afach, D. Aybas, J. W. Blanchard, D. Budker, G. Centers, M. Engler, N. L. Figueroa, A. Garcon, P. W. Graham, H. Luo, S. Rajendran, M. G. Sendra, A. O. Sushkov, T. Wang, A. Wickenbrock, A. Wilzewski, and T. Wu. Overview of the cosmic axion spin precession experiment (casper), 2018.

[174] L.F. Abbott and P. Sikivie. A cosmological bound on the invisible axion. *Physics Letters B*, 120(1):133–136, 1983.

[175] Luca Di Luzio, Belen Gavela, Pablo Quilez, and Andreas Ringwald. Dark matter from an even lighter QCD axion: trapped misalignment. *JCAP*, 10:001, 2021.

[176] John Preskill, Mark B. Wise, and Frank Wilczek. Cosmology of the Invisible Axion. *Phys. Lett. B*, 120:127–132, 1983.

[177] G. Hinshaw et al. Five-Year Wilkinson Microwave Anisotropy Probe (WMAP) Observations: Data Processing, Sky Maps, and Basic Results. *Astrophys. J. Suppl.*, 180:225–245, 2009.

[178] Planck Collaboration. Planck 2013 results. XXVI. Background geometry and topology of the Universe. *Astron. Astrophys.*, 571:A26, November 2014.

[179] Alan H. Guth. Inflationary universe: A possible solution to the horizon and flatness problems. *Phys. Rev. D*, 23:347–356, Jan 1981.

[180] Michael S. Turner. Coherent Scalar Field Oscillations in an Expanding Universe. *Phys. Rev. D*, 28:1243, 1983.

[181] Andrei D. Linde. Axions in inflationary cosmology. *Phys. Lett. B*, 259:38–47, 1991.

[182] Andrei D. Linde. Inflation and Axion Cosmology. *Phys. Lett. B*, 201:437–439, 1988.

[183] Jeff A. Dror, Hitoshi Murayama, and Nicholas L. Rodd. Cosmic axion background. *Phys. Rev. D*, 103(11):115004, 2021. [Erratum: Phys.Rev.D 106, 119902 (2022)].

[184] C. J. Hogan and M. J. Rees. AXION MINICLUSTERS. *Phys. Lett. B*, 205:228–230, 1988.

[185] Edward W. Kolb and Igor I. Tkachev. Axion miniclusters and Bose stars. *Phys. Rev. Lett.*, 71:3051–3054, 1993.

[186] Pierre Sikivie. Axion Cosmology. *Lect. Notes Phys.*, 741:19–50, 2008.

[187] Masahiro Kawasaki, Ken'ichi Saikawa, and Toyokazu Sekiguchi. Axion dark matter from topological defects. *Phys. Rev. D*, 91(6):065014, 2015.

[188] Alexander Vilenkin and Allen E. Everett. Cosmic strings and domain walls in models with goldstone and pseudo-goldstone bosons. *Phys. Rev. Lett.*, 48:1867–1870, Jun 1982.

[189] R. A. Battye and E. P. S. Shellard. Axion string constraints. *Phys. Rev. Lett.*, 73:2954–2957, Nov 1994.

[190] Michael Dine and Willy Fischler. The Not So Harmless Axion. *Phys. Lett. B*, 120:137–141, 1983.

[191] T W B Kibble. Topology of cosmic domains and strings. *Journal of Physics A: Mathematical and General*, 9(8):1387, aug 1976.

[192] Edmund J. Copeland, Robert C. Myers, and Joseph Polchinski. Cosmic F and D strings. *JHEP*, 06:013, 2004.

[193] J. Richard Gott. Closed timelike curves produced by pairs of moving cosmic strings: Exact solutions. *Phys. Rev. Lett.*, 66:1126–1129, Mar 1991.

[194] Edmund J. Copeland and T. W. B. Kibble. Cosmic Strings and Superstrings. *Proc. Roy. Soc. Lond. A*, 466:623–657, 2010.

[195] Bruce Allen and E. P. S. Shellard. Cosmic string evolution: a numerical simulation. *Phys. Rev. Lett.*, 64:119–122, 1990.

[196] T. W. B. Kibble. Topology of Cosmic Domains and Strings. *J. Phys. A*, 9:1387–1398, 1976.

[197] David Ellis, David J. E. Marsh, and Christoph Behrens. Axion Miniclusters Made Easy. *Phys. Rev. D*, 103(8):083525, 2021.

[198] P. J. E. Peebles. *The large-scale structure of the universe*. 1980.

[199] Volker Springel, Carlos S. Frenk, and Simon D. M. White. The large-scale structure of the Universe. *Nature*, 440:1137, 2006.

[200] Naoki Yoshida. Star Formation in the Early Universe. In *38th COSPAR Scientific Assembly*, volume 38, page 2, January 2010.

[201] V. Mukhanov. *Physical Foundations of Cosmology*. Cambridge University Press, Oxford, 2005.

[202] Malcolm Fairbairn, David J. E. Marsh, Jérémie Quevillon, and Simon Rozier. Structure formation and microlensing with axion miniclusters. *Phys. Rev. D*, 97(8):083502, 2018.

[203] Lawrence M. Widrow and Nick Kaiser. Using the Schroedinger Equation to Simulate Collisionless Matter. *The Astrophyscal Journal*, 416:L71, October 1993.

[204] Virgile Dandoy, Thomas Schwetz, and Elisa Todarello. A self-consistent wave description of axion miniclusters and their survival in the galaxy. *JCAP*, 09:081, 2022.

[205] Alan H. Guth, Mark P. Hertzberg, and C. Prescod-Weinstein. Do Dark Matter Axions Form a Condensate with Long-Range Correlation? *Phys. Rev. D*, 92(10):103513, 2015.

[206] Mohammad Hossein Namjoo, Alan H. Guth, and David I. Kaiser. Relativistic Corrections to Nonrelativistic Effective Field Theories. *Phys. Rev. D*, 98(1):016011, 2018.

[207] Eric Braaten, Abhishek Mohapatra, and Hong Zhang. Nonrelativistic Effective Field Theory for Axions. *Phys. Rev. D*, 94(7):076004, 2016.

[208] Lam Hui, Jeremiah P. Ostriker, Scott Tremaine, and Edward Witten. Ultralight scalars as cosmological dark matter. *Phys. Rev. D*, 95(4):043541, 2017.

[209] Xinyu Li, Lam Hui, and Tomer D. Yavetz. Oscillations and Random Walk of the Soliton Core in a Fuzzy Dark Matter Halo. *Phys. Rev. D*, 103(2):023508, 2021.

[210] Tomer D. Yavetz, Xinyu Li, and Lam Hui. Construction of wave dark matter halos: Numerical algorithm and analytical constraints. *Phys. Rev. D*, 105(2):023512, 2022.

[211] Lawrence M. Widrow and Nick Kaiser. Using the Schrodinger equation to simulate collisionless matter. *Astrophys. J. Lett.*, 416:L71–L74, 1993.

[212] Shan-Chang Lin, Hsi-Yu Schive, Shing-Kwong Wong, and Tzihong Chiueh. Self-consistent construction of virialized wave dark matter halos. *Phys. Rev. D*, 97(10):103523, 2018.

[213] Neal Dalal, Jo Bovy, Lam Hui, and Xinyu Li. Don't cross the streams: caustics from Fuzzy Dark Matter. *JCAP*, 03:076, 2021.

[214] J. Sakurai and Jim Napolitano. *Modern Quantum Mechanics Pearson New International Edition*. Pearson Deutschland, 2013.

[215] Rudolph E. Langer. On the connection formulas and the solutions of the wave equation. *Phys. Rev.*, 51:669–676, Apr 1937.

[216] A. S. Eddington. The distribution of stars in globular clusters. *MNRAS*, 76:572–585, May 1916.

[217] Albert R. Hibbs Richard P. Feynman. *Quantum Mechanics and Path Integrals: Emended Edition*. McGraw-Hill Education, 1965.

[218] Herman Feshbach Philip M. Morse. *Methods of Theoretical Physics, Part II*. McGraw-Hill Text, 1953.

[219] James Binney and Scott Tremaine. *Galactic Dynamics: Second Edition*. Princeton University Press, rev - revised, 2 edition, 2008.

[220] Yan Guo and Gerhard Rein. Isotropic Steady States in Galactic Dynamics. *Communications in Mathematical Physics*, 219(3):607–629, January 2001.

[221] Gerhard Rein and Alan D. Rendall. Compact support of spherically symmetric equilibria in nonrelativistic and relativistic galactic dynamics. *Math. Proc. Cambridge Phil. Soc.*, 128:363–380, 2000.

[222] Arthur S. Eddington. *The Internal Constitution of the Stars*. Cambridge Science Classics. Cambridge University Press, 1988.

[223] Alejandro Álvarez Melcón et al. Axion Searches with Microwave Filters: the RADES project. *JCAP*, 05:040, 2018.

[224] John David Jackson. *Classical Electrodynamics*. Wiley, 1998.

[225] Joshua W. Foster, Yonatan Kahn, Rachel Nguyen, Nicholas L. Rodd, and Benjamin R. Safdi. Dark Matter Interferometry. *Phys. Rev. D*, 103(7):076018, 2021.

[226] Joshua W. Foster, Nicholas L. Rodd, and Benjamin R. Safdi. Revealing the Dark Matter Halo with Axion Direct Detection. *Phys. Rev. D*, 97(12):123006, 2018.

[227] H. Peng et al. Cryogenic cavity detector for a large scale cold dark-matter axion search. *Nucl. Instrum. Meth. A*, 444:569–583, 2000.

[228] Asher Berlin, Raffaele Tito D'Agnolo, Sebastian A. R. Ellis, Christopher Nantista, Jeffrey Neilson, Philip Schuster, Sami Tantawi, Natalia Toro, and Kevin Zhou. Axion Dark Matter Detection by Superconducting Resonant Frequency Conversion. *JHEP*, 07(07):088, 2020.

[229] Giovanni Pierobon, Javier Redondo, Ken'ichi Saikawa, Alejandro Vaquero, and Guy D. Moore. Miniclusters from axion string simulations. 7 2023.

[230] Fabrizio Nesti and Paolo Salucci. The Dark Matter halo of the Milky Way, AD 2013. *JCAP*, 07:016, 2013.

[231] Benedikt Eggemeier, Javier Redondo, Klaus Dolag, Jens C. Niemeyer, and Alejandro Vaquero. First Simulations of Axion Minicluster Halos. *Phys. Rev. Lett.*, 125(4):041301, 2020.

[232] Jonah Herzog-Arbeitman, Mariangela Lisanti, Piero Madau, and Lina Necib. Empirical Determination of Dark Matter Velocities using Metal-Poor Stars. *Phys. Rev. Lett.*, 120(4):041102, 2018.

[233] Katherine Freese, Mariangela Lisanti, and Christopher Savage. Colloquium: Annual modulation of dark matter. *Rev. Mod. Phys.*, 85:1561–1581, 2013.

[234] Mattias Blennow, Juan Herrero-Garcia, and Thomas Schwetz. A halo-independent lower bound on the dark matter capture rate in the Sun from a direct detection signal. *JCAP*, 05:036, 2015.

[235] Stefano Magni. *Astrophysical aspects of dark matter direct detection*. PhD thesis, 11 2015.

[236] Ralph Schönrich, James Binney, and Walter Dehnen. Local kinematics and the local standard of rest. *Monthly Notices of the Royal Astronomical Society*, 403(4):1829–1833, apr 2010.

[237] Bradley J. Kavanagh, Thomas D. P. Edwards, Luca Visinelli, and Christoph Weniger. Stellar disruption of axion miniclusters in the Milky Way. *Phys. Rev. D*, 104(6):063038, 2021.

[238] Xuejian Shen, Huangyu Xiao, Philip F. Hopkins, and Kathryn M. Zurek. Disruption of Dark Matter Minihaloes in the Milky Way environment: Implications for Axion Miniclusters and Early Matter Domination. 7 2022.

[239] Peter Tinyakov, Igor Tkachev, and Konstantin Zioutas. Tidal streams from axion miniclusters and direct axion searches. *JCAP*, 01:035, 2016.

[240] V. I. Dokuchaev, Yu. N. Eroshenko, and I. I. Tkachev. Destruction of axion miniclusters in the Galaxy. *J. Exp. Theor. Phys.*, 125(3):434–442, 2017.

[241] J. Binney and S. Tremaine. *Galactic Dynamics*. Princeton University Press, Princeton, NJ USA, 2008.

[242] Leanne D. Duffy and Karl van Bibber. Axions as Dark Matter Particles. *New J. Phys.*, 11:105008, 2009.

[243] Pierre Sikivie and Pierre Sikivie. Dark matter axions. *International Journal of Modern Physics A*, 25:554–563, 2009.

[244] Masahiro Kawasaki and Kazunori Nakayama. Axions: Theory and cosmological role. *Annual Review of Nuclear and Particle Science*, 63:69–95, 2013.

[245] Roy J. Glauber. Coherent and incoherent states of the radiation field. *Phys. Rev.*, 131:2766–2788, 1963.

[246] Wei-Min Zhang, Da Hsuan Feng, and Robert Gilmore. Coherent States: Theory and Some Applications. *Rev. Mod. Phys.*, 62:867–927, 1990.

[247] Wei-Min Zhang. Coherent states in field theory. pages 297–323, 8 1999.

[248] Didier Robert and Monique Combescure. *Introduction to Coherent States*, pages 3–26. Springer International Publishing, Cham, 2021.

[249] Jean-Pierre Gazeau. Coherent states in quantum physics: an overview. *Journal of Physics: Conference Series*, 2667(1):012052, dec 2023.

[250] Lasha Berezhiani and Michael Zantedeschi. Evolution of coherent states as quantum counterpart of classical dynamics. *Phys. Rev. D*, 104(8):085007, 2021.

[251] E. T. Jaynes and F. W. Cummings. Comparison of quantum and semiclassical radiation theories with application to the beam maser. *IEEE Proc.*, 51:89–109, 1963.

[252] Bruce Shore and P. Knight. The jaynes-cummings model. *Journal of Modern Optics - J MOD OPTIC*, 40:1195–1238, 07 1993.

[253] Christopher Gerry and Peter Knight. *Introductory Quantum Optics*. Cambridge University Press, 2004.

[254] Tao Wang, Derek F. Jackson Kimball, Alexander O. Sushkov, Deniz Aybas, John W. Blanchard, Gary Centers, Sean R. O' Kelley, Arne Wickenbrock, Jiancheng Fang, and Dmitry Budker. Application of Spin-Exchange Relaxation-Free Magnetometry to the Cosmic Axion Spin Precession Experiment. *Phys. Dark Univ.*, 19:27–35, 2018.

[255] Asher Berlin and Kevin Zhou. Discovering QCD-Coupled Axion Dark Matter with Polarization Haloscopes. 9 2022.

[256] Jeff A. Dror, Stefania Gori, Jacob M. Leedom, and Nicholas L. Rodd. Sensitivity of Spin-Precession Axion Experiments. *Phys. Rev. Lett.*, 130(18):181801, 2023.

[257] Peter W. Graham and Surjeet Rajendran. New Observables for Direct Detection of Axion Dark Matter. *Phys. Rev. D*, 88:035023, 2013.

[258] Werner Bernreuther and Mahiko Suzuki. The electric dipole moment of the electron. *Rev. Mod. Phys.*, 63:313–340, 1991. [Erratum: Rev.Mod.Phys. 64, 633 (1992)].

[259] V.I. MAN'KO, G. MARMO, P. VITALE, and F. ZACCARIA. A GENERALIZATION OF THE JORDAN-SCHWINGER MAP: THE CLASSICAL VERSION AND ITS q DEFORMATION. *International Journal of Modern Physics A*, 09(31):5541–5561, dec 1994.

[260] Rotating-wave approximation. `https://en.wikipedia.org/wiki/Rotating-wave_approximation`.

[261] Gilbert Grynberg Claude Cohen-Tannoudji, Jacques Dupont-Roc. *Optical Bloch Equations*, chapter 5, pages 353–405. John Wiley & Sons, Ltd, 1998.

[262] Pierre Meystre and Murray Sargent. *Interaction Between Atoms and Quantized Fields*, pages 286–306. Springer Berlin Heidelberg, Berlin, Heidelberg, 1999.

[263] J.R. Johansson, P.D. Nation, and Franco Nori. Qutip: An open-source python framework for the dynamics of open quantum systems. *Computer Physics Communications*, (8):1760–1772, 2012.

[264] J.R. Johansson, P.D. Nation, and Franco Nori. Qutip 2: A python framework for the dynamics of open quantum systems. *Computer Physics Communications*, 184(4):1234–1240, 2013.

[265] Aaron Meurer, Christopher P. Smith, Mateusz Paprocki, Ondřej Čertík, Sergey B. Kirpichev, Matthew Rocklin, AMiT Kumar, Sergiu Ivanov, Jason K. Moore, Sartaj Singh, Thilina Rathnayake, Sean Vig, Brian E. Granger, Richard P. Muller, Francesco Bonazzi, Harsh Gupta, Shivam Vats, Fredrik Johansson, Fabian Pedregosa, Matthew J. Curry, Andy R. Terrel, Štěpán Roučka, Ashutosh Saboo, Isuru Fernando, Sumith Kulal, Robert Cimrman, and Anthony Scopatz. Sympy: symbolic computing in python. *PeerJ Computer Science*, 3:e103, January 2017.

[266] Ara N. Ioannisian, Narine Kazarian, Alexander J. Millar, and Georg G. Raffelt. Axion-photon conversion caused by dielectric interfaces: quantum field calculation. *JCAP*, 09:005, 2017.

[267] E. Aprile et al. Projected WIMP sensitivity of the XENONnT dark matter experiment. *JCAP*, 11:031, 2020.

[268] Silvia Garbari, Justin I. Read, and George Lake. Limits on the local dark matter density. *Monthly Notices of the Royal Astronomical Society*, 416(3):2318–2340, September 2011.

[269] J. Diemand, M. Kuhlen, P. Madau, M. Zemp, B. Moore, D. Potter, and J. Stadel. Clumps and streams in the local dark matter distribution. *Nature*, 454(7205):735–738, August 2008.

[270] Jo Bovy and Scott Tremaine. On the Local Dark Matter Density. *The Astrophysical Journal*, 756(1):89, September 2012.

[271] Volker Springel, Jie Wang, Mark Vogelsberger, Aaron Ludlow, Adrian Jenkins, Amina Helmi, Julio F. Navarro, Carlos S. Frenk, and Simon D. M. White. The Aquarius Project: the subhalos of galactic halos. *Mon. Not. Roy. Astron. Soc.*, 391:1685–1711, 2008.

[272] L. Gao, C. S. Frenk, M. Boylan-Kolchin, A. Jenkins, V. Springel, and S. D. M. White. The statistics of the subhalo abundance of dark matter haloes. *Monthly Notices of the Royal Astronomical Society*, 410(4):2309–2314, February 2011.

[273] Tomoaki Ishiyama, Steven Rieder, Junichiro Makino, Simon Portegies Zwart, Derek Groen, Keigo Nitadori, Cees de Laat, Stephen McMillan, Kei Hiraki, and Stefan Harfst. The cosmogrid simulation: Statistical properties of small dark matter halos. *The Astrophysical Journal*, 767(2):146, April 2013.

[274] R. Bernabei et al. First results from DAMA/LIBRA and the combined results with DAMA/NaI. *Eur. Phys. J. C*, 56:333–355, 2008.

[275] Z. Ahmed et al. Search for Weakly Interacting Massive Particles with the First Five-Tower Data from the Cryogenic Dark Matter Search at the Soudan Underground Laboratory. *Phys. Rev. Lett.*, 102:011301, 2009.

[276] X. Xu and E. R. Siegel. Dark Matter in the Solar System. 6 2008.

[277] Nicolás Bernal, Matti Heikinheimo, Tommi Tenkanen, Kimmo Tuominen, and Ville Vaskonen. The Dawn of FIMP Dark Matter: A Review of Models and Constraints. *Int. J. Mod. Phys. A*, 32(27):1730023, 2017.

[278] Annika H. G. Peter. Dark matter in the solar system I: The distribution function of WIMPs at the Earth from solar capture. *Phys. Rev. D*, 79:103531, 2009.

[279] Audun Theodorsen, Odd Erik Garcia, and Martin Rypdal. Statistical properties of a filtered Poisson process with additive random noise: Distributions, correlations and moment estimation. *Phys. Scripta*, 92(5):054002, 2017.

[280] Emanuel Parzen. *Stochastic Processes*. Society for Industrial and Applied Mathematics, 1999.

[281] G. E. Uhlenbeck and L. S. Ornstein. On the theory of the brownian motion. *Phys. Rev.*, 36:823–841, Sep 1930.

[282] V. Kontorevich and V. Lyandres. Impulsive noise: A nontraditional approach. *Signal Processing*, 51(2):121–132, 1996.

[283] Tomasz Rolski. A note on the history of the poisson process. *Antiquitates Mathematicae*, 13:null, 2019.

[284] Janine Baerbel Illian, A Penttinen, H Stoyan, and D Stoyan. *Statistical Analysis and Modelling of Spatial Point Patterns*. John Wiley & Sons, Ltd, United States, 2008.

[285] Steven M. Kay. *Fundamentals of statistical signal processing / Steven M. Kay.* Prentice Hall signal processing series. Prentice Hall, Englewood Cliffs, N.J, 2013 - 2013.

[286] Alan V. Oppenheim, Ronald W. Schafer, and John R. Buck. *Discrete-time signal processing / Alan V. Oppenheim, Ronald W. Schafer, with John R. Buck.* Prentice-Hall signal processing series. Prentice Hall, Upper Saddle River, N.J, second edition. edition, 1999 - 1999.

[287] Joseph Goodman. Statistical properties of laser speckle patterns. *Laser Speckle and Related Phenomena*, 9:57, 12 1963.

[288] Peter A. Sturrock, J. D. Scargle, G. Walther, and M. S. Wheatland. Combined and comparative analysis of power spectra. *Solar Phys.*, 227:137–153, 2008.

[289] Student. The probable error of a mean. *Biometrika*, 6(1):1–25, 1908.

[290] B. L. Welch. The generalization of 'student's' problem when several different population variances are involved. *Biometrika*, 34(1/2):28–35, 1947.

[291] Frank Wilcoxon. Individual comparisons by ranking methods. *Biometrics Bulletin*, 1(6):80–83, 1945.

[292] H. B. Mann and D. R. Whitney. On a Test of Whether one of Two Random Variables is Stochastically Larger than the Other. *The Annals of Mathematical Statistics*, 18(1):50 – 60, 1947.

[293] Jun-Qian Jiang, Gen Ye, and Yun-Song Piao. Return of Harrison–Zeldovich spectrum in light of recent cosmological tensions. *Mon. Not. Roy. Astron. Soc.*, 527(1):L54–L59, 2023.

[294] George F. Smoot et al. Structure in the COBE differential microwave radiometer first year maps. *Astrophys. J. Lett.*, 396:L1–L5, 1992.

[295] W. J. G. de Blok. The Core-Cusp Problem. *Advances in Astronomy*, 2010:789293, January 2010.

[296] Ben Moore, Thomas R. Quinn, Fabio Governato, Joachim Stadel, and George Lake. Cold collapse and the core catastrophe. *Mon. Not. Roy. Astron. Soc.*, 310:1147–1152, 1999.

[297] V. C. Rubin, Jr. Ford, W. K., and N. Thonnard. Extended rotation curves of high-luminosity spiral galaxies. IV. Systematic dynamical properties, Sa -> Sc. *The Astrophysical Journall*, 225:L107–L111, November 1978.

[298] E. Athanassoula, editor. *Internal kinematics and dynamics of galaxies*, volume 100 of *IAU Symposium*, January 1983.

[299] S. M. Kent. Dark matter in spiral galaxies. I. Galaxies with optical rotation curves. *The Astronomical Journal*, 91:1301–1327, June 1986.

[300] T. K. Chan, D. Kereš, J. Oñorbe, P. F. Hopkins, A. L. Muratov, C. A. Faucher-Giguère, and E. Quataert. The impact of baryonic physics on the structure of dark matter haloes: the view from the FIRE cosmological simulations. *Mon. Not. Roy. Astron. Soc.*, 454(3):2981–3001, 2015.

[301] Claude-André Faucher-Giguère, Dušan Kereš, and Chung-Pei Ma. The baryonic assembly of dark matter haloes. *Monthly Notices of the Royal Astronomical Society*, 417(4):2982–2999, November 2011.

[302] Shengqi Yang, Xiaolong Du, Zhichao Carton Zeng, Andrew Benson, Fangzhou Jiang, Ethan O. Nadler, and Annika H. G. Peter. Gravothermal Solutions of SIDM Halos: Mapping from Constant to Velocity-dependent Cross Section. *Astrophys. J.*, 946(1):47, 2023.

[303] Sophia Nasr. Gravothermal evolution of self-interacting dark matter halos in the short mean free path regime - virtual, feb 2024. PIRSA:24020064 see, `https://pirsa.org`.

[304] Dehghani, R., Salucci, P., and Ghaffarnejad, H. Navarro-frenk-white dark matter profile and the dark halos around disk systems□. *A&A*, 643:A161, 2020.

[305] Jürg Diemand and Ben Moore. The Structure and Evolution of Cold Dark Matter Halos. *Advanced Science Letters*, 4(2):297–310, February 2011.

[306] W. J. G. de Blok. The Core-Cusp Problem. *Adv. Astron.*, 2010:789293, 2010.

[307] A. Burkert. The structure of dark matter halos in dwarf galaxies. *The Astrophysical Journal*, 447(1):L25, jul 1995.

[308] Se-Heon Oh, W. J. G. de Blok, Elias Brinks, Fabian Walter, and Jr. Kennicutt, Robert C. Dark and Luminous Matter in THINGS Dwarf Galaxies. *The Astronomical Journal*, 141(6):193, June 2011.

[309] David N. Spergel and Paul J. Steinhardt. Observational evidence for selfinteracting cold dark matter. *Phys. Rev. Lett.*, 84:3760–3763, 2000.

[310] Thomas Hambye. Hidden vector dark matter. *JHEP*, 01:028, 2009.

[311] Francesco D'Eramo and Jesse Thaler. Semi-annihilation of Dark Matter. *JHEP*, 06:109, 2010.

[312] Sean Tulin and Hai-Bo Yu. Dark Matter Self-interactions and Small Scale Structure. *Phys. Rept.*, 730:1–57, 2018.

[313] W. J. G. de Blok, F. Walter, E. Brinks, C. Trachternach, S-H. Oh, and R. C. Kennicutt, Jr. High-Resolution Rotation Curves and Galaxy Mass Models from THINGS. *Astron. J.*, 136:2648–2719, 2008.

[314] Mark Vogelsberger, Jesús Zavala, Katelin Schutz, and Tracy R. Slatyer. Evaporating the Milky Way halo and its satellites with inelastic self-interacting dark matter. 5 2018.

[315] Abraham Loeb and Neal Weiner. Cores in Dwarf Galaxies from Dark Matter with a Yukawa Potential. *Phys. Rev. Lett.*, 106:171302, 2011.

[316] Katelin Schutz and Tracy R. Slatyer. Self-Scattering for Dark Matter with an Excited State. *JCAP*, 01:021, 2015.

[317] Hiroya Nishikawa, Kimberly K. Boddy, and Manoj Kaplinghat. Accelerated core collapse in tidally stripped self-interacting dark matter halos. *Phys. Rev. D*, 101(6):063009, 2020.

[318] Jun Koda and Paul R. Shapiro. Gravothermal collapse of isolated self-interacting dark matter haloes: N-body simulation versus the fluid model. *Monthly Notices of the Royal Astronomical Society*, 415(2):1125–1137, August 2011.

[319] Shmuel Balberg and Stuart L. Shapiro. Gravothermal collapse of selfinteracting dark matter halos and the origin of massive black holes. *Phys. Rev. Lett.*, 88:101301, 2002.

[320] Shmuel Balberg, Stuart L. Shapiro, and Shogo Inagaki. Selfinteracting dark matter halos and the gravothermal catastrophe. *Astrophys. J.*, 568:475–487, 2002.

[321] Nadav Joseph Outmezguine, Kimberly K. Boddy, Sophia Gad-Nasr, Manoj Kaplinghat, and Laura Sagunski. Universal gravothermal evolution of isolated self-interacting dark matter halos for velocity-dependent cross-sections. *Mon. Not. Roy. Astron. Soc.*, 523(3):4786–4800, 2023.

[322] DEBORAH TEPPER HAIMO. Expansions in terms of generalized heat polynomials and of their appell transforms. *Journal of Mathematics and Mechanics*, 15(5):735–758, 1966.

[323] Xiaoyong Chu and Camilo Garcia-Cely. Core formation from self-heating dark matter. *JCAP*, 07:013, 2018.

[324] Martin J. White. The Mass of a halo. *Astron. Astrophys.*, 367:27, 2001.

[325] Yonit Hochberg, Eric Kuflik, Hitoshi Murayama, Tomer Volansky, and Jay G. Wacker. Model for Thermal Relic Dark Matter of Strongly Interacting Massive Particles. *Phys. Rev. Lett.*, 115(2):021301, 2015.

[326] Rupa Basu, Debasish Majumdar, Ashadul Halder, and Shibaji Banerjee. Addressing the self-interaction for ELDER dark matter from the 21-cm signal. 4 2023.

[327] R. N. Mohapatra, Fredrick I. Olness, R. Stroynowski, and V. L. Teplitz. Searching for strongly interacting massive particles (SIMPs). *Phys. Rev. D*, 60:115013, 1999.

[328] Yonit Hochberg. SIMP Dark Matter. *SciPost Phys. Lect. Notes*, 59:1, 2022.

[329] Joshua J. Adams, Joshua D. Simon, Maximilian H. Fabricius, Remco C. E. van den Bosch, John C. Barentine, Ralf Bender, Karl Gebhardt, Gary J. Hill, Jeremy D. Murphy, R. A. Swaters, Jens Thomas, and Glenn van de Ven. Dwarf Galaxy Dark Matter Density Profiles Inferred from Stellar and Gas Kinematics. *The Astrophysical Journal*, 789(1):63, July 2014.

[330] Se-Heon Oh et al. High-resolution mass models of dwarf galaxies from LITTLE THINGS. *Astron. J.*, 149:180, 2015.

[331] Tri Nguyen, Siddharth Mishra-Sharma, Reuel Williams, and Lina Necib. Uncovering dark matter density profiles in dwarf galaxies with graph neural networks. *Phys. Rev. D*, 107:043015, Feb 2023.

[332] H. Fritzsch, M. Gell-Mann, and H. Leutwyler. Advantages of the color octet gluon picture. *Physics Letters B*, 47(4):365–368, 1973.

[333] David J. Gross and Frank Wilczek. Ultraviolet behavior of non-abelian gauge theories. *Phys. Rev. Lett.*, 30:1343–1346, Jun 1973.

[334] A.A. Belavin, A.M. Polyakov, A.S. Schwartz, and Yu.S. Tyupkin. Pseudoparticle solutions of the yang-mills equations. *Physics Letters B*, 59(1):85–87, 1975.

[335] G. ’t Hooft. Symmetry Breaking through Bell-Jackiw Anomalies. *Physical Review Letters*, 37(1):8–11, July 1976.

[336] Stefan Vandoren and Peter van Nieuwenhuizen. Lectures on instantons. 2 2008.

[337] Jihn E. Kim and Gianpaolo Carosi. Axions and the Strong CP Problem. *Rev. Mod. Phys.*, 82:557–602, 2010. [Erratum: Rev.Mod.Phys. 91, 049902 (2019)].

[338] William J. Marciano and Heinz Pagels. Quantum Chromodynamics: A Review. *Phys. Rept.*, 36:137, 1978.

[339] D J Wallace. Solitons and instantons: An introduction to solitons and instantons in quantum field theory. *Physics Bulletin*, 34(1):29, jan 1983.

[340] M.A. Shifman, A.I. Vainshtein, and V.I. Zakharov. Instanton density in a theory with massless quarks. *Nuclear Physics B*, 163:46–56, 1980.

[341] C.G. Callan, R.F. Dashen, and D.J. Gross. The structure of the gauge theory vacuum. *Physics Letters B*, 63(3):334–340, 1976.

[342] R. Jackiw and C. Rebbi. Vacuum Periodicity in a Yang-Mills Quantum Theory. *Phys. Rev. Lett.*, 37:172–175, 1976.

[343] Jihn E. Kim. Light Pseudoscalars, Particle Physics and Cosmology. *Phys. Rept.*, 150:1–177, 1987.

[344] Maxim Pospelov and Adam Ritz. Theta vacua, QCD sum rules, and the neutron electric dipole moment. *Nucl. Phys. B*, 573:177–200, 2000.

[345] F. K. Guo, R. Horsley, U. G. Meissner, Y. Nakamura, H. Perlt, P. E. L. Rakow, G. Schierholz, A. Schiller, and J. M. Zanotti. The electric dipole moment of the neutron from 2+1 flavor lattice QCD. *Phys. Rev. Lett.*, 115(6):062001, 2015.

[346] Eigo Shintani, Thomas Blum, Taku Izubuchi, and Amarjit Soni. Neutron and proton electric dipole moments from $N_f = 2 + 1$ domain-wall fermion lattice QCD. *Phys. Rev. D*, 93(9):094503, 2016.

[347] Measurement of the permanent electric dipole moment of the neutron. *Phys. Rev. Lett.*, 124:081803, Feb 2020.

[348] Gerard 't Hooft. Symmetry Breaking Through Bell-Jackiw Anomalies. *Phys. Rev. Lett.*, 37:8–11, 1976.

[349] Michael Dine, Willy Fischler, and Mark Srednicki. A Simple Solution to the Strong CP Problem with a Harmless Axion. *Phys. Lett. B*, 104:199–202, 1981.

[350] Jihn E. Kim. Weak-interaction singlet and strong CP invariance. *Phys. Rev. Lett.*, 43:103–107, Jul 1979.

[351] Xinyu Li, Lam Hui, and Greg L. Bryan. Numerical and Perturbative Computations of the Fuzzy Dark Matter Model. *Phys. Rev. D*, 99(6):063509, 2019.

[352] Philip Mocz, Mark Vogelsberger, Victor H. Robles, Jesús Zavala, Michael Boylan-Kolchin, Anastasia Fialkov, and Lars Hernquist. Galaxy formation with BECDM – I. Turbulence and relaxation of idealized haloes. *Mon. Not. Roy. Astron. Soc.*, 471(4):4559–4570, 2017.

[353] Hsi-Yu Schive, Tzihong Chiueh, and Tom Broadhurst. Cosmic Structure as the Quantum Interference of a Coherent Dark Wave. *Nature Phys.*, 10:496–499, 2014.

[354] Bodo Schwabe, Jens C. Niemeyer, and Jan F. Engels. Simulations of solitonic core mergers in ultralight axion dark matter cosmologies. *Phys. Rev. D*, 94(4):043513, 2016.

[355] Bodo Schwabe, Mateja Gosenca, Christoph Behrens, Jens C. Niemeyer, and Richard Easther. Simulating mixed fuzzy and cold dark matter. *Phys. Rev. D*, 102(8):083518, 2020.

[356] Stefan Knirck, Alexander J. Millar, Ciaran A. J. O'Hare, Javier Redondo, and Frank D. Steffen. Directional axion detection. *JCAP*, 11:051, 2018.

[357] Hsi-Yu Schive, Ming-Hsuan Liao, Tak-Pong Woo, Shing-Kwong Wong, Tzihong Chiueh, Tom Broadhurst, and W. Y. Pauchy Hwang. Understanding the Core-Halo Relation of Quantum Wave Dark Matter from 3D Simulations. *Phys. Rev. Lett.*, 113(26):261302, 2014.

[358] Tak-Pong Woo. High Resolution Simulation on Structure Formation with Extremely Light Bosonic Dark Matter. *Astrophys. J.*, 697:850–861, 2009.

[359] Nicholas Wheeler. *Lecture notes in Quantum Mechanics (Miscellaneous Essays): Angular Momentum, Spin - Spin Matrices for Arbitrary Spin*. Reed College Physics Department, 2000.

[360] I. M. Duck, P. M. Stevenson, and E. C. G. Sudarshan. The sense in which a "weak measurement" of a spin-½ particle's spin component yields a value 100. *Phys. Rev. D*, 40:2112–2117, Sep 1989.

[361] Norbert Wiener. Generalized harmonic analysis. *Acta Mathematica*, 55:117–258, 1930.

[362] P. A. Blight. The Analysis of Time Series: An Introduction. *Journal of the Royal Statistical Society Series C*, 40(1):178–179, March 1991.

[363] Robert S. Strichartz. A guide to distribution theory and fourier transforms. 1994.

[364] Günter Last and Mathew Penrose. *Poisson Processes*, page 19–25. Institute of Mathematical Statistics Textbooks. Cambridge University Press, 2017.

[365] S.M. Ross. *Stochastic processes*. Wiley series in probability and statistics: Probability and statistics. Wiley, 1996.

[366] Farzad Zangeneh-Nejad and Romain Fleury. Disorder-induced signal filtering with topological metamaterials, 2020.

[367] M. Berton, I. Björklund, A. Lähteenmäki, E. Congiu, E. Järvelä, G. Terreran, and G. La Mura. Line shapes in narrow-line seyfert 1 galaxies: a tracer of physical properties? *Contributions of the Astronomical Observatory Skalnaté Pleso*, 50(1), Jan 2020.

[368] Michael P. Fay and Michael A. Proschan. Wilcoxon-Mann-Whitney or t-test? On assumptions for hypothesis tests and multiple interpretations of decision rules. *Statistics Surveys*, 4(none):1 – 39, 2010.

[369] *Mann–Whitney Test*, pages 327–329. Springer New York, New York, NY, 2008.

[370] George W. Divine, H. James Norton, Anna E. Barón, and Elizabeth Juarez-Colunga. The wilcoxon–mann–whitney procedure fails as a test of medians. *The American Statistician*, 72(3):278–286, 2018.

[371] Ronán M. Conroy. What hypotheses do "nonparametric" two-group tests actually test? *The Stata Journal*, 12(2):182–190, 2012.

[372] Roy C. Milton. An extended table of critical values for the mann-whitney (wilcoxon) two-sample statistic. *Journal of the American Statistical Association*, 59(307):925–934, 1964.

[373] J.L. Fleiss, B. Levin, and M.C. Paik. *Statistical Methods for Rates and Proportions*. Wiley Series in Probability and Statistics. Wiley, 2013.

[374] George Casella and Roger L. Berger. *Statistical Inference Vol. 70*. Duxbury Press Belmont, Ca, 1990.

[375] Yonit Hochberg, Eric Kuflik, Tomer Volansky, and Jay G. Wacker. Mechanism for thermal relic dark matter of strongly interacting massive particles. *Phys. Rev. Lett.*, 113:171301, Oct 2014.

Acknowledgements

I would like to thank Prof. Joerg Jaeckel for his support and commitment to my process throughout these four years and for his always engaging physics discussions. The work we did together has taught me a lot and it has given me many valuable tools to continue my professional journey. I would also like to thank Prof. Laura Covi for her interesting discussions on physics and for the valuable insights gained from the project we worked on together. It was truly a pleasure to collaborate.

I would like to thank my colleagues Vigile Dandoy and Cedric Quint, the work we did in collaboration opened valuable discussion spaces that contributed greatly to my professional training and to the development of this thesis.

A Julián Calle y Carlos Gaviria, quiero agradecerles por haber abierto siempre espacio para la discusión científica. Nuestras discusiones me dieron claridad y dirección en muchas ocasiones. Gracias por apoyar y contribuir a mi formación.

A mi familia y a mis amigos gracias por creer siempre en mi, por celebrar mis triunfos y vivir los momentos dificiles conmigo. Me mostraron que su amor supera la distancia que nos separa. Para ustedes y para mi, mil y mil gracias.